IEKP-KA/2003-23

Untersuchungen zur Strahlenhärte von Siliziumsensoren

Alexander Dierlamm

Zur Erlangung des akademischen Grades eines
DOKTORS DER NATURWISSENSCHAFTEN
von der Fakultät für Physik
der Universität Karlsruhe (TH)

genehmigte

DISSERTATION

von

Dipl. Phys. Alexander Dierlamm
aus Pforzheim

Tag der mündlichen Prüfung: 31.10.2003
Referent: Prof. Dr. Wim de Boer, Institut für Experimentelle Kernphysik
Koreferent: Prof. Dr. Thomas Müller, Institut für Experimentelle Kernphysik

Deutsche Zusammenfassung

Das Standardmodell der Teilchenphysik ist eine umfassende Theorie, die Elementarteilchen und ihre Wechselwirkungen beschreibt. Bis zu den heute erreichbaren Energien ($E_{cm} = 200\,GeV$ bei LEP[1]) hat es die härtesten Tests bestanden. Bei höheren Energien erwartet man die Entdeckung neuer Teilchen wie des Higgs-Bosons und supersymmetrischer Partner unserer Materie, die von den dazu gehörenden Theorien[2] vorhergesagt werden.
Mit der neuen Generation von Teilchenbeschleunigern wird dem Experimentalphysiker dieser Energiebereich eröffnet. Der Large Hadron Collider am CERN wird eine solche Maschine, die Protonen mit einer Schwerpunktsenergie von $14\,TeV$ an vier Wechselwirkungspunkten zur Kollision bringt. Einer der vier Teilchendetektoren ist der Compact Muon Solenoid (CMS). Er ist optimiert um nach neuen Teilchen zu suchen, insbesondere um das Higgs-Boson im gesamten theoretisch möglichen Massebereich nachzuweisen. Hierzu benötigt man unter anderem einen hochauflösenden Spurdetektor, der zusammen mit dem Müon-Detektorsystem eine hohe Impulsauflösung erreicht. Eine weitere wichtige Aufgabe ist die Suche nach isolierten Leptonen von semi-leptonischen Zerfällen und b-Tagging.
Dieser Spurdetektor wird bei CMS vollständig aus 24328 Siliziumstreifensensoren bestehen mit einer aktiven Gesamtfläche von $206\,m^2$. Die enorme Größe (Durchmesser 2,4 m, Länge 5,4 m), die Anzahl der Komponenten und die erschwerte Zugänglichkeit erfordern ein hohes Maß an Qualitätssicherung während der Produktion.
Da die Strahlenbelastung am LHC sehr groß sein wird, wird neben der Kontrolle der elektrischen Eigenschaften der gelieferten Sensoren auch eine Qualifizierung der Strahlenhärte durchgeführt. Die Streifensensoren werden nach 10 Jahren einer maximalen Fluenz ausgesetzt sein, die $1{,}6 \cdot 10^{14}$ Neutronen pro cm^2 bei $1\,MeV$ entspricht.
Der Aufbau des Bestrahlungstestzentrums (Irradiation Qualification Centre) in Karlsruhe ist ein Hauptteil dieser Arbeit. Als Teilchenquelle dient das Kompaktzyklotron am Forschungszentrum Karlsruhe. Die Bestrahlung wird dort mit 26 MeV-Protonen bei einem Strom von etwa 2 μA durchgeführt. Qualifiziert werden etwa 1% der Sensoren (15 unterschiedliche Geometrien mit einer durchschnittlichen Fläche von $\sim 80\,cm^2$) und 5% der Minisensoren ($23 \times 16\,mm^2$), die auf den freien Flächen der Wafer prozessiert werden. Diese werden bei Temperaturen von $\lesssim -10°C$ bestrahlt, um das Ausheilen der Strahlenschäden zu kontrollieren und thermisch erzeugte Defekte zu verhindern.
Strahlenschäden in Silizium entstehen durch das Herausschlagen von Siliziumatomen aus dem Kristallgitter, was zu Fehlstellen und Zwischengitteratomen führt. Diese können durch das Gitter wandern und komplexe Defekte formen, deren elektrische Eigenschaften sich vom unbestrahlten Material unterscheiden. Dabei erhöht sich der Leckstrom und die effektive Dotierung N_{eff} des Materials wird verändert. Bei hohen Fluenzen wächst die Depletionsspannung ($V_{fd} \sim N_{eff}$), linear mit der Fluenz an. Die volle Ladungssammlung wird erst ab der Depletionsspannung erreicht, weshalb diese nicht die Durchbruchspannung des Sensors oder die maximale Versorgungsspannung überschreiten darf.
Vor und nach der Bestrahlung werden die Sensoren elektronisch vermessen. Dazu gehören die globalen IV[3]- und CV[4]-Kurven, aus denen die Durchbruchfestigkeit, der Leckstrom und die Depletionsspannung gewonnen werden. Desweiteren werden auf einigen Streifen folgende Parameter bestimmt: Leckstrom, Biaswiderstand, Kopplungskapazität, Leckstrom durch das Oxid, Zwischenstreifenwiderstand und -kapazität.
Das so genannte "Hamburg-Modell" liefert eine Parametrisierung der effektiven Dotierung in

[1] Ringbeschleuniger für Elektronen und Positronen am CERN
[2] Higgs-Feld mit spontaner Symmetriebrechung und das minimal supersymmetrische Standardmodell
[3] Strom über Spannung
[4] Totale Kapazität über Spannung

Abhängigkeit von Fluenz und Ausheilzeit auf der Grundlage von reaktions-kinetischen Überlegungen. Das Modell kann an die gemessenen Daten von Minisensoren angepaßt werden. Mit den gewonnen Parametern wird die Entwicklung der Depletionsspannung während der Laufzeit des Experimentes für unterschiedliche Szenarien für Temperatur und Fluenz berechnet.
Da Protonen nicht nur mit dem Gitter sondern auch mit den Elektronen wechselwirken, erzeugen sie im Gegensatz zu Neutronen auch Oberflächenschäden. Dabei lädt sich das Oxid positiv auf und stört dadurch das Feld zwischen den Streifen. Die Zwischenstreifenkapazität erhöht sich und damit auch das elektronische Rauschen in der Ausleseelektronik. Bei Minisensoren mit erhöhter Flachbandspannung, welche ein Maß für die Oxidqualität ist, wurde auch ein größerer Anstieg der Zwischenstreifenkapazität nach Bestrahlung gemessen. Daraufhin wurde eine maximale Flachbandspannung von $10\,V$ festgelegt, welche in der Prozeß-Kontrolle überprüft wird.
Das Depletionsverhalten von Diode und Minisensor wurde noch eingehender untersucht, da davon die Signalhöhe abhängt. Unbestrahlt liegt die Depletionsspannung (gemessen über die CV-Kurve) von Streifensensoren etwa 20% (abhängig von Dicke und dem Verhältnis von Streifenbreite zu Streifenabstand) höher als in gleich dotierten Dioden. Nach der Bestrahlung konnte der Unterschied nicht mehr beobachtet werden. Das liegt an der Inversion der effektiven Dotierungskonzentration, welche mit Hilfe der Transient Current Technique[(1)] (TCT) gemessen wurde. Die Depletion des Sensors beginnt nun an der unstrukturierten Elektrode der Rückseite und wandert bis zu den Streifen.
Die Ladungssammlung der Sensoren wurde mit der TCT und einem infraroten Laser gemessen, der ein minimal ionisierendes Teilchen simuliert. Vor Bestrahlung erreicht die Diode die maximale Ladungssammlung bei der Depletionsspannung, die aus der CV-Kurve gewonnen wurde. Bei Minisensoren hat sich schon vor Bestrahlung eine Verschiebung der maximalen Ladungssammlung zu höheren Spannungen gezeigt, die mit der Flachbandspannung zu korrelieren scheint.
Die strahleninduzierten Defekte können freie Ladungsträger kurzfristig binden (Trapping) und reduzieren somit die Ladungssammlungseffizienz. Mit zunehmender Spannung nimmt der Effekt ab, da die Driftzeit kürzer wird und weniger Zeit für den Einfangprozeß bleibt.
Wenn die Strahlenbelastung noch größer wird als bei LHC, wird die Ladungssammlungseffizienz sehr gering. Das Kühlen der Sensoren auf unter $130\,K$ ermöglicht dann einen weiteren Betrieb, da die Defekte neutralisiert und in diesem Zustand eingefroren werden können. Die Ladungssammlungseffizienz steigt dann gemäß dem Lazarus-Effekt wieder an.
Die Ablenkung der generierten Ladungsträgern im Silizium bei diesen Temperaturen und Magnetfeldern um $4T$ wird allerdings sehr groß und muß bei der Positionsbestimmung des Teilchendurchtritts berücksichtigt werden. Diese sogenannte Lorentzverschiebung kann von Raumtemperatur bis etwa $150\,K$ mit einer einfachen Formel ($\tan\Theta_L = \mu_H B$) berechnet werden. Bei tieferen Temperaturen wird die gemessene Lorentzverschiebung viel größer. Hier wird ein alternativer Ansatz vorgeschlagen, der die zufällige Streuung durch die drei häufigsten Streuprozesse - Phononenstreuung, Streuung an ionisierten Störstellen und Streuung zwischen den Energieminima im Leitungsband - und die Anisotropie der effektiven Elektronenmassen in Silizium berücksichtigt. Das Zusammenspiel der Anisotropie und den energieabhängigen Streuzeiten bewirkt eine Umverteilung der Ladungsträger in Leitungsbandminima, wo sie eine große Lorentzverschiebung erfahren. Damit konnte der gemessene Anstieg bei sinkender Temperatur berechnet werden.

[(1)] Bei der TCT werden Ladungsträger mit einem roten Laser oberflächennah erzeugt. Der induzierte Strom dieser driftenden Ladungswolke is proportional der Driftgeschwindigkeit, welche wiederum proportional zum elektrischen Feld ist. Damit ist das gemessene Signal ein ungefähres Abbild des elektrischen Feldes.

Studies on the Radiation Hardness of Silicon Sensors

Alexander Dierlamm

November 24, 2003

Contents

Introduction

In the 1970's Josef Kemmer started to adapt microelectronic technology to produce the first silicon detectors needed by experimental particle physicists. This started a fast development of silicon sensors for particle detection at high rates and high resolution.
Modern experiments in high energy physics are equipped with silicon micro-strip sensors as tracking devices. For example, DELPHI[(1)] was equipped with a silicon tracker with an active area of $1.5\,m^2$, CDF[(2)] has a silicon strip tracker with an active area of $7.5\,m^2$ and the silicon strip tracker of CMS[(3)] will have a huge active area of $206\,m^2$! This enormous size is made possible by the use of large silicon wafers supplied by industry, which reduces the number of individual sensors.
This large area is necessary to cope with the huge amount of particles produced in collisions at higher energies, since the occupation of the tracker has to be small in order to allow track separation in the analysis. In addition a high resolution improves the reconstruction. Strip sensors with a pitch of about $100\,\mu m$ achieve resolutions below $5\,\mu m$ making use of charge sharing between capacitively coupled strips and analogue read-out.
At high energies the cross section decreases and the luminosity has to be increased to get acceptable event rates. As a result the silicon sensors are operated in a harsh radiation environment, especially at hadron colliders like the future Large Hadron Collider (LHC) at CERN.
Radiation damage has consequences for the operation of the sensors. The full depletion voltage increases and may exceed the breakdown voltage of the sensor. Then one has to operate the sensor in under-depleted mode and part of the signal is lost. Generated charges are also lost by trapping, when the de-trapping time is longer than the integration time of the read-out electronics. The increased leakage current increases noise and might heat the sensor to a level where a thermal run-away occurs. In addition to the bulk defects, the oxide on the surface is charged up by ionising radiation and the electric field between the strips is modified. This affects the inter-strip capacitance, which strongly influences the strip noise.
In the CMS experiment at the LHC all tracker components have to undergo a detailed quality assurance including irradiation qualification during production.
This thesis concentrates on the functionality of silicon strip sensors under LHC conditions.
Chapter 1 introduces the operation of silicon sensors and discusses radiation damage. An overview of the LHC and the CMS experiment is given in Chapter 2 including some particle physics background. The irradiation qualification of the CMS silicon strip sensors with protons is presented in Chapter 3. Therein the setup for the irradiation is described and the results of the performed tests are discussed. The measured full depletion voltages can be parameterised by

[(1)] **DE**tector for **L**epton, **P**hoton and **H**adron **I**dentification at the Large Electron Positron Collider, CERN, Geneva
[(2)] **C**ollider **D**etector at **F**ermilab at the Tevatron, Fermi National Laboratory, Chicago
[(3)] **C**ompact **M**uon **S**olenoid at the Large Hadron Collider, CERN, Geneva

the 'Hamburg' model. This parametrisation can in turn be used to calculate the full depletion voltage for different scenarios concerning fluences and annealing times.
In Chapter 4 further studies on the depletion behaviour and the charge collection of non-irradiated and irradiated sensors using the Transient Current Technique are performed.
At radiation levels even higher than at LHC trapping effects reduce the charge collection efficiency dramatically. This problem can be cured operating the silicon sensors at cryogenic temperatures ($\lesssim 130\ K$). But at low temperatures and high magnetic fields (as used for momentum measurement), the Lorentz shift in silicon sensors shows a steep increase, which would worsen the position resolution without a good knowledge of the shift. This strong increase is not expected using the usual formula $\tan\Theta_L = \mu_H B$. Therefore an alternative approach is presented in Chapter 5 considering random scattering processes and the anisotropic effective masses in silicon.

Chapter 1

Principles of Silicon Detectors

Many semiconductor materials (Si, Ge, GaAs ...) are used as radiation detectors. They have different intrinsic properties such as absorption length or number of generated electron-hole pairs per minimum ionising particle. One could choose the best material for the application of interest. Cost and availability has also to be considered, in which case silicon has made advantages. One can get large ($6 - 8$" diameter) wafers of very pure single crystals, which are necessary to build large silicon strip detectors for high energy physics experiments at low cost.
This chapter describes the basics of silicon detectors, which are necessary for the understanding of the following chapters. In the second section the design and read-out of a strip sensor is discussed. Finally, the mechanisms and effects of radiation damage in silicon are introduced. A more extended introduction to semiconductor physics and radiation detectors is given in [Lut99, Bla68, Sze81, ES92].

1.1 Basic Properties of Silicon

1.1.1 Intrinsic Case

Single crystals of silicon are of diamond lattice type in which every atom has four covalently bound neighbours. At finite temperatures these bonds can break due to lattice vibrations and a valence electron can escape. This is a transition from a valence state to a conduction state of the electron. The probability that such an electronic state is occupied is given by the Fermi-Dirac function:

$$\mathcal{F}(E) = \frac{1}{1 + \exp\left(\frac{E - E_F}{k_B T}\right)} \tag{1.1}$$

where E is the energy of the electronic state, E_F is the Fermi energy, k_B is the Boltzmann constant and T is the temperature. Obviously, E_F is the energy at which the occupation probability is one half. If $|E - E_F| > 3k_B T$ this can be approximated for electrons and holes by:

$$\mathcal{F}_n(E) \approx \exp\left(-\frac{E - E_F}{k_B T}\right) \qquad \mathcal{F}_p(E) = 1 - \mathcal{F}_n(E) \approx \exp\left(-\frac{E_F - E}{k_B T}\right) \tag{1.2}$$

The density of states near the bottom of the conduction band is given by

$$N(E) = \frac{(2m_D^*)^{3/2}}{2\pi^2\hbar^3}\sqrt{E - E_C} \tag{1.3}$$

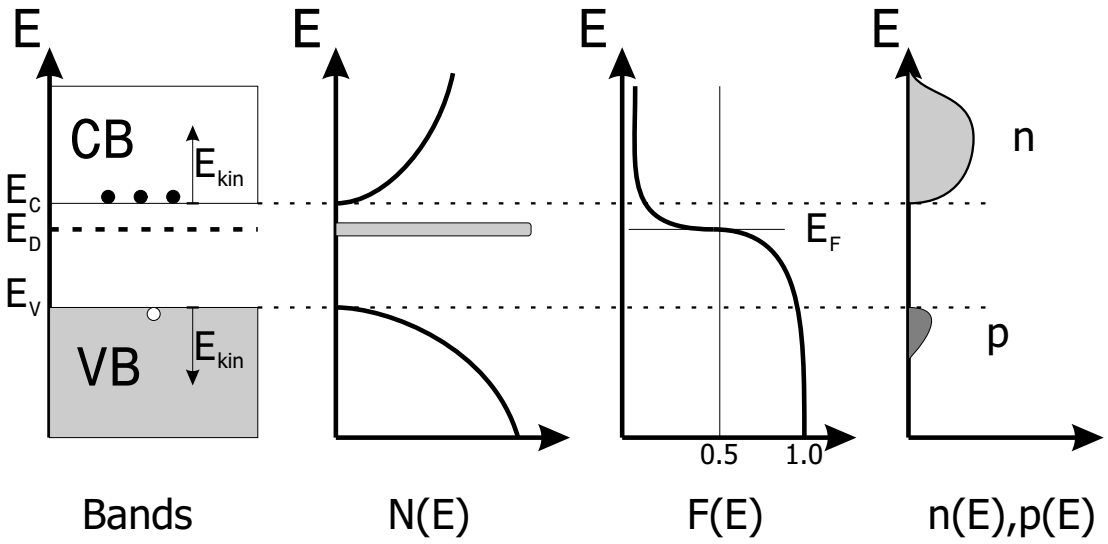

Figure 1.1: Illustration of a semiconductor in the band model representation on the left followed by the density of states $N(E)$, occupation probability $\mathcal{F}(E)$ and density of free charge carrier $n(E)$ and $p(E)$. The additional energy level E_D is only present in the extrinsic case, when donors are added (see Section 1.1.2). It causes a shift of the Fermi level E_F and increases the electron density.

with the energy of the conduction band edge E_C and the density of states effective mass m_D^* (see (1.22)).
The density of free electrons n is a convolution of the density of states and their occupation probability:

$$n = \int_{E_C}^{\infty} N(E) \cdot F(E)\, dE = \frac{2}{h^3}(2\pi m_D^* k_B T)^{\frac{3}{2}} \exp\left(-\frac{E_C - E_F}{k_B T}\right) = N_C \exp\left(-\frac{E_C - E_F}{k_B T}\right) \quad (1.4)$$

with N_C being the density of states at the conduction band edge. The density of holes is $p = N_V \exp(-\frac{E_F - E_V}{k_B T})$, where E_V is the energy of the valence band edge. An illustration of (1.3) and (1.4) is shown in Figure 1.1. Electrons in bound states are represented by the valence band (VB) and free electrons by the conduction band (CB). Between these two bands lies the forbidden band gap ($E_g = E_C - E_V$) which is responsible for the specific properties of semiconductors.
The Fermi energy is defined by the following considerations: Without any defects or dopants the semiconductor is said to be intrinsic and there must be as many electrons as holes $n = p = n_i$ ($n_i \approx 1.45 \cdot 10^{10} cm^{-3}$ at $300\,K$) since a hole is just the empty place left by an electron excited to the conduction band. This condition gives the density of charge carriers

$$n_i = \sqrt{N_C N_V} \exp\left(-\frac{E_g}{2k_B T}\right) \quad (1.5)$$

and the Fermi energy in the intrinsic case:

$$E_i = \frac{E_C + E_V}{2} + \frac{3k_B T}{4} \ln\left(\frac{m_p}{m_n}\right) \quad (1.6)$$

1.1.2 Extrinsic Case

The intrinsic properties of silicon, which has four valence electrons, can be modified by adding small quantities of elements with three or five valence electrons such as boron or phosphorus, respectively.
The excess electron of e.g. phosphorus, has a very low binding energy ($45\,meV$) and can easily be excited to the conduction band, which increases the amount of free electrons. The material is said to be n-type material and such elements are called donors.
Lifting an intrinsic valence electron by $45\,meV$ to the energy level of boron leaves a hole. This gives rise to an excess of free hole. The elements are called acceptors and the corresponding material is called p-type.
In Figure 1.1 donors are indicated by an energy level in the band gap just below the conduction band. At room temperature all these shallow dopants are ionised and additional charge carriers are set free. Usually the doping concentration is much higher than the intrinsic concentration of charge carriers (n_i) and the electron concentration in n-type material is just the doping concentration $n = N_D$. With (1.4) one gets the Fermi level in n-type material:

$$E_C - E_F = k_B T \ln \frac{N_C}{N_D} \tag{1.7}$$

And for p-type material it reads:

$$E_F - E_V = k_B T \ln \frac{N_V}{N_A} \tag{1.8}$$

The Fermi level defines the electron and hole concentration in general:

$$n = n_i \exp\left(\frac{E_F - E_i}{k_B T}\right) \qquad p = n_i \exp\left(\frac{E_i - E_F}{k_B T}\right) \tag{1.9}$$

From these definitions one gets the mass-action law:

$$n \cdot p = n_i^2 \tag{1.10}$$

This expresses the fact that one type of charge carriers can only increase in density if the other type is reduced.
At low temperatures not all doping levels might be ionised and the occupation follows the Fermi-Dirac distribution. For donors:

$$N_D^+ = N_D \left[1 - \frac{1}{1 + \frac{1}{2}\exp\left(\frac{E_D - E_F}{k_B T}\right)}\right] \tag{1.11}$$

and for acceptors:

$$N_A^+ = \frac{N_A}{1 + 4\exp\left(\frac{E_A - E_F}{k_B T}\right)} \tag{1.12}$$

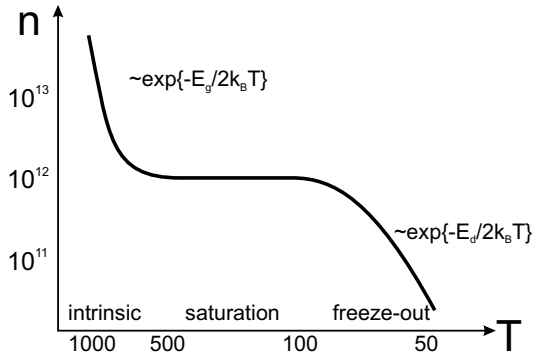

Figure 1.2: Electron density as a function of temperature for $N_D = 10^{12}$

The Fermi level must be determined by solving the neutrality condition $n = N_D^+ + p$ which leads to

$$n \simeq \sqrt{\frac{N_D N_C}{2}} \exp\left(-\frac{E_d}{2k_B T}\right) \tag{1.13}$$

with $E_d = E_C - E_D$ and $N_D \gg \frac{1}{2} N_C \exp(\frac{E_d}{k_B T}) \gg N_A$. The electron density is shown schematically in Figure 1.2 on the page before. In the temperature range from $\sim 100\,K$ to $500\,K$ all donors are ionised and the approximation $N_D^+ = N_D$ is valid. At lower temperatures (depending on the concentration) the donors start to freeze out, i.e. they catch their missing electron and become neutral again.

1.1.3 Carrier Transport

Inhomogeneity conditions in semiconductors can be caused by an applied electric (and magnetic) field and/or by inhomogeneous concentrations. Driven by the field, the charge carriers drift through the device, and the differences in concentration are levelled out by diffusion. In equilibrium the charge carriers have a mean kinetic energy of $\frac{3}{2} k_B T$, which is equivalent to a velocity of about $10^7 \frac{cm}{s}$ at room temperature.

Drift

The drift velocity in an electric field can be parameterised by:

$$v_{dr} = \frac{\mu_0 |\vec{E}|}{\left(1 + \left(\frac{\mu_0 |\vec{E}|}{v_s}\right)^{\beta}\right)^{\frac{1}{\beta}}} \tag{1.14}$$

where μ_0 is the low field mobility, $v_s \simeq \sqrt{\frac{8\hbar\omega_{op}}{3\pi m^*}} \approx 10^7 \frac{cm}{s}$ the saturation velocity derived from optical phonon scattering [Sze81] and $\beta \approx 0.75$, a parameter that defines the transition from low to high field behaviour [CMMO75]. At low fields ($\mu_0 |\vec{E}| \ll v_s$) v increases linear with the electric field, but it saturates at high fields. Since the charge carriers gain more and more energy between two scattering processes by acoustic phonons, a new scattering process becomes possible by optical phonons, which have an energy of about $60meV$. This decreases the scattering time and the mobility with increasing electric field. In [Sze81] on can find the ratio of electron temperature to lattice temperature derived from the rate equation in silicon

$$\frac{T_e}{T} = \frac{1}{2}\left[1 + \sqrt{1 + \frac{3\pi}{8}\left(\frac{\mu_0 |\vec{E}|}{u_L}\right)^2}\right] \tag{1.15}$$

which gives the electron velocity $v_{dr} = \mu_0 |\vec{E}| \sqrt{T/T_e}$. Comparing the results of this formula with the parametrisation above suggests the use of $\beta \approx 0.75$ for a wide $\mu_0 |\vec{E}|$-range (see Figure 1.3). The low field mobility is defined by the average scattering time $\langle \tau \rangle$ and effective mass m^* of the charge carrier:

$$\mu_0 = \frac{q_{el}}{m^*} \langle \tau \rangle \tag{1.16}$$

The averaging is performed over all contributing energy states [Bla68]:

$$\langle \tau \rangle = \frac{4}{3\sqrt{\pi}} \int_0^{\infty} \tau(E) x^{\frac{3}{2}} \exp(-x)\, dx \tag{1.17}$$

with $x = E/k_B T$. There are different scattering processes in semiconductors caused by lattice vibrations (phonons), impurities and defects. The scattering times for the most important processes are:

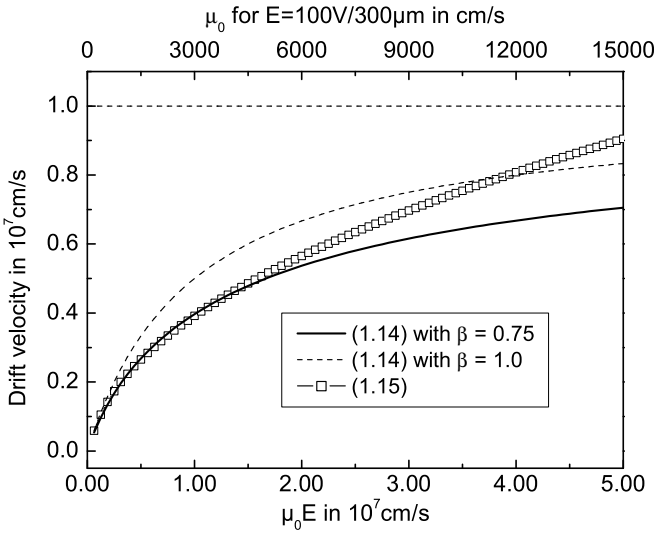

Figure 1.3: Parametrisation (1.14) compared to formula (1.15) derived from the rate equation for silicon. For small $\mu_0|\vec{E}|$ a β of 0.75 is preferred. This is also the range where (1.15) is valid, since v_{dr} should saturate at about $10^7\ cm/s$.

Acoustic phonon scattering

$$\tau_L = \frac{\hbar\rho u_l^2}{2\pi k_B T N(E)\mathcal{E}_1^2} \overset{(1.3)}{=} \frac{\pi\hbar^4\rho u_l^2}{(2m_D^*)^{\frac{3}{2}}\mathcal{E}_1^2}\frac{E^{-\frac{1}{2}}}{k_B T} = \tau_0\frac{1}{k_B T\sqrt{E}} \tag{1.18}$$

where ρ is the density, $u_l = 9037\ m/s$ the velocity of sound in silicon, $\mathcal{E}_1$ the deformation potential and m_D^* is the density of states effective mass (after [Bla68]).
Acoustic phonons can be excited with small energies, since the dispersion relation starts at the origin. There are usually three branches: one longitudinal and two transversal modes.

Ionised impurity scattering

$$\begin{aligned} \tau_i &= \frac{\sqrt{2m_D^*}\varepsilon^2}{\pi q_{el}^4 N_I}\frac{E^{\frac{3}{2}}}{F(b)} \\ F(b) &= \ln(1+b) - b/(1+b) \\ b &= \frac{2m^* E\varepsilon k_B T}{\pi q_{el}^2 n'\hbar^2} \\ n' &= n + (n+N_m)\left(1 - \frac{n+N_m}{N_M}\right) \end{aligned} \tag{1.19}$$

N_I, N_m, N_M are the concentrations of impurities, minority and majority charge carriers, respectively (after [Bla68]). This scattering time increases with energy, i.e. it is more pronounced at low temperatures and low fields. Ionised impurities are all charged atoms in the crystal.

Inter-valley scattering

$$\tau_{iv} = \frac{1}{\alpha_\pm(n_{iv} + \frac{1}{2} \pm \frac{1}{2})} \tag{1.20}$$

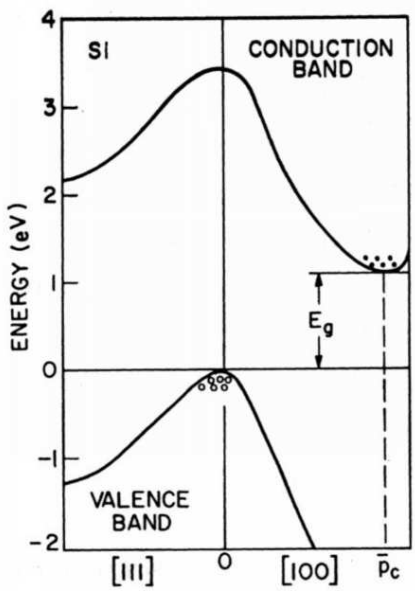

(a) Band structure of silicon from [Lut99]

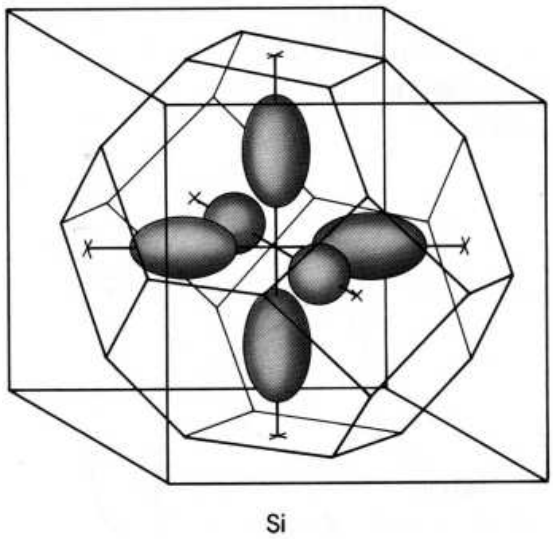

(b) Constant energy surfaces in silicon from [Bla68]

Figure 1.4: The band structure of silicon shows a global minimum of the conduction band in the $\langle 100 \rangle$-direction and not at the origin like in GaAs. Thus six equivalent valleys are occupied with conduction electrons. This makes silicon a many-valley semiconductor with an indirect band-gap.

with

$$\text{abbreviation} \qquad \alpha_{\pm} = \frac{1}{l_{iv}} \sqrt{\frac{2(E \pm k_B T_i)}{m_D^*}} \Theta(E \pm k_B T_i)$$

$$\text{scattering length} \qquad l_{iv} = \frac{2\rho k_B T_i \pi \hbar^2}{D_i^2 m_D^{*2}}$$

$$\text{inter-valley phonon density} \qquad n_{iv} = \frac{1}{exp(k_B T_i / k_B T) - 1}$$

T_i and D_i are the temperature and coupling constant of the i's phonon involved (after [SL89]). There are two possible transitions to the opposite (g) and perpendicular (f) valleys. Selection rules allow scattering with longitudinal optic phonons ($\Delta_2'(LO)$) for g-transitions and scattering with longitudinal acoustic and transversal optical phonons ($\Sigma_1(LA, TO)$) for f-transitions [Str70].

The last scattering process already indicates that the minimum of the conduction band of silicon is not at the origin of the $\vec{k}$-space, where the maximum of the valence band is, but at a wave-vector $|\vec{k}| = 0.85 \cdot \frac{2\pi}{a} \approx 10^8\, cm^{-1}$ in $\langle 100 \rangle$-direction, which makes silicon a many-valley semiconductor. The constant energy surface also deviates from a sphere which results in different effective masses along the symmetry axis ($m_{\parallel} = 0.92\, m_0$) and perpendicular to it ($m_{\perp} = 0.19\, m_0$). The effective

mass m^* in (1.16) is thus given by

$$\frac{1}{m_c} = \frac{1}{3}\left(\frac{1}{m_\parallel} + \frac{2}{m_\perp}\right) \qquad \Rightarrow \quad m_c = 0.26\, m_0 \tag{1.21}$$

and called conduction effective mass. At room temperature the dominant scattering mechanism is acoustic phonon scattering (see (1.18)) which contains a factor $m_D^{*3/2}$ from density of states. Taking into account the non-spherical energy surface, one gets the density of states effective mass:

$$m_D^* = \sqrt[3]{m_\parallel m_\perp^2} \qquad = 0.32 m_0 \tag{1.22}$$

For pure acoustic phonon scattering the mobility should decrease with temperature ($\mu \sim T^{-\frac{3}{2}}$) and increase with smaller effective masses:

$$\mu_L = \frac{2^{\frac{3}{2}} q_{el} \sqrt{\pi} h^4 \rho u_l^2}{3 m_c m_D^{*\frac{3}{2}} \mathcal{E}_1^2} (k_B T)^{-\frac{3}{2}} \tag{1.23}$$

The conductivity $\sigma = en\mu$ contains the carrier concentration n, which is strongly temperature and doping dependant, and thus is not a proper parameter to describe drift properties.

Diffusion

If there is an inhomogeneous charge carrier distribution, random movement and statistics are the driving forces to smear out the cloud of charge carriers. The diffusion equation gives the flux of electrons F_n in terms of the diffusion constant D_n:

$$\vec{F_n} = -D_n \vec{\nabla} n \tag{1.24}$$

The diffusion constant and the mobility are related to each other by the Einstein equation:

$$D_n = \frac{k_B T}{q_{el}} \mu_n \tag{1.25}$$

Together with the drift term one gets the total electron current density as

$$\vec{J_n} = -q_{el} \mu_n n \vec{E} - q_{el} D_n \vec{\nabla} n \tag{1.26}$$

1.1.4 Generation and Recombination of Charge Carriers

Thermal generation

At room temperature and below ($k_B T < 25.6\, meV$) the probability of exciting an electron from the valence band into the conduction band in an intrinsic material is very low as discussed in Section 1.1.1 on page 3. Thermal ionisation of shallow dopants is much easier and thus leads to a constant offset of one type of charge carriers (Section 1.1.2 on page 5). An additional excitation path is through intermediate states in the band gap created by crystal imperfections and impurities. If all charge carriers are removed (e.g. by applying an electric field) the system tries to come back to equilibrium by thermal generation. The time this would take at a thermal generation rate of G_{th} is given by the generation lifetime [Lut99]:

$$\tau_g = \frac{n_i}{G_{th}} = \frac{1}{N_t}\left[\frac{1}{v_{th,p}\sigma_p} \exp\left(\frac{E_t - E_i}{k_B T}\right) + \frac{1}{v_{th,n}\sigma_n} \exp\left(\frac{E_i - E_t}{k_B T}\right)\right] \tag{1.27}$$

where E_t is the energy level of the intermediate state and v_{th} and σ are the thermal velocities and cross sections for electrons and holes. For $v_{th,n}\sigma_n = v_{th,p}\sigma_p$ (1.27) reduces to $\tau_g = 2\cosh(\frac{E_t-E_i}{k_BT})/(N_t v_{th}\sigma)$ and is of the order of $\sim 1\,ms$. The current density in depleted diodes, where trap assisted thermal generation dominates, is given by:

$$j = \sum_{traps} qG_{th} \approx \frac{n_i}{\tau_g} = \frac{N_t\sigma v_{th} n_i}{2\cosh\left(\frac{E_t - E_i}{k_BT}\right)} \sim T^2 \exp\left(-\frac{E_g}{2k_BT}\right) \Big/ \cosh\left(\frac{E_t - E_i}{k_BT}\right) \tag{1.28}$$

where q is the charge of the charge carrier. The temperature dependance results from $v_{th} \sim \sqrt{T}$ and $n_i \sim T^{3/2}\exp(-E_g/2k_BT)$ given in (1.5), whereas N_t and σ are constant.

Generation by electromagnetic radiation

This is the basic process made use of in photo detectors. The energy of a photon is transferred to an electron, if the final energy state is allowed. For a direct (electric dipole) transition to the conduction band the energy must be as high as $3.4\,eV$ in silicon. The excess energy is subsequently transferred to the lattice by phonons and the electrons move down to the minimum of the conduction band. The momentum transfer from the photon can be neglected since $q \approx 4 \cdot 10^4\,cm^{-1} \ll k_{min}$. The absorption coefficient for allowed direct transition is $\alpha \sim (h\nu - E_g(k=0))^{\frac{1}{2}}$.
For photon energies below $3.4\,eV$ an indirect transition is possible. This is a second order process involving phonon absorption or emission. First the electron is excited to a free intermediate state of the energy $E^* \geq E_g(|\vec{k}| = 0)$ with $q \approx 0$ and within a time $(E_i - h\nu)/\hbar$ it is scattered by a phonon with $q \approx |\vec{k}_{min}|$. Thus the transition probability depends not only on the density of states factor, electron-photon and electron-phonon interaction but also on the difference $E_i - h\nu$. This makes transitions for electrons with $|\vec{k}| = |\vec{k}_{min}|$ in the valence band ($E_V \approx -3\,eV$) to the minimum in the conduction band rather impossible. For allowed indirect transitions one gets [Bla68]:

$$\alpha_i = C_i\left[\frac{(h\nu - E_g + \hbar\omega_q)^2}{e^{\hbar\omega_q/k_BT} - 1} + \frac{(h\nu - E_g - \hbar\omega_q)^2}{1 - e^{-\hbar\omega_q/k_BT}}\right] \tag{1.29}$$

The left term represents phonon absorption and the right term phonon emission. The denominator gives the density of phonons with energy $\hbar\omega_q$. The absorption coefficient of several semiconductors vs. the energy is given in Figure 1.5.

Generation by charged particles

Energy is transferred to the electron cloud by elastic collisions (Coulomb interaction) when charged particles traverse matter. This process was investigated in depth first by Bohr and later by Bethe, Bloch and Landau. The Bethe-Bloch formula is given by [Lut99] as:

$$\frac{dE}{dx} = 2\pi N_L r_e^2 m_e c^2 \rho \frac{Zz^2}{A\beta^2}\left[\ln\left(\frac{2m_e\gamma^2 v^2 W_{max}}{I^2}\right) - 2\beta^2 - \delta - 2\frac{C}{Z}\right] \tag{1.30}$$

where

x is the path length in g/cm^2,
$2\pi N_L r_e^2 m_e c^2 = 0.1535\,MeVc^2/g$,

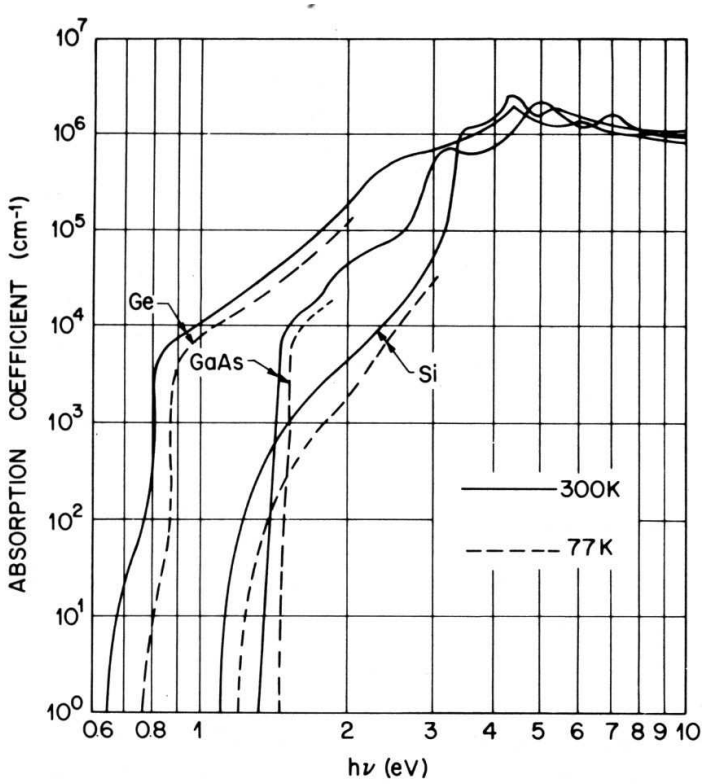

Figure 1.5: Absorption coefficient in several semiconductors from [Sze81].

$r_e = q_{el}^2/4\pi m_e c^2 = 2.817 \cdot 10^{-13}\, cm$ is the classical electron radius,
ρ is the density of the matter,
Z and A are the atomic number and weight, respectively,
z is the charge of the traversing particle
$\beta = v/c$ and $\gamma = 1/\sqrt{1-\beta^2}$,
I is the effective ionisation potential averaged over all electrons
δ is a density correction which flattens the relativistic rise
C is a shell correction relevant at very low velocities
W_{max} is the maximum energy transfer in a single collision

In Figure 1.6 the stopping power is plotted versus the kinetic energy of electron and protons in silicon. A minimum ionising particle (MIP) is defined after the common minimum in these plots as a particle that deposits $\sim 1.6\, MeV/cm$ in silicon.
The energy loss calculated with (1.30) is the mean energy loss per length in the material and only part of this energy loss is used to create electron-hole pairs. In silicon the average energy to produce one electron-hole pair is $3.6\, eV$.
The fluctuations around this mean values are described by the Landau distribution. The probability $\phi(E)dE$ that a charged particle looses energy between E and $E + dE$ is

$$\phi(E)dE = \frac{2\pi N q_{el}^4 Z}{m_e v^2 A} \cdot \frac{1}{E^2} \tag{1.31}$$

Together with the mean energy loss Landau got a probability distribution for the deviation from the mean value $\lambda = E - E_{mean}$:

$$\omega(\lambda) = \frac{1}{\pi}\int_0^\infty e^{-u\ln u - \lambda u}\sin(\pi u)du \approx \frac{1}{\sqrt{2\pi}}e^{-\frac{1}{2}(\lambda+e^{-\lambda})} \tag{1.32}$$

The approximation is taken from [Moy55].

Recombination

The direct band-to-band recombination is suppressed in silicon since a large momentum has to be transferred to the lattice as mentioned above. The recombination process is assisted by localised states in the band gap caused by defects. These states can change their charge by emission or capture of electrons or holes. If the charge of the defect level can be changed from neutral to positive it is said to be a donor (see Section 1.3 on page 25).
In n-type semiconductor the recombination time is given by $\tau_r = (\beta n_0)^{-1}$ and for indirect semiconductors the recombination factor β is given by [Lut99]:

$$\beta = \frac{N_t v_{th,n}\sigma_n v_{th,p}\sigma_p}{v_{th,n}\sigma_n\left[n + n_i e^{\frac{E_t-E_i}{k_B T}}\right] + v_{th,p}\sigma_p\left[p + n_i e^{\frac{E_i-E_t}{k_B T}}\right]} \tag{1.33}$$

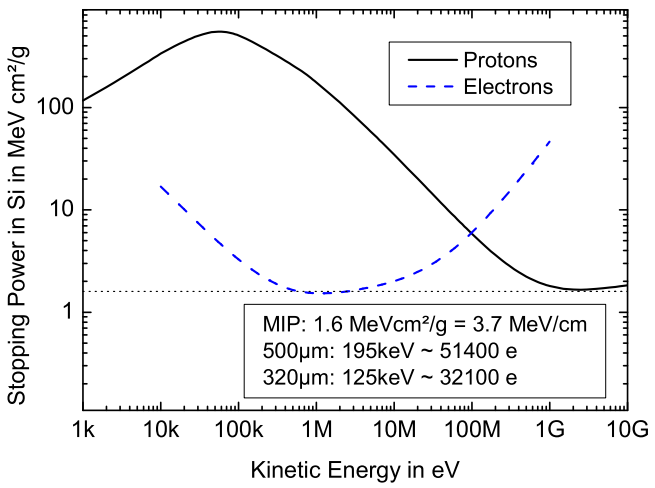

Figure 1.6: Stopping power of electrons and protons in silicon obtained by ESTAR and PSTAR, which use methods from the International Commission on Radiation Units and Measurements for the calculation. These databases are accessible via the National Institute of Standards and Technology (http://physics.nist.gov).
There is a minimum in the energy deposition for all charge particles, which has a common value of about 3.7 MeV/cm in silicon. A particle with this energy loss is called minimum ionising particle (MIP).

1.2 Strip Sensors

1.2.1 pn-Junction

The basic silicon sensor structure is the pn-junction or diode. It consists of two extrinsic regions of opposite doping. When brought together the majority carriers (electrons in the n-doped region and holes in the p-doped region) diffuse into the other region and recombine. The remaining ionised donors and acceptors create the so called space charge region (SCR). As a result an electric field is created which counteracts the diffusion of the charge carriers. The corresponding

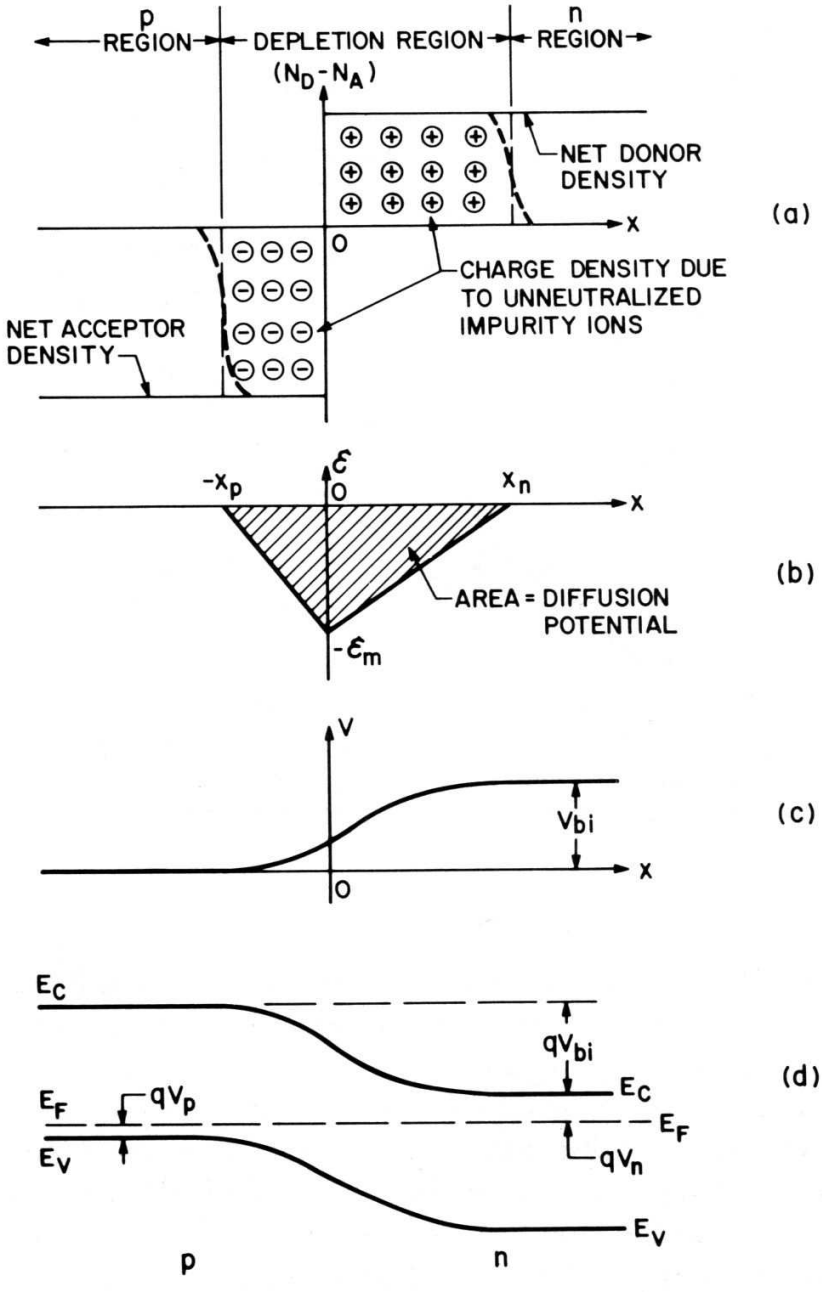

Figure 1.7: Abrupt pn-junction in thermal equilibrium. (a) Space charge distribution. The dashed lines indicate the majority carrier distribution tails. (b) Electric field distribution. (c) Potential variation with distance. (d) Energy band diagram. (from [Sze81])

potential drop is given by the difference of the intrinsic energy levels in the neutral regions and called built-in voltage:

$$V_{bi} = \frac{1}{q_{el}}(E_i^p - E_i^n) = \frac{k_B T}{q_{el}} \ln \frac{N_A N_D}{n_i^2} \tag{1.34}$$

which is in the order of $0.5\,V$. The width of the space charge region W and the maximum electric field are given by [Lut99]:

$$\begin{aligned} W &= x_n + x_p \\ &= \sqrt{\frac{2\varepsilon\varepsilon_0 V_{bi}}{q_{el}(N_A + N_D)}} \left[\sqrt{\frac{N_A}{N_D}} + \sqrt{\frac{N_D}{N_A}} \right] \\ &= \sqrt{\frac{2\varepsilon\varepsilon_0 (N_A + N_D) V_{bi}}{q_{el} N_A N_D}} \end{aligned} \tag{1.35}$$

$$E_{max} = \frac{q_{el}}{\varepsilon\varepsilon_0} N_D x_n = \sqrt{\frac{2q_{el}}{\varepsilon\varepsilon_0} \frac{N_A N_D}{N_A + N_D} V_{bi}} \tag{1.36}$$

For a very asymmetric junction and application of a reverse voltage ($V_{bias} < 0$) the SCR mainly covers the low doped bulk and the thickness d is defined by the space charge therein (replacing V_{bi} by $V_{bi} - V_{bias}$ in (1.36)). The voltage at which the SCR reaches the thickness of the diode (D) is called the full depletion voltage and can be calculated as:

$$V_{fd} = \frac{q_{el}}{2\varepsilon\varepsilon_0} |N_{eff}| D^2 \tag{1.37}$$

where the effective space charge concentration might be slightly compensated by opposite type of doping $N_{eff} = N_D - N_A$.
The current-voltage characteristic can be derived from the minority carrier concentration at the edge of the neutral region

$$n_p = n_n e^{-q_{el} \frac{V_{bi} - V_{bias}}{k_B T}} = n_{p0} e^{q_{el} \frac{V_{bias}}{k_B T}} \qquad p_n = p_{n0} e^{q_{el} \frac{V_{bias}}{k_B T}} \tag{1.38}$$

Since the minority carrier diffusion current is proportional to the deviation from thermal equilibrium the current is expected to have exponential characteristic:

$$J = J_s \left(e^{q_{el} \frac{V_{bias}}{k_B T}} - 1 \right) \tag{1.39}$$

with

$$J_s = q \left(\frac{n_{p0} D_n}{\sqrt{D_n \tau_{r,n}}} + \frac{p_{n0} D_p}{\sqrt{D_p \tau_{r,p}}} \right)$$

This is the diode current with the saturation current J_s for reverse bias under the assumption that no charge is generated in the space charge region. In the case of reverse biased diodes ($n \cdot p \ll n_i^2$) thermal generation dominates and the volume generated current is given by $J_V \approx -q_{el} \frac{n_i}{\tau_g} W$ (see (1.28)).
The capacitance-voltage characteristic can be used to determine the doping profile and the full depletion voltage. Let's consider a highly doped p-region on a n-type bulk and set the potential

to zero in the neutral n-region. The change of the surface charge on the p-side when increasing the SCR from x to $x + dx$ is $qN_D dx$. This causes an electric field change of $qN_D dx/(\varepsilon_s \varepsilon_0)$ and a surface voltage change of $xq_{el}N_D dx/(\varepsilon_s \varepsilon_0)$. This has to be integrated from $x = 0$ to the width W of the SCR which results in:

$$Q_p = -\int_0^W q_{el} N_D(x) dx \qquad \Psi_p = \int_0^W \frac{x q_{el} N_D(x)}{\varepsilon_s \varepsilon_0} dx \tag{1.40}$$

The potential difference Ψ_p must equal the difference $V_{bi} - V_{bias}$, where reverse bias is negative. The capacitance per area of the diode is given by $C = \partial Q_p / \partial V \approx \varepsilon\varepsilon_0 / W$. The doping profile can be derived from:

$$\frac{\partial(1/C^2)}{\partial V} = \frac{\partial(1/C^2)/\partial W}{\partial V/\partial W} = \frac{2W/(\varepsilon\varepsilon_0)^2}{qN_D W/(\varepsilon\varepsilon_0)} = \frac{2}{qN_D \varepsilon\varepsilon_0} \tag{1.41}$$

1.2.2 MOS-Structure

A combination of metal, oxide and semiconductor is called MOS-structure. This device can be used to investigate surface damage as will be discussed in Section 1.3.6 on page 35. The operation principle of a MOS-structure is explained, e.g. in [Lut99], and will be summarised in this section. In Figure 1.8 the band model for an n-type MOS-structure is presented. Metal and semiconductor are separated by the isolating oxide and no current flows. The important potentials

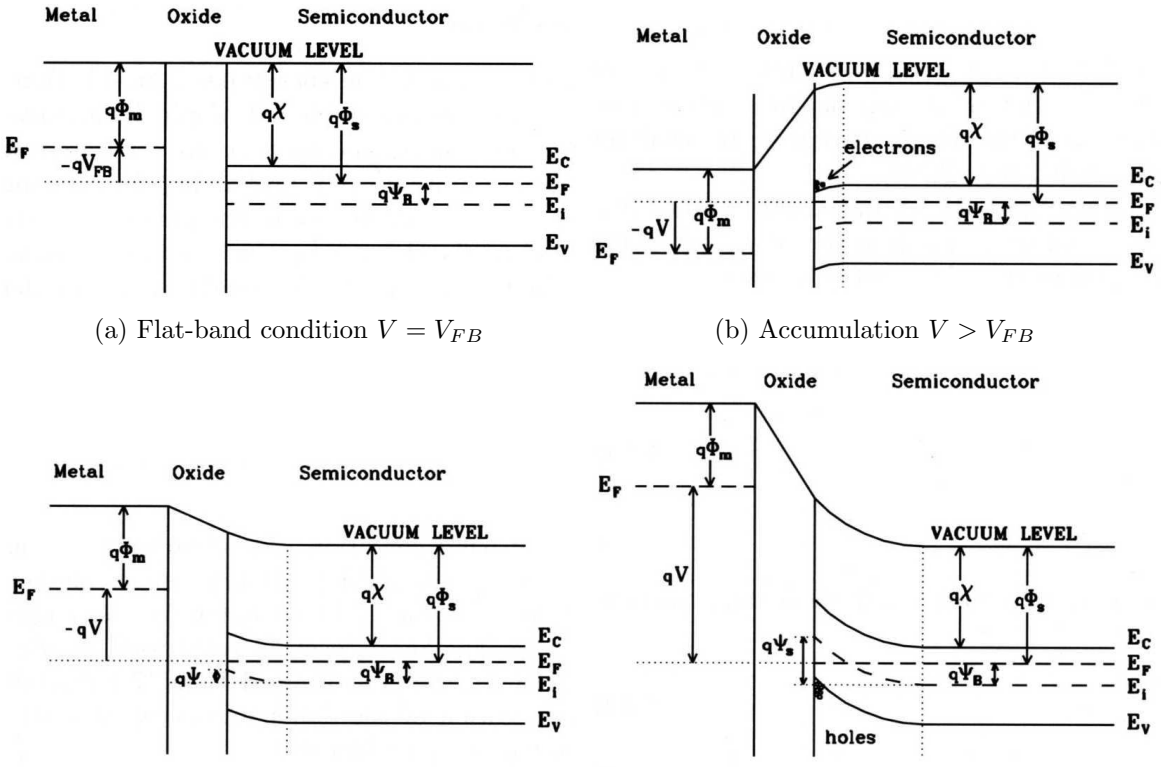

(a) Flat-band condition $V = V_{FB}$

(b) Accumulation $V > V_{FB}$

(c) Surface depletion $V < V_{FB}$, $\Psi_s < \Psi_B$

(d) Inversion $V < V_{FB}$, $\Psi_s > \Psi_B$

Figure 1.8: Operation conditions of an n-type MOS-structure from [Lut99]

are the work functions in the metal ($q_{el}\Phi_m = 4.1\,eV$ for Al on SiO_2) and in the semiconductor ($q_{el}\Phi_s = q\chi + E_C - E_F$), the doping-independent electron affinity ($q_{el}\chi = 0.56\,eV$ for Si) and the distance of the Fermi level from the intrinsic level ($q_{el}\Psi_B = E_F - E_i = k_B T \ln(N_D/n_i)$).

Flat-band condition ($V = V_{FB}$)

In the flat-band condition the potentials are flat in the silicon bulk and since no charge is present in the oxide the vacuum level should be constant throughout the device (see Figure 1.8(a)). This implies that an additional voltage has to be applied, since the work functions are not the same for metal and semiconductor. This voltage is called flat-band voltage and is the difference of the work functions:

$$V_{FB} = \Phi_m - \Phi_s \qquad \text{(no oxide charges)} \tag{1.42}$$

Accumulation ($V > V_{FB}$)

Applying a more positive voltage than the flat-band voltage the conduction band bends towards the Fermi level thus increasing the electron concentration according to the thermal equilibrium condition $n = n_i \exp\{(E_F - E_i)/k_B T\}$. The very thin charge layer at the silicon-oxide interface has a surface charge of:

$$Q_{acc} = -\varepsilon_{ox}\varepsilon_0 \frac{V - V_{FB}}{d_{ox}} = -C_{ox}(V - V_{FB}) \tag{1.43}$$

This condition is shown in Figure 1.8(b) on the page before.

Surface depletion ($V < V_{FB}$, $\Psi_s < \Psi_B$)

When a voltage $V < V_{FB}$ is applied, the bands are bent upwards. The band bending, which is the difference of the intrinsic level at the boundary and deep in the bulk, is given by $\Psi_s = -q_{el}N_D d_s^2/2\varepsilon_s\varepsilon_0$. This results in a depleted zone in the semiconductor of depth d_s:

$$d_s = \sqrt{\frac{\varepsilon_s\varepsilon_0}{qN_D}(V_{FB} - V) + \left(\frac{\varepsilon_s}{\varepsilon_{ox}}d_{ox}\right)^2} - \frac{\varepsilon_s}{\varepsilon_{ox}}d_{ox} \tag{1.44}$$

Inversion ($V < V_{FB}$, $\Psi_s > \Psi_B$)

A more negative voltage with $\Psi_s < \Psi_B$ moves the intrinsic level above the Fermi level and creates more holes than electrons at the silicon-oxide interface. In a "strong" inversion the hole concentration is even higher than the electron concentration in the bulk (for $\Psi_s < -2\Psi_B$). The surface charge density of the inversion layer is given by:

$$Q_{inv} = (V_T - V)C_{ox} \tag{1.45}$$

with the threshold voltage $V_T = V_{FB} - 2\Psi_B - d_{ox}/\varepsilon_{ox}\varepsilon_0 \cdot \sqrt{4q_{el}N_D\varepsilon_s\varepsilon_0\Psi_B}$. This inversion charge layer of minority carriers is followed by a still isolating SCR. The thickness of this depleted region is not varying with the applied voltage but given by $d_{max} = \sqrt{4\varepsilon_s\varepsilon_0\Psi_B/q_{el}N_D}$.

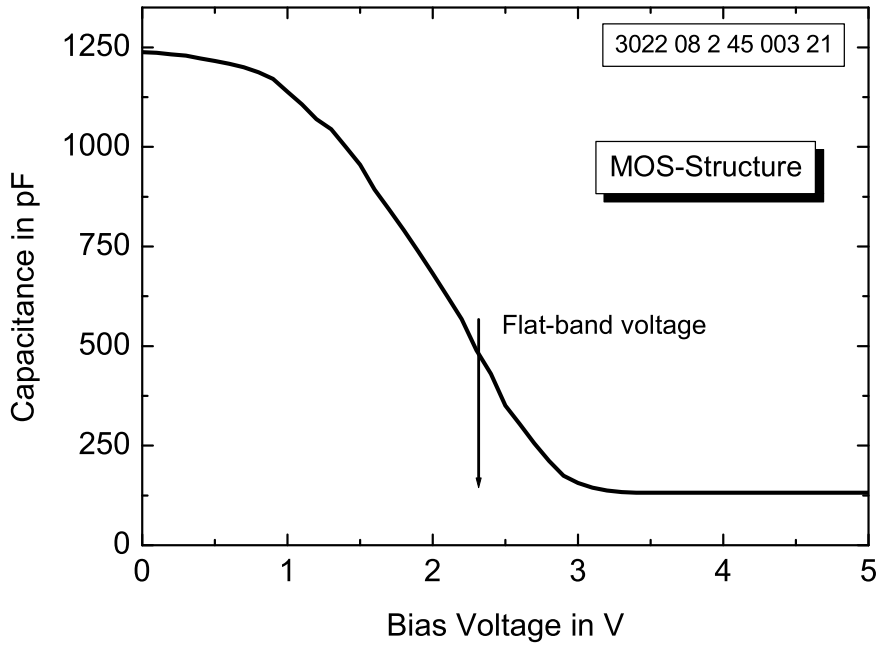

Figure 1.9: CV-curve on a MOS-structure at high frequency (1 MHz). The flat-band voltage is reached at the inflection point.

CV-characteristic

Applying a time varying voltage also the time dependence of the participating processes have to be considered. In the accumulation case the majority charge carriers at the silicon-oxide interface are attracted and repelled very fast, since it is a drift process defined by the mobility. The measured capacitance is then $C = C_{ox}$ (see (1.43)) for all frequencies.
In the depletion case the same arguments hold and one measures the serial capacitance of the oxide C_{ox} and the bulk C_{bulk}: $C = C_{ox}C_{bulk}/(C_{ox} + C_{bulk})$.
Between both cases the flat-band condition is fulfilled and thus indicated by the drop of the capacitance. Precisely, it is the inflection point in the CV-curve. An example is shown in Figure 1.9
In the inversion case the minority charge carriers are created by generation and recombination processes, which proceed at a much longer time scale. For low frequencies the depletion layer stays constant and the minority carriers are moved, resulting in a measurement of the oxide capacitance $C = C_{ox}$. At high frequencies the inversion layer does not feel the varying field but the depletion layer width follows the voltage. Again the serial capacitance is measured.

1.2.3 Design of Strip Sensors

Without any segmentation a silicon sensor, which consists of the described pn-junction, is called a pad sensor. To get a homogeneous doped space charge region one uses slightly doped bulk material and a thin and highly doped region of opposite type on the front. Then the SCR covers

mostly the homogene bulk and not the highly doped surface region (see (1.35)). To achieve a good ohmic contact on the back side another highly doped region is produced, but of the same type as the bulk. To get position information of the generated charge carriers, one can segment the highly doped regions. A common way is, for example, to put p-type strips on n-type bulk. The generated charges can be measured individually for each strip on one end of the strips, which provides an easy access to read-out.
If 2-dimensional position information is necessary, two strip sensors can be mounted with tilted strip orientation and each responding strip represents the coordinates of the hit.
To save material one can also segment both sides. But there are two main problems to be solved. First, there is an electron-accumulation (below the oxide) between n^+-strips on n-type bulk, which shortens the strips (see Figure 1.8(b) on page 15). One solution is an additional implantation of p-type strips between the n^+-type strips [Lut99]. A second problem arises when high bias voltages become necessary after high irradiation. Since the read-out electronics should be kept on ground, at least half of the bias voltage will drop at the oxide layer (coupling capacitance), which then must stand few hundreds of volts. A thick oxide layer might stand the voltage, but a high coupling capacitance is necessary in oder not to loose too much of the charge and this requires a thin oxide. The high voltage drop could be avoided if the electronics are put on a high virtual ground, which requires optical connections to the hybrid.
Using crossed strips more than one hit on the sensor during read-out time results in ambiguity. When working with high occupancy a 2-dimensional segmentation is necessary, which makes the read-out more complicated. The so called pixel sensors have to be bump bonded to the read-out electronics on top, which is a difficult process [Fis03, K^+01, C^+00].
Here the layout of the CMS silicon strip sensors should serve as an example for modern strip sensors (see Figure 1.10). Highly boron doped strips are implanted ($\sim 1\,\mu m$ deep) on an n-type (phosphorous doped) high resistivity ($\sim 2\,k\Omega cm$) bulk. Each strip is connected to the bias ring, which surrounds the whole structure, via a bias resistor realised by poly-silicon deposition with a wiggle-shaped structure doped with phosphorus. Another possibility is punch-through biasing which avoids the poly-silicon technology. The depleted zone under the p^+-bias ring grows with increasing bias voltage and reaches the strips after a few volts. A current starts flowing and the strips are almost at the bias potential.

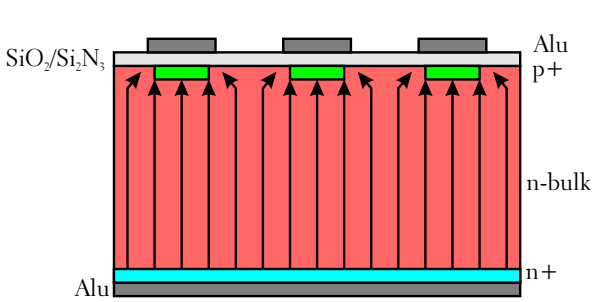

(a) **Perpendicular to strips** Metal overhang reduces the field strength at the implant, since some field lines end at the metal.

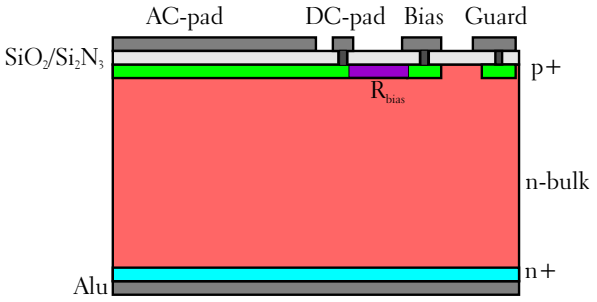

(b) **Along strips** The DC-pad is connected to the implanted strip by one "via". The bias and guard ring have many vias, which contact the implant. The bias resistor (R_{bias}) is a wiggle shaped poly-silicon structure.

Figure 1.10: Schematic cross sections of a capacitively coupled strip sensor

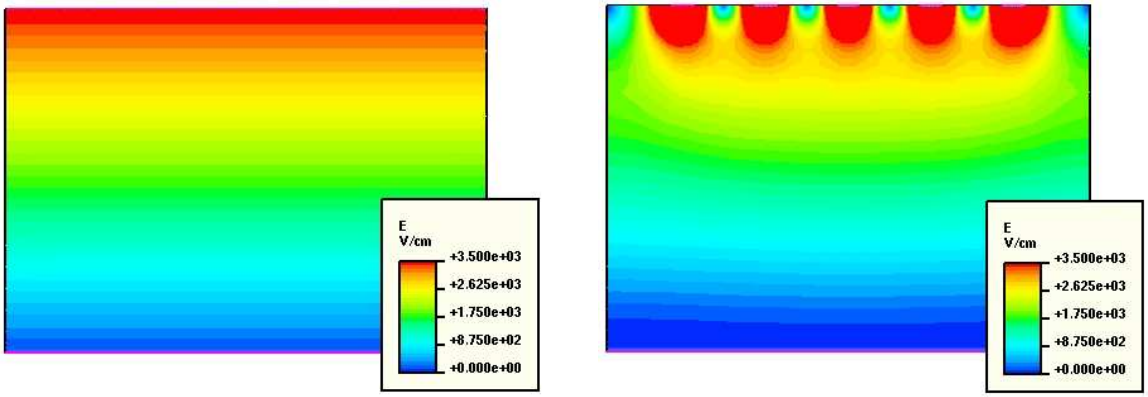

(a) **Pad sensor** There is just a linear electric field in an unstructured device.

(b) **Strip sensor** The electric field is very high below the strips and decays rapidly. At the backplane the field is lower than in the pad sensor.

Figure 1.11: Electric field distribution in a pad and a strip sensor with a pitch of 120 μm *and a strip width of* 30 μm*. Both devices are* 500 μm *thick and biased at* 90 V*, which is the nominal full depletion voltage of the diode. The simulation was performed using ISE T-CAD (see Appendix D on page 127).*

The strips can be directly connected (DC-pad) to the read-out electronics, which requires current sensitive amplifiers. Another way is capacitive coupling of the strips (ac-coupling via the AC-pad). Charge transfer is realised by a thin oxide layer covering the whole silicon area and aluminium strips just above the p^+-strips. This coupling protects the read-out electronics from high leakage currents, which may decrease the dynamic range or even drive the electronics into saturation.

1.2.4 Consequences for Operation

The described differences in the design of diode and strip sensor have some consequences for the operation of such strip sensors.

Field distribution and full depletion voltage

The electrode segmentation changes the electric field distribution in the device. There are high field regions around the implants and low field regions between the strips as shown in Figure 1.11. For different ratios of width/pitch and pitch/thickness the electric field at the opposite side is reduced with respect to the field present in a diode at the same bias voltage (see Figure 1.12). A consequence is that strip sensors are fully depleted at higher bias voltages than necessary for diodes with the same thickness. In [B^+00b] a semi-analytical solution of the Poisson equation for the full depletion voltage is given:

$$V_{fd} = V_{fd,diode}\left(1 + 2\frac{p}{D} \cdot f(w/p)\right) \tag{1.46}$$

with the numerical approximation of f

$$f(x) = -0.00111x^{-2} + 0.0586x^{-1} + 0.240 - 0.651x + 0.355x^2 \tag{1.47}$$

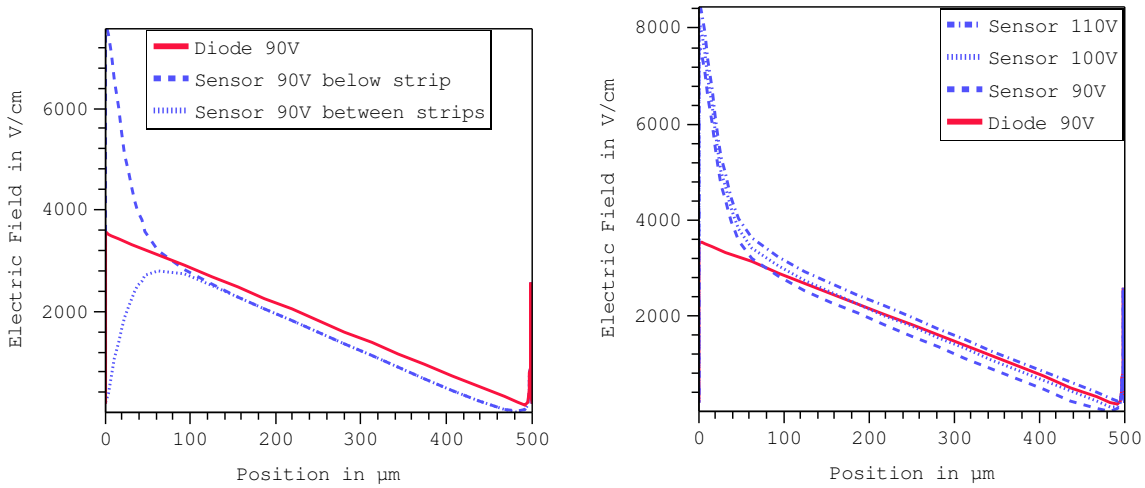

(a) Electric fields at different positions

(b) Electric fields with different bias voltages

Figure 1.12: Comparison of the electric field in a strip sensor from Figure 1.11(b) on the preceding page with the field in a pad sensor. The field at the n^+-side is slightly lower resulting in a higher full depletion voltage of about $V_{fd} \approx 105\,V$.

For a width to pitch ratio of $w/p = 0.25(f(0.25) = 0.31608)$, a thickness of $d = 500(320)\,\mu m$ and a pitch of $120\,\mu m$ the full depletion voltage of a strip sensor increases by about 15.2(23.7)%.

Signal formation

The geometry of the read-out electrodes affects the generated current signal. To get the induced current of moving charges in a multi electrode system one uses the Reciprocity Theorem:

$$\sum_{electrodes} Q'_n\, V_n = \sum_{electrodes} Q_n\, V'_n \tag{1.48}$$

From this equation one can derive the change in potential ($V_n \rightarrow V'_n$) for a given change in charge ($Q_n \rightarrow Q'_n$). E.g., for a simple plate capacitor with two electrodes one can put electrode 1 on potential V_1 with Q_1 and electrode 2 on ground ($V_2 = 0$, Q_2) to get one state. The other state puts electrode 2 on potential V'_2 with Q'_2 and induces charge Q'_1 on electrode 1. This gives according to (1.48)

$$Q'_1\, V_1 = Q_2\, V'_2 \quad \Rightarrow \quad \frac{Q'_1}{V'_2} = \frac{Q_2}{V_1} \quad \Rightarrow \quad C_{21} = C_{12} \tag{1.49}$$

We have now derived the fact that the capacitance between two electrodes does not dependent on the side, where the measurement is performed.
Considering a drifting charge Q_{dr} as an electrode on potential V_{dr} with all other electrodes on ground one can select a sensing electrode with induced charge Q_s. As a second state one puts the sensing electrode on potential V'_s and gets the potential V'_{dr} at the charge's position with $Q'_{dr} = 0$

$$Q'_s\, V_s + Q'_{dr}\, V_{dr} = Q_s\, V'_s + Q_{dr}\, V'_{dr} \tag{1.50}$$

$$0 + 0 = Q_s\, V'_s + Q_{dr}\, V'_{dr} \tag{1.51}$$

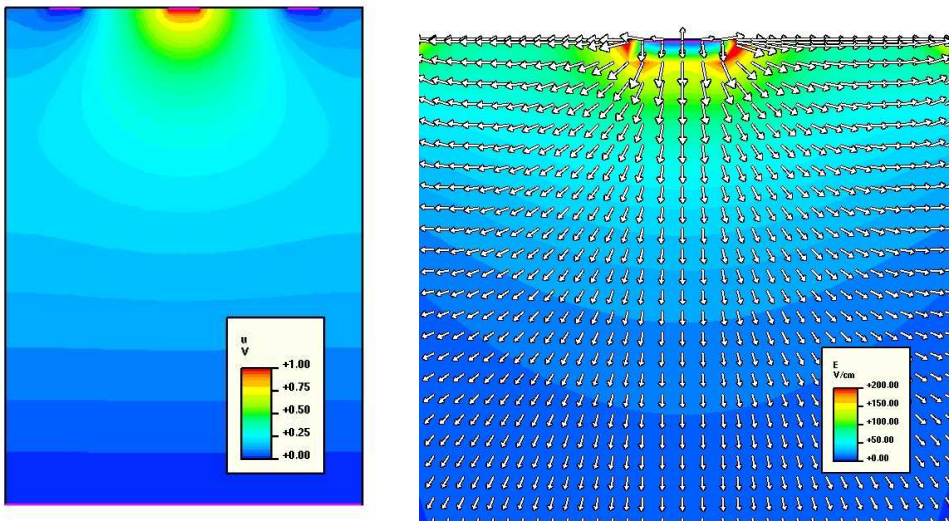

(a) Weighting potential (b) Closeup of the weighting field at the strip

Figure 1.13: Weighting potential and field for a 30 μm-strip with a pitch of 120 μm on a 500 μm thick sensor.

The current induced at the sensing electrode can be calculated by:

$$I = \frac{dQ_s}{dt} = -\frac{d(Q_{dr}\, V'_{dr}/V'_s)}{dt} = -Q_{dr}\frac{dV_W}{dt} = -Q_{dr}\frac{dV_W}{d\vec{r}}\frac{d\vec{r}}{dt} = -Q_{dr}\vec{\nabla}V_W \cdot \vec{v} \tag{1.52}$$

with the velocity of the drifting charge $\vec{v}$ and the weighting field $\vec{E}_W = -\vec{\nabla}V_W$. This field expresses the electrostatic coupling between the point $\vec{r}$ and the sensing electrode. It is calculated by solving the Laplace equation with the boundary condition $V_W = 1$ at the sensing electrode and $V_W = 0$ at any other electrode. Formula (1.52) is also known as Ramo's theorem.
One example is shown in Figure 1.13. This indicates that moving charges hardly contribute to the induced current when they are between adjacent strips and in a depth of $100\,\mu m$ the contribution drops below 30%.
In an unsegmented diode the weighting field is simply a constant ($|\vec{E}_W| = 1/D$), which means that the transient signal is directly proportional to the drift velocity. The Transient Current Technique (see Section 4.1 on page 79) takes advantage of this fact.
The induced current leads to a voltage drop at the bias resistor and a charge is influenced at the capacitive coupled aluminium strip.

1.2.5 Read-Out

A digital read-out chip collects all charges in a given time interval and sends its coordinates to the front-end electronics if the collected charge is above a certain limit. If the charge cloud is smaller than the strip pitch p the measurement precision of digital read-out is given by the variance:

$$\langle \Delta x^2 \rangle = \frac{1}{p}\int_{-p/2}^{+p/2} x^2\, dx = \frac{p^2}{12} \tag{1.53}$$

With analogue read-out and charge-sharing among the strips one can reach higher precision of about $\Delta x \approx (N/S)p$ [Lut99]. The analogue read-out chip used in the CMS Tracker integrates the

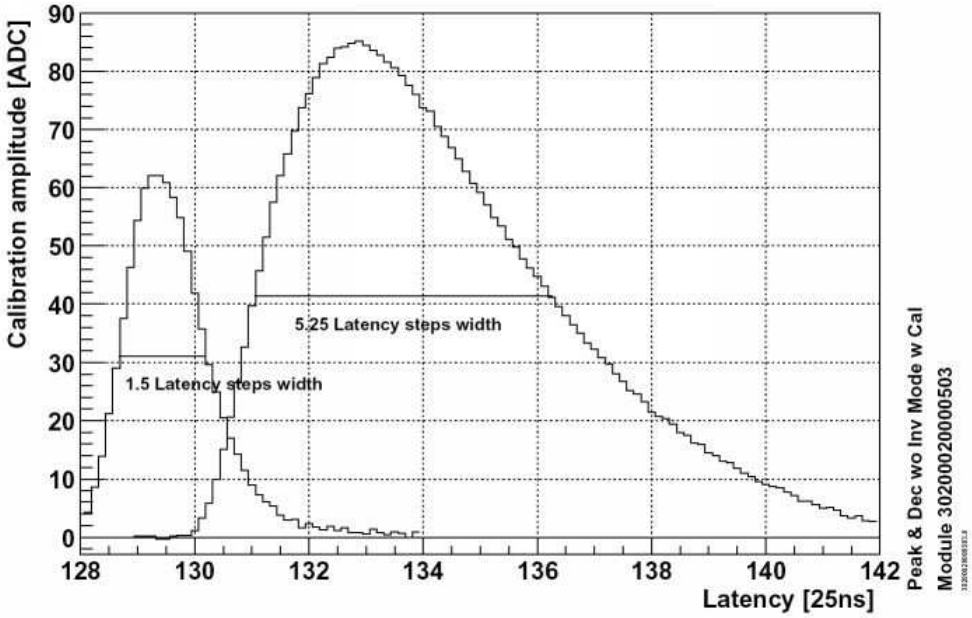

Figure 1.14: Calibration pulse shape in Peak and Deconvolution mode (from [Dir03]). At a bunch-crossing rate of 40 MHz *and high luminosity using the Peak mode would result in fake hits, since the signal is still high when successive bunch-crossings are triggered. In Deconvolution mode the signal is folded back to get a short signal in the correct pipeline cell.*

charge over a period of 50 ns[(1)] in the preamplifier and shapes (CR-RC filter) the signal pulse, which results in well defined voltage pulses with a rise time of 50 ns. The height of this pulse is then proportional to the collected charge. These pulses are sampled every 25 ns and stored in one of the 192 pipeline cells. In such a way, the data can be stored up to 4 μs allowing triggering within that time scale. The signal processing can be performed in two modes [J+99]:

Peak mode The shaped signal, which has a rise time of 50 ns and a width of $\sim$ 130 ns, is stored directly in the pipeline (Figure 1.14). Since the bunch-crossing time at LHC will be 25 ns, one would see hits from the previous bunch-crossing, which do not belong to the actual signal. With the correct latency the peak value of the voltage curve is read out.

Deconvolution mode To overcome the problem of the Peak mode without reducing the integration time, the shaped signal is folded back to get a signal on the time scale of the original pulse of the sensor (see again Figure 1.14). This procedure reduces the signal height and thus the signal to noise ratio, but guarantees clean assignment of the hits.

During the high luminosity phase at LHC only the deconvolution mode is used.

1.2.6 Noise

There are different sources of noise in the read-out of a silicon strip sensor. Let's derive the total noise of such a device with the help of Figure 1.15. One strip is represented by a diode,

(1) A shorter integration time would result in higher noise.

the equivalent capacitance C_{back} and a current source i_{shot} which reflects the shot noise current. This noise is caused by the leakage current and is a consequence of the discrete nature of electric charge. The statistic fluctuation of the number of charge carrier passing a boundary gives rise to fluctuations of the current, which is the shot noise:

$$\frac{d\langle i_{shot}^2 \rangle}{df} = 2q_{el}I_{leak} \tag{1.54}$$

In the bias resistance thermal fluctuations of the electron distribution leads to parallel thermal noise:

$$\frac{d\overline{i_{n,bias}^2}}{df} = \frac{4k_BT}{R_{bias}} \tag{1.55}$$

The resistance of the metal strip is in series with the read-out line and contributes a serial thermal noise voltage:

$$\frac{d\overline{u_{n,strip}^2}}{df} = 4k_BTR_{metal} \tag{1.56}$$

The dominant noise source of the amplifier comes from the input transistor and is represented by a voltage source $u_{n,amp}$. It is common practice to represent the noise as the charge necessary to compensate for the noise source. The equivalent noise charge at the proper amplifier is $Q_{n,p} = -u_{n,amp}(C_{strip} + C_{in} + C_f)$ and $Q_{n,s} = u_{n,amp}C_{strip}$ is fed into the capacitive network, which is seen by the adjacent amplifiers. The total capacitance of a strip C_{strip} is composed of the coupling capacitance C_c, the inter-strip capacitance C_{int} and the capacitance to back plane $C_{back} = C_{back,tot}/N_{strips}$ like:

$$C_{strip} = \frac{C_c(2C_{int} + C_{back})}{C_c + (2C_{int} + C_{back})} \approx 2C_{int} + C_{back} \tag{1.57}$$

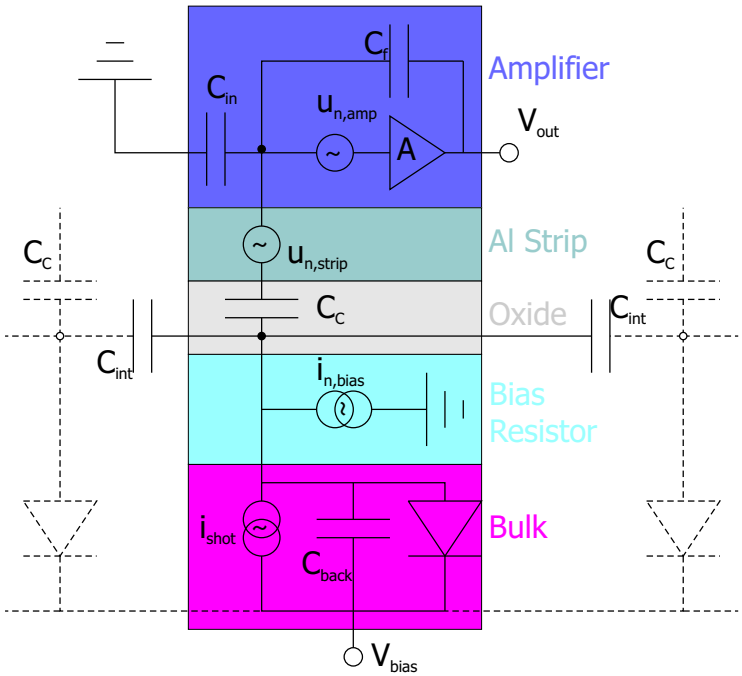

Figure 1.15: Equivalent circuit diagram for a capacitive coupled strip detector connected to a charge-sensitive amplifier. The dashed lines represent adjacent strips, which influence the capacitive load at the amplifier input. The coloured boxes represent different parts of the sensor as indicated on the right side.

Noise source (Type)	ENC (RMS e^-)	Formula at $T = -10°C$ for Peak mode	Deconvolution mode
Reverse bias current (parallel)	$\sqrt{\frac{q_{el} i_{n,bias} T_s}{4}}$	$\approx 108 \cdot \sqrt{i_{n,bias}(\mu A) T_s(ns)}$ ($\simeq 50 - 1320$)	$\times 0.45$
Bias resistance (parallel)	$\sqrt{\frac{k_B T T_s}{2R_{bias}}}$	$\approx 22.5 \cdot \sqrt{\frac{T_s(ns)}{R_{bias}(M\Omega)}}$ ($\simeq 170$)	$\times 0.45$
Metal strip resistance (series)	$C_{strip}\sqrt{\frac{k_B T R_{metal}}{6T_s}}$	$\approx 13 \cdot C_{strip}(pF)\sqrt{\frac{R_{metal}(\Omega)}{T_s(ns)}}$ ($\simeq 390$)	$\times 1.45$
Front-end electronics (series)		$246 + 36 \cdot C_{strip}(pF)$ ($\simeq 785$)	$396 + 59 \cdot C_{strip}(pF)$ ($\simeq 1280$)
Total		895-1595	1400-1525

Table 1.1: Noise sources, types and equivalent noise currents (ENC) evaluated for the CMS read-out system [Pro98, Col00]. The values in brackets are calculated for a TOB module with two sensors using $T_s = 50\,ns$, $R_{bias} = 1.8\,M\Omega$, $R_{metal} = 2 \times 100\,\Omega$, $C_{strip} = 2 \times 7.5\,pF$ and $I_{leak} = 2 - 1500\,nA$. The high leakage current is expected after 10 years at LHC.

since a typical coupling capacitance is $C_c \sim 40\,pF/cm$, which is much larger than $2C_{int} + C_{back} \approx 500\,fF/cm$.
The total noise is the quadratic sum of all mentioned noise sources:

$$Q^2_{total} = 2q_{el} I_{leak} F_i + \frac{4k_B T}{R_{bias}} F_i + F_u C^2_{strip} 4k_B T R_{metal} + F_u C^2_{strip} u^2_{n,amp} \tag{1.58}$$

where F_x are form factors considering the pulse shape. They can be calculated from the system's pulse response $W(t)$ and a characteristic time T_s, which is the rise time of the shaper ($50\,ns$):

$$F_i = \frac{1}{2T_s}\int_{-\infty}^{\infty} W(t)^2 dt, \quad F_u = \frac{T_s}{2}\int_{-\infty}^{\infty}\left[\frac{dW(t)}{dt}\right]^2 dt \tag{1.59}$$

The noise sources are collected in Table 1.1 with the evaluated form factors for the CMS conditions.
For a TOB module with two sensors having a typical strip length of $10\,cm$ each, the noise can be calculated using the formulas in Table 1.1. The characteristic time is the rise time of the shaper $T_s = 50\,ns$. The bias resistances are typically $R_{bias} = 1.8\,M\Omega$. The metal resistance including both sensors and the pitch adapter is of the order of $R_{metal} = 200\,\Omega$. The strip leakage current can vary from $2\,nA$ (at RT) up to $1.5\,\mu A$ (at $-10°C$ after irradiation) and the strip capacitance is around $7.5\,pF$ for one sensor. With these numbers one can calculate a noise of $895\,e^-/1400\,e^-$ before irradiation and $1595\,e^-/1525\,e^-$ with the high leakage current after irradiation for peak and deconvolution mode, respectively. An increase of the strip capacitance up to $1.3\,pF/cm$ after

irradiation would result in a noise of 1845 e^-/2110 e^-, which is an increase of 38% in deconvolution mode! This dramatic impact of the strip capacitance on the noise is the reason why this parameter has to be watched carefully in the irradiation qualification described in Chapter 3 on page 51.

1.3 Radiation Damage

The main topic of this work is radiation damage in silicon detectors and the consequences for functionality and performance. This section will give an introduction to basic damage mechanisms and an overview about the affected sensor properties.

1.3.1 Basic Damage Mechanisms

One of the interactions of radiation with matter is ionisation. Charged particles and photons interact with the electron cloud and generate electron-hole pairs. This process is reversible if no damage is induced. In contrast, interactions with the crystal lattice might lead to irreversible damage and limit the detector lifetime. The NIEL (Non-Ionising Energy Loss) scaling hypothesis, which is used to compare the damage induced by different particles, relies on the proportionality of NIEL and induced damage.
To kick a silicon atom from its lattice site a minimum recoil energy of $T_{min} \sim 15\,eV$ is needed. The energy, at which the probability to displace an atom is one half, is $E_d = 25\,eV$, since it depends on the recoil direction [vLFL$^+$80]. Below this value the energy is dissipated as phonons. For displacement energies just above the threshold a silicon atom is kicked out off its lattice site and one or more vacancy-interstitial pairs (Frenkel pairs) can be created. The maximum recoil energy T_{max} of a particle with mass m in a head-on collision with silicon ($M \approx 28\,m_p$) is:

$$T_{max} = \frac{4Mm}{(M+m)^2}E \tag{1.60}$$

In Table 1.2 on the following page maximum and average recoil energies for several particles are given.
The hit silicon atom (primary knock-on atom; PKA) moves through the crystal creating further damage on its track of range [vLFL$^+$80]:

$$R \approx 32\,\frac{nm}{keV}\sqrt{E_R} \qquad \text{for} \quad E_R < 10\,keV \tag{1.61}$$

where E_R is the recoil energy. A rate of energy loss can be derived from the range as $dE_R/dz \sim \sqrt{E_R}$.
At low recoil energies ($1 - 2\,keV$) only isolated point defects are created. For higher energies ($E_R \gtrsim 10\,keV$) additional clusters appear at the end of the path, which are dense accumulations of point defects. Both the rate of energy loss and the mean free path between two collisions decrease with decreasing recoil energy along the path, but the mean free path is reduced faster than $\sim \sqrt{E_R}$. Below $5\,keV$ the mean free path is of the order of 10 $\mathring{A}$ and the created defects are close together.
Silicon atoms hit by the PKA (secondary process) might also cause further damage if the recoil energy is high enough (ternary process) and so on. The result of such a cascade of damaging processes is shown in Figure 1.16(a) on the next page, where the spatial distribution of vacancies

	Electron	**Proton**	**Neutron**	**Si^+**
Scattering mechanism	Coulomb	Coulomb and nuclear	Elastic nuclear	Coulomb
$E_{R,max}/E_{R,av}$ in keV for 1 MeV-particles	0.155/0.046	133.7/0.21	133.9/50	1000/0.265
min. energy for point defect/cluster in keV	260/4600	0.19/15	0.19/15	0.025/2

Table 1.2: Characteristics of typical interactions with silicon after [Lut99]. Indicated are the main scattering processes, the maximum ($E_{R,max}$) and average ($E_{R,av}$) recoil energy from an incident 1 MeV-particle of the listed type and the minimum energy necessary to produce a point defect or a cluster.

was simulated for a 50 keV-PKA. This is the average recoil energy by a collision with a 1 MeV neutron (see Table 1.2). The displacement damage can be calculated by:

$$D(E) = \sum_i \sigma_i(E) \cdot \int_0^{T_{max}} f_i(E,T) P(T)\, dT \tag{1.62}$$

where the sum runs over all possible interactions. σ_i is the cross section of the process and $f_i(E,T)$ is the probability of having a collision of a particle with kinetic energy E, which transfers a recoil energy of T. The Lindhard partition function $P(T)$ [LN62] gives the fraction of energy which goes into displacement of a silicon atom, e.g. $P(T) \approx 50\%$ for 10 MeV-protons, $P(T) \approx 42\%$ for

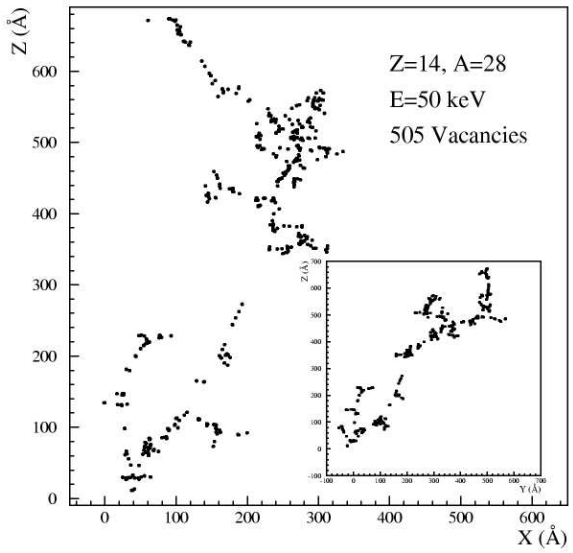

(a) Spatial distribution of vacancies created by a 50 keV Si-ion in silicon, which is the mean energy for a PKA by 1 MeV neutrons. At the ends of the tracks cluster are formed.

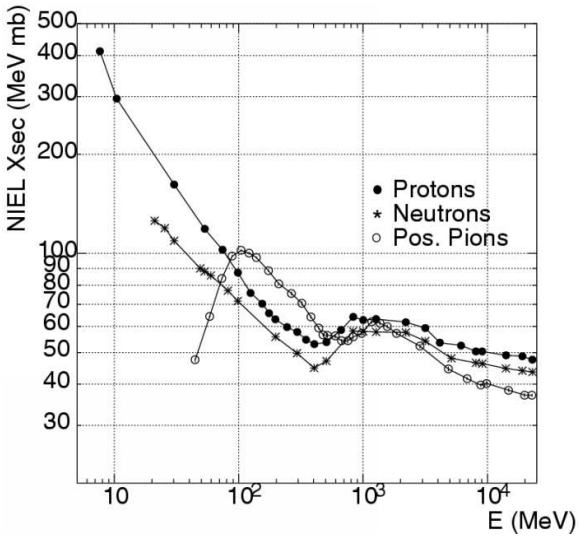

(b) Simulated NIEL cross-section for positive pions, protons and neutrons

Figure 1.16: Simulations of vacancy distribution and NIEL cross-section from [Huh01]

24 GeV-protons and $P(T) \approx 43\%$ for 1 MeV-neutrons [Huh01]. Simulated values of the NIEL cross-section are shown in Figure 1.16(b).
It is common use to scale the fluence to the equivalent fluence of 1 MeV-neutrons. The damage factor for neutrons at 1 MeV was defined to be $D_{neutron}(1\,MeV) = 95\,MeVmb$[(1)] since there are many resonances at this energy and the experimental approach is difficult. The hardness factor κ is defined as the ratio of the convolutions of the damage factors for the used particles and 1 MeV-neutrons with the used energy spectrum $\phi(E)$

$$\kappa = \frac{\int D(E)\phi(E)\,dE}{95\,MeV\,mb \cdot F} = \frac{F_{eq}}{F} \tag{1.63}$$

where $F = \int \phi(E)dE$ is the irradiation fluence. With help of the hardness factor one can calculate the equivalent fluence F_{eq} needed for 1 MeV-neutrons to produce the same damage as the used particles.

1.3.2 Defect Properties

During annealing the initial vacancies (V) and interstitials (I) can form defect complexes. Two or more vacancies can form n-vacancies V_n, where the di-vacancies are most common. Vacancies also combine with oxygen to the A-centre (VO) or even with an already formed A-centre to a V_2O-complex. The so called E-centre is a combination of vacancy and phosphorus atom (VP). These defects can appear as:

Generation-recombination centres An alternate capture/emission of electrons and holes lead to higher leakage current.

Trapping centres Electrons or holes are captured and re-emitted with a time delay, which might reduce the charge collection efficiency (CCE). Charges, which do not move during read-out time can not contribute to the signal.

Additional charge density in the space charge region This influences the full depletion voltage of the sensor and might reduce the sensitivity. In addition, the resistivity and capacitance of the bulk is changed.

The electrically active defects have minimum two charge states. E.g. a phosphorus dopant is a donor, which can only be in a neutral or positive state. The transition from neutral to positive can be performed by electron emission to the conduction band or by hole capture from the valence band. The other transition can be realised by hole emission or electron capture. The electron occupation probability is determined by the probability of these four processes. From thermal equilibrium considerations one gets the electron capture rate:

$$R_n = \sigma_n v_{th,n} n_i N_d (1 - \mathcal{F}) \exp\left(\frac{E_F - E_i}{k_B T}\right) \tag{1.64}$$

and the electron generation rate

$$G_n = N_d \mathcal{F} \epsilon_n \tag{1.65}$$

[(1)] Millibarn: $1\,mb = 10^{-27} cm^2$

Defect	Charge state	Energy level in eV
Interstitial	I^- I^0 I^+	$E_C - 0.39$ $E_V + 0.4$
Vacancy	V^{--} V^- V^0 V^+ V^{++}	$E_C - 0.09$ $E_C - 0.4$ $E_V + 0.05$ $E_V + 0.13$
Di-vacancy	V_2^{--} V_2^- V_2^0 V_2^+	$E_C - 0.23$ $E_C - 0.39$ $E_V + 0.21$
A-centre	VO^- VO^0	$E_C - 0.18$
E-centre	VP^- VP^0	$E_C - 0.44$
Phosphorus	P^0 P^+	$E_C - 0.045$
Boron	B^- B^0	$E_V + 0.045$

Table 1.3: Characteristics of important defects in silicon from [Lut99]

with the Fermi level $\mathcal{F} = \mathcal{F}(E_d) = 1/(1 + \exp\frac{E_d - E_F}{k_B T})$. From these rates one derives for the electron emission probability:

$$\epsilon_n = \sigma_n v_{th,n} n_i \exp\left(\frac{E_d - E_i}{k_B T}\right) \tag{1.66}$$

This relation holds also in non-equilibrium conditions, since it does not depend on the Fermi energy. For holes we have:

$$R_p = \sigma_p v_{th,p} n_i N_d \mathcal{F} \exp\left(\frac{E_i - E_F}{k_B T}\right) \qquad \text{and} \qquad \epsilon_p = \sigma_p v_{th,p} n_i \exp\left(\frac{E_i - E_d}{k_B T}\right) \tag{1.67}$$

These relations can be used to estimate the charge state of the defect in the SCR of a depleted sensor. For low leakage currents there are hardly charge carriers in the SCR and capture processes can be ignored. The charge state is than given by the ratio of electron and hole emission:

$$\frac{f^-}{f^+} = \frac{\epsilon_n}{\epsilon_p} = \frac{\sigma_n v_{th,n}}{\sigma_p v_{th,p}} \exp\left(2\frac{E_d - E_i}{k_B T}\right) \tag{1.68}$$

where $f^\pm$ is the fraction of defects in the more positive/negative state. From this we can conclude that defects at an energy level above E_i have a higher emission probability for electrons than for

holes and are thus in a more positive state. Defect levels below E_i are in the more negative state. Here we have assumed that the absorption cross-section and thermal velocities of electrons and holes are of same magnitude.
For heavily irradiated sensors the leakage current might become very high and the charge fraction is given by [Lut99]:

$$\frac{f^-}{f^+} = \frac{\epsilon_n + pc_p}{\epsilon_p + nc_n} = \frac{c_n n_i \exp(\frac{E_d - E_i}{k_B T}) + pc_p}{c_p n_i \exp(-\frac{E_d - E_i}{k_B T}) + nc_n} \tag{1.69}$$

There are also defects with several energy levels assigned to different charge states (see Table 1.3 on the preceding page), for which one derives similar expressions of the emission probabilities for electrons (holes):

$$\epsilon_{n(p),l} = \frac{g_{l-1(l)}}{g_{l(l-1)}} \exp\left((-)\frac{E_{t,l} - E_i}{k_B T}\right) n_i c_{n(p),l} \tag{1.70}$$

The degeneration factor g was introduced for defects, which appear in several configurations with the same charge and energy level.

1.3.3 Annealing

The initially created defects can migrate in the crystal and form new complexes. At high enough temperatures the complexes can also dissociate. Migration into sinks and dissociation can be described by the rate $\dot{N}_d = k_\gamma N_d^\gamma$, with the rate constant $k_\gamma = k_0 \exp(-E_A/k_B T)$ (Arrhenius relation), which reflects a faster reaction at elevated temperatures depending on the activation energy E_A. The order of the reaction is $\gamma = 1$ for single defects and $\gamma = 2$ for reactions of two defects of the same concentration. The time dependence of the defect concentration is for the two orders of reaction:

$$\text{1. order :} \qquad N_d(t) = N_{d0} \exp(-k_1 \cdot t) \tag{1.71}$$

$$\text{2. order :} \qquad N_d(t) = N_{d0} \frac{1}{1 + k_2 N_{d0} t} \tag{1.72}$$

Thus for second order processes the vanishing of the defect depends on the initial defect concentration, which is not the case for first order processes. A detailed discussion of annealing can be found in [Mol99].

1.3.4 Implications on Sensor Properties

As already mentioned on page 27 the introduced defects mainly affect leakage current, full depletion voltage and charge collection.

Leakage current

In many experiments it was shown that a single parameter can describe the increase in leakage current with irradiation fluence:

$$\frac{\Delta I}{V} = \alpha F_{eq} \tag{1.73}$$

where V is the volume of the diode and F_{eq} the equivalent fluence of $1\,MeV$-neutrons after NIEL scaling. The current related damage rate α is independent of the material as shown in Figure 1.17.

Annealing temperature in $°C$	21	49	60	80
α_0 in $10^{-17}\ A/cm$	7	6	5	4
τ_I in min	140000	260	94	9

Table 1.4: Parameters for annealing of the leakage current from [Mol99]. Below room temperature τ_I becomes larger than 100 days and the exponential term in (1.74) vanishes, which means hardly any annealing of the leakage current any more.

It was also observed that the leakage current and thus the α-parameter drops with time. This annealing behaviour can be parameterised after [Mol99] as

$$\alpha(t) = \alpha_I \exp(-t/\tau_I) + \alpha_0 - \beta \ln(t/t_0) \tag{1.74}$$

where $\alpha_I \sim 1.25 \cdot 10^{-17}\ A/cm$, $\beta \sim 3 \cdot 10^{-18}\ A/cm$ and $t_0 = 1\ min$. In Table 1.4 the values of the temperature dependent parameters τ_I and α_0 are shown. After $80\ min$ at $60°\ C$ the average damage rate is $4 \cdot 10^{-17}\ A/cm$.

Full depletion voltage ('Hamburg' model)

The maximum sensitivity of a sensor can only be reached when the space charge region covers the whole bulk. For a pad sensor this is done by applying the full depletion voltage according to (1.37) on page 14, which is proportional to the effective space charge concentration. During irradiation this N_{eff} is changed by many defect formation processes. E.g. donors are removed by the reaction $P+V \Rightarrow VP$. The created E-centre is in the more positive state (see (1.68)) which is the neutral state (see Table 1.3 on page 28). This process is able to reduce the space charge with increasing amount of vacancies, which is not bad at all. But in addition, acceptor type defects are created like the V_2O complex with an energy level of $E_C - 0.5\ eV$ and an introduction rate of about $0.9\ cm^{-1}$ [MHG96]. The microscopic description becomes more and more complicated

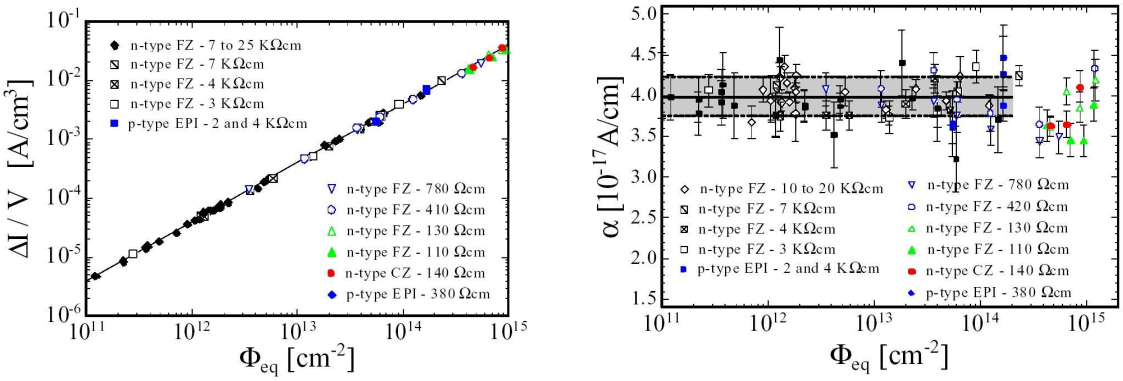

(a) Increase of leakage current vs. equivalent fluence

(b) Current related damage rate α vs. equivalent fluence

Figure 1.17: Increase of the leakage current for several materials taken from [Mol99]. The diodes were measured after annealing for 80 min at 60°C. The current related damage rate α is a constant for the measured samples and can be used to calculate the equivalent fluence.

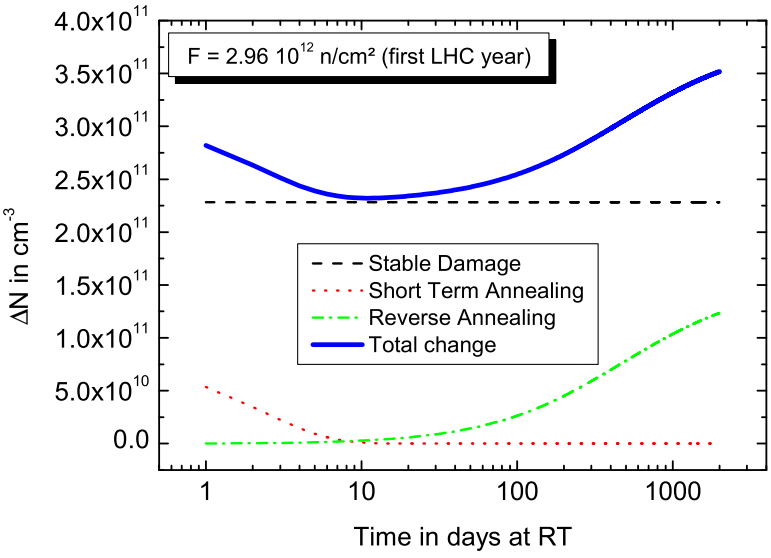

Figure 1.18: Annealing of the three damage components after the first year at LHC. A minimum in N_{eff} and thus in the full depletion voltage is reached after 14 days at room temperature.

as more defects are considered.
To parameterise the change in the space charge with fluence and annealing time the so called 'Hamburg' model was proposed [Mol99]. The change of the initial effective space charge concentration $\Delta N_{eff} = N_{eff,0} - N_{eff}$ has three components:

$$\Delta N_{eff} = N_C(F_{eq}) + N_A(F_{eq}, t) + N_Y(F_{eq}, t) \tag{1.75}$$

indicated in Figure 1.18. The components represent:

Stable damage $\mathbf{N_C}$ There is always a stable component of additional space charge, which does not change with time.

$$N_C(F_{eq}) = N_{C,0}(1 - \exp(-cF_{eq})) + g_c F_{eq} \tag{1.76}$$

The first part considers donor removal, where $N_{C,0}/N_{eff,0}$ is the fraction of removable donors, which depends on oxygen concentration. High oxygen concentration ($> 10^{16}\ cm^{-3}$) suppresses donor removal, since many vacancies are catched in E-centres, and the ratio $r_C = N_{C,0}/N_{eff,0}$ drops from about 80% to 10%. Neutron irradiated samples also show a suppressed donor removal, since the defects are in clusters and not homogeneously distributed. On average the initial donor removal rate is $N_{C,0} \cdot c = (7.5 \pm 0.6) \cdot 10^{-2}\ cm^{-1}$.
The second part reflects a constant increase with fluence and the introduction rate was measure to be $g_c = (1.49 \pm 0.04) \cdot 10^{-2}\ cm^{-1}$ [Mol99].

Short term annealing $\mathbf{N_A}$ Immediately after irradiation an increase in N_{eff} with time is observed. If N_{eff} was negative it becomes smaller and thus the full depletion voltage decreases. This process in then called beneficial annealing. It might be expressed as a sum of first order processes:

$$N_A(F_{eq}, t) = F_{eq} \sum_i g_{a,i} \exp\left(\frac{t}{\tau_{a,i}}\right) \tag{1.77}$$

Annealing temperature in $°C$	-10	0	10	20	40	60	80
Short term annealing (τ_a)	306 d	53 d	10 d	55 h	4 h	19 min	2 min
Reverse annealing (τ_y)	516 y	61 y	8 y	475 d	17 d	21 h	92 min

Table 1.5: Temperature dependence of the time constants for short term and reverse annealing from [Mol99]

where the introduction rate of the defect with the longest time constant was measured to be $g_a = (1.81 \pm 0.14) \cdot 10^{-2}\, cm^{-1}$. The time constant for several annealing temperatures is given in Table 1.5.

Reverse annealing $\mathbf{N_Y}$ After a longer annealing period acceptor type defects are created in a second order process:

$$N_Y(F_{eq}, t) = N_{Y,\infty}\left(1 - \frac{1}{1 + k_y N_{Y,\infty} t}\right) \tag{1.78}$$

Again the measured values are: $N_{Y,\infty} = (5.16 \pm 0.09) \cdot 10^{-2}\, cm^{-1} F_{eq}$ and $k_y \cdot N_{Y,\infty} \approx 1/\tau_y$ given in Table 1.5.

In Figure 1.19 on the next page two examples of this parametrisation are given for a 320 μm-diode with $\rho = 2.2\, k\Omega cm$ and a 500 μm-diode with $\rho = 4.4\, k\Omega cm$. A drop of the full depletion voltage with fluence is seen down to the inversion point, where the initial n-type bulk becomes effective p-type and the full depletion voltage starts rising again (stable damage). After irradiation beyond the inversion point V_{fd} is reduced down to a minimum, which is reached after two weeks at room temperature. Longer annealing time will increase the full depletion voltage, which has to be avoided in experiments.

Trapping

As already mentioned in Section 1.3.2, defects above the intrinsic level are in a more positive state in the SCR and are able to trap electrons. This is true for both donors and acceptors. Defects below E_i are able to trap holes. The time it takes to trap a free electron (hole) in the SCR is given by:

$$\frac{1}{\tau_{tr}^{n(p)}} = \sigma_{n(p)} v_{th,n(p)} P_d^{n(p)} N_d \tag{1.79}$$

where $P_d^{n(p)}$ is the probability that the defect is in the more positive (negative) state. This corresponds to $f^{\pm}$ for single level defects and is much more complicated to derive for many level defects [Lut96]. To get an effective trapping time one has to sum over all trapping centres.
The trapped charge carriers do not drift and thus do not contribute to the induced current (see (1.52)). If the integration time is shorter than the de-trapping time (electron or hole emission see (1.66)) the charge collection efficiency will be reduced according to $I \sim \exp(-t/\tau_{tr})$.

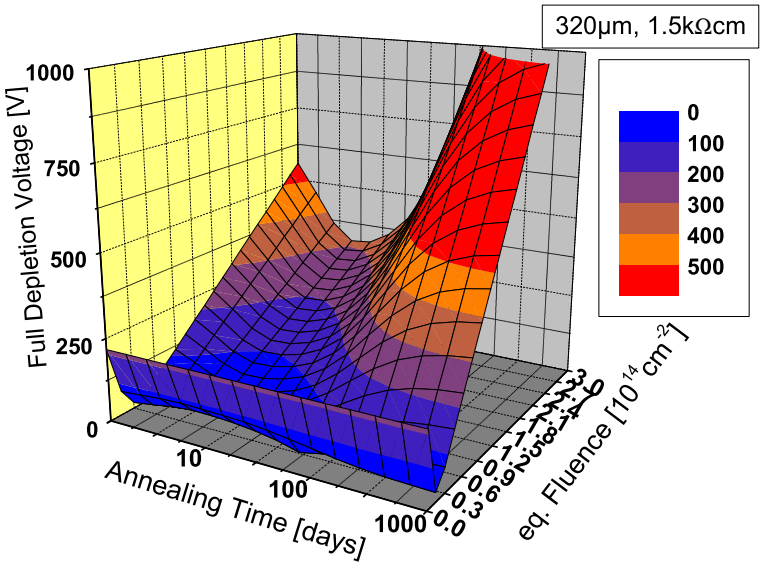

(a) 320 μm-diode with $\rho = 1.5\ k\Omega cm$

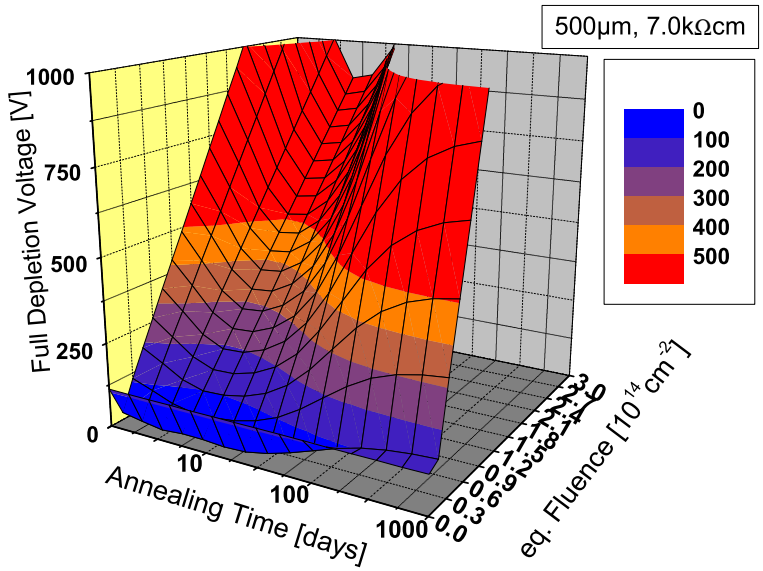

(b) 500 μm-diode with $\rho = 7.0\ k\Omega cm$

Figure 1.19: Two examples for the evolution of full depletion voltage according to the 'Hamburg' model. At a given annealing time the full depletion voltage drops at low fluences. After inversion it starts rising again resulting in a linear increase at high fluences.
At a given fluence past the inversion the beneficial annealing reduces the full depletion voltage within the fist two weeks at room-temperature. After the minimum reverse annealing increases N_{eff} reaching a plateau after strong annealing.

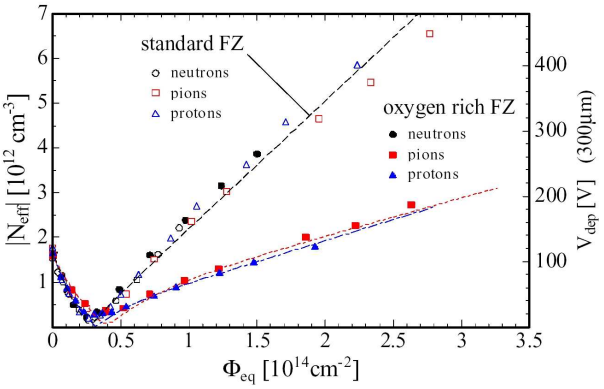

(a) Full depletion voltage vs. equivalent fluence for 23 GeV-protons, 192 MeV-pions and reactor neutrons [Mol00]

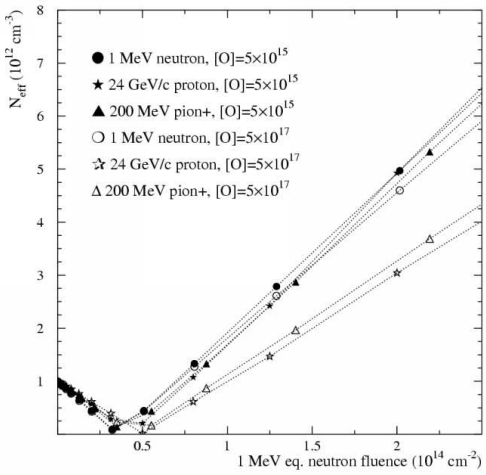

(b) Simulation of similar scenarios from [Huh01]

Figure 1.20: Full depletion voltage in oxygenated diodes is reduced for irradiation with charged particles in comparison with standard material. Neutrons do not show this beneficial effect, which violates the NIEL saling. An important role in the explanation plays the agglomeration of defects in clusters, which is not considered by the NIEL hypothesis.

1.3.5 NIEL Violation

All these parameterisations use the equivalent fluence, which relies on the NIEL scaling hypothesis. But experiments have shown that this hypothesis is violated in some cases. In this section two examples of NIEL violation are presented.

Full depletion voltage of oxygenated sensors

In Figure 1.20(a) you see measurements of full depletion voltage after irradiation with 23 GeV-protons, 192 MeV-pions and reactor neutrons. The fluence was scaled to 1 MeV-neutron equivalent following the NIEL scaling hypothesis, thus N_{eff} should be the same for the same material and different types of irradiation. But there is a clear violation of the NIEL scaling for oxygenated material. N_{eff} is much lower for irradiations with charged particles than for irradiations with neutrons. It was shown in [Huh01] that the different spatial distributions of defects contribute to the beneficial effect of oxygenation on full depletion voltage. The ratio of point defects to clusters is different for different particles and energies. In Figure 1.21 the initial distribution of vacancies is shown for 10 MeV and 24 GeV protons and for 1 MeV neutrons. The high density of point defects created by low energetic proton irradiation reflects a high fraction of Coulomb interaction, which transfers only small energy portions below the threshold of cluster creation ($T_{av} \approx E_d \ln(T_{max}/E_d)$). At higher proton energies the average recoil energy is high enough to produce clusters as can be seen in the middle of Figure 1.21. In case of neutrons, the interaction is elastic scattering at the nucleus, which results in a much higher average recoil energy of $T_{av} \approx T_{max}/2$ and thus producing clusters. The difference in spatial distributions is not considered by the NIEL scaling hypothesis. In the dense vacancy clusters only a small fraction of oxygen is present and the formation of e.g. A-centres, which are not charged and do not contribute to

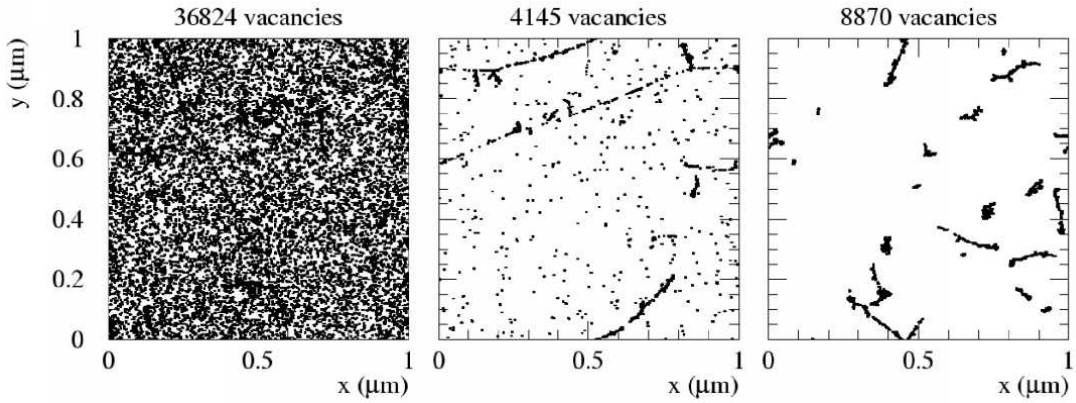

Figure 1.21: Initial distribution of vacancies produced by $10\,MeV$ *protons (left),* $24\,GeV$ *protons (middle) and* $1\,MeV$ *neutrons (right) from [Huh01]. The plots are projections over* $1\,\mu m$ *of depth and correspond to a fluence of* $10^{14}\,cm^{-2}$.

N_{eff}, is suppressed. Simulations of the effective doping concentration including spatial distributions and annealing effects are shown in Figure 1.20(b) on the preceding page, which demonstrate that these assumptions lead to a qualitative reproduction of the measurements.

Leakage current after γ-irradiation

The main contribution to leakage current as considered by NIEL scaling comes from clusters, where higher order vacancy complexes can form. Clusters are produced by neutrons and high energy charged particles. In this view $24\,MeV$-protons are still high energetic. In contrast γ-radiation only produces isolated point defects and the formation of e.g. V_2-complexes is suppressed [MFF+97]. This reduces the leakage current with respect to the NIEL expectation. In addition no annealing but a material dependency was observed [FKL+98].

1.3.6 Surface Damage

Surface damage is rather different from the bulk damage, described above. The silicon-oxide interface is already highly irregular and further crystal damage would not affect its properties. The main damage process here is ionisation! Generated charge carriers can also be captured by the defects, but the emission is strongly suppressed since the band gap is much larger in the insulator layer ($E_g = 8.8\,eV$ in SiO_2 and $E_g = 5.0\,eV$ in Si_3N_4). In SiO_2 the mobility of electrons is several orders of magnitude larger than the mobility of holes. Thus there is an accumulation of positive charge at the silicon-oxide interface, which saturates at about $N_{ox} \approx 3 \cdot 10^{12}\,cm^{-2}$ [W+01]. It was also

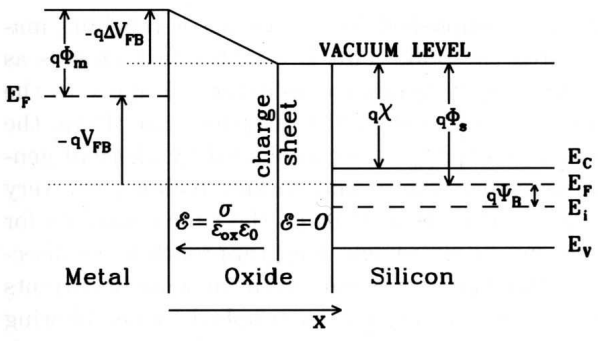

Figure 1.22: Flat-band voltage change due to oxide charges from [Lut99]

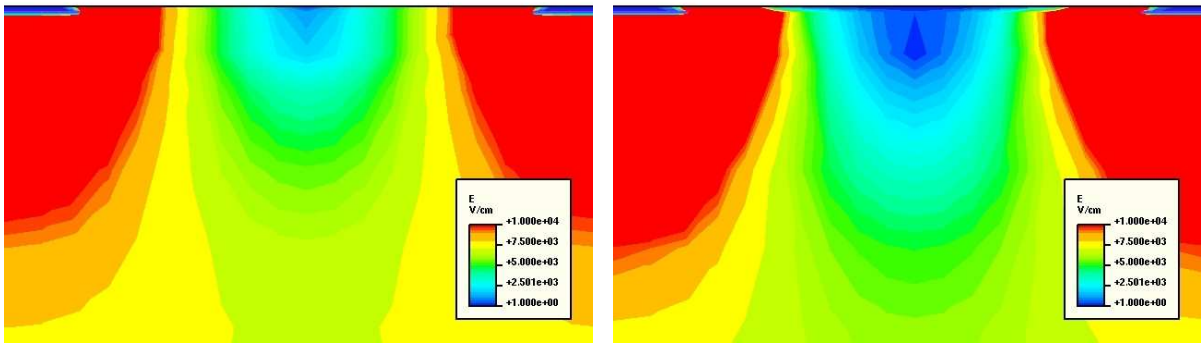

(a) Electric field with no oxide charge

(b) Electric field with $N_{ox} = 3 \cdot 10^{11}\ cm^{-2}$

Figure 1.23: Change in the electric field distribution by additional oxide charge. The region between two adjacent strips above full depletion was simulated with ISE-T-CAD. In the low field region charge carriers are present, which increase the polarisability of the medium and thus the capacitance.

shown in [W$^+$01] that an electric field, applied to the oxide, increases the charge accumulation. An electric field of 1 MV/cm increases the charge concentration by a factor of three.
The additional surface charge is accompanied by an increase in flat-band voltage as illustrated in Figure 1.22. A positive charge sheet in the oxide at a distance x from the metal influences charges in the metal and a constant electric field $E = \sigma/\varepsilon\varepsilon_0$ is generated in between. This means a linear increase in the potential as indicated in Figure 1.22, which changes the flat band voltage. An interface charge sheet and a charge density in the oxide can be integrated to gain the total change of the flat-band voltage:

$$\Delta V_{FB} = -\frac{1}{\varepsilon_{ox}\varepsilon_0}\left(\sigma_{int} d_{ox} + \int_0^{d_{ox}} \rho(x) x \, dx\right) \tag{1.80}$$

where σ_{int} is the surface charge at the silicon-SiO_2 interface and $\rho(x)$ is an additional charge density in the oxide volume. Measuring the flat-band voltage of MOS-structures thus is a diagnostic tool to investigate surface damage.
The additional charge modifies the field distribution between the strips and thus influences inter-strip capacitance and inter-strip resistance (see Figure 1.23).

Chapter 2

The CMS Experiment at the LHC

2.1 The Large Hadron Collider at CERN[1]

In the last years experimentalists have tested the Standard Model to a fraction of at least 1%. A big contribution was made by LEP[2], which was able to reach a centre-of-mass energy of 209 GeV. These results are of high accuracy and thus sensitive to phenomena occurring at even higher energies. All evidence indicate that new physics should be found around 1 TeV.
The new Large Hadron Collider (LHC) will be installed in the 27 km long LEP tunnel (see Figure 2.1(a)) using existing particle sources and pre-accelerators. It will accelerate protons up to an energy of 7 TeV, that is more than 1 TeV for the constituents of the proton (quarks and gluons) and ten times higher than at colliders like LEP or Tevatron[3]. To achieve the same amount of collisions at higher energies one has to increase the particle density in space and time,

[1] Centre Européenne de la Recherche Nucléaire near Geneva, Swiss
[2] Large Electron Positron collider at CERN
[3] Accelerator for protons and anti-protons at the Fermi National Accelerator Laboratory near Chicago, USA

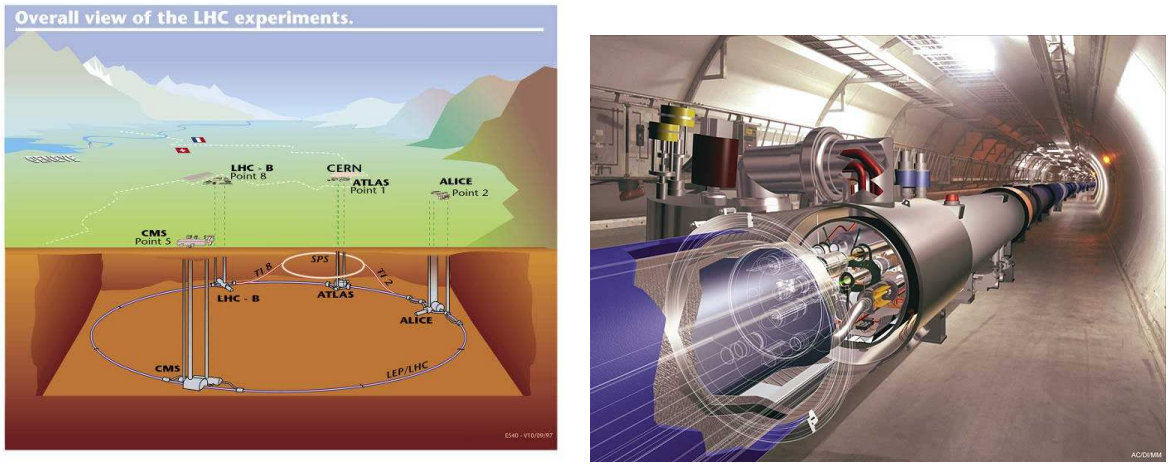

(a) Drawing of the LHC area from [LHCa]

(b) LHC tunnel from [LHCb]

Figure 2.1: Images of the LHC area and the tunnel

which is expressed by the luminosity L, proportional to the energy squared. Since the De Broglie wavelength of the particle decreases with $\sim 1/E$ one gets a proportionality for the cross section of $\sim 1/E^2$ which has to be counterbalanced by higher luminosity. Instead of $L \approx 10^{32} cm^{-2} s^{-1}$ at the past colliders, LHC has to reach $L \approx 10^{34}\, cm^{-2} s^{-1}$ for the same production rate. This luminosity is realised by filling each of the two rings with 2835 bunches consisting of 10^{11} protons. They will be accelerated by superconducting cavities ($d_{max} = 689\, mm$) reaching a maximum electric field of $5\, MV/m$. The stored energy per beam will be $350\, MJ$! The proton beams need to be bend on their circular track (Figure 2.1(b)) by a magnetic field of up to $8\, T$, which is provided by a system of superconducting magnets. The synchrotron radiation[(1)], which limits acceleration of electrons in colliders, is about $0.6\, W/m$ for the proton beam. This energy loss is no problem for acceleration. But evaporation of absorbed gases at the beam pipe worsen the high vacuum and the cooling system, which keeps the magnets at cryogenic temperatures might be affected.
With an inelastic proton-proton cross section of $70\, mb$ at $14\, TeV$ and a bunch crossing rate of $40\, MHz$ one will get on average *seventeen* collisions per bunch crossing. This means a total of 3000 charged and neutral particles together with the event of interest [Mül98]. Most of these minimum bias events are hadrons with low transverse momentum p_T and can be eliminated by the trigger and in the analyses by a cut on p_T.

2.2 Physics at the LHC

2.2.1 Higgs Physics

A major physics goal at LHC is the discovery of the Higgs boson.
The Higgs mechanism is an elegant way to generate masses of the vector bosons ($W^{\pm}$ and Z) and fermions (quarks and leptons), which are massless in the Standard Model. A spontaneous breaking of the electro-weak symmetry leads to the mass terms and leaves the theory renormalisable. This mechanism also predicts the existence of a new particle: the Higgs boson.

Production

The dominant production channel at LHC will be gluon-gluon fusion for all possible Higgs masses. Other processes like vector boson fusion and associated production with W or $t\bar{t}$-pairs are also important because of their special signatures, which help reducing the background. The corresponding Feynman diagrams are shown in Figure 2.2 on the facing page.

Detection

The detection of the Higgs boson depends strongly on the Higgs mass (see Figure 2.3).
For a **light** Higgs ($m_H < 130\, GeV/c^2$) two decay modes are important: $H \to b\bar{b}$ with a branching ratio close to one and $H \to \gamma\gamma$. The huge QCD background, which results in many di-jets, makes it rather impossible to detect a Higgs in the $H \to b\bar{b}$ decay mode. Associated production of a Higgs with W or $t\bar{t}$ improves the situation by high energy leptons from their decay, which can be used as a trigger. B-tagging has to be applied to identify the jets from b-quarks. The energy resolution suffers from escaping neutrinos and energy outside the jet cone. For the $Ht\bar{t}$-channel additional combinational problems arise with the four b-quarks in the final state.

[(1)] $E_{sync} = \frac{4\pi}{3} \frac{e^2}{R} (\frac{pc}{mc^2})^4$

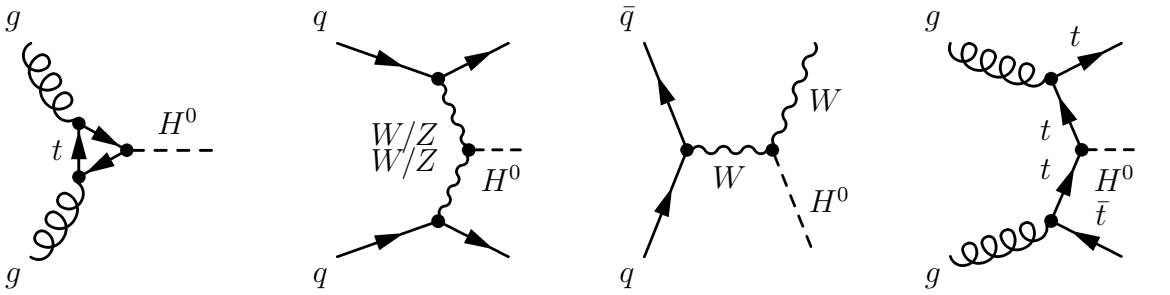

(a) Gluon-gluon fusion ($\sigma \approx 20\,pb$)

(b) Vector boson fusion ($\sigma \approx 2\,pb$)

(c) Associative production with W ($\sigma \approx 0.3pb$)

(d) One of the diagrams for associative production with $t\bar{t}$-pair ($\sigma \approx 0.05\,pb$)

Figure 2.2: Feynman diagrams of important Higgs production channels at LHC. In brackets you find approximate production cross-sections for a Higgs with a mass of 200 GeV.

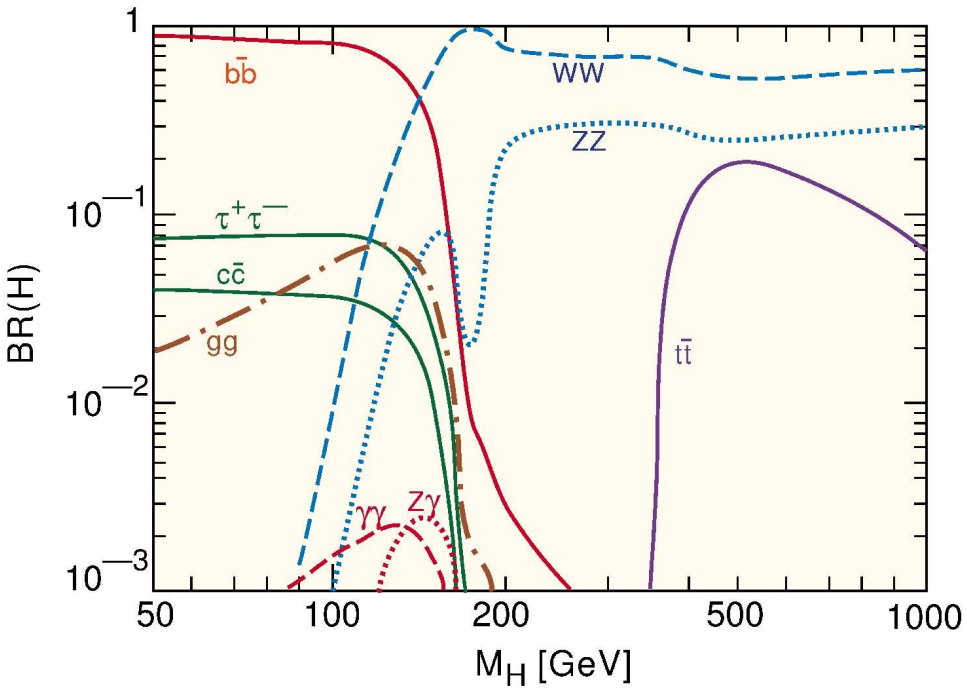

Figure 2.3: Branching ratio of the Higgs boson depending on its mass

Despite the small branching ratio, the $H \to \gamma\gamma$ decay mode is quite promising in this mass range. The two isolated electromagnetic clusters give a clear signature. The main background comes from direct photon production and jets faking photons.
For **intermediate** Higgs masses ($130\,GeV/c^2 < m_H < 2m_Z = 2 \cdot 91.2\,GeV/c^2$) the most powerful channels are $H \to ZZ^* \to 4l$ and $H \to WW^{(*)} \to l\nu l\nu$. To reduce the background of the first process one has to look for four isolated electrons, apply a mass cut on one lepton pair of the Z-mass and require at least $20\,GeV/c^2$ for the other two. In the WW^*-channel the missing energy and the lepton masses have to be combined.
A **heavy** Higgs ($2m_Z < m_H < 500\,GeV/c^2$) will be detected in the gold plated channel $H \to ZZ \to 4l$ with two Z's on their mass shell. An additional cut of $p_T \gtrsim m_H/2$ on one of the Z's will reduces most backgrounds.
For an even higher Higgs mass the decrease in the production cross-section has to be compensated by including the decay modes $H \to ZZ \to l\nu l\nu$ and $H \to WW \to l\nu jj$.

2.2.2 Supersymmetry

"Supersymmetry (SUSY) postulates a deeper relationship between matter particles (spin-1/2 or 'fermions') and force carriers (integer spin or 'bosons') than the Standard Model. In SUSY, each fermion has a 'superpartner' of spin-0 while each boson has a spin-1/2 superpartner. The Higgs sector is also extended to at least five Higgs bosons in the Minimal Supersymmetric Standard Model (MSSM). As of today, no superpartners have been observed: SUSY must be a broken symmetry, i.e. the superpartners must have masses different than those of their partner particles. Despite the doubling of the spectrum of particles, SUSY has many merits: it is elegant; assuming the existence of superpartners with TeV-scale masses, the Strong, Weak and Electromagnetic force strengths become equal at the same energy of $\sim 10^{16}\,GeV$ (the "GUT scale"); it also provides a natural explanation of why the Higgs mass can be low ($< 1\,TeV$). SUSY theories explain the dark matter in the Universe as being due to "neutralinos", the SUSY particles of the cosmic background. If SUSY is a true symmetry of nature and it is realised at the TeV-scale, it will almost certainly be seen in CMS." [Outb]

2.2.3 Heavy Ion Physics

"The LHC will not only collide proton beams: some periods of time will be spent colliding beams of heavy nuclei, such as calcium (Ca) or lead (Pb). Collisions between these nuclei will produce 'little bangs' at an equivalent temperature around 100,000 times that of the centre of the sun, and a density up to 20 times that of normal nuclear matter. Under these extreme conditions, which mimic those of the very early Universe - less than 1 second after the Big Bang, the constituent protons, neutrons and gluons (the carriers of the inter-quark force) 'melt' to form a 'quark-gluon plasma (QGP)'. CMS is very well suited to study some aspects of the formation of the QGP through the detection of muons and jets." [Outa]

2.3 The CMS Detector

CMS (Compact Muon Solenoid) is one of two general purpose experiments at LHC. The detector is designed to detect clean signatures of new physics such as Higgs physics and Supersymmetry. To reach this goal a robust tracking and vertex reconstruction in the strong magnetic field and the high background of minimum bias events is necessary.
Its layout is shown in Figure 2.4. The whole detector consists of several subdetectors:

Silicon Tracker: The Tracker consists of an inner pixel detector and an outer strip detector. The three layers of high granular pixel sensors ($100\,\mu m \times 150\,\mu m$) start at a closest distance to the beam axis of $4.3\,cm$. Together with two end disks on each side there are about 45 million pixels, which permit a primary vertex resolution below $50\,\mu m$ [KS01].
The strip detector will be discussed in more detail in Section 2.4.

Electromagnetic Calorimeter: A high precision electromagnetic calorimeter using lead tungstate ($PbWO_4$) crystals (61,200 in the barrel and 16,000 in the end caps) is important to reconstruct the $H \rightarrow \gamma\gamma$ decay for Higgs bosons with low mass. Lead tungstate is a dense crystal, which is relatively easy to grow. The scintillation light is detected by two silicon avalanche photodiodes on each crystal in the barrel region ($|\eta|$ <1.48) and vacuum phototriodes in the endcap region (1.48< $|\eta|$ <3.0). The expected energy resolution can be

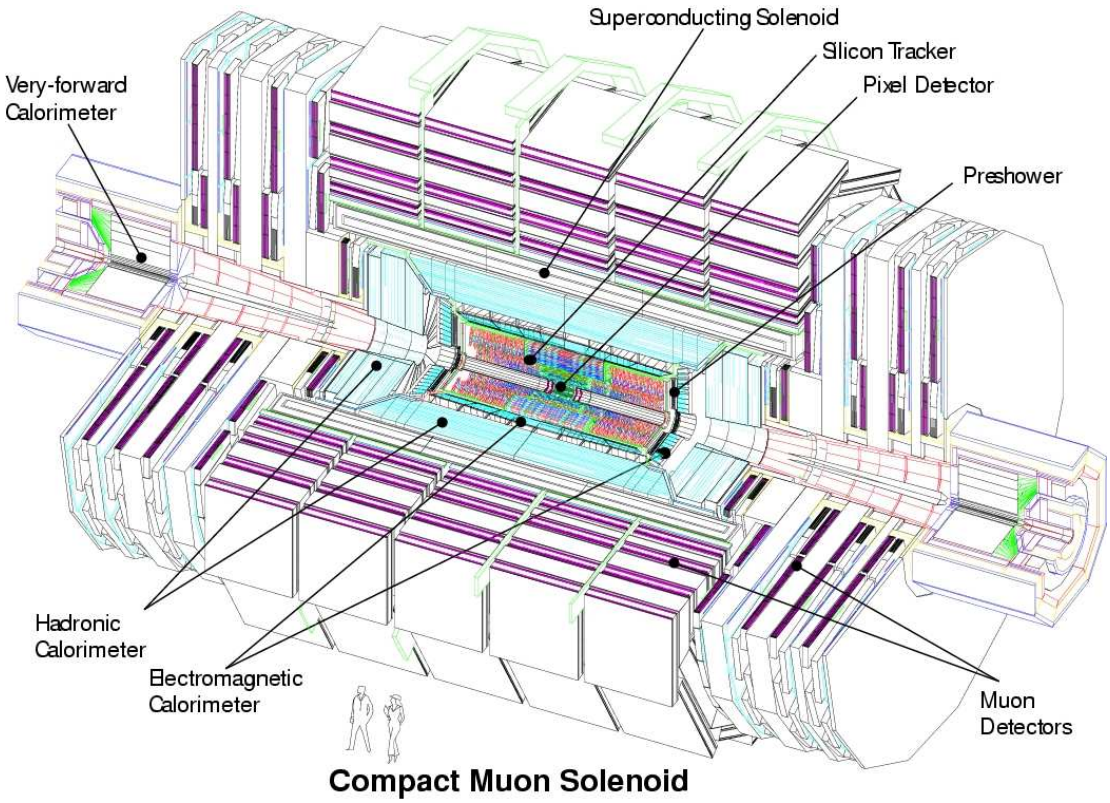

Figure 2.4: Layout of the CMS Detector from [CMS]

parameterised by

$$\left(\frac{\sigma_E}{E}\right)^2 = \left(\frac{a}{\sqrt{E}}\right)^2 \oplus \left(\frac{b}{E}\right)^2 \oplus c \tag{2.1}$$

For the barrel the stochastic term is $a = 2.7\%$, the noise is $b = 150 - 210\,MeV$ depending on luminosity and the constant term is $c = 0.55\%$. For the end cap one expects $a = 5.0\%$, $b = 205 - 245\,MeV$ and $c = 0.55\%$ [H$^+$97].
In addition, a pre-shower detector is used to distinguish between single photons and photons from π^0 decay. It is placed before the end cap and consist of two lead converters and silicon strip sensors with a pitch of $1.9\,mm$. Using the charge-weighted-average it is possible to get a position resolution of $300\,\mu m$ at $50\,GeV$.
In total a single photon reconstruction efficiency of 74.5% is expected.

Hadronic Calorimeter: The hadronic calorimeter barrel consists of alternating layers of copper and scintillators with a coverage up to $\eta = 1.3$. The light is channelled by clear fibres fused to wave-length shifting fibres embedded in scintillator plates. A similar design is used for the endcap region ($1.3 < \eta < 3$). The forward region ($\eta < 5.0$) is equipped by a steel/quartz fibre calorimeter. The Cerenkov light emitted in the quartz fibres is detected by photomultipliers.

Magnet: The magnetic field of $4\,T$ for momentum measurements is generated with the largest superconducting solenoid of its kind ($13\,m$ long and large bore of $5.9\,m$ in diameter). During operation it is kept at liquid helium temperature and stores an energy of $2.7\,GJ$. It is outside the electromagnetic and hadronic calorimeters thus improving their accuracy. The return yoke is combined with the muon chambers.

Muon Chambers: The muon detector is made of 3 different sub-detectors to ensure redundancy and robustness: Drift Tubes in the barrel region, Cathode Strip Chambers in the endcap region and Resistive Plate Chambers as dedicated trigger detectors in both the barrel and the endcap. It is embedded in the return yoke of the magnet. The muon system has a stand-alone momentum resolution of $8-15\%$ at $10GeV$ and $20-40\%$ at $1TeV$ and provides a clear bunch crossing identification and an efficient first level single/di-muon trigger. Together with the Tracker system a global muon momentum resolution of $1.0-1.5\,\%$ can be achieved if the constrains on the alignment are fulfilled.

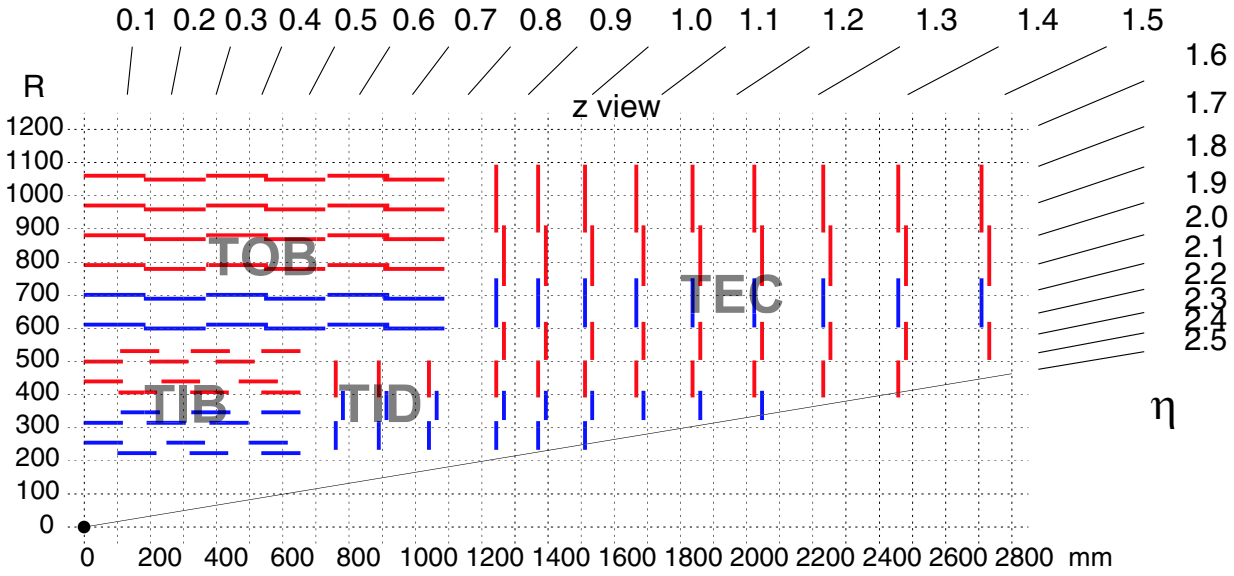

Figure 2.5: Layout of the Strip Tracker. There are single sided (red) and double sided (blue; 200 mm < R < 400 mm and 600 mm < R < 750 mm) modules. The abbreviations stand for Tracker Inner Barrel (TIB), Tracker Outer Barrel (TOB), Tracker Inner Disk (TID) and Tracker Endcap (TEC).

2.4 The Silicon Strip Tracker

2.4.1 Layout

The Silicon Strip Tracker (SST) [Pro98, Col00] has an outer diameter of 2.4 m and a length of 5.4 m. There is an inner barrel ($20 - 55\,cm$) with 4 layers of modules (see Sec. 2.4.3), an outer barrel ($60 - 110\,cm$) made of 6 layers and two endcaps each consisting of 9 disks segmented in 7 rings. In total there are 24328 sensor, which have a total active area of 206 m^2. Ten million read-out channels have to be wire bonded to 75,000 read-out chips (APV25 with 128 channels). Such a huge silicon detector can only be built since industry supplies 6 inch wafers. This reduces costs and allows the use of large area sensors in the outer part, which are combined to get modules with strip lengths of up to 19 cm. In the inner barrel the maximum strip length is 12 cm. Since strip capacitance (C_{strip}) increases with longer strips and noise increases with C_{strip}, one has to increase the signal to get the same signal-to-noise ratio. This issue is solved by using thicker silicon (500 μm) in the outer regions ($R > 60\,cm$, see Figure 2.5) than in the inner regions (320 μm). The thin sensors are delivered by Hamamatsu Photonics K.K.[(1)] (HPK) and the thick ones by ST Microelectronics[(2)] (STM). An active cooling system will keep the whole Tracker at a temperature of $-10°C$ to reduce leakage current and annealing effects of the silicon sensors. The cooling pipes are integrated in the support structures of the sub-systems, i.e. 'rods' in the barrel region and 'petals' in the endcap region (see Figure 2.6).

[(1)] Hamamatsu City, Japan
[(2)] Catania, Italy

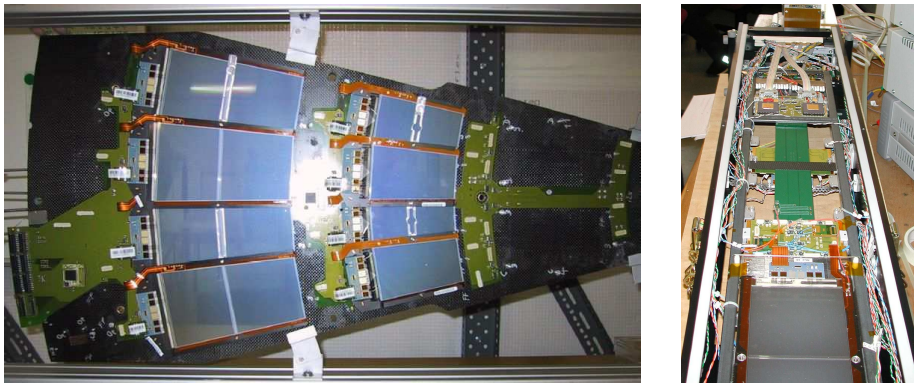

(a) Petal (b) Rod

Figure 2.6: The modules are assembled on support structures called 'petal' in the end-cap and 'rod' in the barrel.

2.4.2 Physics Performance

With the chosen layout (Figure 2.5) one has a hit multiplicity of at least eight (see Figure 2.7(a)) for $|\eta| < 2.4$ and 50% double sided hits, and the occupancy[(1)] is still low (≈ 0.02) even with 24 minimum bias events. This is a good starting point for high precision track reconstruction. One of the most important events for CMS is the decay of a Higgs into four muons. Tracks in the muon chambers can be traced back to the tracker and identify muons, which can be tracked with an efficiency of 100% over most of the η coverage [Len01]. The transverse momentum resolution is shown in Figure 2.7(b). Many of the interesting events at LHC include gauge bosons (W and Z). Their leptonic decay gives a nice signature in the Tracker and the momentum has to be measured

[(1)] Occupancy=no. of strips in reconstructed cluster/total no. of strips

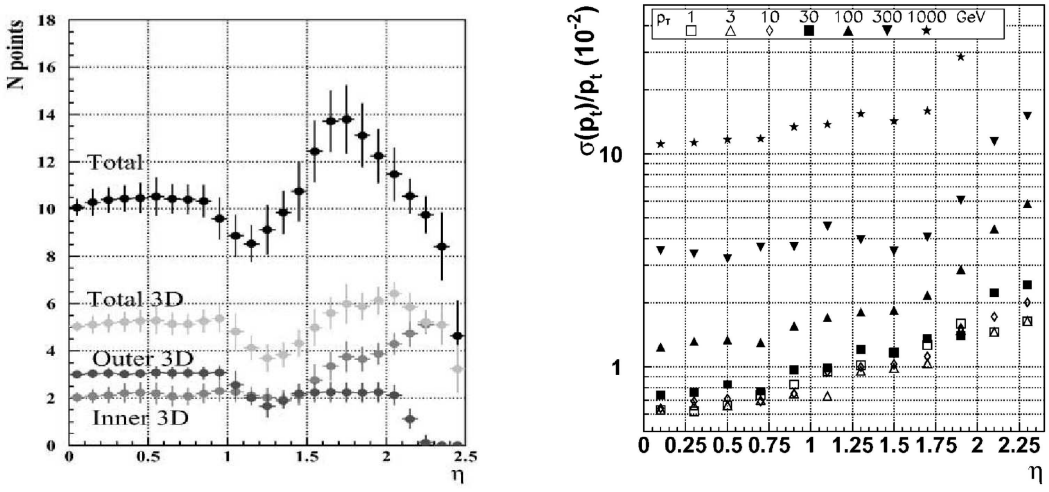

(a) Number of intersected detectors (b) Transverse momentum resolution

Figure 2.7: Hit multiplicity and transverse momentum resolution as a function of pseudo-rapidity for single muons with several p_t values after [Len01].

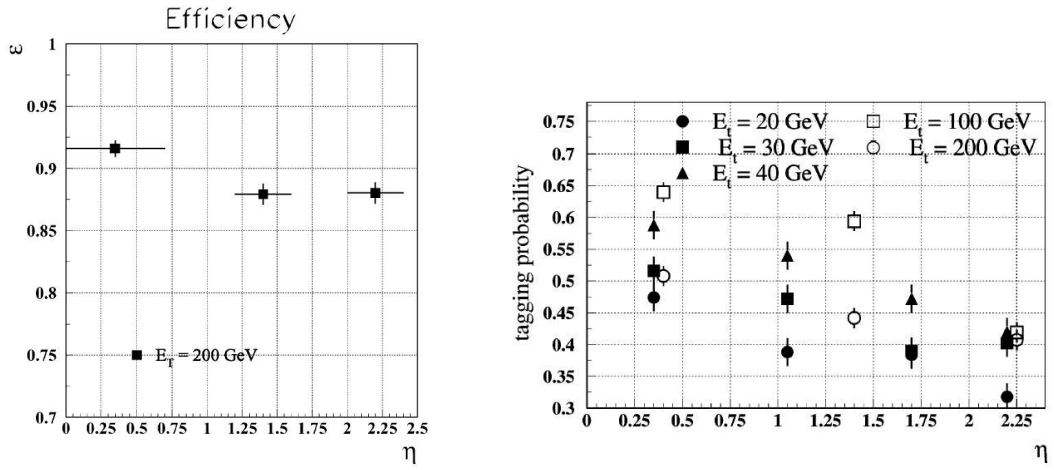

(a) Track finding efficiency in jets

(b) B-tagging efficiency

Figure 2.8: Efficiency of track finding and b-tagging. The track finding fake rate and the mistagging rate are below 1% *[Len01].*

with highest precision. To distinguish between electromagnetic clusters of isolated photons and electrons and verify that they are indeed isolated an efficient isolated lepton reconstruction is required. The efficiency of track finding in jets is shown in Figure 2.8(a). This will suppress $t\bar{t}$ and $Zb\bar{b}$ background and allow the observation of Higgs decay into four leptons.
For B-physics and the $H \rightarrow Zb\bar{b}$-channel one needs good tagging and reconstruction of b-jets, for which the efficiency is shown in Figure 2.8(b). More information can be found in the TDR [Pro98].

2.4.3 The Modules

The smallest subunit of the detector is the module (see Figure 2.9). It consists of the sensor(s), read-out electronics and a support frame. The latter is made of carbon fibre to guarantee stiffness and good thermal conductivity. Between the carbon frame and the sensor a kapton foil is glued, which provides the bias lines to the sensor backplane and electrically isolates the support frame. The read-out electronics are integrated on a so called hybrid, i.e. a kapton PCB with four to six read-out chips and connections to the power supplies. Opto-hybrids send the signals via optical fibers to the outside. The APVs are wire bonded to a pitch adapter, which itself is bonded to the AC-pads of the sensor. There are also modules with two sensors bonded together resulting in longer strips and larger active area. Another kind are double sided modules which consist of two sensors mounted back to back tilted by an angle of 100 $mRad$ to get unambiguous hits (see Figure 2.5).

2.4.4 The Sensors

All micro-strip silicon sensors are single-sided and AC coupled [BMFM03]. The bulk material is n-doped silicon with a resistivity for thin/thick sensors of $1.5 - 3.0\ k\Omega cm / 3.5 - 7.5\ k\Omega cm$, respectively, which causes the same range of full depletion voltages of $V_{fd} \approx 220\,V - 110\,V$.
The silicon is not oxygenated though there is a beneficial effect of oxygenation on the full depletion voltage after irradiation with protons and pions (see Section 1.3.5 on page 34). There are two

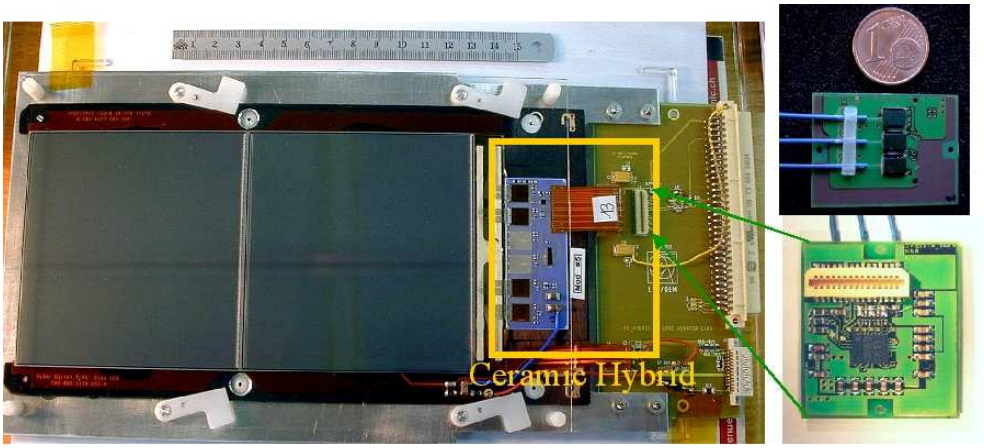

Figure 2.9: Picture of a complete module on a carrier plate made of aluminium together with a magnified opto-hybrid.

reasons for this decision. First, there is no beneficial effect if silicon is irradiated with neutrons, which make $20-50\%$ of the expected fluence depending on the position (Figure 3.1 on page 52). And second, industry does not offer oxygenation as a standard process and no guarantee is given on the quality of this process.
The $\langle 100 \rangle$ orientation of the crystal was chosen since experiments have shown more surface damage after irradiation using $\langle 111 \rangle$ oriented silicon [B^+00b].
The strips are realised by p^+-implants, which have a ratio of strip width to strip distance (pitch) of 0.25 for all layouts. This is a compromise between lower electric field peaks (at the edges of the implants) at smaller values and higher resolution at higher values of the width/pitch ratio.
Each p^+-strip is connected to the bias ring through a bias resistor ($(1.5 \pm 0.5)\ M\Omega$) which is

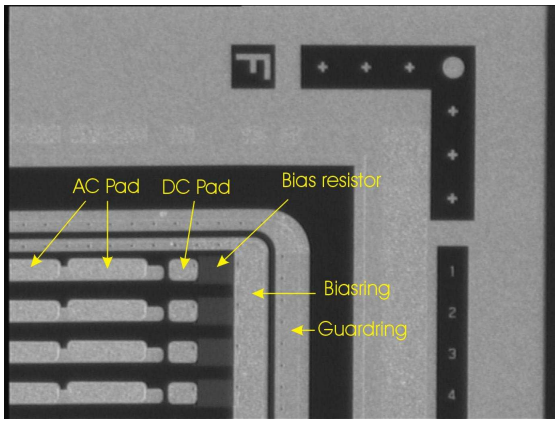

(a) The magnification shows the long AC-pads, the small DC-pads, the bias-resistors, the bias ring and the guard ring. In the upper right corner are alignment marks and on the right side the strip numbering.

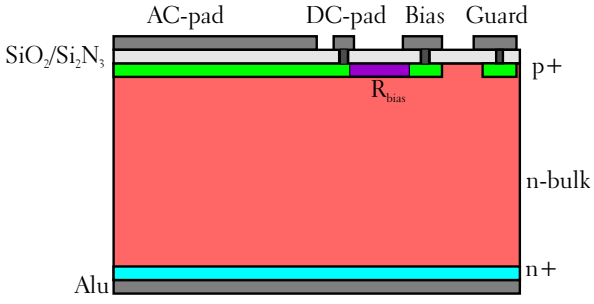

(b) Schematic cross sections of a strip sensor along the strips

Figure 2.10: Illustration of the contacts to a CMS strip sensors

realised by deposition of phosphorus doped polysilicon (Figure 2.10(b)) with a wiggle-shaped structure.
The whole sensor is covered with silicon oxide (SiO_2) and silicon nitride (Si_2N_3) layers, which serve as the coupling capacitance since the aluminium strips on top are connected to the read-out chips (see Figure 2.10(b)). The multi layer structure avoids the occurrence of pinholes, which is an ohmic contact through the dielectric layer. The charge sensitive read-out chips might be deteriorated by a DC current and thus connections to pinholes have to be avoided.
The aluminium strips are in addition a bit broader (metal overhang) to reduce the field strength near the implants. These efforts result in sensors with guaranteed breakdown voltage of more than $500\,V$. Most of them even stand $1000\,V$. The full depletion voltage after ten years at LHC will be around $300\,V$ and this allows to operate the sensors above full depletion during operation of the experiment.
There are probe pads at the via between bias resistor and p^+-implant for testing purposes (DC-pads). The AC-pads will be wire-bonded to the read-out electronics. Figure 2.10(a) on the facing page shows a magnified corner of the front side of a sensor with the described elements.
There are 15 different sensor geometries reviewed in Appendix B on page 123. Each sensor is processed on one 6"-wafer. The four cut-offs (so called half-moons) are used to process test-structures (TS) for quality assurance (see Section 2.5). The TS on one half-moon are identical for all geometries and both suppliers, which allows automatised and comparable measurements. For irradiation qualification the most important TS on the half-moon is an operative small replica of a sensor called mini-sensor. It has a rectangular shape ($16\,mm \times 23\,mm$) with 192 strips at a pitch of $120\,\mu m$. All relevant parameters can be measured on a statistical sample on this mini-sensor.

2.5 Quality Assurance Scheme for the Strip Sensors

One can imagine that the equipment of a tracker with such an amount of sensor modules is not a trivial task. It has to work for at least ten years and no maintenance during data taking is possible. Thus *all* components have to undergo a detailed quality assurance before assembly.

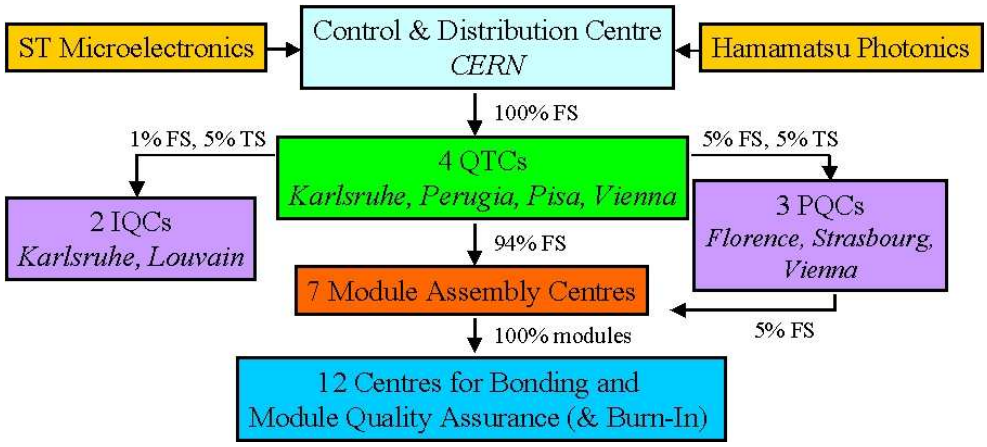

Figure 2.11: Logistics of the SST production and quality assurance. (FS=full sensors; TS=test-structures)

This is clearly not possible within considerable time and effort. Thus the following strategy was chosen [Har01, K$^+$03] (see flow chart in Figure 2.11). All delivered components have to be tested on critical parameters by the companies. They arrive at CERN where they are registered in a global database and redistributed to four Quality Test Centres (QTC), which are established at different collaborating institutes (HEPHY Vienna, IEKP Karlsruhe, INFN Perugia, INFN Pisa). The **QTC**s check the quality of delivered sensors on a subset depending on the actual quality. That means, the fraction of tested sensors is 100% at the beginning and can be relaxed to 5% for satisfying quality.
After an optical inspection, by which scratches, broken edges and bad dimensions are detected, the following electrical measurements are performed:

- Global tests:

  CV-characteristic Measuring the total capacitance (at $1\,kHz$) of the sensor depending on the applied bias voltage ($0 - 550\,V$) one can extract the full depletion voltage, which must not exceed $500\,V$ during operation period.

  IV-characteristic Leakage current over voltage measurement is a good indication for sensor quality. There are stringent limits on leakage current level ($I < 10\,\mu A$ at $300\,V$ and $I < 20\,\mu A$ at $450\,V$) and increase ($\Delta I < 10\,\mu A$ from $450\,V$ to $550\,V$). This measurement should ensure breakdown voltage of more than $500\,V$.

- Strip-by-strip tests at $400\,V$:

  Coupling capacitance On every strip the coupling capacitance between aluminium strip and implant is measured. This is an indication for oxide quality/homogeneity, shorts between adjacent strips and pinholes.

  Dielectric current In addition, the current through the dielectric (oxide) can be measured applying $10\,V$ between aluminium strip and implant. The measured current should be at noise level of few pA. At a level of $1\,nA$ the strip is classified as defect called *pinhole*. Strips with a pinhole must not be bonded to the read-out chip since the charge amplifying chip might be deteriorated by the high current flowing into a channel [Dir03].

  Bias resistance To get the bias resistance one measures the current between AC- and DC-pad applying $2\,V$. Higher voltages have to be avoided since they will disturb the field configuration near the implants and change the measured resistance[(1)].

  Strip leakage current Most of the bad IV-characteristics are due to few leaky strips which can be found measuring the leakage current of individual strips.

A sensor is rejected if IV- or CV-characteristics fail or 1% of all strips on the sensor are faulty.
The QTCs choose subsets (5% of sensors and 5% of TS) of the delivered batches and send them to the **Process Qualification Centre**s. They measure inter-strip resistance and capacitance on dedicated test-structures, IV on mini-sensor and gate-controlled diode, CV on diode and MOS device (flat-band voltage), the set of resistances of poly-silicon, aluminium and p^+-implants, coupling capacitances and the breakdown voltage of the oxide. In addition long time tests are done with full sensors measuring the leakage current.

[(1)] In parallel to the bias resistance are two inter-strip resistances ($\sim G\Omega$), which are affected by changing the field configuration.

(a) QTC-probe station for the electrical tests on the sensors

(b) IQC-probe station with humidity shield for operation at $-10°C$

Figure 2.12: Pictures of the probe stations for QTC and IQC at Karlsruhe. The measurements are performed fully automatic controlled by a LabView program.

1% of sensors and 5% of TS are foreseen to go to the two **Irradiation Qualification Centre**s (IQC), which study the performance of the sensors after irradiation to an equivalent fluence corresponding to ten years LHC. There is one IQC in Louvain responsible for neutron irradiation and one in Karlsruhe responsible for proton irradiation. Results from the latter are discussed in the next chapter. The sensors sent to these centres are lost for production but the remaining 99% are sent to the **Module Assembly Centre**s. There they are glued onto the frames using precise positioning systems (gantry see Figure 2.13(a) on the following page). Industrial bonding machines connect read-out chips and sensors (Figure 2.13(b) on the next page). Thereafter the complete modules are tested. Noise, pedestals and calibration runs are taken with a low noise read-out system. A cooling cycle down to $-10°\,C$ should reveal bad wire bonds or glue points. Using a LED array [W$^+$03] one can check, if the strips are responding and one can find shorted or broken strips. The LEDs can also be used for constant illumination generating higher leakage current, which reveals all existing pinholes. On some strips the dielectric current is inconspicuous at low leakage current of the sensor. An increase of the leakage current shifts the potential at the implant and a potential difference between implant and read-out ($V_{\text{virtual ground}} = 0.7\,V$) is built up. This enables the flow of a current through the pinhole. This kind of pinhole was hidden before, since the potentials were equal [Dir03]. This method allows to find the worst defects on the final module, since the high dc-current might saturate a complete chip and 128 channels are lost.

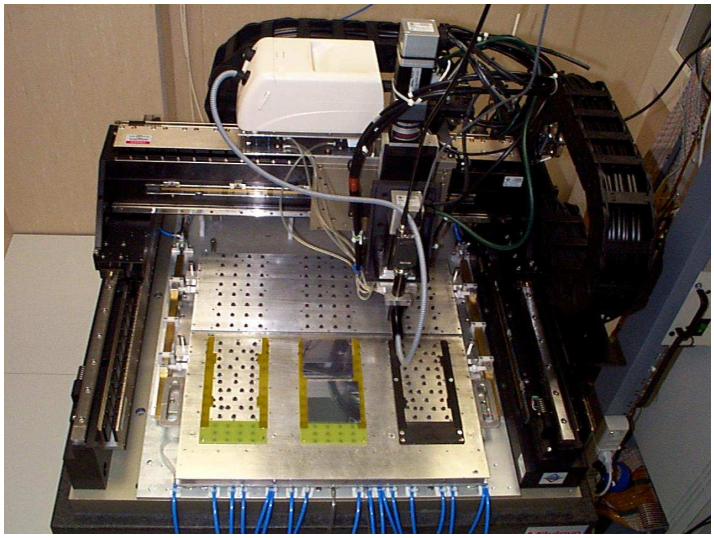

(a) Gantry at Bari

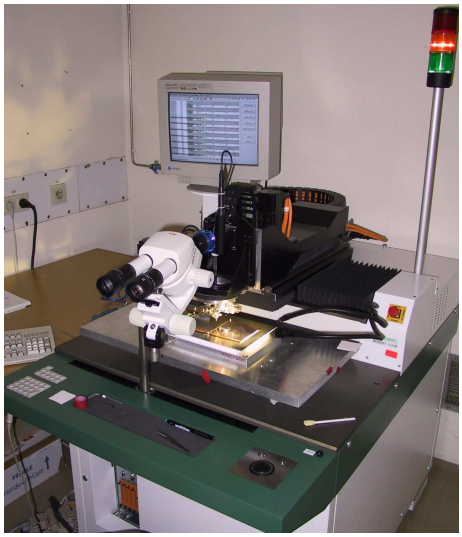

(b) Bonder at Karlsruhe

Figure 2.13: Pictures of an assembly robot and an industrial bonder used in the module construction of CMS

Chapter 3

Irradiation Qualification for the CMS all-silicon Strip Tracker

The qualification of the functionality of the sensors after radiation, equivalent to the harsh conditions at LHC, is an important part of the total quality assurance [K$^+$03, Die03].
One of the two Irradiation Qualification Centres was setup in Karlsruhe. The cyclotron at the Forschungszentrum Karlsruhe (FZK) is used as the proton source. For the measurements a fully equipped probe-station is used which is shared with the QTC. This chapter gives detailed information about irradiation and measurement procedure and the results.

3.1 Requirements

The irradiation qualification has to assure the operation of the sensors after an irradiation equivalent to ten years at the LHC. In the Technical Design Report simulations about the expected radiation environment are presented (see Figure 3.1). On the bases of these results the following maximal 1 MeV-equivalent neutron fluences were found for the two different thicknesses: $1.6 \cdot 10^{14}\ n_{1MeV}/cm^2$ and $0.35 \cdot 10^{14}\ n_{1MeV}/cm^2$ for 320 μm and 500 μm thick sensors, respectively. For safety reasons a 50% higher fluence was chosen as qualifying fluence thus resulting in $F = 2.4(0.5) \cdot 10^{14}\ n_{1MeV}/cm^2$. The sensors should be irradiated homogeneously and kept at $-10^\circ\,C$ during irradiation. This temperature was chosen to control annealing and to prevent thermal runaway due to the increase of leakage current during irradiation. Another reason is to be as close to operation conditions as possible. The sensors should also be biased at $400\,V$ which is possible with neutrons but not with protons. At proton currents used for qualification the ionising protons generate so many charge carriers in the sensors that one has a short circuit during irradiation. This would damage the sensors in a way that is not possible during real operation, hence another biasing scheme was pursued (see Section 3.2).
After irradiation a controlled annealing for 80 minutes at $60^\circ\,C$ has to be performed. This drives full depletion voltage in a minimum where the results are more stable and can be compared in a better way.
The electrical tests are performed before and after irradiation including global tests (CV and IV) and strip-by-strip measurements like in the QTCs. In addition the inter-strip capacitance and resistance are measured:

Inter-strip capacitance This parameter affects the noise of the device and scales with the

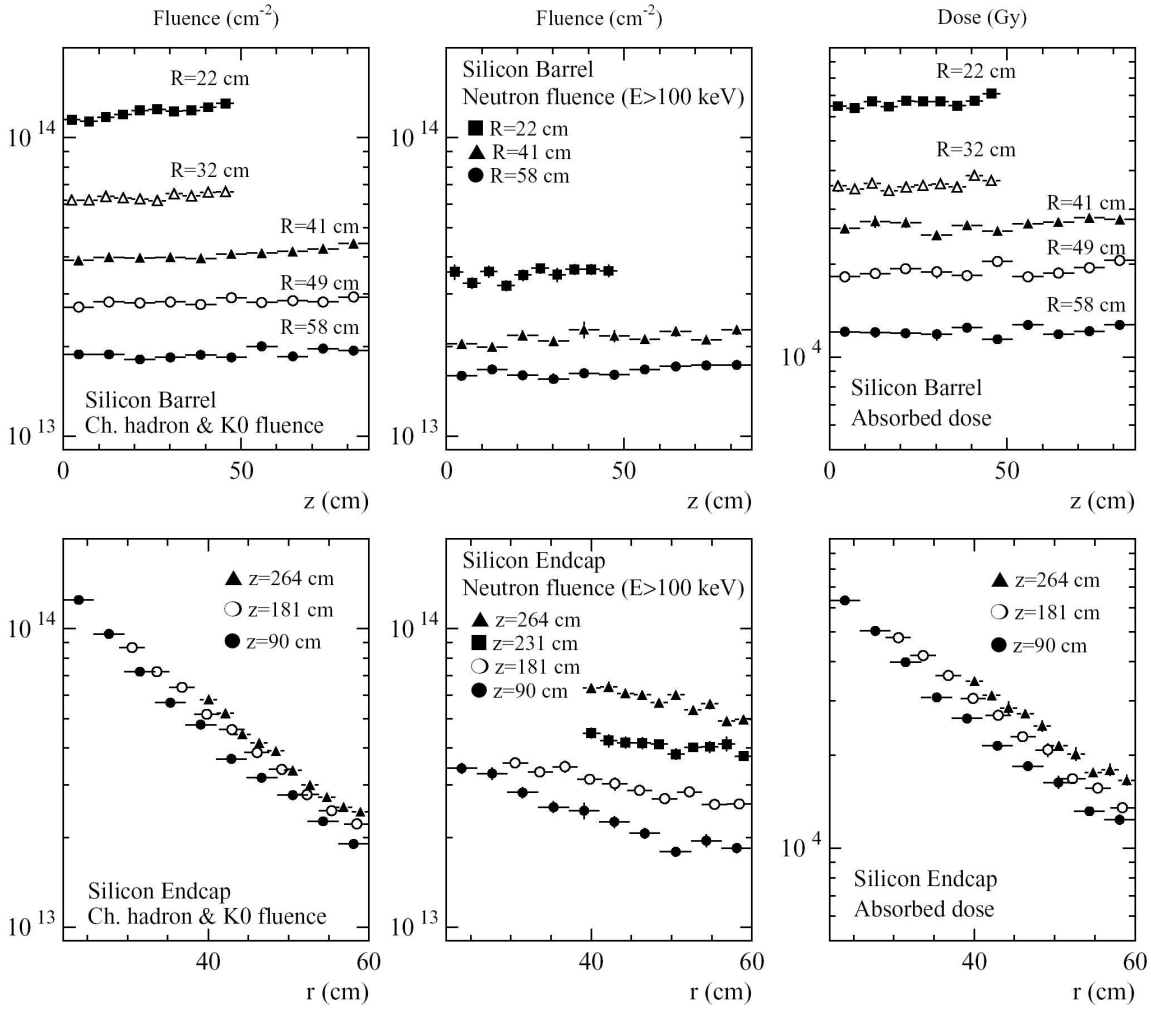

Figure 3.1: Expected fluence and dose in the silicon tracker according to [Pro98]. The maximum fluence for thin sensors is $F = 1.6 \cdot 10^{14}\, n_{1MeV}/cm^2$ *and for thick sensors* $F = 0.35 \cdot 10^{14}\, n_{1MeV}/cm^2$*. The maximum dose is expected to be* $67\, kGy$*.*

length of the strips and the oxide properties. These are changed by irradiation and thus influence this value, which should not exceed $1.3\, pF/cm$. It was shown in [B$^+$00b] that $\langle 100 \rangle$-material has no significant increase in C_{int} after irradiation, whereas $\langle 111 \rangle$-material had a 70% higher C_{int} at full depletion voltage and showed a further drop above, not reaching the $\langle 100 \rangle$-value at the double full depletion voltage.
The measurement is done with a frequency of $1\, MHz$ between two adjacent DC-pads using a LCR-metre. This applies a small voltage ($\sim 1\, V$) and measures amplitude and phase of the generated current. An example of this measurement on a wedge shaped sensor is shown in Figure 3.2(a) where the drop in the centre is caused by different strip lengths ($\Delta l \approx 45\, \mu m$). Modifications of the electric field near the edges cause an additional drop in C_{int} at the margins.

Inter-strip resistance A high resistance between the strips limits the cross talk and increases

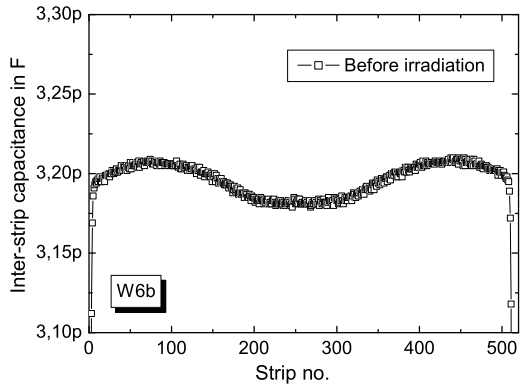

(a) Inter-strip capacitance on wedge shape sensor. The shape reflects the length of the strips. Strip 400 is only 45 μm longer than strip 256!

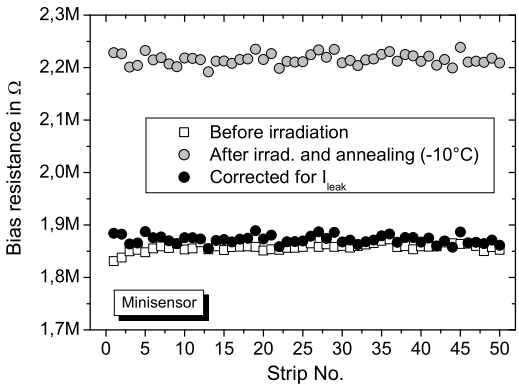

(b) Bias resistance corrected for increased leakage current, which is measured in addition to the measurement current.

Figure 3.2: Inter-strip capacitance measurement and correction of the bias resistance for leakage current

resolution. This parameter depends also on the oxide properties and might decrease due to irradiation. Usually the inter-strip resistance is of the order of $G\Omega$ and should be larger than 20 $M\Omega$ after 10 years at LHC. To measure such high resistances without destroying the field configuration a voltage ramp up to $2V$ is performed between two adjacent DC-pads and the slope of the measured current is analysed. In the $G\Omega$-range the measured currents are of the order of the noise and only an upper limit can be given.

The measured value of the bias resistances has to be corrected for the high strip leakage current after irradiation since this current is added to the current generated by applying $V_a = 2\,V$. The measured resistance is given by $R_{meas} = V_a/I_{meas}$ and has to be corrected for the strip leakage current I_{leak} by

$$R_{bias} = \frac{V_a}{V_a/R_{meas} + I_{leak}} \tag{3.1}$$

An example is shown in Figure 3.2(b).
Most of the strip parameters (R_{bias}, I_{leak}, C_{int} and R_{int}) are, in addition, measured during a voltage ramp, which should give an indication to the problem, when the qualification fails.

Figure 3.3: Picture of the isochron cyclotron at the Forschungszentrum Karlsruhe

3.2 Preparing an Irradiation

3.2.1 The Proton Source

The KIZ (**K**arlsruher **I**sochron **Z**yklotron at the FZK; see Figure 3.3) provides H_2^+ ions accelerated up to 52 MeV (26 MeV per proton). About half of the electrons are stripped at the foil closing the beam pipe. Connecting the foil to ground one can measure a foil current proportional to the proton current ($I_{p^+} \approx 4 \cdot I_{foil}$). This serves as an online monitor of the beam current since the usual current measurement is done on the internal beam stops before and after irradiation. The current is logged every second and stored on a file for each irradiation. Limits (usually $\pm 20\%$) are applied in the control system of the cyclotron, which initiates a beam stop when the current exceeds these limits. Reasons for this can be either large fluctuations in the beam current, which prevent homogeneous irradiations, or a total beam loss. But most of the time one gets a constant current as shown in Figure 3.4(a). When performing several irradiations the same current can be reproduced (Figure 3.4(b)) within the resolution of the current measurement of 10 nA.

3.2.2 The Irradiation Setup

A thermally insulated box was developed using Styrodur© plates, an aluminium cover for stability and two double mylar windows. The window at the back allows the proton beam to pass through avoiding activation of the box. Two layers of mylar foil with a distance of 1 cm prevent condensation on the outside together with a flow of dry air from a nozzle near the beam line. Nitrogen gas was chosen as the cooling medium. It is led through a heat exchanger in a liquid nitrogen bath and distributed in the box by means of a perforated tube. The temperature is measured by nine platinum resistors (PT100) and controlled by a mass flow controller. The box is put on a X-Z-stage in front of the beam pipe, which ends in an experimental hall as shown in

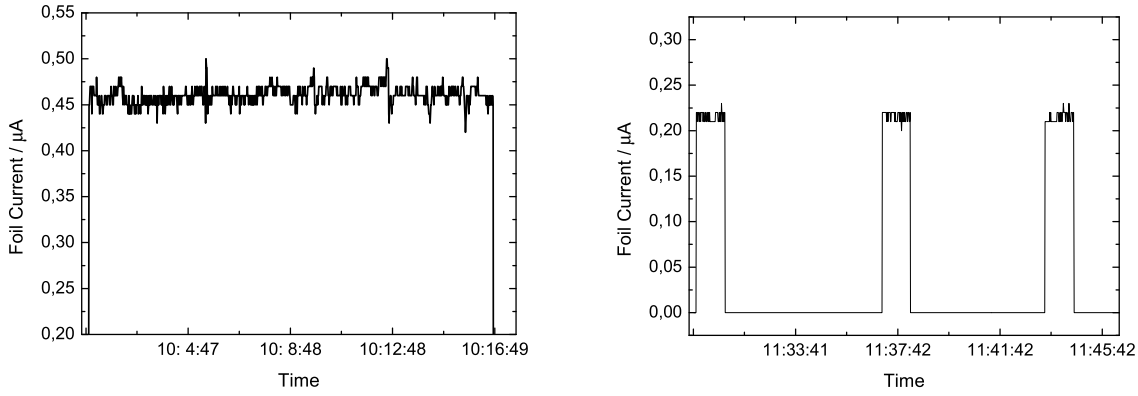

(a) The beam current is constant during irradiation...

(b) ... and reproducible.

Figure 3.4: Performance of the beam current

Figure 3.5(a). Full sensors and test-structures are stacked in frames (Figure 3.5(b)), which are then arranged in the box. Since the protons loose energy by passing through the silicon not more than two layers are stacked behind each other. In total one can put six frames in the box and one frame can hold three test-structures or one full sensor. To get a homogeneous irradiation using a proton beam with 2 cm diameter one has to move the beam spot over the whole area. Here we use the X-Z-stage to scan the sensor area with a continuous movement in X-direction and a 1 mm stepping in Z-direction. The starting point of the area to be scanned can be marked using a laser, which points along the beam axis. Therefore the box can be steered by a joystick and the starting position can be stored. The stage is computer controlled from outside. A LabView program was written to do the scanning and handle the interlocks. The motor controller is connected to the

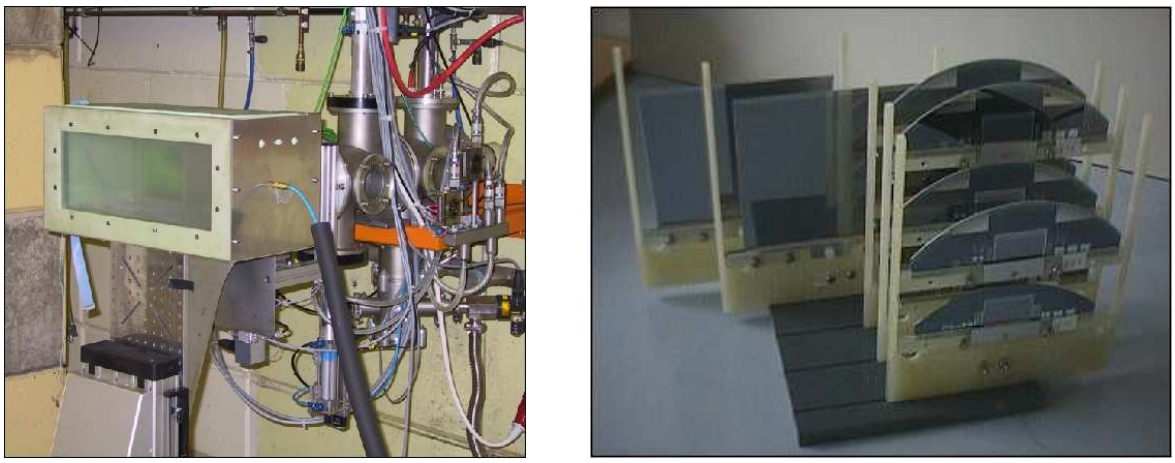

(a) Insulated box on the X-Z-stage. The beam pipe can be seen on the right.

(b) Sensors and TS in frames. The picture does not represent the positions in the box!

Figure 3.5: Pictures of the insulated box with beam pipe and frames

control system of the cyclotron, which controls the beam stops. Hence, the proton beam can only leave the beam line when the controller is ready, and an automatic stop is initiated if the beam current exceeds certain limits. The movement will be stopped at the next turning point and can be started again when the beam is back to the desired current. Usually a proton current of $2\,\mu A$ is selected and the irradiation of one frame lasts about $15\,min$.

3.2.3 Estimating the Fluence

If one has a uniform irradiation with a proton current I on the whole area A for the time t the fluence can simply be calculated by

$$F = \frac{I \cdot t}{q_{el} \cdot A}. \tag{3.2}$$

Using the scanning procedure the irradiation can only be stopped when the beam has covered the whole area, otherwise the irradiation is inhomogeneous. Hence the irradiation is done in multiples of complete area scans. The scan speed must be adapted to the desired fluence and the beam current. To motivate the used formula let's start with the simple fact that the beam has a certain profile and the total current results from the integration over this profile:

$$I = \iint j(x,z)\,dx\,dz = \iint j(v_x t, z) \cdot v_x\,dt\,dz \tag{3.3}$$

In the second step dx was replaced by $v_x dt$ where v_x represents the scan speed. The integral limits can always be set in a way that the whole profile is included. This is realised during the scanning by using a larger area (margin of one beam radius) than the target size. When integrating over time one gets that part of the fluence, which contributes at profile height z:

$$I = \int q_{el} F(z) \cdot v_x\,dz \approx \sum q_{el} F(z) \cdot v_x \cdot \Delta z \tag{3.4}$$

The z-integration is realised by a stepping of $\Delta z (= 1\,mm)$ (again including all contributing parts of $F(z)$), which gives the total fluence for every point in the target area after one complete scan considering the relevant margins:

$$F \approx \frac{I}{q_{el} \cdot v_x \cdot \Delta z} \tag{3.5}$$

In addition one needs the number of scans and the speed can be calculated to reach the desired fluence. For high and low fluences a scanning speed of $97.5\,mm/s$ (5 scans) and $177.5\,mm/s$ (4 scans) are chosen, respectively.

3.2.4 Measuring the Fluence

Cross checks were made with nickel foils which are put behind the sensors during irradiation. The foil is activated by proton collisions and the electron capture of $^{57}_{28}Ni$ is observed with γ-spectrometry. Therefore the foils are weighed, dissolved in sulfuric acid and filled in standardised vessels since the spectrometer is calibrated with this geometry. The dominating γ-line at $1377.6\,keV$ is used to determine the specific activity $a(t_{meas})$ of $^{57}_{28}Ni$. This is assigned to the proton current by a calibration factor f_{cal} derived from a previous calibration with $26\,MeV$ pro-

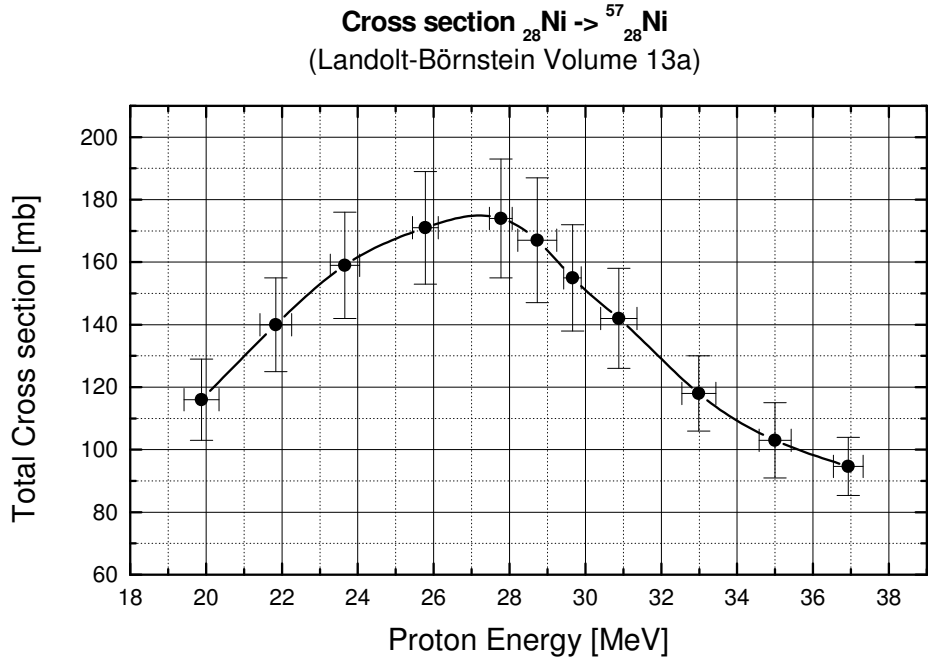

Figure 3.6: Nickel foils are used for dosimetry. The activity was calibrated to give the proton fluence for 26 MeV-protons. With the cross section of $^{58}_{28}Ni \rightarrow ^{57}_{28} Ni$ it is possible to correct the calibration factor for different proton energies.

tons. This calibration used the activity after 3.77 days. To get the activity at that time one has to take into account the half life of $^{57}_{28}Ni$, which is $\tau_{1/2} = 35.6\,h$:

$$a(3.77\,d) = a(t_{meas}) \cdot \exp\left(-\frac{(3.77\,d - t_{meas}) \cdot \ln 2}{\tau_{1/2}}\right) \tag{3.6}$$

If the foil is hit by protons with an energy different from $26\,MeV$ one has to correct the calibration factor according to the different cross sections:

$$f_{cal}(\sigma_E) = \frac{\sigma_E}{\sigma_{26MeV}} \cdot 19.28 \frac{kBq \cdot cm^2}{mg \cdot \mu Ah} = \frac{\sigma_E}{\sigma_{26MeV}} \cdot 8.57 \cdot 10^{-13} \frac{Bq \cdot cm^2}{mg \cdot p} \tag{3.7}$$

where $\sigma_{26MeV} = 172\,mb$ and σ_E is taken from Figure 3.6. The fluence is simply calculated by

$$F = \frac{a(3.77\,d)}{f_{cal}(\sigma_E)} \tag{3.8}$$

This represents the mean fluence on the whole foil area used for activity measurement.

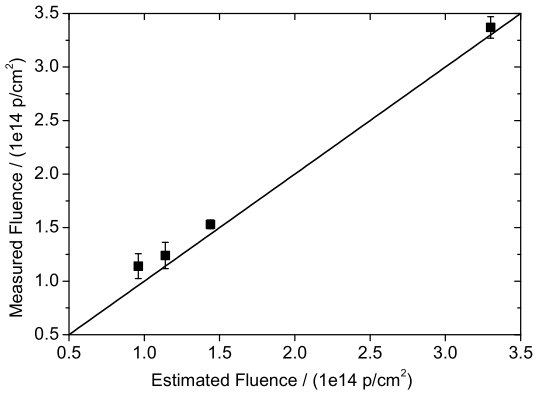

(a) Correlation of estimated and measured fluence. The estimation was done with formula (3.5) and the fluence was measured by dosimetry of the nickel foils.

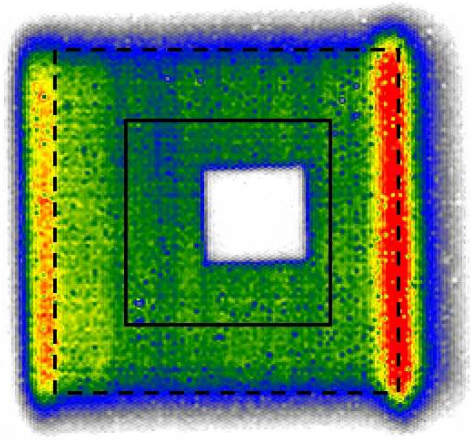

(b) Autoradiography scan representing fluence distribution. The area surrounded by the straight line is used for irradiation of the structures. The outer dashed line marks the scanned area. At the white area the foil was cut out for quantitative spectrometry.

Figure 3.7: Fluence estimation and distribution

3.2.5 Verifying the Scanning Procedure

With this scanning procedure one should be able to perform a homogeneous irradiation up to the desired fluence. The estimated fluence should equal the measured one. Four nickel foil were irradiated by scanning a large area of approximately $10\,cm \times 10\,cm$ with different scanning speeds ($50\ mm/s$, $100\ mm/s$ and twice $110\ mm/s$). Assuming the same beam current the fluence is proportional to the speed. There are always some fluctuations in the beam current so that for this analysis the mean current was calculated by the current integral divided by the irradiation time. The proton current integral was derived from the foil current which is proportional by a factor of 0.26 ± 0.02. This means that the online measured foil current is about a quarter of the proton current. The mean proton current than enters (3.5) giving the estimated fluence. Both fluences are put in the correlation graph in Figure 3.7(a). The fluence is always underestimated but within a deviation of 10%. To get a picture of the homogeneity of the fluence a large nickel foil was irradiated using the scanning procedure. The activation of the foil represents the fluence and was measured by autoradiography. The resulting picture is shown in Figure 3.7(b). The dashed line marks the scanned area of $50\ mm \times 50\ mm$. At the turning points the fluence is increased since the procedure of stopping, moving $1\,mm$ up or down and accelerating again takes more time than just passing. Therefore one beam radius ($1\ cm$) is skipped at each border and only the inner area (straight line) is used for irradiation of the structures.

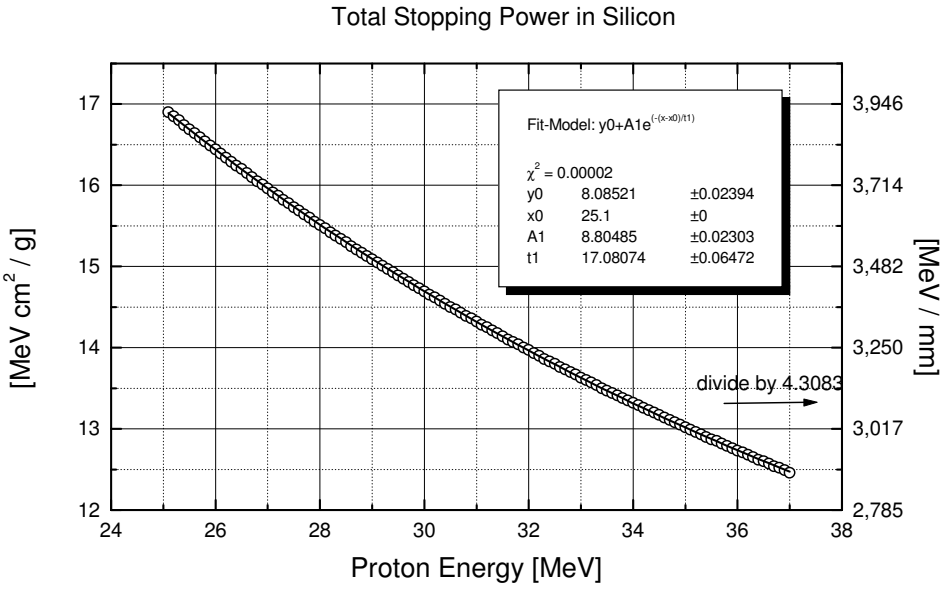

Figure 3.8: Stopping power of protons in silicon

3.2.6 Calculating the Dose

To calculate the dose, one needs to know the stopping power of protons in silicon (Figure3.8). Taking data from NIST[(1)] the stopping power can be parameterised as:

$$P_{Stopping}(E) = 8.1\ MeV\,cm^2/g + 8.8 MeV\,cm^2/g \cdot \exp\left(-\frac{E - 25.1\ MeV}{17.1\ MeV}\right) \tag{3.9}$$

To get the stopping power in MeV/mm one has to divide by 4.3083. The dose is then calculated by:

$$D = F \cdot P_{Stopping} \cdot 1.6022 \cdot 10^{-13} \frac{J}{MeV} \tag{3.10}$$

Using the stopping power in $MeV cm^2/g$ the unit of the dose D is $J/g = 1000\,J/kg = 1000\,Gy = 100\,kRad$. For high fluence and 26 MeV protons ($P(26\ MeV) = 16.4\ MeV cm^2/g$) the dose is about $340\,kGy$, which is much more than what is expected in the experiment for the inner silicon layer ($\sim$ 67 kGy see Figure 3.1). Already at $\sim$ 50 kGy the charge concentration in the oxide saturates [W$^+$01], which is the main problem of oxide damage. Thus, if surface damage after this proton irradiation does not deteriorate the sensor functionality, then they will survive in the experiment.

(1) National Institute of Standards and Technology, http://physics.nist.gov/

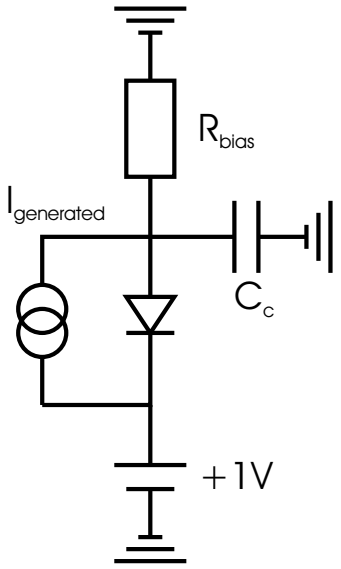

(a) Biasing scheme during irradiation. The proton beam generates enough charge carrier that the potential of the backplane lies at the implants and therefore across the oxide.

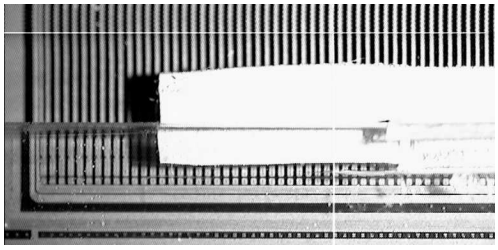

(b) If not bonded the metal strips are connected via conductive rubber. The rubber is pressed on the strips by a clamp and with a metal foil it is connected to the bias cable (not shown in the picture).

Figure 3.9: Biasing scheme during irradiation and connection of the metal strips with conductive rubber.

3.2.7 Biasing scheme

Since about half of the energy loss of protons goes into ionisation, a proton current of 1 μA would cause a generated current of about 280 mA in a fully depleted 500 μm-sensor. This current would locally heat the sensor and produce further damage not directly caused by radiation. Such current would not occur during the experiment. Thus it is not possible to fully deplete the sensors during irradiation. The important point for biasing during irradiation is the influence of an electric field in the oxide region (see Section 1.3.6 on page 35) on the radiation damage. During the experiment we have a small potential drop across the oxide between the p^+-implant (connected to ground via a bias resistor) and the metal strips of $+0.7\,V$, which is the virtual ground of the read-out electronics. The potential of the implant might be increased by $1.5\,V$ due to increased leakage current ($\sim 1\,\mu A$/strip) through the bias resistance of about 1.5 $M\Omega$. Thus the potential drop changes from $+0.7\,V$ to about $-0.8\,V$ during the experiment. Only an electric field, which accelerates the holes into the oxide, may increase the oxide charge. Such a field has to be simulated during our irradiation test. Our solution was to put the backplane on a small positive voltage ($+15\,V$), which drops across the small depleted area. The metal strips and the bias ring are grounded either by bonding or by a piece of conductive rubber as shown in Figure 3.9(b). As far as no current flows through the bias resistors no electric field is present in the oxide. But when the proton beam hits the sensor and many charge carriers are generated, the leakage current is increased and the potential of the implants is raised to a large fraction of the potential of the backplane. To guarantee at least a voltage of $1\,V$ across the oxide the higher voltage of $15\,V$ was chosen for the backplane.

3.3 Summary of the Performed Irradiations

During this work irradiation qualification was performed for the Milestone 200 and the pre-qualification. The Milestone 200 [Die02] was a first real test of the qualification and production scheme building 200 modules with the logistics described in Section 2.5 on page 47. The aim was to calibrate the test centres, establish the necessary logistics and to qualify the delivered material. The irradiated set consisted of two full sensors (FS) and eight half-moons each 500 μm thick.
The next step was to check if the companies are capable producing sensors of the desired quality. In this pre-qualification phase samples of several geometries were produced and extensively inspected.
In this section the results of the irradiation qualification with protons are presented according to the investigated parameters.

3.3.1 Full Depletion Voltage

The full depletion voltage is extracted from the CV-characteristic plotting the reciprocal total capacitance squared (C^{-2}) over the bias voltage. In Figure 3.10 you see, the measured CV-curves for the two sensors (one OB2 from STM and one W6b from HPK) of the Milestone 200 set. The initial CV-curves show the typical constant slope during the growth of the depletion zone and a plateau when the full depletion voltage is reached. The full depletion voltage is obtained by the intersection of two linear extrapolations. Both sensors have $V_{fd} \approx 190\,V$. The effective doping concentration can not be calculated by (1.37) using this full depletion voltage but the one scaled to the equivalent voltage in a diode, which is 15% lower (see (1.46)).

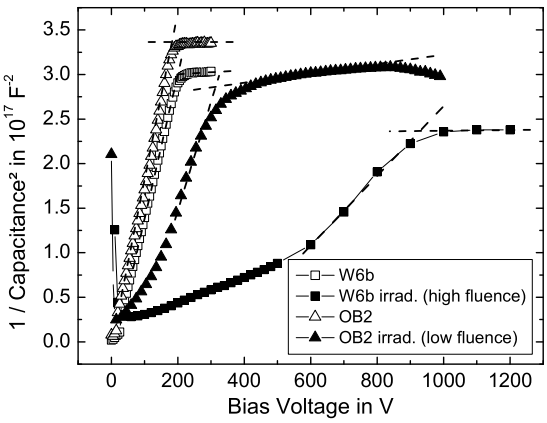

Figure 3.10: CV-curves for the two sensors of the Milestone 200 set before and after irradiation with high ($\sim 3 \cdot 10^{14}\, n_{1MeV}/cm^2$) and low ($\sim 0.7 \cdot 10^{14}\, n_{1MeV}/cm^2$) fluences. After irradiation the sensors were annealed 80 min *at* $60°C$ *and measured at about* $-10°C$.

After irradiation with an equivalent fluence of $0.7 \cdot 10^{14}\, n_{1MeV}/cm^2$ and annealing for $80\,min$ at $60°C$ the full depletion voltage is increased as discussed in Section 1.3.4 on page 30. The full depletion voltage is about $320\,V$ and thus below the $500\,V$ limit even for the slightly higher fluence than defined as the qualification fluence for 500 μm-material ($0.5 \cdot 10^{14}\, n_{1MeV}/cm^2$, see Section 3.1 on page 51).
A harsh test was performed with the second sensor. The 500 μm-material was exposed to a fluence equivalent to 60 years at LHC ! The full depletion voltage was determined to be about $900\,V$. The high breakdown voltage of that device, which is higher than $1200\,V$, is remarkable. The full depletion voltage for a similar 320 μm-sensor can be extrapolated to be $370\,V$ ($\sim d^2$). This result can be used to estimate that thin sensors might stand the higher fluence.
During the pre-qualification many mini-sensors were qualified. Most of the measured full depletion voltages are plotted vs. the equivalent fluence in Figures 3.11 and 3.12. The 'Hamburg'

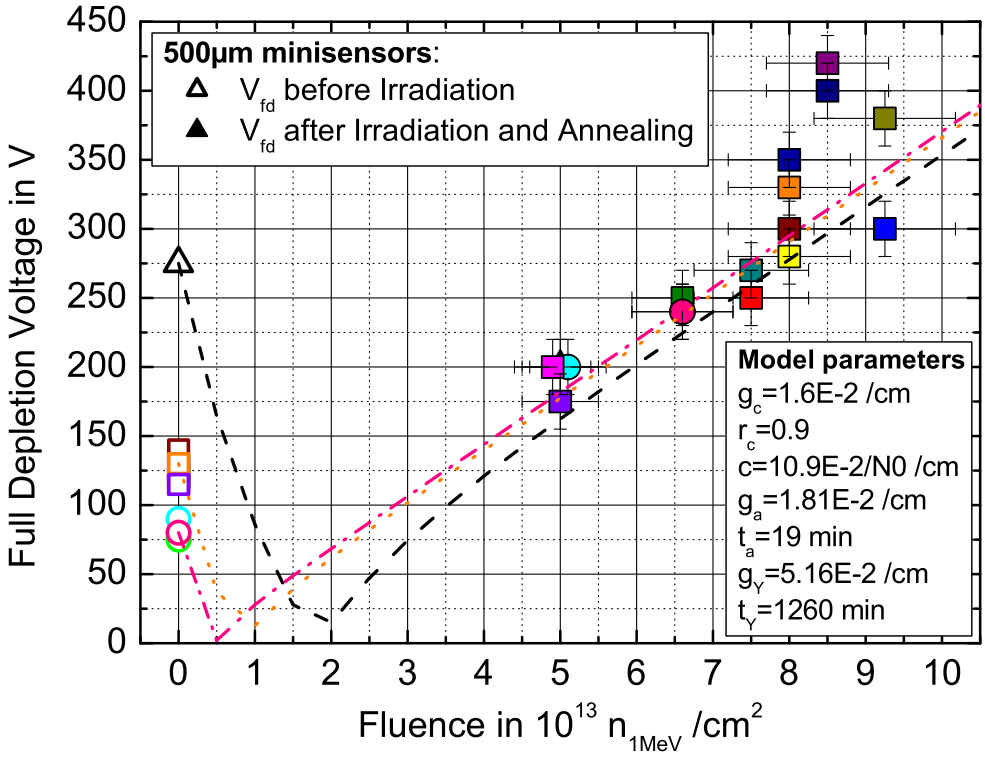

Figure 3.11: Full depletion voltage vs. fluence for 500 μm*-mini-sensors. The lines are calculations with the model described in Section 1.3.4 on page 30. The used parameters are given in the box in the lower right corner. The same shading (colour) represents the same sensor.*

model (Section 1.3.4 on page 30) was used to calculate the expected full depletion voltage vs. fluence. The results are represented as lines in Figure 3.11 and 3.12. The parameters, which are average values extracted from measurements on diodes taken from [Mol99], are given in the white box in the lower right corners.

The presented measurements of 320 μm thick mini-sensors (Figure 3.12) show an initial full depletion voltage of about 180 V. As it came out during the investigations, the thickness of the n-type bulk of these sensors was $\sim 290\,\mu m$, since the implantation on the n^+-side is 10 μm deep and decays further into the bulk ($\sim 20\,\mu m$). This further increases the full depletion voltage for the same doping concentration. The initial N_{eff} has to be calculated by the 26% lower full depletion voltage of a corresponding diode. After inversion no correction according to Section 1.2.4 on page 19 is necessary, since depletion starts at the unstructured back electrode (see Section 4.3.2 on page 93). The measured full depletion voltages can be well described with the average parameters and $r_C \approx 0.9$.

The 500 μm thick mini-sensors in Figure 3.11 have different initial full depletion voltages (15% higher than $V_{fd,diode}$), which form three groups with 275 V, $\sim 130\,V$ and $\sim 80\,V$. The corresponding model curves are shown for the similar parameters as for the thin mini-sensors. Only the

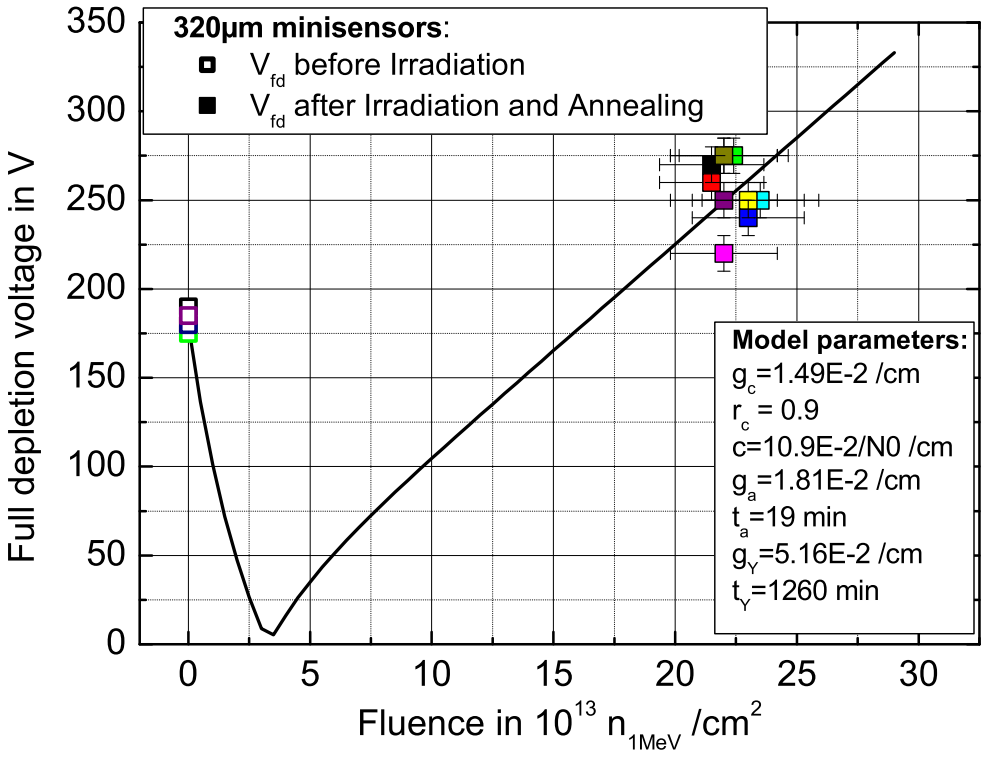

Figure 3.12: Full depletion voltage vs. fluence for 320 *µm-mini-sensors. The lines are calculations with the model described in Section 1.3.4 on page 30. The used parameters are given in the box in the lower right corner. The same shading (colour) represents the same sensor.*

slope of the linear increase of stable damage is slightly increased ($g_c = 1.6 \cdot 10^{-2}\, cm^{-1}$ instead of $g_c = 1.49 \cdot 10^{-2}\, cm^{-1}$). Most of the measured full depletion voltages can be described by the model.
This samples of measurements is not suitable to verify the model parameters, since only a small fluence range is covered. But this comparison verifies the use of the average parameters and a simulation of the full depletion voltage during the ten years of running the experiment can be performed.
In the first three years not the full design luminosity is reached (10% in the first, 33% in the second and 67% in the third year). This requires a scaling of the fluence per year, which results in:

Year	Part of total fluence
1	1.23%
2	4.07%
3	8.27%
4-10	12.34%

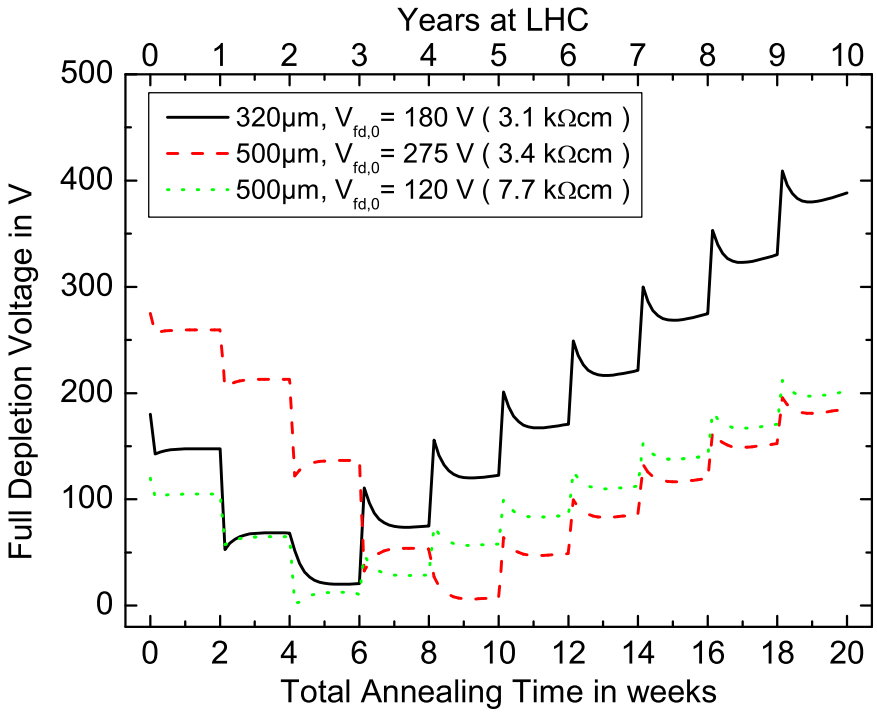

Figure 3.13: Full depletion voltage of sensors with pitch of $120\mu m$ *vs. annealing time at* $20°C$*. Each sharp step reflect the cumulated damage of one 'year' of data-taking. The shown progression shows the effect of annealing during a maintenance period of 14 days when the tracker is at room-temperature. Thin sensors are exposed to* $F = 2.4 \cdot 10^{14}\, n_{1MeV}/cm^2$ *and thick ones to* $F = 0.5 \cdot 10^{14}\, n_{1MeV}/cm^2$*.*

In Figure 3.13 the results of such simulations are presented for similar initial full depletion voltages and sensor thicknesses as found during the qualifications. The progression of the full depletion voltage is only shown during the annealing phase at room-temperature ($20°C$). This is caused by a maintenance period of 14 days each year, during which the Tracker is warmed up. The rest of the year the Tracker should be kept at $-10°C$ and annealing is suppressed. The sharp steps reflect the cumulated damage of one "year" of data-taking, which lasts about 100 days. These calculations show that both materials[(1)] are expected to have a full depletion voltage below $500\,V$ after ten years of data-taking. Longer annealing time should be avoided, otherwise thin sensors exposed to the maximum fluence might reach $450\,V$ and the range for over-depletion is reduced. This can be seen by the increase of the full depletion voltage at the end of the annealing time after five years. Remember that the reverse annealing part increases with time and the damage produced in the first year anneals for the whole maintenance periods. The reverse annealing becomes obvious at $20°C$ for longer maintenance periods and is responsible for the strong increase of the full depletion voltage in Figure 3.14. Thus full operation can be guaranteed for low temperatures ($\sim 10°C$)

[(1)] 320 μm-sensors with $1.5 - 3.0\, k\Omega cm$ and 500 μm-sensors with $3.5 - 7.5\, k\Omega cm$

during maintenance.

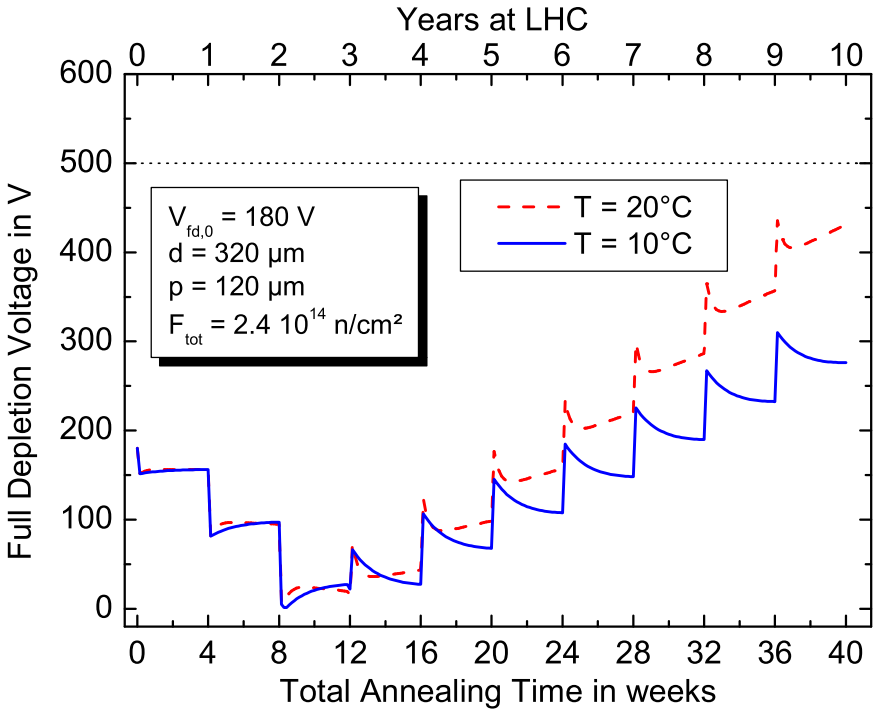

Figure 3.14: Full depletion voltage of a 320 μm-sensor with pitch of 120 μm and $V_{fd,0} = 180\,V$ vs. annealing time at 20°C and 10°C. Each sharp step reflect the cumulated damage of one 'year' of data-taking. The shown progression shows the effect of annealing during a maintenance period of 28 days per year.

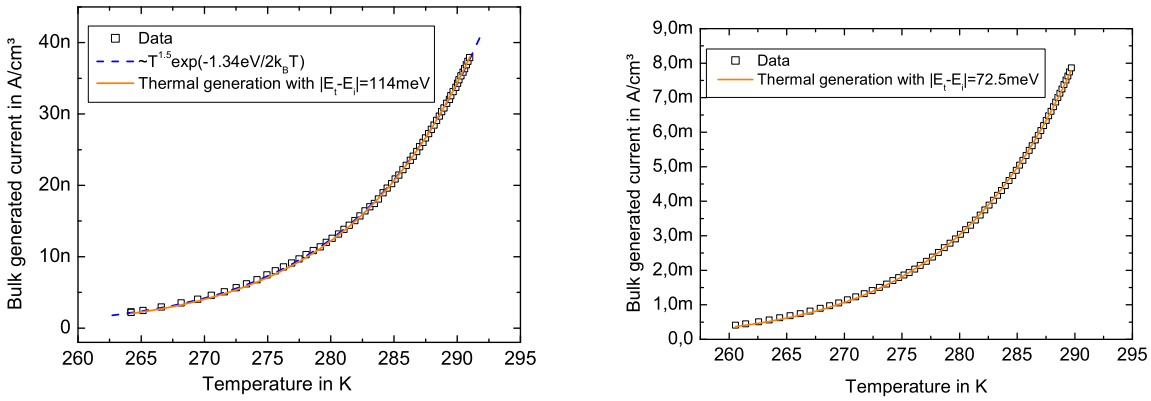

(a) Non-irradiated; measured at 200 V

(b) Irradiated; measured at 400 V

Figure 3.15: Bulk generated current measured on 320 μm*-mini-sensors and fitted by (1.28). The data can also be fitted by the temperature dependence of* n_i *with an effective band gap of* $E_g = 1.34\,eV$ *as indicated in (a). The leakage current increases from* $-10°C$ *to* $20°C$ *by a factor of* 25.5 *for the non-irradiated sensor and by a factor of* 21.5 *for the irradiated one.*

3.3.2 Leakage Current and Power Consumption

The leakage current of silicon sensors strongly depends on the temperature (see (1.28)). Thus this section starts with a discussion of the temperature dependence. Thereafter results of the qualification are presented.

Temperature dependance

The measured leakage current at 200 V of a non-irradiated mini-sensor (320 μm) from $-10°C$ up to room temperature is shown in Figure 3.15(a). The fit according to (1.28) describes well the data and an effective[(1)] trap level of $|E_t - E_i| = 114meV$ can be extracted. If only the temperature dependence of the intrinsic carrier concentration ($\sim T^{1.5}\exp(-E_g/2k_BT)$) is taken into account one gets an effective energy gap of $E_g = 1.34\,eV$, which one can use as a parametrisation. Important for comparisons is the scaling from $-10°C$ to room temperature which is a factor of 25.5 in this case.

In Figure 3.15(b) the same measurement on an irradiated ($F \approx 2.4 \cdot 10^{14} n_{eq}/cm^2$) mini-sensor is presented. The bulk generated current is much higher since more trapping centres are generated and the effective trap level is closer to mid-gap ($|E_t - E_i| = 72.5\,meV$) as extracted by the fit. The scaling factor from $-10°C$ to room temperature is 21.5 for this mini-sensor. This indicates that there is a material and/or irradiation dependence of the increase in leakage current, which increases the error of scaled data.

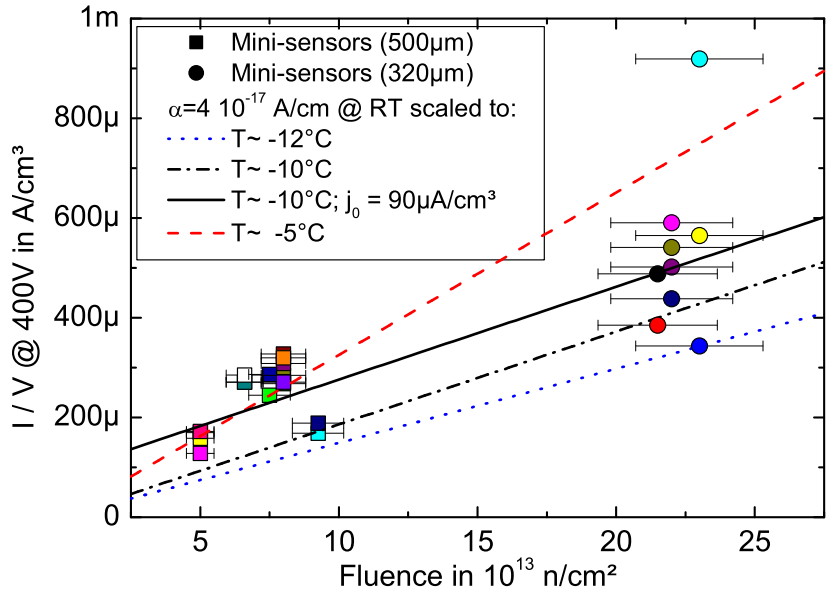

Figure 3.16: Leakage current density vs. fluence for mini-sensors. The leakage current was measured without the use of the guard ring, which increases the measured current. Hence the comparison with $\alpha = 4 \cdot 10^{-17}\ A/cm$ can only be a qualitative one.

Qualification

As described in Section 1.3.4 on page 29, there is a general current related damage rate for diodes at room-temperature ($20°C$). Since the measurements for the qualification are performed at temperatures about $-10°C$, the currents have to be scaled to room-temperature for comparison. This scaling might have an error of about 20% as stated before. In addition the temperature measurement has an uncertainty of $2\ K$, which only allows for a qualitative comparison with $\alpha = 4 \cdot 10^{-17}\ A/cm^2$ at room-temperature. In Figure 3.16 the current densities of mini-sensors measured at $450\ V$ and temperatures of about $-10°C$ are plotted versus the received fluence. The straight lines represent current densities for the general current related damage rate scaled down to the indicated temperatures using the scaling from Figure 3.15(b), i.e. a factor of 21.5.
For the operation it is important to know the power dissipation of the sensors, which should be kept at $-10°C$. The largest $500\ \mu m$-sensors are the OB1 and OB2, which have a volume of $4.30\ cm^3$ (see Appendix B on page 123). From Figure 3.16 we find the highest current density to be $\sim 200\ \mu A/cm^3$ at a fluence of $0.5 \cdot 10^{14}\ n_{1MeV}/cm^2$, which results in a leakage current of $860\ \mu A$ for OB1 and OB2 after 10 years at LHC. With the maximum bias voltage of $500\ V$ a power dissipation of $430\ mW$ for one sensor can be calculated.
The geometry with the largest volume exposed to the high fluence is W2 with $2.78 cm^3$. Excluding the highest current in Figure 3.16 one might have a leakage current of up to $1.67\ mA$ at $-10°C$, which causes a power dissipation of up to $834\ mW$ at a bias voltage of $500\ V$. Considering the

(1) Only one type of traps is assumed but there are certainly more.

highest value as the worst case one would end up with a heating power of 1.3 W! Operating the cooling system at $-20°C$ allows to keep the sensors below $-10°C$ even at a power dissipation of 1.8 W according to [FGH98].

3.3.3 Inter-strip Capacitance and Inter-strip Resistance

The electronic noise is strongly dependent on the capacitive load at the input of the amplifier, which is the strip capacitance. As discussed in Section 1.2.6 on page 22, the strip capacitance C_{strip} is composed of the capacitance to the backplane ($C_{back} \approx 200 - 400\ fF/cm$ at 1 MHz) and the inter-strip capacitance ($C_{int} \approx 500\ fF/cm$). What we measure is the strip capacitance to one neighbour (Figure 3.17(a)), which is

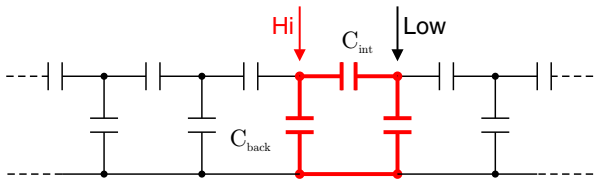

(a) Capacitance measurement to one neighbour

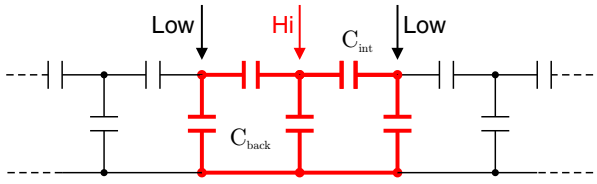

(b) Capacitance measurement to two neighbours

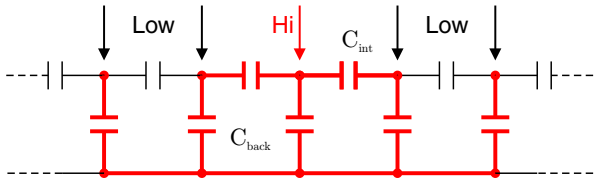

(c) Capacitance measurement to four neighbours

Figure 3.17: Strip capacitance measurement to one, two and four neighbours. These networks are used to determine (3.11)-(3.14).

$$C_{strip,1N} = C_{int} + \left(\frac{1}{C_{back}} + \frac{1}{C_{back}}\right)^{-1} = C_{int} + \frac{1}{2}C_{back} \tag{3.11}$$

The measured capacitances to two neighbours (Figure 3.17(b)), four neighbours (Figure 3.17(c)) and all strips are:

$$C_{strip,2N} = 2C_{int} + \left(\frac{1}{C_{back}} + \frac{1}{2C_{back}}\right)^{-1} = 2C_{int} + \frac{2}{3}C_{back} \tag{3.12}$$

$$C_{strip,4N} = 2C_{int} + \left(\frac{1}{C_{back}} + \frac{1}{4C_{back}}\right)^{-1} = 2C_{int} + \frac{4}{5}C_{back} \tag{3.13}$$

$$C_{strip,all} = 2C_{int} + \left(\frac{1}{C_{back}} + \frac{1}{C_{back,tot}}\right)^{-1} \approx 2C_{int} + C_{back} \tag{3.14}$$

The result is, that we just measure half of the strip capacitance to all neighbours, on which the limit of 1.3 pF/cm has to be applied. This is also the parameter, which enters in the noise calculation. Since $C_{int} > 0.5C_{back}$ and $C_{strip,1N} \approx C_{int}$ we call the measured parameter C_{int}!
The measurement of capacitances around 1 pF are very sensitive and even the capacitance between the two needles in air influences the result, i.e. for different positions of the needles, one would get different values. It is necessary to correct for these parasitic capacitances before each measurement of the inter-strip capacitance. This was realised during the pre-qualification and early measurements might not be reliable.
In Figures 3.18(a) and 3.18(b) each two examples of strip scans are shown. These measurements were done with all necessary calibrations for the capacitance measurement. No reliable measurement showed an increase in C_{int} of more than 20%. The thin mini-sensors from HPK showed hardly any increase, but some of the thick mini-sensors from STM showed an increase of about

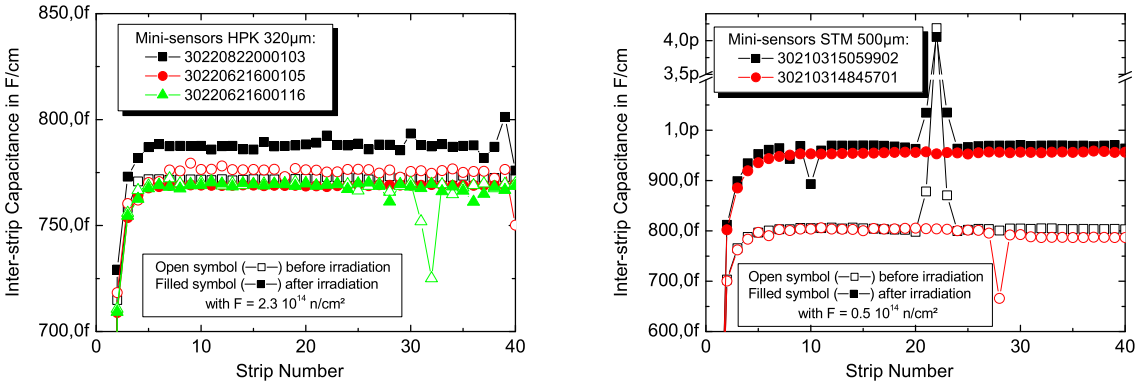

(a) 320 μm-material after high fluence

(b) 500 μm-material after low fluence

Figure 3.18: Strip capacitance for some mini-sensors before and after irradiation. No significant change can be observed for the thin material. The thick material shows an increase of 150 fF/cm. *In addition, one mini-sensors had a single strip defect, still present after irradiation.*

150 fF/cm, which results in an inter-strip capacitance of $\sim 1\,pF/cm$.
Another big difference of the two materials is visible in the so called "IQC-ramps". For diagnostic purpose all strip parameters, except the coupling capacitance, are measured ramping the bias voltage. In Figure 3.19 two representative examples are shown. The thin material with an inconspicuous CV-curve shows an immediate saturation of the strip capacitance at low voltages for many measured strips.
The thick material has a somewhat unusual CV-characteristic. The kink, which represents the full depletion voltage, is followed by a minimum in the capacitance (a maximum in Figure 3.19(b), since $1/C^2$ is plotted vs. bias voltage).
The strip capacitance drops from $\sim 1.6\,pF/cm$ to $\sim 1.3\,pF/cm$ for low voltages up to the first kink. Another steep drop can be observed for higher voltages. The strip capacitances reach a common value of 1.05 pF/cm for all measured strips at the bias voltage, at which the total capacitance reaches its minimum. This effect is clearly correlated with the segmentation, since diodes on the same test-structure do not show this feature (see Figure 3.20). It is assumed that a high concentration of oxide charges dominate the field configuration until the electric field in the sensor is high enough to suppress this effect.
Despite of this peculiarity the strip capacitance is below the limit of $\sim 1.3\,pF/cm$ at the qualification voltage of 400 V and thus the material is accepted.
The inter-strip resistance is derived by measuring the current performing a voltage ramp from 0 V to 2 V, which does not deteriorate the field configuration at the strips. This would be the case for a direct resistance measurement with the used device, since a high voltage ($\sim$ 100 V) would be applied to measure resistances of the order of few hundred $M\Omega$.
The measured data points are fitted linear and the mean square error (MSE) is used as an indication for the reliability of the measurement. The measured current at inter-strip resistances above $\sim$ 1 $G\Omega$ are of the order of the device noise and thus only lower limits can be given for conservative reasons. In Figure 3.21 a limiting value is represented by open symbols and the

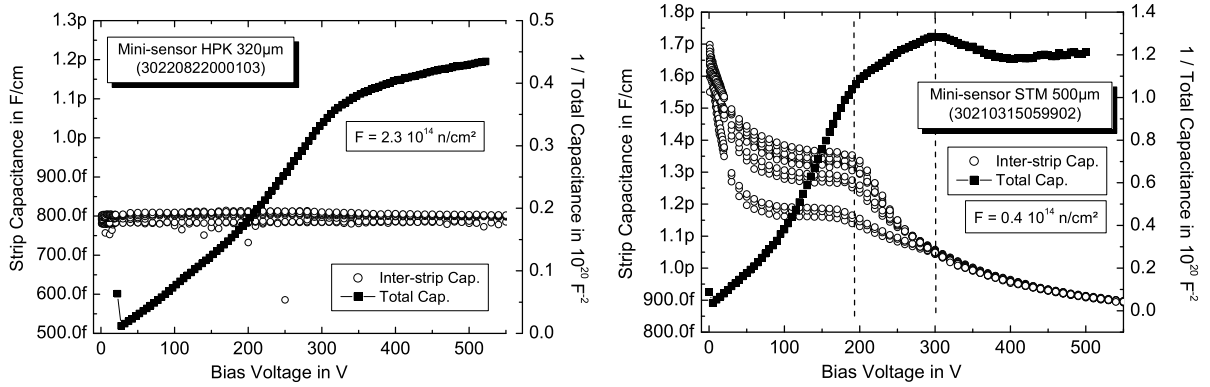

(a) 320 μm-material after high fluence (b) 500 μm-material after low fluence

Figure 3.19: Comparison of strip capacitance and total capacitance vs. bias voltage. The different curves of the strip capacitance correspond to measurements on different strips. The thin material shows an immediate saturation in the strip capacitance for low voltages. The corresponding CV-curve looks inconspicuous with the kink for full depletion at around $320\,V$.
The thick material shows an unusual CV-curve with the kink at $\sim 190\,V$ *and a maximum (minimum in the capacitance) at* $300\,V$. *The strip capacitance depends strongly on the bias voltage and the course is reflected in the CV-curve.*

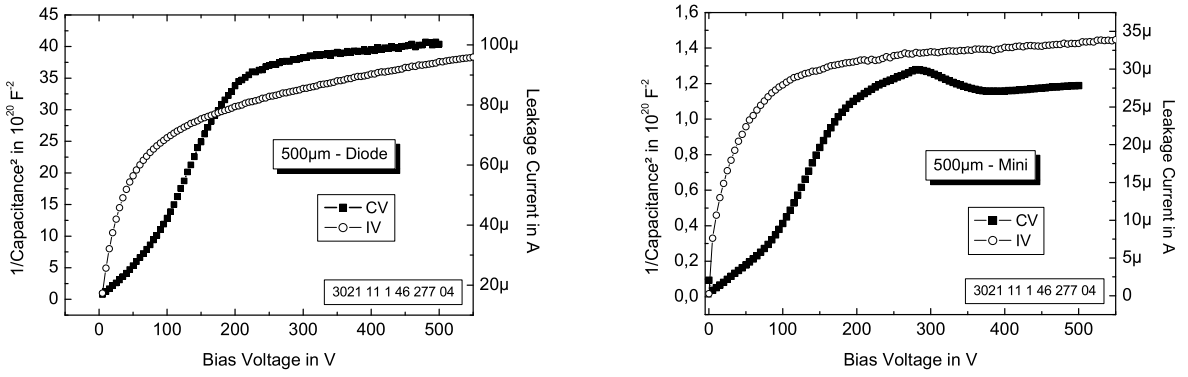

(a) 500 μm-Diode (b) 500 μm-Mini

Figure 3.20: CV and IV-curve for $500\,\mu m$ *thick diode and mini-sensor after irradiation up to the same fluence of* $0.8 \cdot 10^{14}\, n_{1MeV}/cm^2$. *The diode does not show the bump visible in the CV-curve of the mini-sensor. This indicates that it is a surface effect correlated with the segmentation.*

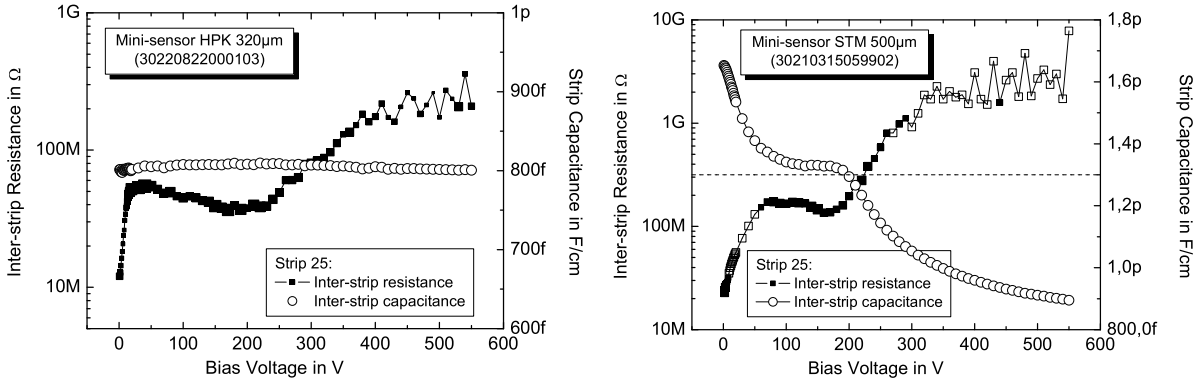

(a) 320 μm-material after high fluence

(b) 500 μm-material after low fluence

Figure 3.21: Comparison of strip capacitance and inter-strip resistance vs. bias voltage for the same strip. The size of the R_{int}-data represents the reliability and open squares are lower limits, since the measurement current reaches the noise of the measurement device.

reliability ($\sim 1/\text{MSE}$) is visualised by the size of the symbol.

3.3.4 Dependance of the Surface Parameters on Initial Oxide Quality

As discussed in Section 1.3.6 on page 35 the quality of the oxide can be inspected by measuring the flat-band voltage. This parameter is measured by the Process Qualification Centres. For some of the delivered batches the flat-band voltage was unexpected high (up to $\sim 40\,V$). For good oxide quality the flat-band voltage is about $1.5\,V$. Now the question was, how does this increased flat-band voltage influence the strip parameters and what limit should be set to the flat-band voltage?

An irradiation of mini-sensors with five different flat-band voltages ($5\,V$, $7\,V$, $14\,V$, $20\,V$, and $38\,V$) was performed to clarify these questions. In Figure 3.22 you can see the results of the inter-strip measurements before and after irradiation. Before irradiation one can already observe an increase in C_{int} with higher flat-band voltage. For $V_{FB} = 38\,V$ the inter-strip capacitance exceeds $1\,pF/cm$ even before irradiation. After irradiation with $F = 0.9 \cdot 10^{14}\,n_{1MeV}/cm^2$ the capacitance is obviously further increased for the mini-sensors with $V_{FB} > 20V$. There have been some contact problems on the mini-sensor with $V_{FB} = 14\,V$, but the measured values already indicate some changes in C_{int}. For safety reasons the limit on the initial flat-band voltage was set to $10\,V$ to avoid a significant increase of the inter-strip capacitance during the operation period. I.e. batches with higher flat-band voltages are not accepted by the quality assurance in the Process Qualification Centres.

The increased flat-band voltage indicates accumulation of oxide charges, which are positive as stated in Section 1.3.6 on page 35. This charge attracts electrons to the silicon-oxide interface between the strips, thus affecting the inter-strip parameters. The electron layer decreases the resistance and increases the ability of the medium to be polarised (dielectric constant), which increases the capacitance.

Half of the strips of the mini-sensors were bonded and connected to ground. The backplane was biased with $15\,V$ as described in Section 3.2 on page 54. As can be seen from Figure 3.22, an

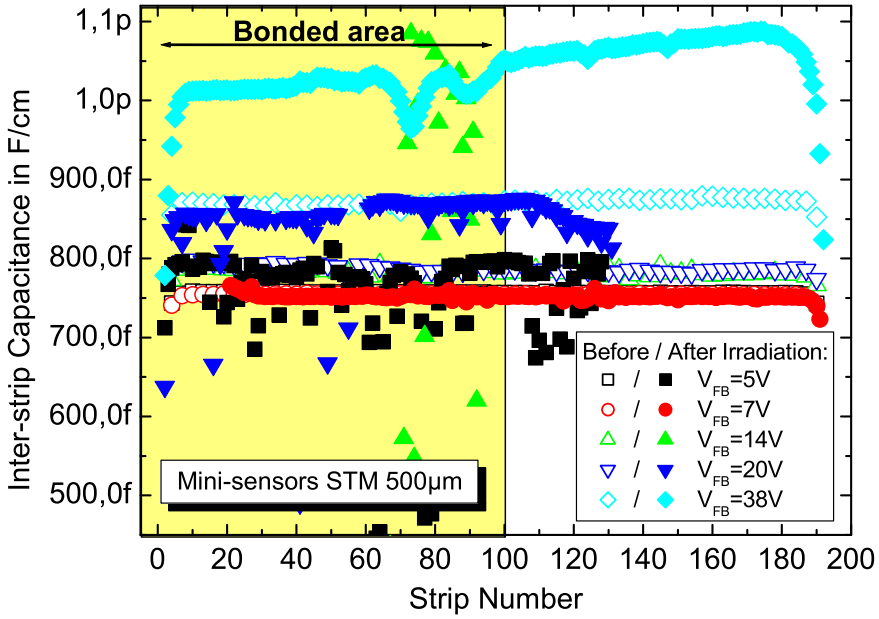

Figure 3.22: Inter-strip capacitance of mini-sensors with different initial flat-band voltages. The increase after irradiation scales with the flat-band voltage before irradiation. Though there were contact problems in the measurement of the mini-sensor with $V_{FB} = 14\,V$ after irradiation, one can already see an increase in C_{int}. Hence, an upper limit of $V_{FB} = 10\,V$ was defined to avoid a significant increase after irradiation. In addition, no difference was observed in the bonded and biased region.

electric field of about $50\,kV/cm$ in the oxide ($\sim 1.5\,\mu m$) during irradiation has no additional effect on the inter-strip capacitance!

3.3.5 Coupling Capacitance and Pinholes

Measuring the coupling capacitance before and after irradiation one can hardly see any changes. Only a tiny decrease of 1% is visible in Figure 3.23. There is also no obvious correlation of flat-band voltage and coupling capacitance as can be seen in Figure 3.24(a). In addition, this figure shows that bonding and biasing on the strips 1 to 96 has no effect on that quantity. The additional electric field across the oxide and possible damage by the bonding process are not visible in any change of the coupling capacitance.
The dielectric current (Figure 3.24(b)) is slightly affected in the bonded area. This increase appears to be proportional to the flat-band voltage, but the current is far below the limit of $1\,nA$, at which the strip is classified as a pinhole.
These measurements indicate that biasing and bonding during irradiation does not have significant impact on the coupling capacitance or the development of pinholes and all measured structures passed the qualification of these quantities.
After these tests the requirement of biasing was relaxed, so that only a fraction of $\sim 10\%$ is biased

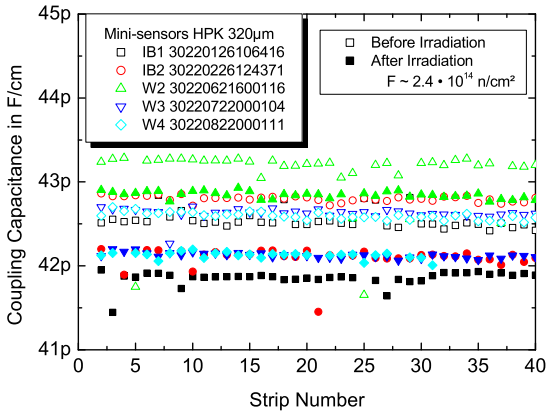

(a) 320 μm-material after high fluence

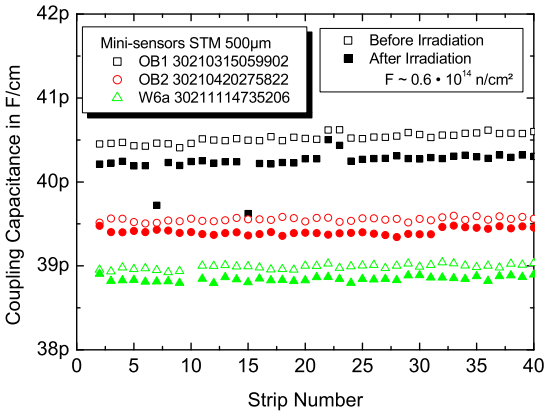

(b) 500 μm-material after low fluence

Figure 3.23: Examples of the measured coupling capacitances before and after irradiation. There is only a tiny drop of about $0.5\,pF/cm$.

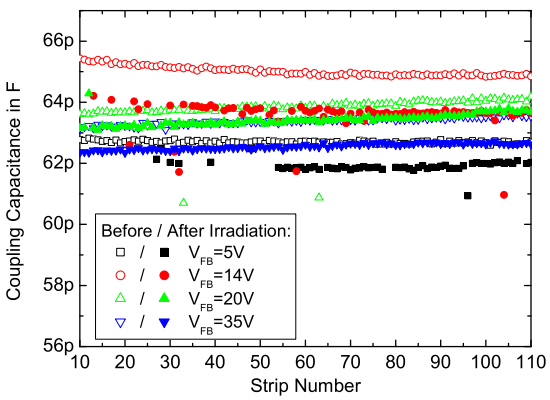

(a) Coupling capacitance of mini-sensors with different flat-band voltages

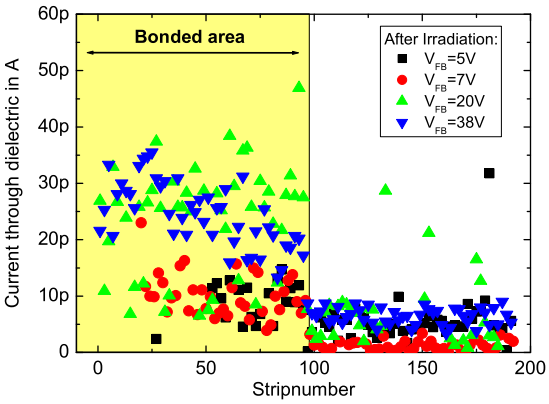

(b) Dielectric leakage current of mini-sensors with different flat-band voltages after irradiation

Figure 3.24: Study on the influence of the flat-band voltage and bonding on the coupling capacitance and on the development of pinholes.

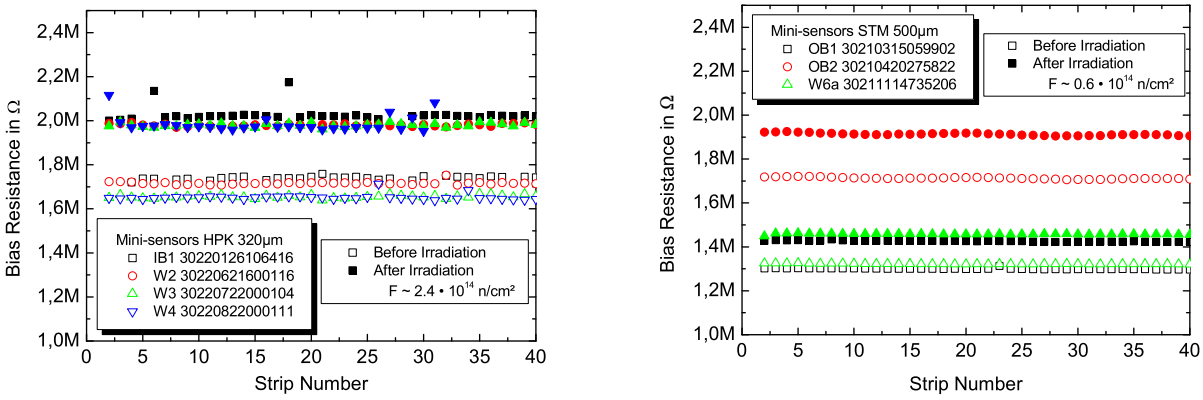

(a) 320 μm-material after high fluence

(b) 500 μm-material after low fluence

Figure 3.25: Examples of the bias resistances before and after irradiation. The increase of the resistance after irradiation corresponds to the reduction of the effective doping concentration of the polysilicon due to radiation damage.

in future.

3.3.6 Bias Resistance

The measurement of the bias resistance after irradiation is affected by the high strip leakage current as discussed in Section 3.1 on page 51. The necessary correction according to (3.1) is done already during data acquisition and the corrected values are stored. In Figure 3.25 you can see some examples for the different geometries and thicknesses. All structures showed an increase in the bias resistance of $200 - 300\,k\Omega$. Remember that the polysilicon is n-doped. This doping concentration is reduced by the generation of acceptor type defects during irradiation. The high doping concentration can not be inverted with the applied fluences but reduced, which causes a decrease in the number of charge carriers and thus an increase in the resistivity.
This increase has no negative effect on the sensor properties, since the separation of the strips is increased and the thermal noise in the resistor is even reduced (see (1.55)).

3.4 Processing the Data and Feeding the Database

All the measured data is stored in several ASCII-files on the local disk. To get the important data in one common XML-file, which is read by the general database of the CMS Tracker, is the task of a user-interface called *IQC-reader* written in LabView (see screenshot in Figure 3.26. The program reads all data files before and after irradiation and enables the user to compare the data and add or modify parameters not stored with the files like the irradiation fluence. There are three different algorithms extracting the full depletion voltage from the CV-curves. Before irradiation they work very well, but after irradiation the CV-curves deviate from the ideal characteristic and the user might correct the proposed full depletion voltage.
The mean values of the strip parameters are compared before and after irradiation and the cuts in Table 3.1 are applied.

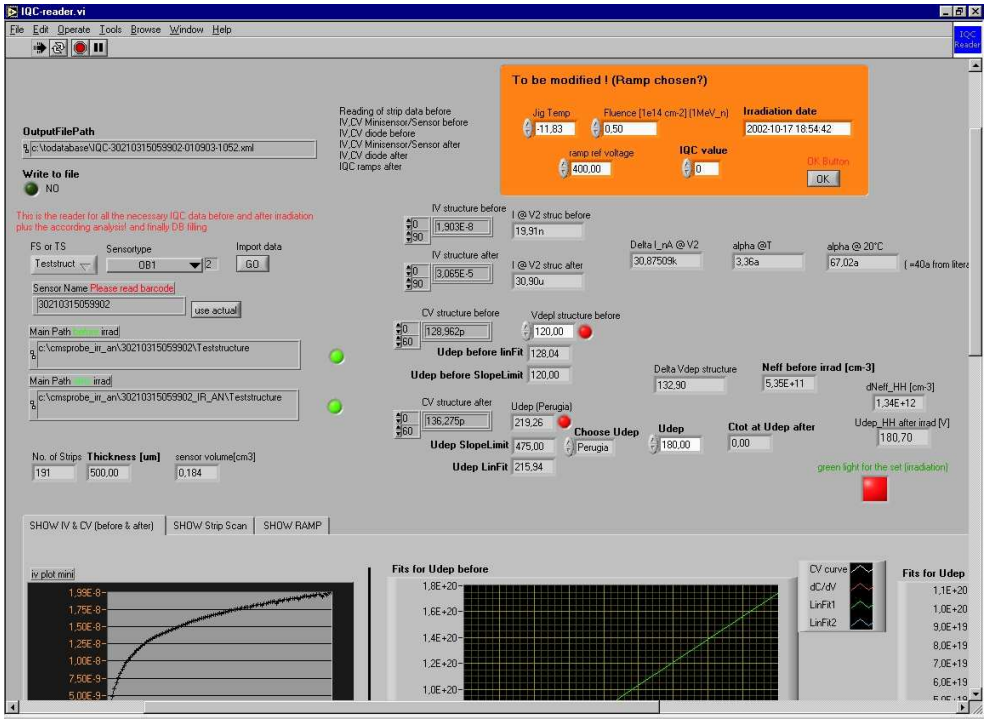

Figure 3.26: Screenshot of the IQC-reader. This LabView program imports all relevant data before and after irradiation, helps to analyse the data and writes the XML-file for the data-transfer to the CMS Tracker Database.

One set of IQC-ramps (voltage ramps for R_{bias}, R_{int}, C_{int} and I_{leak}) must be chosen to be put into the database.
From these data the XML-file is generated. An example can be found in Appendix C on page 125. This file is then uploaded into the general database and the whole collaboration has access to these data.

Parameter	Value	Type
R_{int}	$20\,M\Omega$	lower limit
I_{leak}	$1\,\mu A$	upper limit
R_{bias}	$2\,M\Omega$	upper limit
C_{int}	$1.3\,pF/cm$	upper limit

Table 3.1: Cuts for the IQC

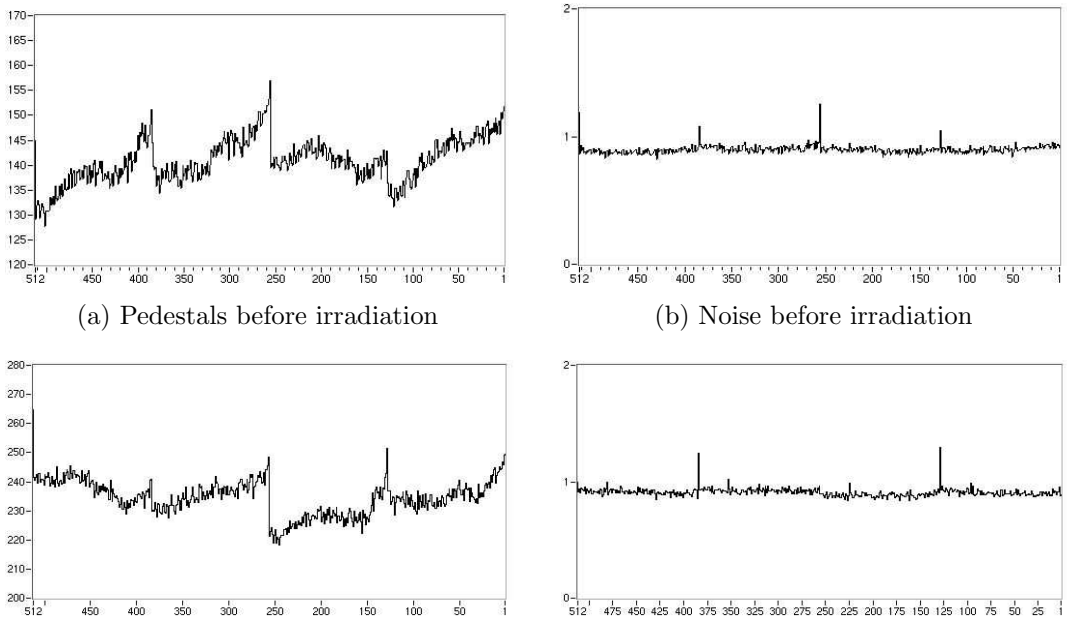

(a) Pedestals before irradiation

(b) Noise before irradiation

(c) Pedestals after irradiation

(d) Noise after irradiation

Figure 3.27: Pedestal and raw noise of a front-end hybrid before and after irradiation [Hei03]

3.5 Irradiation of other Tracker components

In addition to the irradiation qualification of sensors and test-structures, the described irradiation setup was used to irradiate other sensitive parts of the CMS Tracker.

3.5.1 Front-end Hybrid

There have been two irradiations of front-end hybrids (ceramic prototype and final kapton version). In collaboration with colleagues from the module test centre in Karlsruhe the hybrids were initialised, clocked and triggered during the irradiation at $-10°C$.
Before and after irradiation the following measurements are performed:

Pedestals are the mean output levels per channel.

Raw noise is the root-mean-square of the output levels.

Calibration pulses can be put at the input of each channel to calibrate the response.

Pipeline scan reveals problems with individual pipeline cells.

After irradiation the pedestals are slightly increased but the raw noise did not change (see Figure 3.27), which is the more sensitive parameter in respect to performance. In both irradiations an increase in the calibration pulses was observed (Figure 3.28). It is not jet clear whether the capacitance was increased by radiation damage or the gain of the amplifier was modified.

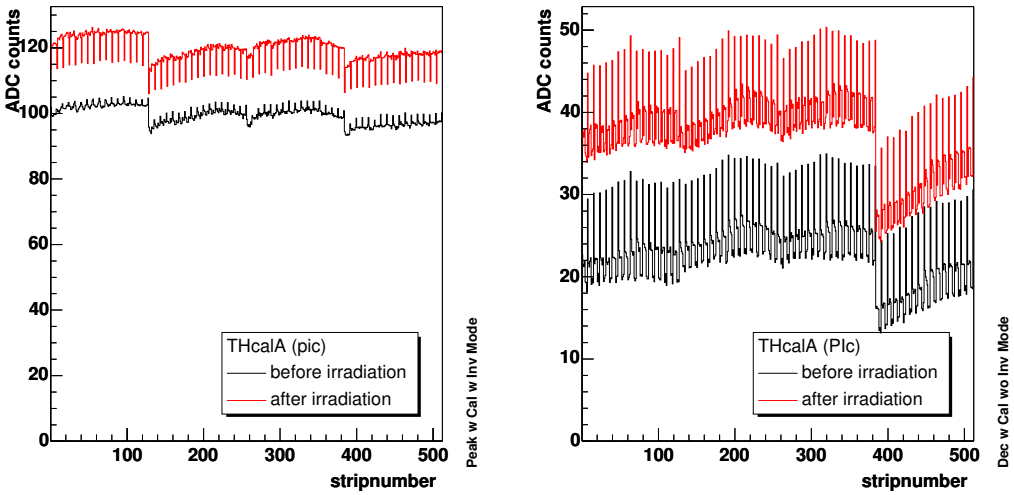

(a) Peak mode (b) Deconvolution mode

Figure 3.28: In both irradiations an increase in the calibration pulses was observed. It is not jet clear whether the capacitance was increased by radiation damage or the gain of the amplifier was modified [Wei03].

3.5.2 Complete Module

In the first module irradiation the hybrid was protected and not irradiated. The aim was to study the silicon behaviour after irradiation without possible degradation of the front-end electronics. A voltage scan of the most probable signal-to-noise ratio is shown in Figure 3.29. The maximum S/N-value is reduced by 7 and the bias voltage necessary to reach this value is increased. No problems occurred operating the module at $-10°C$. The leakage current was below 1 mA in the whole voltage range.

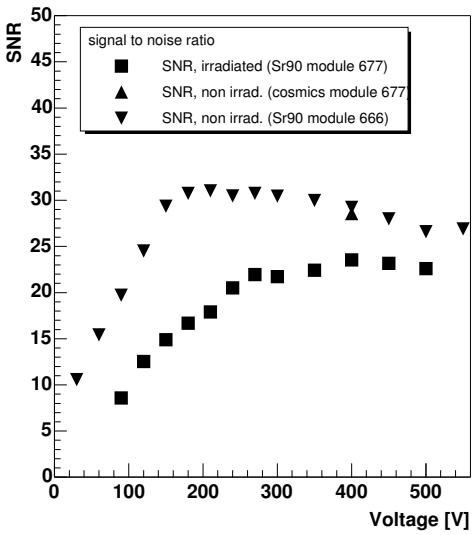

Figure 3.29: Voltage scan of the most probable signal-to-noise ratio before and after irradiation of TOB modules. The maximum S/N-value is reduced by 7 and the bias voltage necessary to reach this value is increased. The drop of the S/N before irradiation is correlated with an increase of the leakage current [Wei03].

3.6 Conclusion

An irradiation qualification procedure was developed in Karlsruhe, which allows a detailed characterisation of sensor properties after irradiation up to a defined proton fluence. One beam line of the cyclotron was equipped with an X-Y-stage and an insulated box for large area and temperature controlled irradiations. With our automatic probe station, shared with the QTC, it is possible to fully characterise sensors and test-structures, optionally with cooling down to $-10°C$. The irradiation qualification was performed after an irradiation with 26 MeV-protons. In the TDR [Pro98] the maximum particle flux is expected to consist of charged pions at about $300\,MeV$ ($\sim 4 \cdot 10^5\ 1/cm^2s$). The flux maximum of protons is at about 80 MeV ten times smaller ($\sim 5 \cdot 10^4\, 1/cm^2s$) than the pion flux. But in this energy range ($10 - 500\,MeV$) there is hardly any difference in the generation of vacancies, which might lead to NIEL violation (see Section 1.3.5). Thus the fluence for charged hadrons (Figure 3.1 on page 52) can be scaled by the NIEL hypothesis and recalculated for 26 MeV-protons. The comparison of the measured full depletion voltages with the Hamburg model using mean values from neutron irradiated diodes verify the NIEL hypothesis for 26 MeV-protons.
In addition to bulk damage protons induce surface damage by ionisation. This enables us also to probe the oxide quality. It was shown that initially contaminated oxide, which results in an increase in the flat-band voltage, increases the sensitivity of the inter-strip capacitance to the irradiation. A systematic study allowed to define a limit on the flat-band voltage before irradiation.
So far, the qualification of the delivered sensors showed no significant deterioration of the operating properties, i.e. the sensors can still be operated after the expected 10 years at LHC.

Chapter 4

Investigation of the Depletion Behaviour of Strip-Sensors before and after Irradiation

For silicon sensors it is very important to know the full depletion voltage, at which one should get the maximum signal. It is known that trapping effects reduce the charge collection after irradiation, but recent measurements on modules show that over-depletion is necessary to get the maximum signal-to-noise ratio even before irradiation [Dir03, Fri01].
In this chapter measurements using the Transient Current Technique are presented for test-structures from the Irradiation Qualification Centre. Using a laser with a small penetration depth the TCT is a powerful tool to get information about the drift velocity, the electric field and the drift time of the charge carriers.
With an infra-red ($1060\,nm$) laser one can simulate a minimum ionising particle (MIP), which is used to study the charge collection.

4.1 The Transient Current Technique

The signal in silicon sensors is the current response to a striking particle. The current is composed of charge generation and drift. To probe the drift properties of the charge carriers through the sensor they are generated on one side and the current response of the device is measured. Two cases can be distinguished:

4.1.1 Fully depleted pad sensor

The transient current is given by:

$$I(t) = q\,\vec{E}_W(\vec{r}(t))\,\vec{v}_{dr}(\vec{r}(t)) \tag{4.1}$$

where $\vec{E}_W$ is the weighting field (see Section 1.2.4 on page 19) and $\vec{v}_{dr}$ is the drift velocity, both taken at the position of the charge carrier at time t. $\vec{r}(t)$ is the solution of the equation of motion in the electric field:

$$\frac{d\,\vec{r}(t)}{d\,t} = \mu(\vec{r}(t))\,\vec{E}(\vec{r}(t)) \tag{4.2}$$

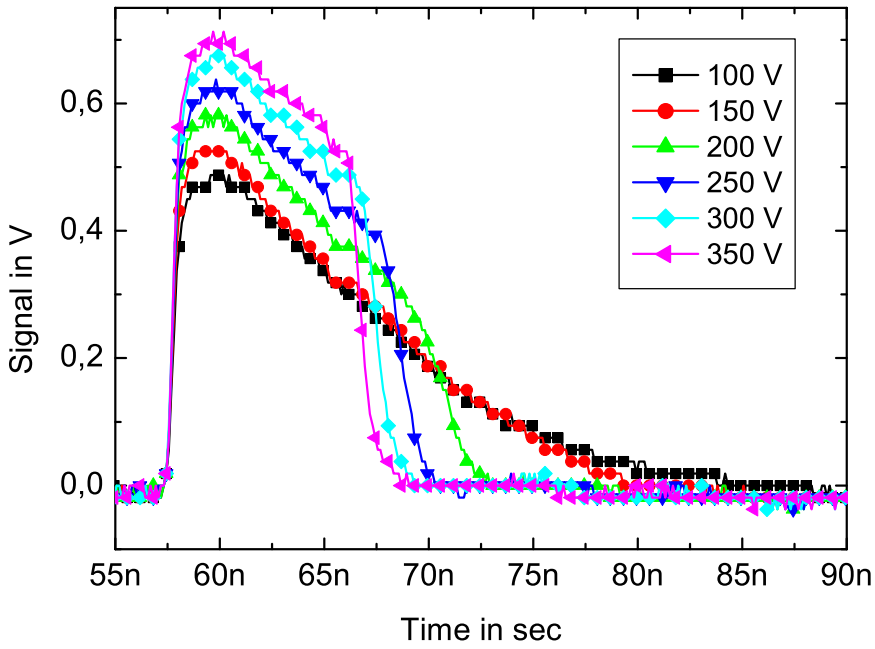

Figure 4.1: TCT signals of a 320 µm-diode at room-temperature

For a diode one gets a constant weighting field $E_W = -1/D$ with the diode thickness D[(1)]. This leads to a diode current of

$$I(t) = -\frac{e \cdot n(t)}{D} v_{dr}(t) \tag{4.3}$$

The electric field in a depleted diode can be parameterised by:

$$E(x) = E_0 \left(1 - \frac{x}{D}\right) + \frac{V_{bias} - V_{fd}}{D} \tag{4.4}$$

with $E_0 = eN_{eff}D/\varepsilon\varepsilon_0 \approx 2V_{fd}/D$. A constant mean mobility $\bar{\mu} = \mu(V_{bias}/D)$ leads to a drift velocity of $v_{dr} = dx/dt = \bar{\mu}E(x=0)\exp(-\bar{\mu}E_0/D \cdot t)$ and a diode current of:

$$I(t) = -\frac{e \cdot n(t)}{D} \bar{\mu} E(x=0) \exp\left[-\frac{\bar{\mu}E_0}{D} t\right] \tag{4.5}$$

For a detailed analysis one needs a parametrisation of the drift velocity like (1.14), which considers saturation effects.
In Figure 4.1 an example of a TCT measurement on a diode is shown. At voltages above full depletion a clear drop of the signal is visible at the end. As soon as the charge carriers reach the contact they do not contribute to the drift any more and hence the measured current is reduced. The time elapsing until the drop occurs is the drift time of the generated charge carriers. The

(1) For strip sensors one has to consider a different weighting field derived from a weighting potential like the one in Figure 1.13 on page 21

drift time is given by:

$$t_{dr} = \int_0^D \frac{dx}{v_{dr}(x)} \tag{4.6}$$

with (4.4), (1.14) and $\beta = 1$

$$t_{dr} \approx \frac{D}{v_s} + \frac{D}{\mu_0 E_0} \ln\left(1 + \frac{E_0\, D}{V_{bias} - V_{fd}}\right) \tag{4.6'}$$

For arbitrary β (4.6) has to be integrated numerically.

4.1.2 Partially depleted pad sensor

In a partially depleted sensor the space charge region does not extend over the whole bulk. A electrically neutral base (ENB) is still present, which has the resistivity of the bulk. The drifting electron cloud in the SCR of an n-type bulk induces positive charges at the n^+-contact and an electric field E_b in the ENB. This field drives a current and additional positive charge is induced at the interface between SCR and ENB (see Figure 4.2).
The transient current density can be derived by considering current density in the ENB [ESVL96]:

$$i(t) = \varepsilon\varepsilon_0 \frac{\partial E_b}{\partial t} + e\mu n E_b \tag{4.7}$$

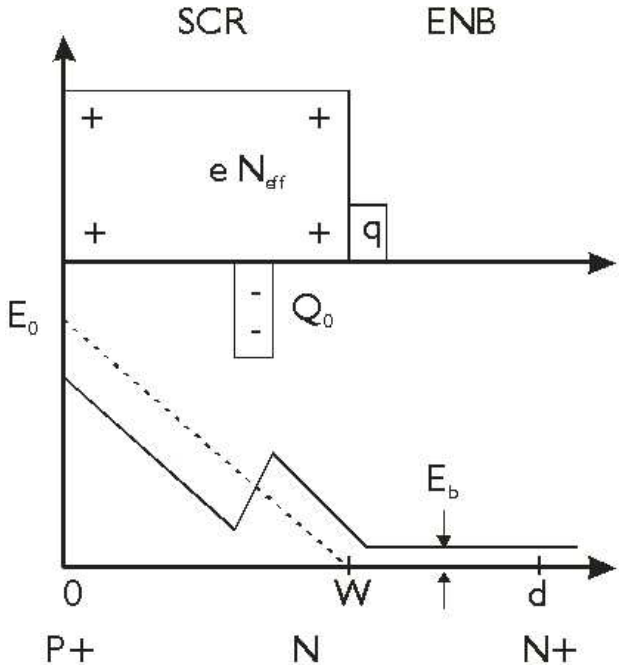

Figure 4.2: Illustration to the signal generation in a partially depleted pad sensor. A drifting charge cloud in the space charge region (SCR) induces an electric field in the electrically neutral base (ENB). The time dependance of this field defines the transient current.

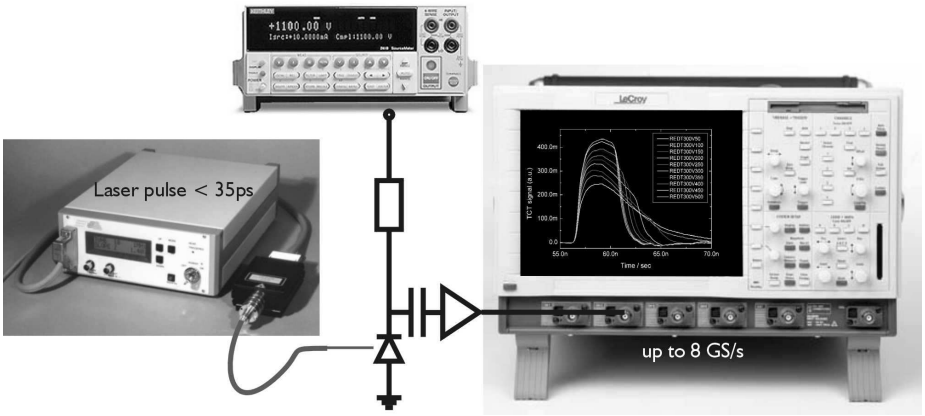

Figure 4.3: Schematics of the TCT-setup

The first part is the displacement current and the second the conduction current in the ENB. The solution of the Poisson equation for the described system gives the electric field depending on the position x of the drifting electron cloud:

$$E_b(x) = -\frac{V_{bias}}{D} - \frac{eN_{eff}W^2}{2\varepsilon\varepsilon_0 D} + \frac{1}{\varepsilon\varepsilon_0}\left(Q\frac{x}{D} + q\frac{W}{D}\right) \tag{4.8}$$

The derivative of this field is

$$\frac{\partial E_b}{\partial t} = \frac{Q}{D}v_{dr} + \frac{W}{D}\frac{\partial q}{\partial t} \tag{4.9}$$

where $v_{dr} = dx/dt = \mu E_0 \exp(-\mu e N_{eff}/\varepsilon\varepsilon_0 \cdot t)$, $E_0 = eN_{eff}W/\varepsilon\varepsilon_0$ and $dq/dt = e\mu n E_b$. Combining these equations results in the time dependance of the electric field in the ENB:

$$E_b(t) = \frac{Q\mu E_0}{\varepsilon\varepsilon_0 D}\left(\frac{1}{\tau_1} - \frac{1}{\tau_2}\right)^{-1}\left[\exp\left(-\frac{t}{\tau_2}\right) - \exp\left(-\frac{t}{\tau_1}\right)\right] \tag{4.10}$$

where

$$\tau_1 = \frac{\varepsilon\varepsilon_0}{e\mu N_{eff}} \qquad \text{and} \qquad \tau_2 = \frac{\varepsilon\varepsilon_0}{e\mu n}\frac{D}{W} \tag{4.11}$$

The transient current is then derived from (4.7):

$$i(t) = \frac{Q\mu E_0}{D}\left(\frac{1}{\tau_1} - \frac{1}{\tau_2}\right)^{-1}\left[\frac{1}{\tau_2}\left(\frac{D}{W} - 1\right)\exp\left(-\frac{t}{\tau_2}\right) - \left(\frac{D}{W\tau_2} - \frac{t}{\tau_1}\right)\exp\left(-\frac{1}{\tau_1}\right)\right] \tag{4.12}$$

The measured TCT-signals of partially depleted pad sensors can be fitted by two exponential functions and one can extract the decay times τ_1 and τ_2. This can be used to obtain the mobility of the electrons.

4.1.3 Measurement Setup

The TCT-setup consists of a simple biasing circuit measuring the potential drop at the read-out resistance by a capacitive coupled amplifier. The main components of our TCT-setup are:

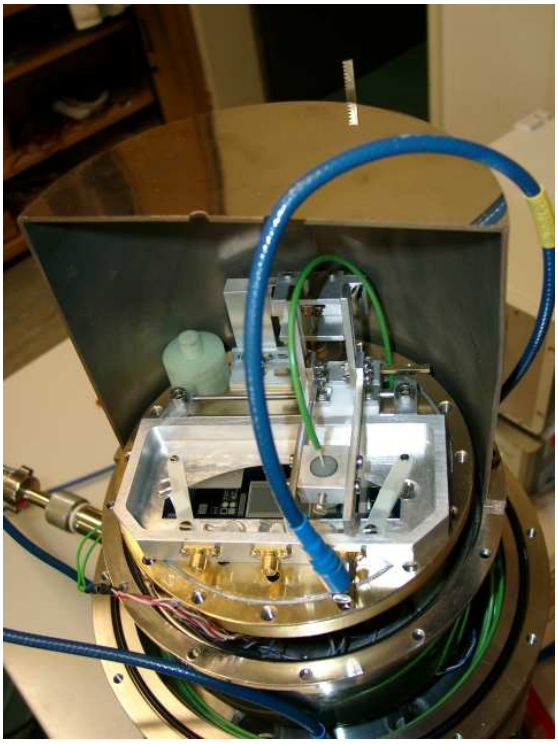

(a) Picture of the cryostat

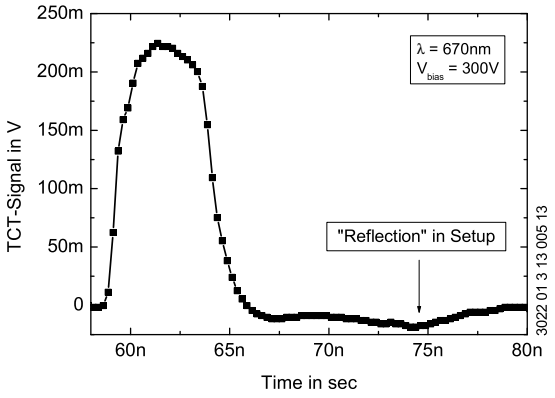

(b) A 'reflection' at 15 ns could not be eliminated

Figure 4.4: In the cryostat flexible SMA cables are connected through the ground plate to an aluminium box containing the test-structure. The optical fibre, which can be moved by micrometre-screws from outside, points to the diode.
Unfortunately, the setup causes a 'reflection' about 15 ns *after the pulse, which could not be eliminated.*

Picosecond laser The picosecond laser PiL067DG with a wavelength of 670 nm from APhS[(1)] is driven by a pulse generator for pulse lengths $< 35\,ps$.

Power supply A Keithley 2410 with maximum output voltage of 1100 V at 1 A is used for biasing.

Amplifier The signal is amplified by a multi level amplifier from Ingenieurbüro Walter[(2)] with a gain of up to 330. The amplifier is usually operated at a gain of 10.

Oscilloscope LC684DXL from LeCroy with 4 channels at 2 GS/s or one channel at 8 GS/s

Cryostat With an evaporation cryostat it is possible to cool complete half-moons down to liquid nitrogen temperature.

The test-structures are fixed on the ground plate of an aluminium box, which is screwed onto the cold plate of the cryostat. The diode and/or read-out strips (DC-pads) are bonded to a piece of PCB, which is soldered to SMA connectors (see Figure 4.4(a)).

(1) Advanced Photonic Systems APhS GmbH, 12489 Berlin
(2) Ingenieurbüro für Elektronik, Horst Walter, 55291 Saulheim

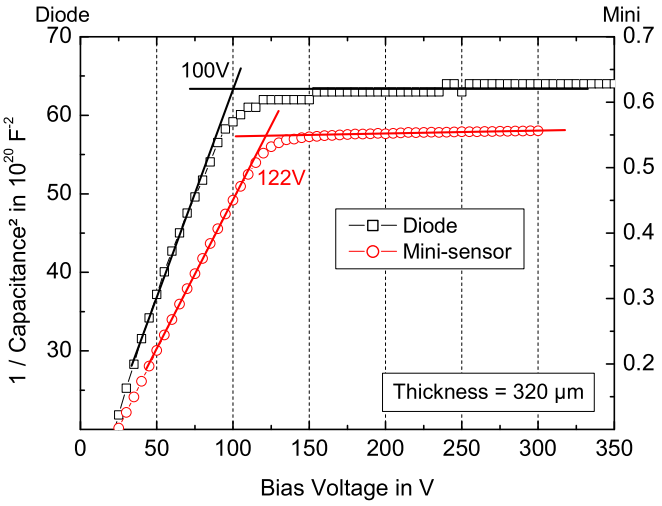

Figure 4.5: CV-characteristic of a diode and a mini-sensor of the same test-structure. The intersection of the two linear extrapolations below and above full depletion indicates the full depletion voltage. For mini-sensors of that geometry the full depletion voltage should be 24% higher than for the diode (see Section 1.2.4). This example is in good agreement with the prediction.

The optical fibre is fixed with a mechanical support, which can be moved along the test-structure by micrometre-screws at the outside of the cryostat.
Unfortunately, there is some kind of reflection in the read-out circuit, which could not be eliminated within this work. The reflection causes a reduction of the signal about $15\,ns$ past the initial rise and is about $4\,ns$ wide (see Figure 4.4(b)).

4.2 Depletion Behaviour before Irradiation

The full depletion voltage is usually extracted from the CV-characteristic of the sensor. Plotting $1/C^2$ versus the bias voltage one gets a linear[(1)] increasing part below full depletion and a plateau above full depletion. This is shown in Figure 4.5 where the intersection of two linear extrapolations indicate the full depletion voltage. The diode and mini-sensor are from the same test-structure, i.e. they are processed on the same wafer and the material should not differ much. These measurements show good agreement with the prediction that the mini-sensor with its altered electric field configuration has a higher full depletion voltage than the diode (see Section 1.2.4 on page 19). This increase in the full depletion voltage is 24% according to (1.46).

4.2.1 Results from the TCT using a $670\,nm$-laser

With means of the TCT and a red laser ($\lambda = 670nm$) one can probe the drift of one type of charge carriers. The absorption coefficient for this wavelength is $\alpha \approx 2100\,/cm$, which corresponds to a short penetration depth of $\sim 5\,\mu m$ at room-temperature generating electron-hole pairs close to the surface. The charge carriers are separated by the electric field and one type immediately reaches the implant, where it is absorbed and does not contribute to the signal current any more. In this work all sensors are illuminated on the p-side, thus the drift of electrons is studied using a red laser.
In Figure 4.6 several TCT-signals are plotted corresponding to selected points on the CV-curve

[(1)] The increase is linear only for constant space charge concentration (see (1.41))

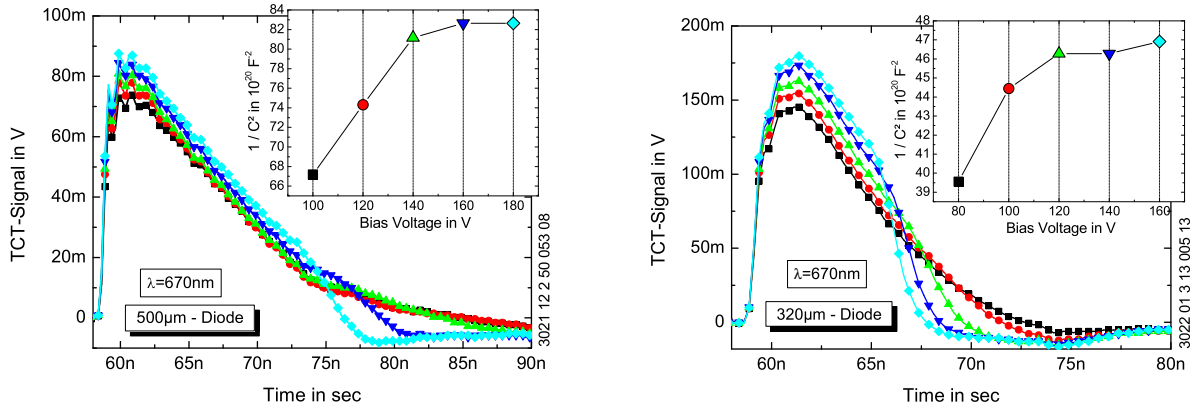

(a) 500μm-diode

(b) 320μm-diode

Figure 4.6: TCT-signals of a thick and thin diode in comparison with the CV-curve. The flattening of the CV-curve is well correlated with appearance of the final drop in the TCT-signal. This is expected, since the drop is caused by the electrons reaching the back contact, which is only possible if the sensor is fully depleted.

in the upper right corner. The signals show a steep increase when the laser pulse generates the charge carriers. In general, one expects a very short pulse at the beginning generated by the drift and recombination of the holes at the surface. Our setup seems not to be fast enough to measure this spike. The main signal is generated by the electrons drifting through the linear decreasing field. This results in an exponential decreasing signal for a constant mobility (see (4.5)). Since the drift velocity starts saturating at higher fields the signal appears to decay linearly. When the electrons reach the back contact they are stopped and the signal drops to zero. This is true above full depletion. Below full depletion the signal is decaying exponentially (see Section 4.1).
The signal of a thick diode in Figure 4.6(a) shows good correlation of the full depletion voltage extracted from the CV-characteristic ($\sim 140\,V$) and the appearance of a drop of the signal, which is steeper than the exponential decay before.
The same is true for the thin diode in Figure 4.6(b), which has a full depletion voltage of $\sim 110\,V$. The signal appears much faster since the distance is shorter.
Figure 4.7(a) is the same kind of plot but for the thick mini-sensor belonging to the same test-structure as the thick diode. The full depletion voltage can be extracted to be slightly above $160\,V$. The higher full depletion voltage of mini-sensors in respect to a diode of the same material and thickness was already mentioned before. For a width/pitch-ratio of 0.25 and a thickness of $500\,\mu m$ the increase is 15% according to (1.46). This is approximately what can be observed for this test-structure.
In the diode we had a linear decrease of the signal above full depletion. The mini-sensor still shows a kind of exponential decay above full depletion. This is due to the weighting potential, which is different for a segmented detector (Figure 1.13 on page 21), and increases the signal close to the strips. It also decreases the signal generated by electrons near the back contact. This suppresses the final sharp drop when reaching full depletion. In addition the 'real' electric field is increased around the strips, which changes the drift of the charge carriers (see Figure 4.7(b)).
The drift time in $500\,\mu m$ thick mini-sensors with $\sim 25\%$ over-depletion is about $25\,ns$. This is

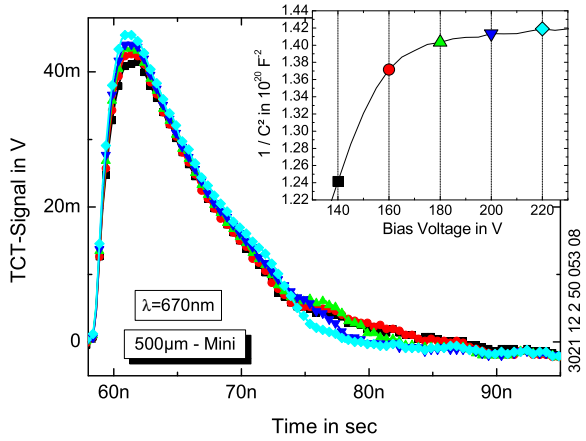

(a) TCT-signals of a thick mini-sensors in comparison with the CV-curve

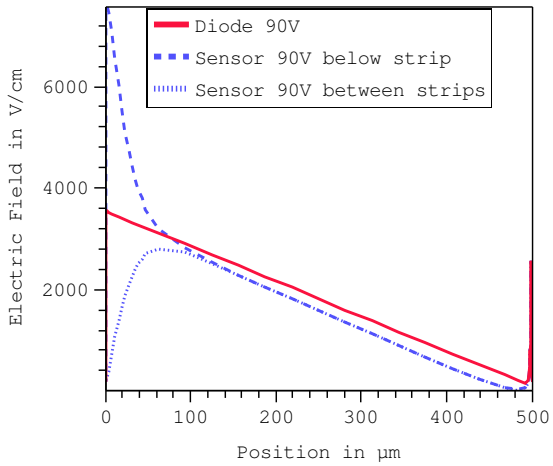

(b) Simulation of the electric field in a strip sensor and in a pad sensor

Figure 4.7: The steep decay of the TCT-signal is caused by the enhanced field at the strips. The final drop of the signal, when the electron cloud reaches the back contact, is suppressed according to the weighting field.

fast enough to collect all charges within a shaping time of 50 ns like with the APV25 at CMS.

4.2.2 Results from the TCT using a 1060 nm-laser

The infra-red laser is used to simulate a particle penetrating the whole device. The charge carriers are generated not only at the surface, but along the path of the laser beam through the sensor, since the penetration depth is $\sim 850\,\mu m$ ($\alpha \approx 12\,/cm$). The generated signal is similar to a MIP, which allows to study the charge collection of the sensor with the infra-red laser.
For absolut charge collection measurements the laser intensity must be calibrated very well and any changes in the fibre distance or additional attenuations have to be avoided. This is not possible with the current setup and only relative changes in the charge collection of the same sensor are investigated in this study.
The infra-red laser is pulsed by a HP8082A. The generated pulse shape is shown in Figure 4.8(a). The pulse is approximately 2 ns long, which is much longer than the charge generation by a traversing MIP and has to be taken into account analysing the TCT-signal.
In Figure 4.8(b) the resulting TCT-signals for a diode and the mini-sensor on the same test-structure using the infra-red laser are shown. The rise time of the signal reflects the long duration of the laser pulse.
Integration of these signals results in a value proportional to the collected charge. The amplifier pulls the signal below zero at the end. This affects the integration in a way that a higher fraction of the signal is subtracted with increasing bias voltage. Within the integration time of 50 ns the signal could be corrected by considering an exponential decay with a time constant of 5 ns. The applied formula reads:

$$V_{Corr} = V_{Meas} + \eta \cdot \sqrt{V_{Meas}^{max}}(1 - \exp[-(t - t^{max})/\tau]) \tag{4.13}$$

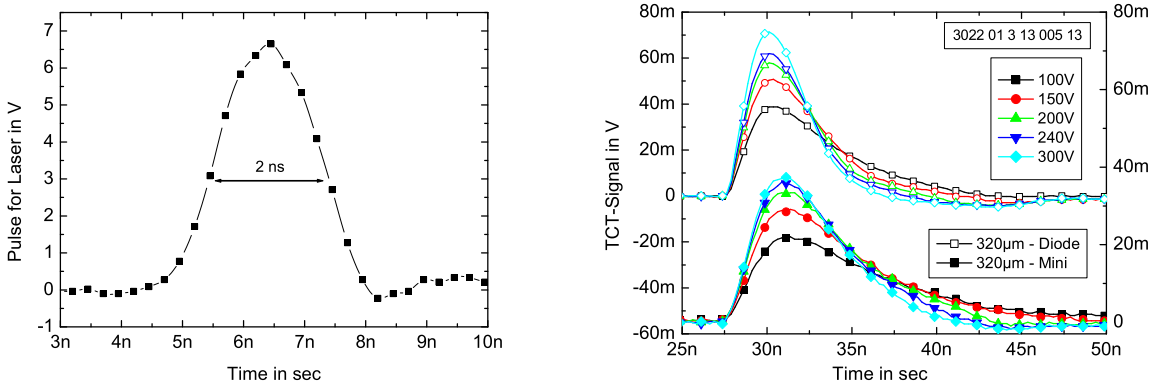

(a) Pulse shape generated by the HP8082A to drive the infra-red laser

(b) TCT-signal generated by the infra-red laser on a thin test-structure

Figure 4.8: Pulse for the laser driver and resulting signals with the infra-red laser.

where $\eta = 0.01 - 0.02$ and $\tau = 5\,ns$. The result of this correction is shown in Figure 4.9.
The described method is not the ideal deconvolution of the signal, but solves the problem of the undershoot. The following plots showing the charge collection are created applying this correction.
In Figure 4.10 the charge collection is compared with the CV-characteristic of the same sensor. It is obvious that the charge collection saturates close to the full depletion voltage extracted from the CV-curve.
A slightly different response to the laser pulse is observed with thick sensors. The TCT-signal is shown in Figure 4.11(a). The kink at $\sim 15\,ns$ past the signal maximum is the already mentioned

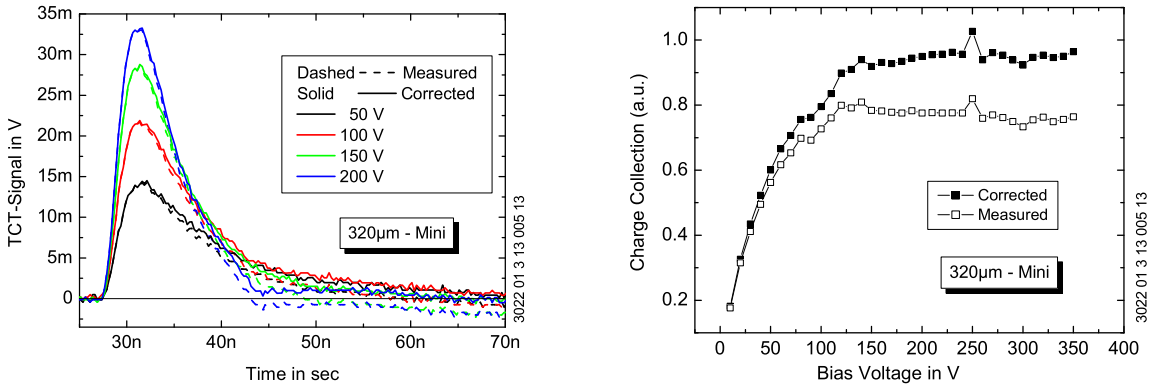

(a) Signals

(b) Charge collection

Figure 4.9: Correction of the amplified signal according to (4.13). The measured signal is partially below zero, which causes the charge collection to decrease with increasing bias voltage. This effect is eliminated with the correction.

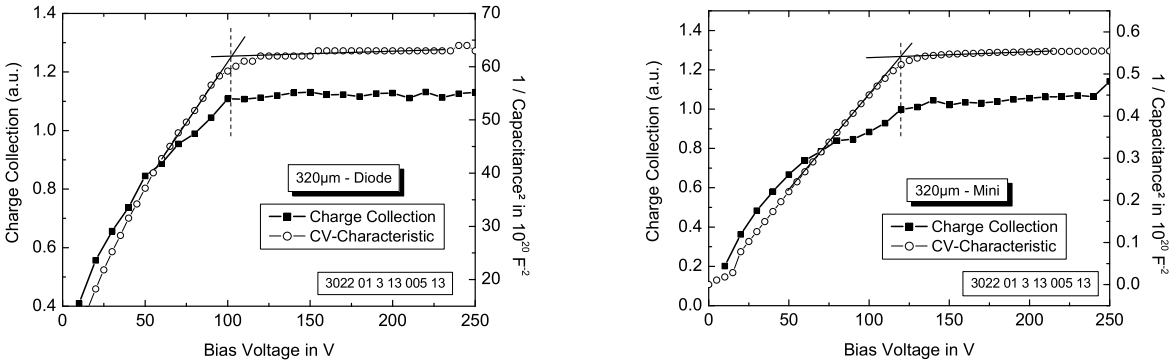

(a) Diode (b) Mini-sensor

Figure 4.10: Charge collection and CV-characteristic for 320 *µm-diode and mini-sensor. Some of the data points show fluctuations to higher values. This is caused by the laser, which sometimes operates unstable.*

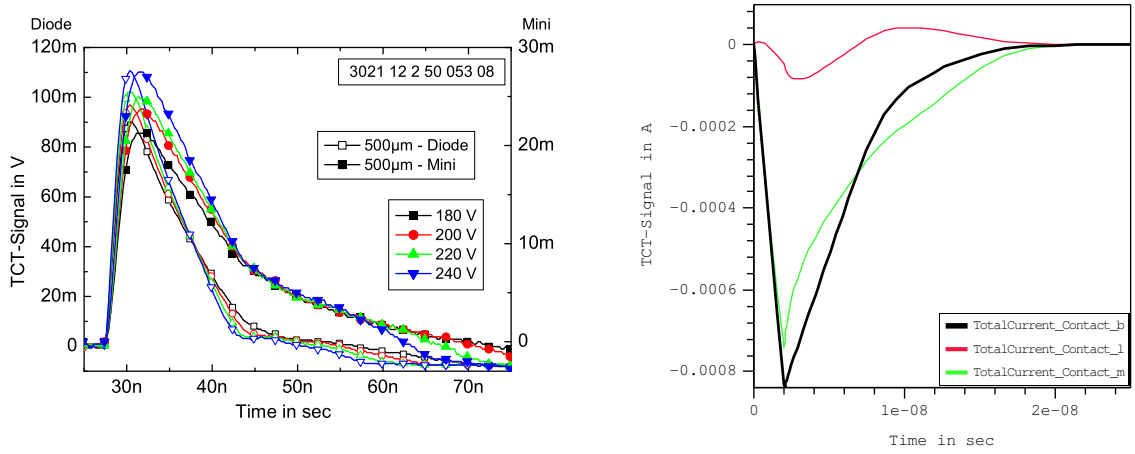

(a) Measurement (b) Simulation

*Figure 4.11: Signals generated in a mini-sensor are different from the signals in a diode. The bipolar pulse at the neighbouring strip influences the signal at the read-out strip causing a steeper slope at the beginning and an increased signal at the end. The simulation shows the current at the read-out strip (*Contact_m*), the next neighbour (*Contact_l*) and the back contact (*Contact_b*).*

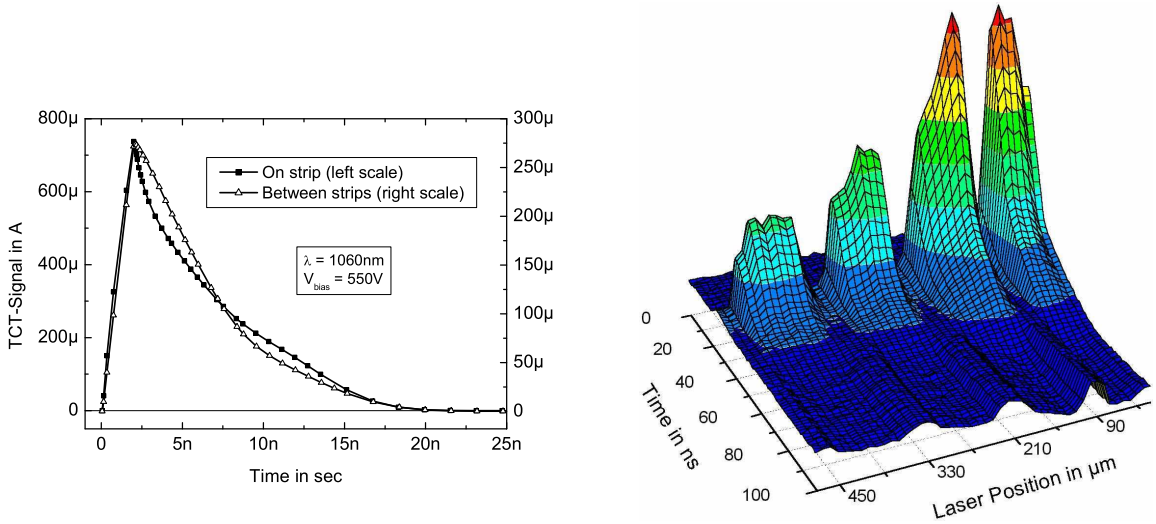

(a) Simulated signals

(b) Measured laser scan

Figure 4.12: Differences in the signal shape at various positions. The bipolar signal at the next neighbour affects the signal shape for MIPs close to the strip. This could be simulated and observed by a scan of the laser position perpendicular to the read-out strip.

'reflection' of the setup and should be ignored.
The difference is at the end of the signal where a drop appears like in the signals generated by the red laser. This effect appears in mini-sensors since the moving charges influence a signal in the neighbouring strip, which is subtracted from the current in the read-out strip.
A simulation performed with ISE T-CAD shows this effect (see Figure 4.11(b)). For the simulation a 500 μm thick strip sensor with a full depletion voltage of about 220 V was modelled (see Figure 4.17(a) for the geometry) and an optical beam (width 10 μm) was generated with a wavelength of 1060 nm at the read-out strip. The induced currents at the read-out strip, at one neighbour and at the back contact are plotted in Figure 4.11(b).
Injecting the same laser pulse at the centre between the read-out strip and its neighbour generates a signal not affected by a bipolar signal, since the neighbouring strip is equivalent to the read-out strip. The simulated signals on and between the strips are compared in Figure 4.12(a).
These differences are also observed in a scan of the laser position on a thick mini-sensor (see Figure 4.12(b)). The signal of one strip was measured for different positions of the laser spot. At the metal strips the signal vanishes since the metal covers the whole spot. Close to the edge of the read-out strip the highest signal is generated with a slight knee at the end, similar to the simulation on the strip. Moving away from the strip the signal reduces since the generated charge is shared among the neighbouring strips.
The missing bipolar shape and the high signal generated at the read-out strip while the laser moves beyond the neighbour can be explained by a diffuse reflection at the back contact. An intensive and collimated beam enters the sensor generating the highest charge carrier density along the path. It is partially absorbed in the n^+-layer and reflected back at the rough (not polished) oxide/metal interface. This reflected beam again generates charge carriers in the bulk, but with a reduced density.
This bipolar effect is not so pronounced in the thin mini-sensors as was observed in Figure 4.8(b).

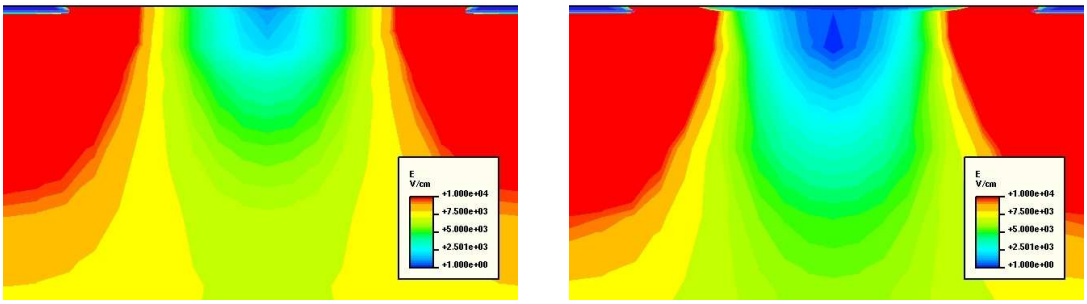

(a) Electric field (b) Electric field

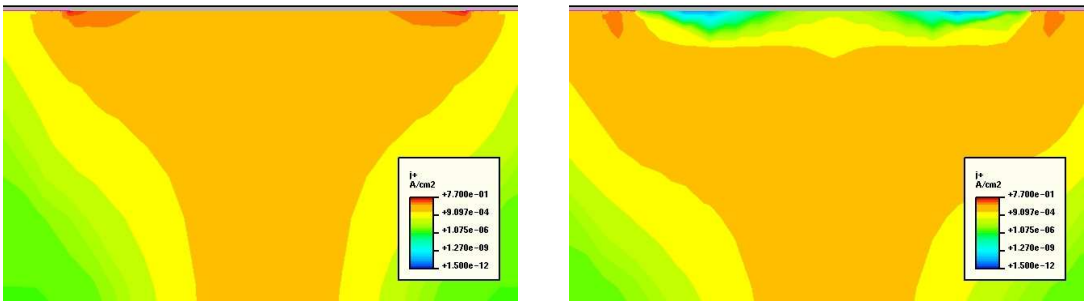

(c) Hole current (d) Hole current

Figure 4.13: Closeup of the area between the strips of a 500 μm *thick mini-sensor at* 250 V 8 ns *after an infra-red laser pulse. On the left are the simulated results without surface charge. On the right the simulation was performed with a uniform surface charge of* $3 \cdot 10^{11}\ /cm^2$*, which corresponds to a flat-band voltage of* 15 V*. The scales are equal for the same parameter.*

This might be due to the increased oxide charge in the thick sensors, which also increases the inter-strip capacitance (see Section 3.3.3 on page 68). Figure 4.13 shows a collection of simulation results showing the effect of oxide charges between the strips. The charge layer at the oxide reduces the electric field near the strips, which also reduces the induced read-out signal.
This might also be responsible for a difference in the charge collection shown in Figure 4.14. The charge collection of the diode still saturates at the full depletion voltage from the CV-measurement. But the mini-sensors need an over-depletion of up to 30% (Figure 4.14(b)) to reach the maximum charge collection. This over-depletion seems to scale with the flat-band voltage representing the oxide quality. The applied bias voltage has to be increased to overcome the field built up by the charge layer and to establish a field configuration that allows full charge collection.
In a simulation the laser beam was generated between the edge of the read-out strip and half the distance to the next neighbour to get an average information of the charge collection between the strips. The result is shown in Figure 4.15 and qualitatively demonstrates the incomplete charge collection in the presence of oxide charges (here $N_{ox} = 3 \cdot 10^{11}\ cm^{-2}$ corresponding to flat-band voltage of $\sim 15\ V$).
The necessity of over-depletion was also reported for the signal-to-noise ratio on complete modules using cosmic rays (see Figure 4.16) and test-beams in [Dir03, Fri01].

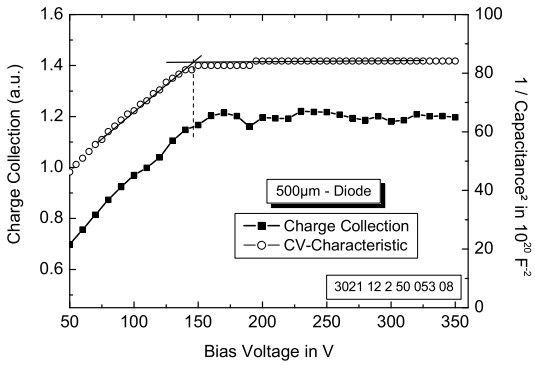

(a) Diode

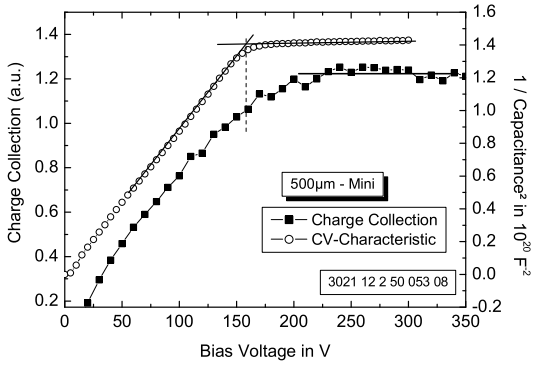

(b) Mini-sensor ($V_{FB} \approx 9\,V$)

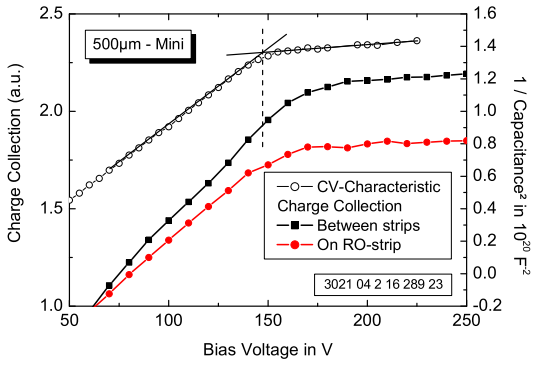

(c) Mini-sensor ($V_{FB} \approx 6.5\,V$)

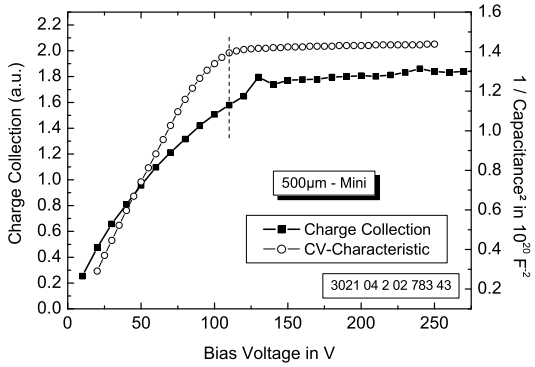

(d) Mini-sensor ($V_{FB} \approx 5\,V$)

Figure 4.14: Charge collection and CV-characteristic for 500 µm-diode and mini-sensors. Some of the mini-sensors reach the maximum charge collection up to 50 V above the full depletion voltage extracted from the CV-curve.

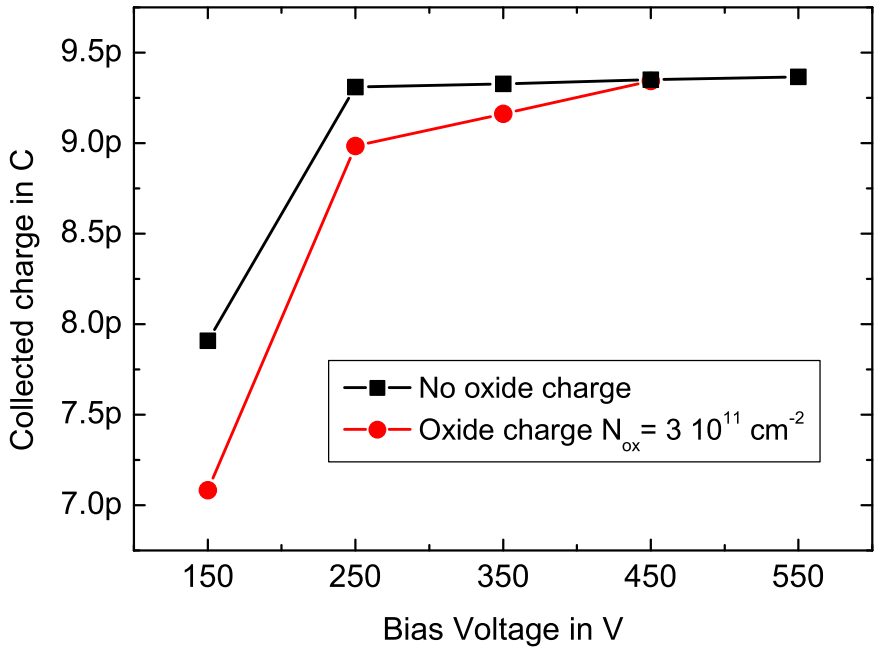

Figure 4.15: Simulation of the incomplete charge collection due to oxide charges. A laser beam was generated between the edge of the read-out strip and half the distance to the next neighbour to get an average information of the charge collection between the strips. The charge collection saturates immediately above the full depletion voltage of about 220 V, but in the presence of charges at the silicon/oxide-interface the maximum is reached not before a bias voltage of 450 V.

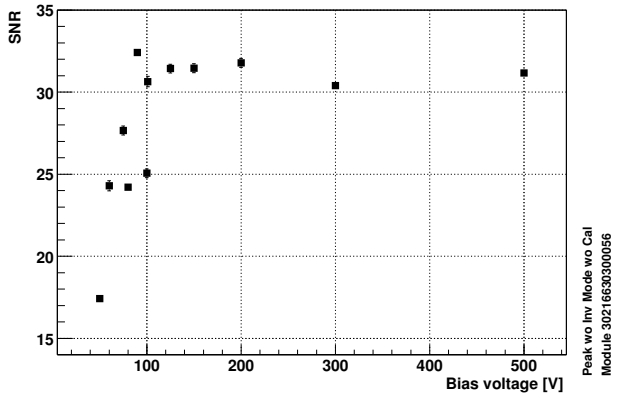

(a) Signal-to-noise ratio in peak mode vs. bias voltage measured using with cosmic rays from [Dir03] for a CMS end-cap module.

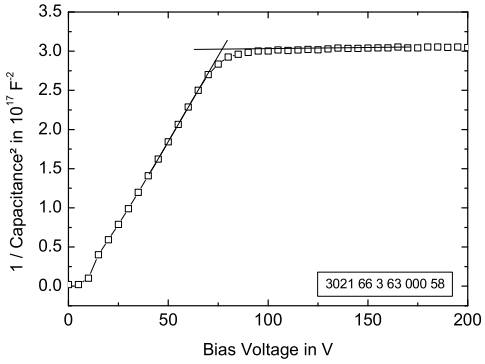

(b) CV-curve for the same module

Figure 4.16: The maximum S/N is reached not until 100 V, whereas the full depletion voltage for the sensors was measure to be ∼ 80 V.

4.3 Depletion Behaviour after Irradiation

4.3.1 Expected field configuration

As discussed in Section 1.3 on page 25 the bulk material of the sensor becomes inverted for high fluences, i.e. the sign of the space charge is changed. In our case the n-type bulk is converted to an effective p-type bulk and the pn-junction is now at the back contact. This means that the slope of the electric field also changes sign and the depletion process starts at the back contact and moves to the front, where the lasers are injected.
The electric field configuration in a mini-sensor before and after irradiation is shown in Figure 4.17 as it was calculated by ISE T-CAD (see Appendix D on page 127). For the simulation of the irradiated sample a neutral electron trap was included with a concentration of $N = 50 \cdot 10^{12}\,/cm^3$, a trap level of $E = E_V - 0.52\,eV$ and cross-sections of $\sigma_n = \sigma_p = 5 \cdot 10^{-15}\,cm^2$. The choice of this effective trap level enabled the author to reproduce full depletion voltage and TCT-signals similar to the observed ones.

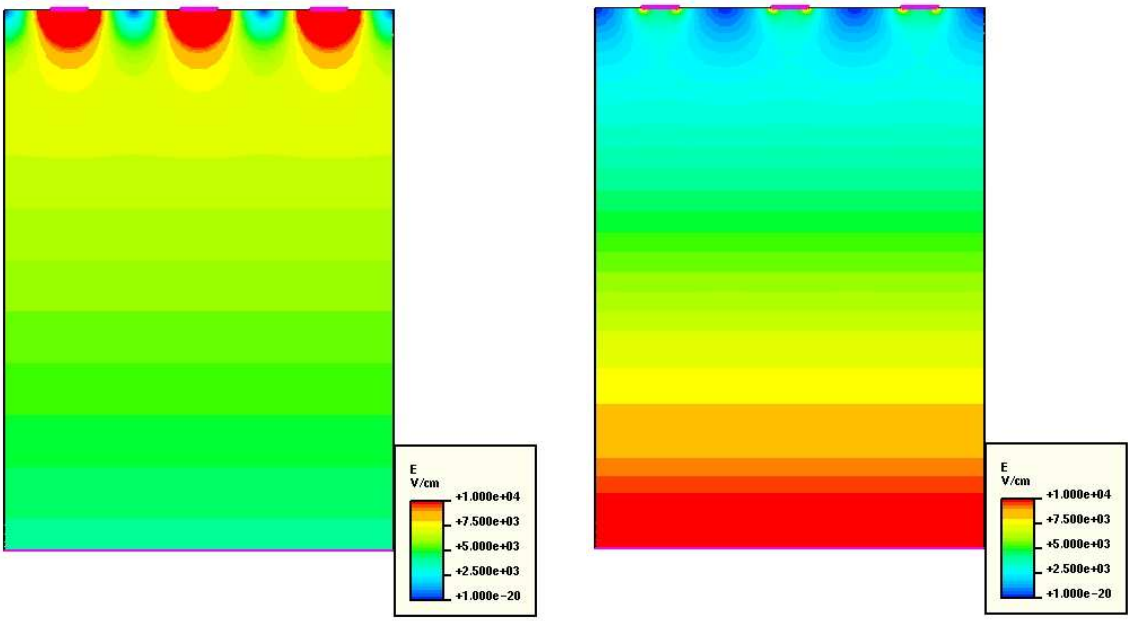

(a) Before irradiation (310 V) (b) After irradiation (300 V)

Figure 4.17: Simulated electric field for a 500 μm thick mini-sensor before irradiation (no traps) and after irradiation (neutral electron trap: $N = 50 \cdot 10^{12}\,/cm^3$, $E = E_V - 0.52\,eV$). The electric field in the bulk is inverted, and the field around the strips is still increased.

4.3.2 CV-characteristic

Some test-structures have been irradiated up to fluences of $0.5 \cdot 10^{14}\ n_{1MeV}/cm^2$ and $2.4 \cdot 10^{14}\ n_{1MeV}/cm^2$ for the thick and thin one, respectively. The measured CV-curves after irradiation and annealing are shown in Figure 4.18. The first observation is the broad transition from the partially depleted to the fully depleted condition, which makes it difficult to extract the

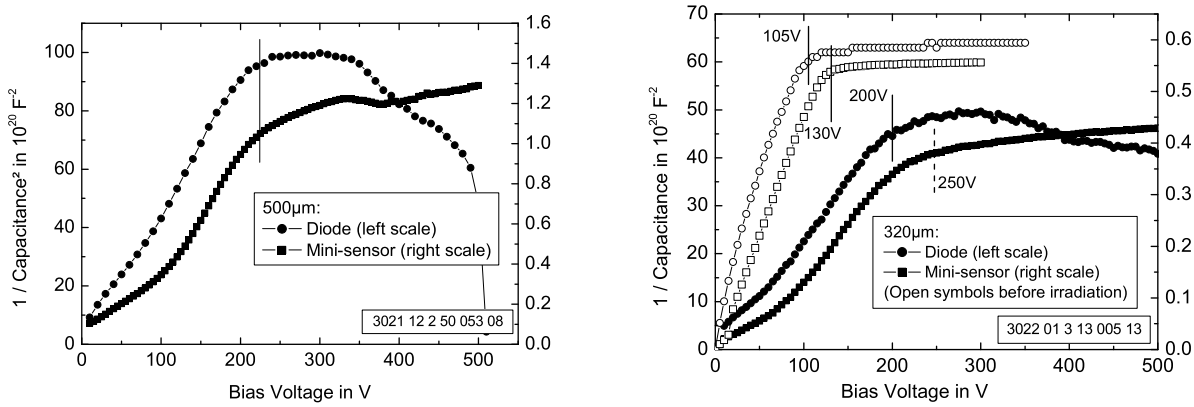

(a) 500 μm (b) 320 μm

Figure 4.18: Comparison of the CV-curves from diodes and mini-sensors after irradiation. The kink in the CV-curve, which indicates full depletion, is much broader after irradiation and the enhancement of the full depletion voltage for the mini-sensor in respect to the diode is not visible any more.
The drop of the CV-curves at high voltages for the irradiated diodes is a problem of the capacitance measurement at high leakage currents. The drop is correlated with a soft breakdown of the diodes.

exact full depletion voltage, if there is any. A second point is the enhanced full depletion voltage of mini-sensors with respect to diodes as observed before irradiation. After irradiation there is no such strong increase. For 320 μm material one expects an increase of 24% (see Section 1.2.4 on page 19), which is obvious from the CV-curves before irradiation in Figure 4.18(b). After irradiation the full depletion voltage of the diode can be extracted as about 200 V. With the same scaling as before irradiation the mini-sensor should have a full depletion voltage of 250 V. But at the dashed line indicating that voltage, the CV-curve of the mini-sensor does not change its slope. The kink in the curve is rather at about 200 V like in the CV-curve of the diode. Since the depleted zone grows from the back side the initial kink appears when the depleted zone in the bulk and around the strips (p^+p-interface) merge. The field configuration between the strips develops further at higher voltages but the total capacitance does not change much. The slight change is still visible, which is responsible for the broad transition.

4.3.3 Results from the TCT using a $670\,nm$-laser

The electron drift from the front contact to the back is inspected with the red laser. On the next pages the measured signals of irradiated and non-irradiated diodes and mini-sensors are presented for easy comparison.
In Figure 4.20(a) the TCT-signal of a $500\mu m$ thick diode is shown for several applied bias voltages. Below full depletion the generated charge carriers are separated in a small depleted region at the p^+p-interface near the surface, which remains after bulk inversion. This gives rise to a small peak, which is visible for small voltages at the beginning of the signal. For higher voltages the space charge region increases $\sim \sqrt{V/V_{fd}}$ and due to the exponential decaying intensity of the illumination and diffusion a second bump appears right below full depletion (signals for $150\,V$ and $200\,V$ in Figure 4.20(a)). Above full depletion ($\gtrsim 225\,V$ as extracted from the CV-curve) the increase of the drift velocity with the increasing electric field is visible. The full depletion voltage is reached when the SCR, growing from the back side, reaches the small depleted zone at the front.
Since the electric field and the weighting potential in a mini-sensor is different to a diode one also expects a different signal. In Figure 4.22(a) and 4.22(b) the TCT-signal of thick and thin mini-sensor is compared with its CV-characteristic at several bias voltages. The first peak is more pronounced according to the high weighting field near the strips. The bulk peak grows when the two depletion zones merge.
One difference of the two measurements is that the small peak at the beginning of the signal of the thick sensor does not vanish even at high voltages. This indicates a strong field at the surface, which might have its origin in a high flat-band voltage.

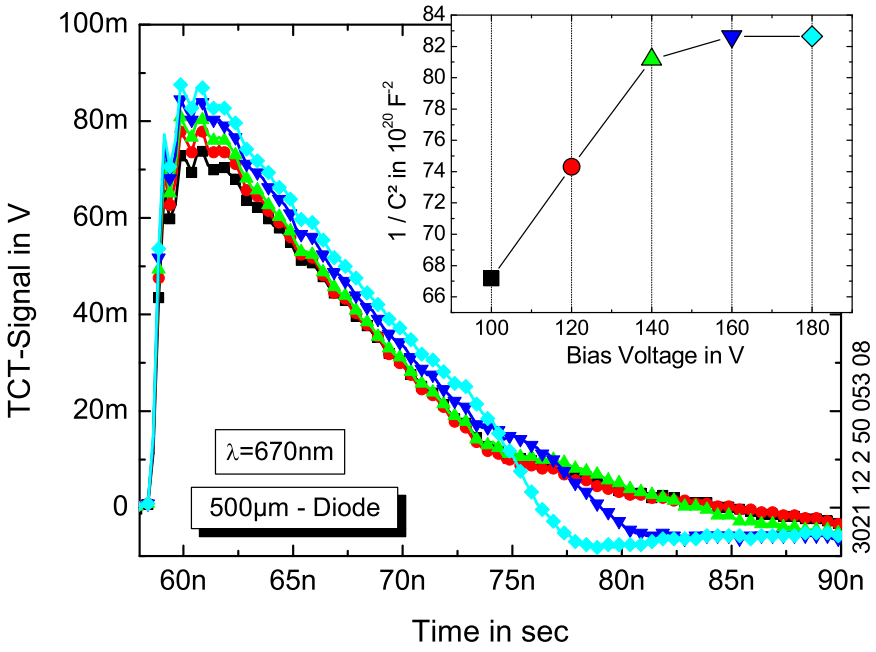

(a) 500 μm diode

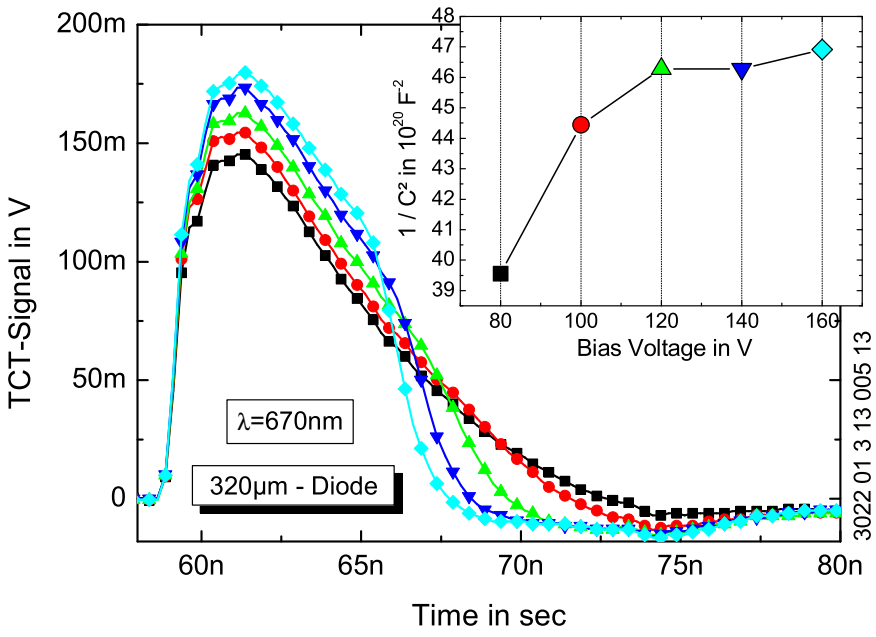

(b) 320 μm diode

*Figure 4.19: TCT-signals for the diodes **before** irradiation repeated for easy comparison. The negative slope indicated a high electric field at the front side decreasing towards the back contact.*

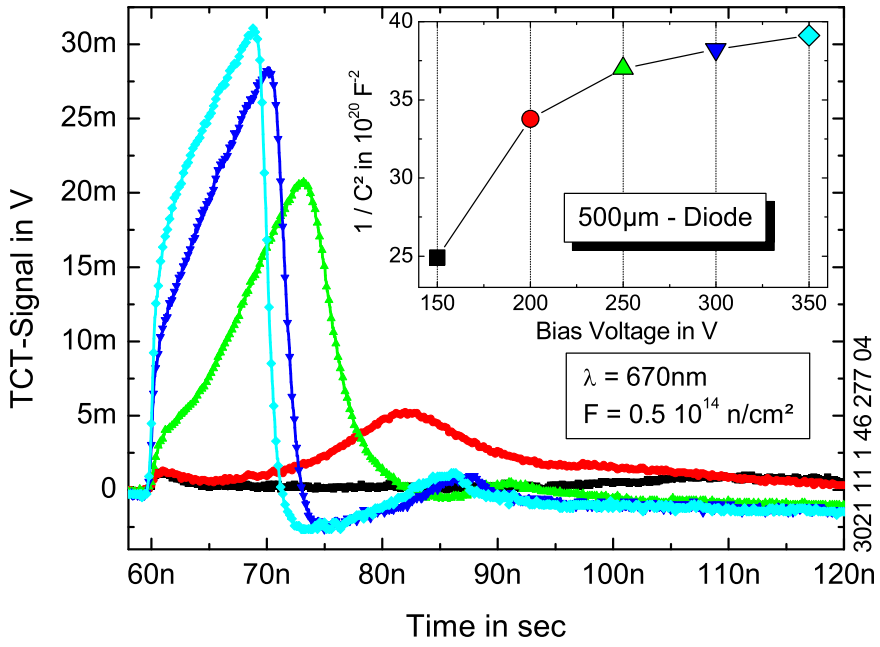

(a) 500 μm diode

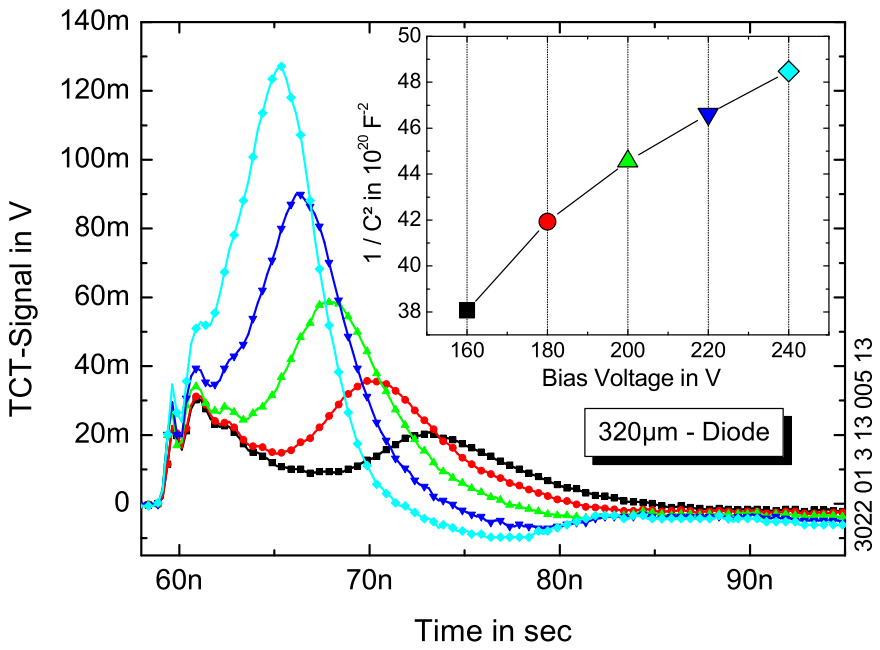

(b) 320 μm diode

*Figure 4.20: TCT-signals for the diodes **after** irradiation. One can clearly see the positive slope, which indicate the inverted electric field. The initial bump is generated in a small depleted zone at the strips (p^+ p-interface).*

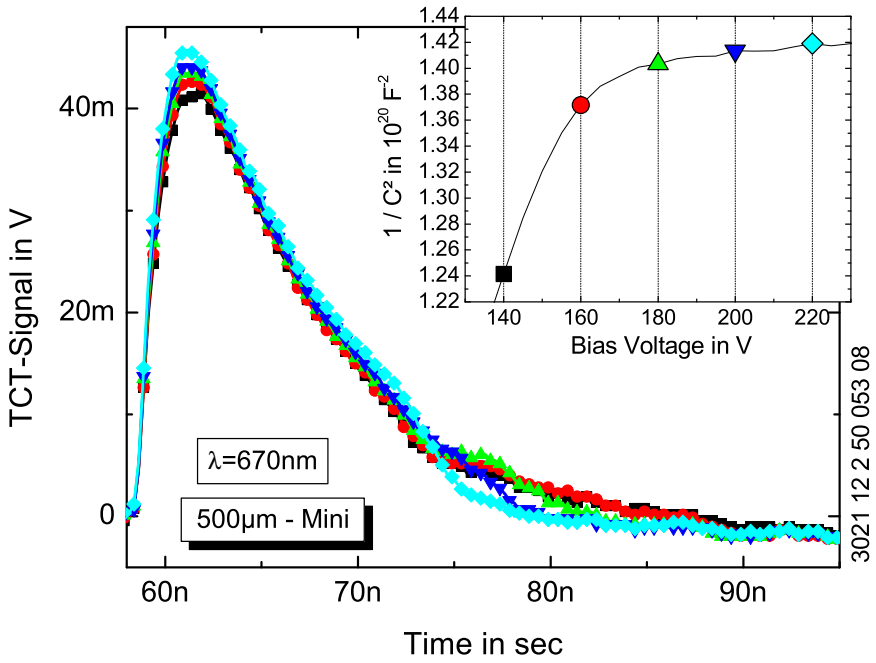

(a) 500 μm mini-sensor

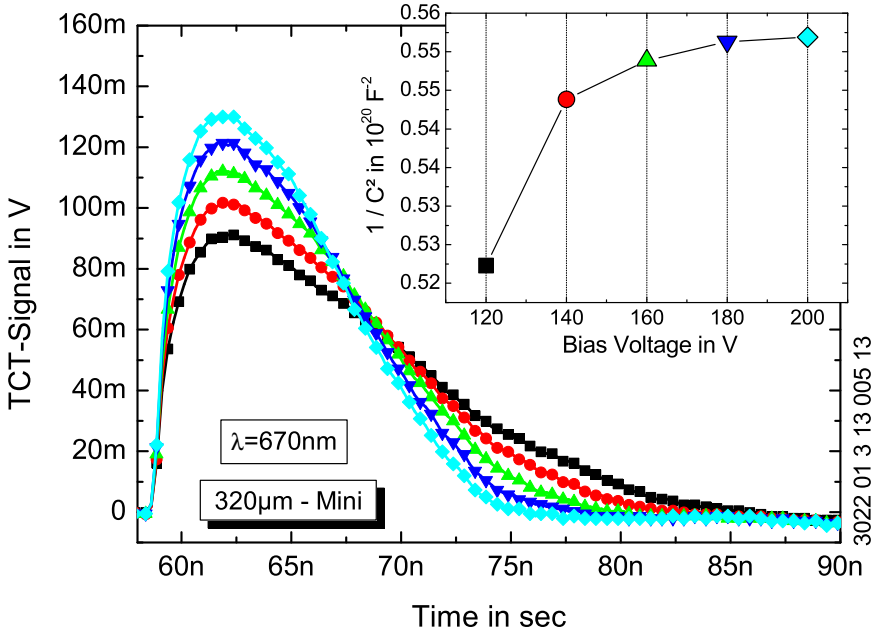

(b) 320 μm mini-sensor

Figure 4.21: TCT-signals for the mini-sensors ***before*** *irradiation, repeated for easy comparison.*

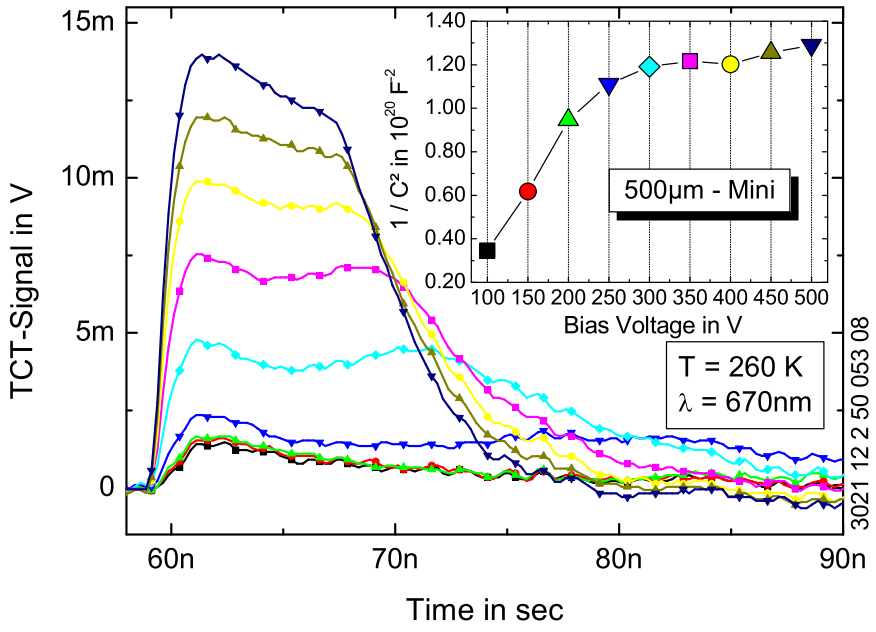

(a) 500 μm mini-sensor

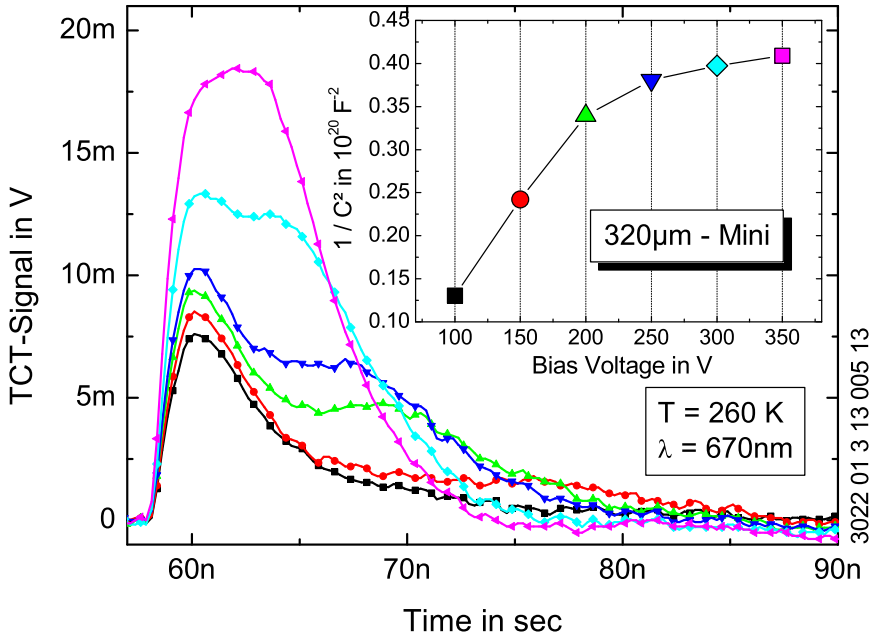

(b) 320 μm mini-sensor

*Figure 4.22: TCT-signals for the mini-sensors **after** irradiation. The initial peak corresponds to a signal generated in the small depleted zone around the strips (p^+p-interface). The second peak arises when the depletion zones of the bulk and the surface merge. The positive slope of the bulk signal is badly visible, since the fist peak is strongly pronounced.*

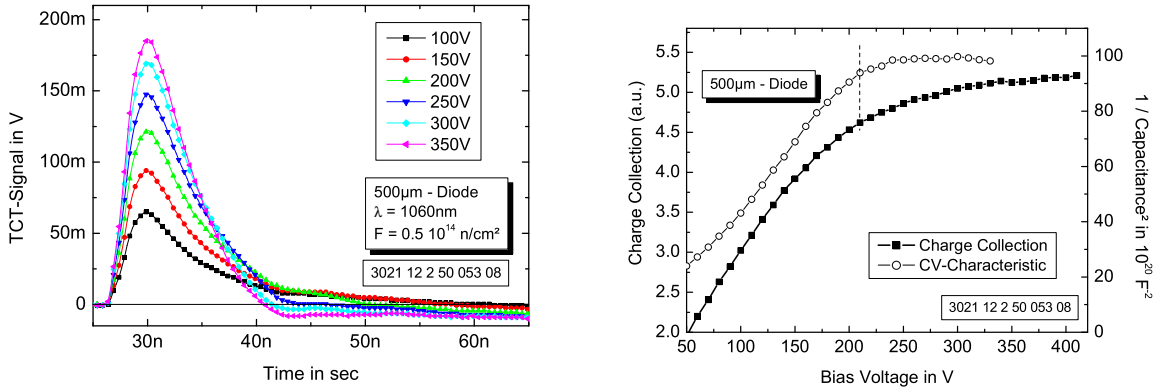

(a) Signals with the infra-red laser

(b) Charge collection

Figure 4.23: The signal generated by the infra-red laser on an irradiated thick diode was summed over 50*ns and plotted vs. the bias voltage. There is an incomplete charge collection at the full depletion voltage extracted from the CV-curve but the collected charge keeps rising with applied voltage.*

4.3.4 Results from the TCT using a 1060 *nm*-laser

It is known that part of the generated charge is lost due to trapping effects after irradiation [Lut99, Kra01]. Since trapped charge is stopped and thus does not contribute to the signal current, it is reduced exponentially: $I \sim \exp(-t/\tau_{eff})$, where τ_{eff} is the effective trapping time. This was also observed analysing the TCT-signals generated with the infra-red laser. The signals generated in a thick diode are shown in Figure 4.23(a). These signals are corrected according to the procedure described in Section 4.2.2 on page 86, integrated and plotted vs. the bias voltage in Figure 4.23(b). It is obvious that the collected charge does not saturate at the full depletion voltage extracted from the CV-curve, but it continues rising with increasing bias voltage. The drift time is reduced at higher bias voltages and thus the amount of trapped charge.
Since the setup is not absolutely calibrated, this charge collection efficiency (CCE) can not be compared with the CCE before irradiation.
The same behaviour can be observed with the thin diode. In addition, the charge collection was measured at room-temperature and plotted in Figure 4.24(b). At that temperature the signal is bigger since the absorption coefficient for the infra-red laser in silicon increases with temperature (see Figure 1.5 on page 11). But the signal shows no saturation below 500 V. This indicates that charge collection is more efficient at lower temperatures, since the drift is faster.
The charge collection was also investigated for mini-sensors using an optical head to focus the infra-red laser. This allows to measure the charge collection at different positions as already described in Section 4.2.2 on page 86. Figure 4.25(a) and 4.25(b) shows the charge collection measured on an irradiated 500 μm thick and thin mini-sensor, respectively. Close to the strip, where the laser spot is partially covered by the metallisation, the charge collection is very efficient due to the high field strength around the strip. As soon as the depletion zones around the strips and in the bulk merge, most available charges are collected.
Injecting the laser between the strips results in charge collection, which does not saturate up to a bias voltage of 500 V. The drift is slower and hence trapping is more effective. Thus it

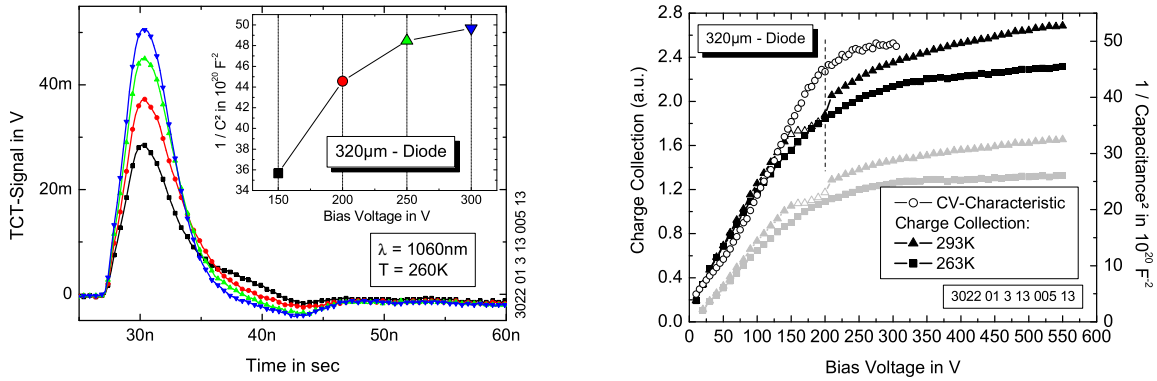

(a) Signals with the infra-red laser

(b) Charge collection

Figure 4.24: The signal generated by the infra-red laser on an irradiated thin diode was summed over 50*ns and plotted vs. the bias voltage. There is an incomplete charge collection at the full depletion voltage extracted from the CV-curve but the collected charge keeps rising with applied voltage. At the higher temperature the absorption coefficient of silicon increases, which increases the number of generated charge carriers and thus the collected charge. The continuing increase above full depletion is stronger at higher temperature.*

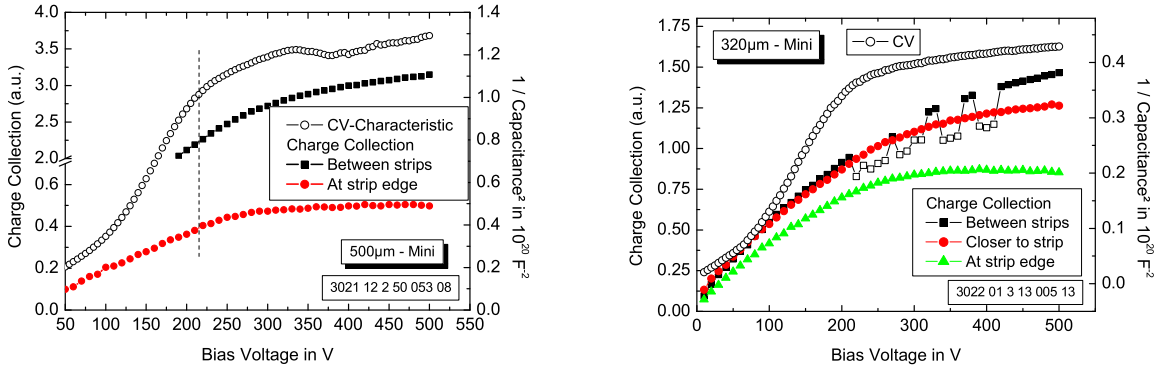

(a) 500 μm mini-sensor

(b) 320 μm mini-sensor

Figure 4.25: Charge collection and CV-characteristic for irradiated mini-sensors. A signal generated near the strip edge is smaller, since the laser spot is covered by the metal strip. The signal saturates at lower bias voltage, since the field is higher close to the strips. The largest amount of charge carriers can be collected if the whole laser spot is between the strips. There the signal keeps rising with increasing bias voltage.

is recommended that inverted sensors should be operated at the highes possible bias voltage to reach a high signal. The breakdown voltage of inverted sensors was measured in Section 3.3.1 on page 61 to be higher than 1000 V. This guarantees the stable operation at high voltages.

4.4 Summary

In this chapter the depletion behaviour of strip sensors was discussed. For non-irradiated sensors the enhanced full depletion voltage with respect to diodes was shown using capacitance measurements and the TCT with a red laser. The charge collection was measured using an infra-red laser. For the available 320 μm thick mini-sensors the charge collection saturates at the full depletion voltage extracted from the CV-curve. For thick mini-sensors a saturation at higher voltages was observes, which might be correlated to an increased flat-band voltage. A necessary over-depletion before irradiation was already reported in [Dir03, Fri01].
After irradiation it was observed that the full depletion voltages extracted from CV-curves become similar for diode and mini-sensor of the same material. The bulk doping is inverted and the depletion starts at the back contact. When this depletion zone reaches the strips, the total capacitance almost saturates, which is visible by the kink in the CV-curve. Further field rearrangement between the strips causes the capacitance to change slightly, which smears out the transition. This allows to extract the effective doping concentration directly from the full depletion voltage of the sensor without considering a correction factor of about 20%. But, since charge collection efficiency after irradiation is reduced by trapping, the full depletion voltage has to be seen as a lower limit for biasing. For higher electric fields the drift is faster and trapping is less effective. Especially, the field is very high near the strips, which results in a charge collection saturating even at small over-depletion. In general, it is recommended to operated the sensors at highest possible bias voltage after irradiation.

Chapter 5

Lorentz Shift in Silicon Sensors

The Lorentz shift has to be considered whenever silicon sensors are placed in a magnetic field. For electrons it is in the order of 35 μm in a 300 μm-sensor at room-temperature and at low magnetic fields ($\sim 1\,T$). This shift is small and can be calculated by a simple formula.
In future, tracking detectors will be operated at higher magnetic fields ($\geq 4\,T$) to achieve good momentum resolution for high energetic particles. In addition, radiation damage increases due to the high luminosity and high collision energies achieved with the upcoming accelerators. This reduces the charge collection efficiency dramatically and the measured signal vanishes. It was proposed by RD39 to operate such 'dead' sensors at cryogenic temperatures. The charge collection efficiency (CCE) after strong irradiation recovers at a temperature of $\sim 130\,K$ as reported in [B$^+$00a, Col02]. This is the so called Lazarus effect. Deep traps are filled with charge carriers which neutralise them. At low temperatures the charges can not be excited and the effective doping concentration is changed. This reduces the full depletion voltage and allows a better charge collection.
For these cryogenic sensors the Lorentz shift in strong magnetic fields becomes very large. This was measured for temperatures down to 80 K [H$^+$02, dB$^+$01a, dB$^+$01b].
This chapter gives a basic understanding of the Lorentz shift in silicon sensors, describes shortly the performed measurements and presents a modelling for the temperature dependance.
The Lorentz shift depends on the drift mobility, which should be known for a wide electric field range, since the charge carriers drift through the varying field of the sensor. Thus the TCT-setup was used to measure the drift mobility in the temperature range of interest.

5.1 Introduction

Charge carriers in an electric and magnetic field are exposed to the Lorentz force:

$$\vec{F} = q(\vec{E} + \vec{v} \times \vec{B}) \equiv q\vec{E}_{eff} \tag{5.1}$$

This can be expressed as a drift in the effective field $\vec{E}_{eff}$. The velocity $\vec{v}$ is parallel to this effective field and the angle to the field $\vec{E}$ is given by:

$$\tan\Theta_L = \frac{vB}{E_{eff}} = \mu_H B \qquad \text{for} \quad \vec{v}\cdot\vec{B} = 0 \quad \text{and} \quad \omega\tau \ll 1 \tag{5.2}$$

The angle Θ_L is the so called Lorentz angle or Hall angle. A more sophisticated derivation of the Hall angle is given in Appendix E on page 133. The cyclotron frequency $\omega_c = eB/m$ and the

scattering time τ define the fraction of a full cycloid during free flight, which is required to be below 1. The Hall mobility $\mu_H = r_H \cdot \mu$ is related to the drift mobility by the Hall factor r_H. It accounts for the energy distribution of the charge carriers. r_H may include an anisotropy factor a, which accounts for the different effective masses of the electrons [Bla68].

$$r_H = r_{H0} a = r_{H0} \frac{3K(2+K)}{(1+2K)^2} \qquad \text{with} \quad K = m_\parallel / m_\perp \tag{5.3}$$

In silicon the anisotropy factor is $a = 0.87$.
Finally, the Hall scattering factor r_{H0} is defined for low magnetic induction as (see Appendix E on page 133)

$$r_{H0} = \frac{\langle \tau^2 \rangle}{\langle \tau \rangle^2} \tag{5.4}$$

where the averaging is performed as in (1.17):

$$\langle \tau \rangle = \frac{4}{3\sqrt{\pi}} \int_0^\infty \tau(E) x^{\frac{3}{2}} \exp(-x)\, dx$$

The value of the Hall scattering factor varies from about 1.18 (pure acoustic phonon scattering) at room-temperature down to ~ 1 at around $100\,K$ and might rise again if scattering from ionised impurities dominates ($r_{H0} = 1.93$).

5.2 Measurement Principle and Setup

To get the Lorentz shift in silicon strip sensors, one can measure the shift of an induced signal in a magnetic field. The charge carriers are generated by red ($630\,nm$) laser light at one side of a depleted strip sensor. One type of the charge carriers drifts through the sensor under the influence of electric and magnetic field (see Figure 5.1). The other type immediately reaches the contact on the "laser side". In strip sensors the induced signal is higher the closer the charges

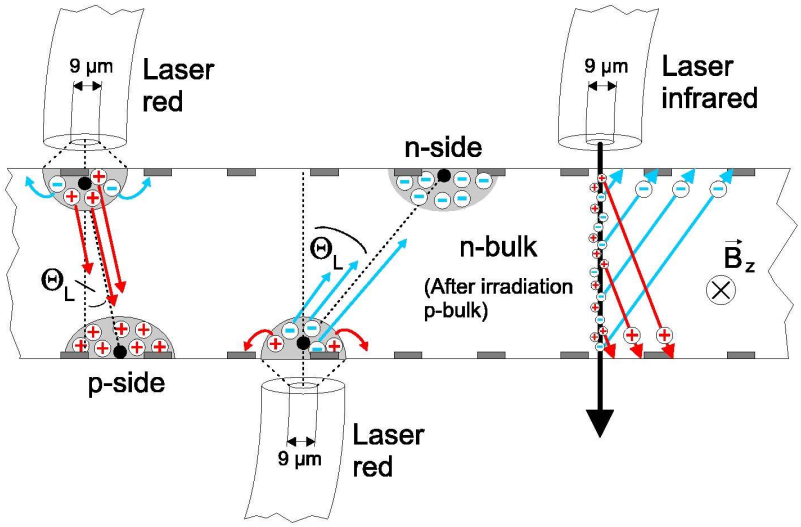

Figure 5.1: Illustration of the Lorentz angle measurement (from [Hau00])

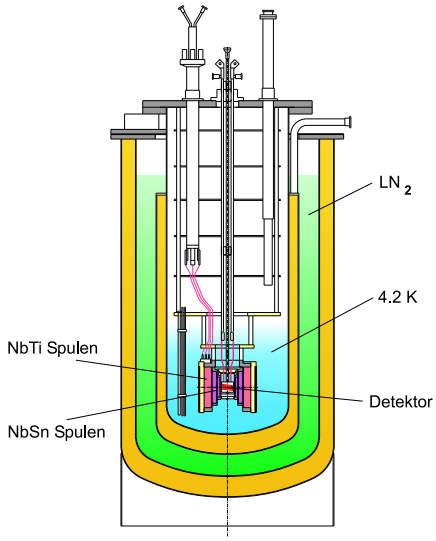

(a) Superconducting magnet JUMBO at the Forschungszentrum Karlsruhe

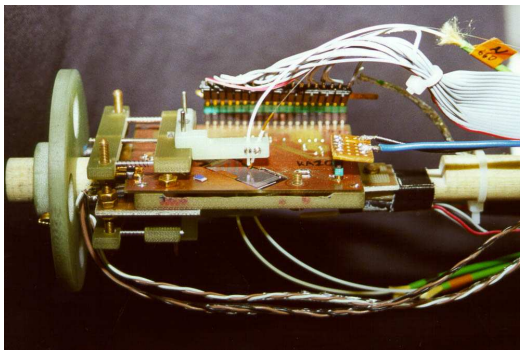

(b) Sensor on read-out hybrid with laser fibres

Figure 5.2: Setup for high field measurements (from [Hau00])

move to the strips (weighting field see Section 1.2.4 on page 19). That is why the signal represents the position of the charge cloud near the strips.
Our setup was already presented in detail in [Hei00, Hau00, Bol00], thus only a short summary of the setup is given here. The measurements were performed with double-sided HERA-B minisensors with a pitch of 50 μm on the p-side and 80 μm on the n-side. The sensors were read out by a 128-channel charge sensitive chip (PREMUX) and a VME-based read-out system. The magnetic field was generated by a superconducting magnet (JUMBO) at the Forschungszentrum Karlsruhe (Figure 5.2(a)). Therefore the read-out hybrid was mounted at the end of a glass-fibre rod which was sunk down into the warm bore of the magnet (Figure 5.2(b)). The temperature was controlled by a flow of cold nitrogen gas and a heater.

5.3 Results of the Measurements

Examples of the measured signals are shown in Figure 5.3. The barycentre of the signals, which extend over 3 to 4 strips, is calculated and taken as the centre position of the charge carrier cloud. A possible motion of the signal on the laser side indicates mechanical stress and can be viewed as a quality factor of the measurement. The shift of the signal is plotted vs. the magnetic field and a linear fit gives the mean shift at $4\,T$, which is used for further analysis.
The temperature dependance of the Lorentz shift at $4\,T$ is given in Figure 5.4. In addition the data are listed in Table 5.1. The Lorentz shift is below $200 \mu m$ for temperatures above $170 K$. This has to be taken into account in the tracking algorithm, but is no severe problem. At temperatures below $150\,K$, where also the Lazarus effect starts curing the loss of signal after irradiation, the Lorentz shift begins to rise dramatically up to $850\,\mu m$ at $80\,K$.
Using the red laser is a good way to investigate the drift behaviour. But in general the signals are generated by particles penetrating the whole sensor like a MIP. This results in a Lorentz shift of

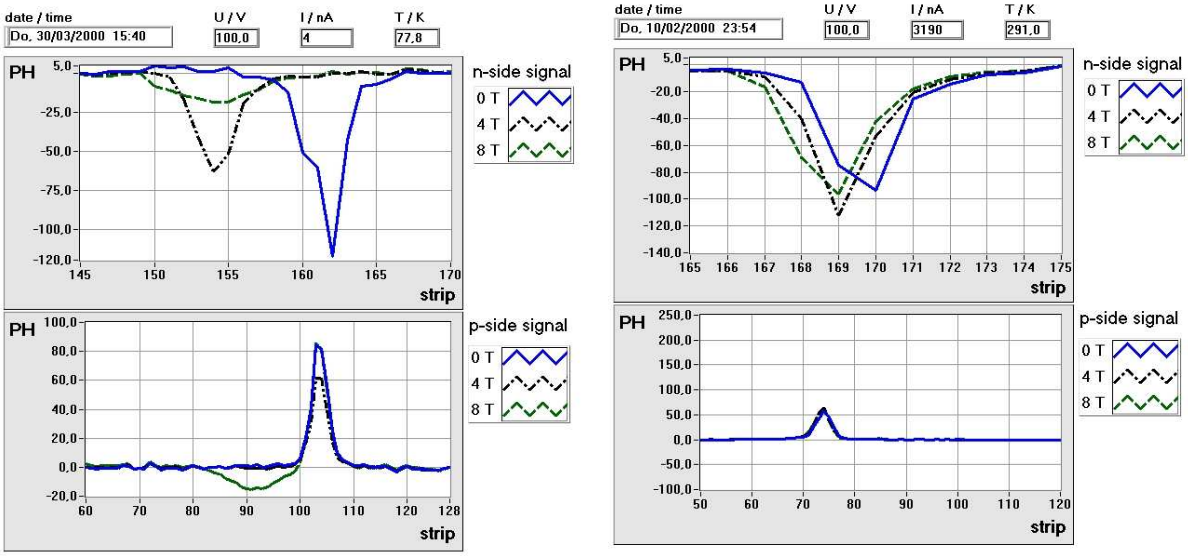

(a) 77 K (b) 290 K

Figure 5.3: Measured signals at magnetic fields of $0\,T$, $4\,T$ *and* $8\,T$.
At $77\,K$ *and* $8\,T$ *the signal reaches a region of defective strips and the signal has to be ignored.*

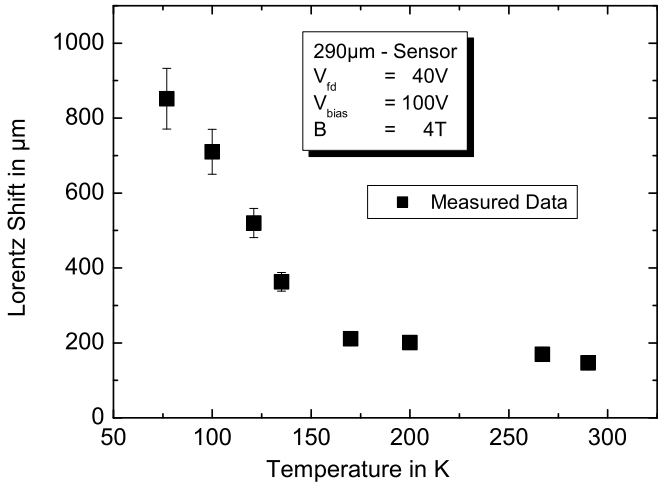

Figure 5.4: Measured temperature dependance of the Lorentz shift at $4\,T$. *The* $290\,\mu m$ *thick strip sensor has a full depletion voltage of* $40\,V$ *and was biased at* $100\,V$. *There is a huge rise at low temperatures, which can not be explained by a simple approach.*

Temperature in K	Lorentz shift in μm
77	852 ± 81
100	710 ± 60
121	520 ± 39
135	363 ± 25
170	221 ± 14
200	201 ± 12
267	170 ± 9
290	147 ± 7

Table 5.1: Measured Lorentz shift values of a 290 µm-sensor ($U_{FD} = 40\,V$, $U_{bias} = 100\,V$) taken from [Hau00]

the barycentre, which is half of the shift measured with a red laser as can be seen in Figure 5.5. The measurement with an infra-red laser (Figure 5.5(a)) shows small shifts in the magnetic field on both sides. The holes generate the signal on the p-side and electrons on the n-side, where the larger mobility of electrons generate a larger shift. When only electrons drift through the whole sensor (illumination with a red laser on the p-side in Figure 5.5(b)) the Lorentz shift is about twice the shift for the MIP.

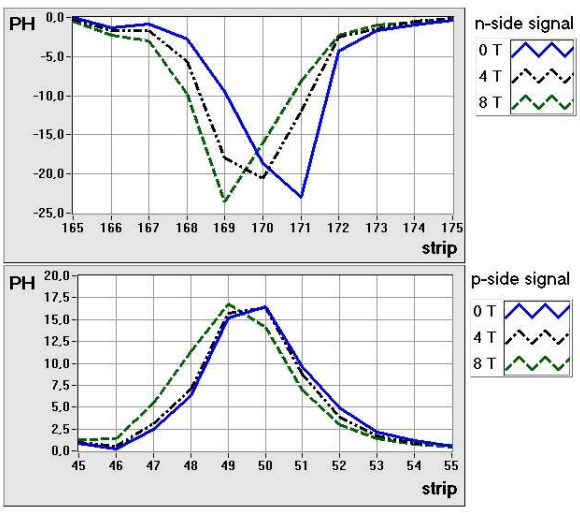

(a) 1060 nm at about $-10°C$

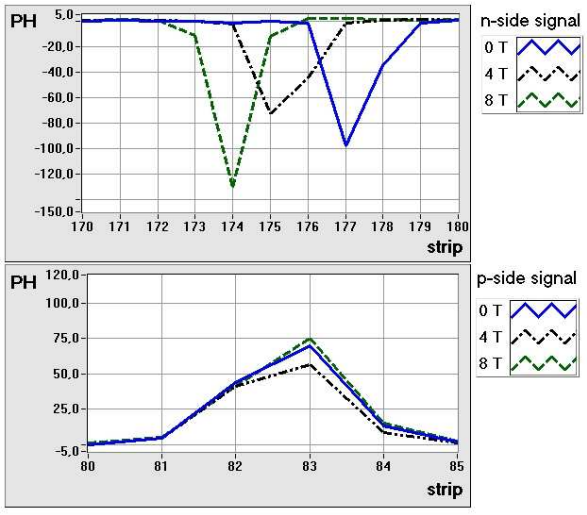

(b) 660 nm on the p-side at about $-25°C$

Figure 5.5: Comparison of signals generated by an infra-red and red laser. The shift of the signal generated by the infra-red laser on the n-side, where electrons are collected, is about half the shift of the signal generated by the red laser.

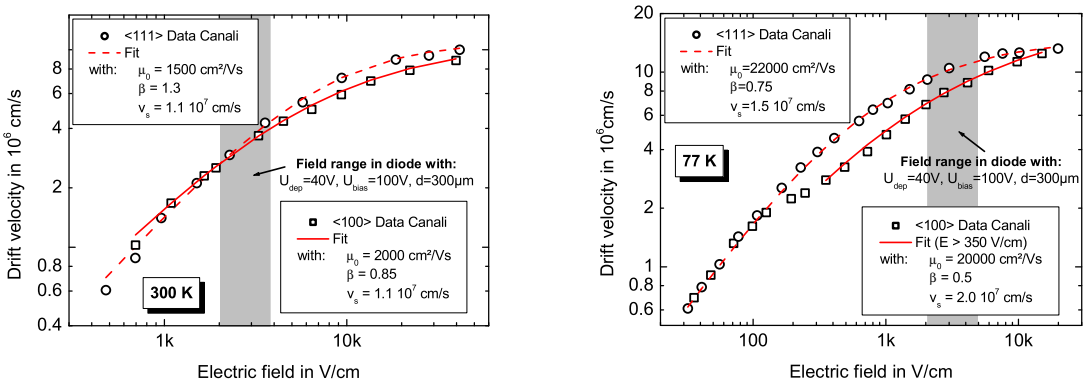

(a) 300 K (b) 77 K

Figure 5.6: Digitised drift velocities for $\langle 111 \rangle$ and $\langle 100 \rangle$ direction from [CJN+75]. The data are parameterised by (1.14). The difference between the two directions is pronounced at low temperatures.

5.4 Drift Mobility

The drift mobility dominates the Lorentz shift in silicon. This parameter was carefully investigated, e.g. in [CJN+75]. The drift velocity was measured for a wide electric field range (see Figure 5.6). These data can be parameterised by equation (1.14):

$$v_{dr} = \frac{\mu_0 E}{\left(1 + \left(\frac{\mu_0 E}{v_s}\right)^{\beta}\right)^{\frac{1}{\beta}}}$$

The results are given in the plots above.
The electric field dependance was only given for three temperatures in [CJN+75]. Thus the TCT-setup was used to measure the drift velocity in the temperature range of the Lorentz shift measurements.

5.4.1 Measurements of the Drift Mobility

Considering a pad sensor above full depletion one can measure the drift time between the rising and falling edge of the TCT-signal. In Figure 5.7 you see an example with arrows approximately indicating the drift time. At higher temperatures the falling edge is broad in comparison with the rising edge. This leads to an uncertainty where to set the end point of the drift. A simulation of the TCT-signal with ISE T-CAD is shown in Figure 5.7. There the maximum electron current has its maximum at the turning point of the total current. This is the time when the barycentre of the electron cloud reaches the contact and thus represents the mean drift time of the generated charge carriers. During data-analysis the falling edge of the signal is fitted by the formula

$$f(t) = \frac{A \exp(-(t - t_0)/\tau_1) - B}{1 + \exp(-(t - t_0)/\tau_2)} + B \tag{5.5}$$

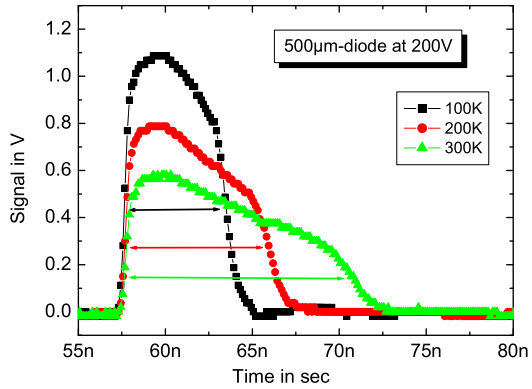

(a) TCT-signals of a 500μm-diode at a bias voltage of 200 V for three different temperatures. The arrows indicate the different drift times.

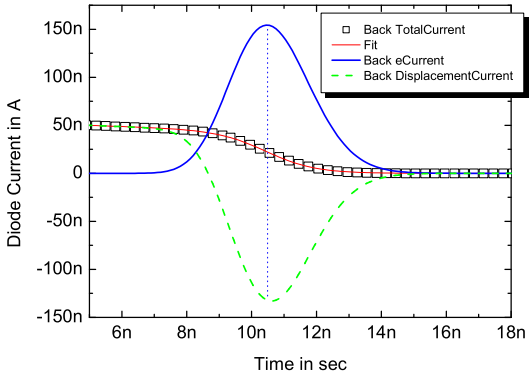

(b) Simulated current response of a diode simulated with ISE T-CAD. The maximum of the electron current represents the mean drift time of the electrons. The fit is done with (5.5).

Figure 5.7: The simulation indicates that the turning point of the falling edge of the TCT-signal corresponds to the arrival of the centre of the charge cloud.

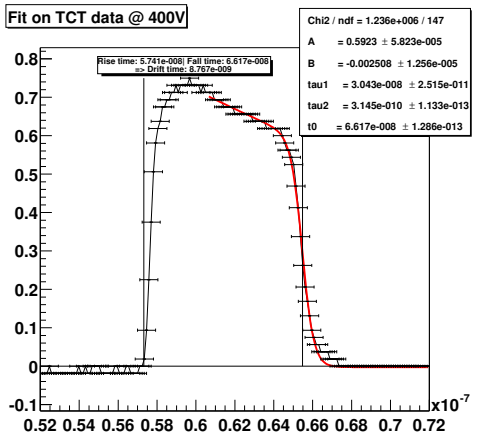

(a) The falling edge of the TCT-signal is fitted by formula (5.5). The straight vertical lines indicate the start and end point of the drift.

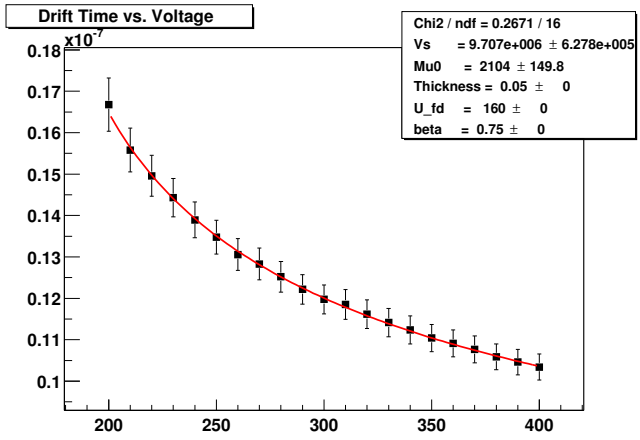

(b) The extracted drift times are fitted by (4.6) using the full parametrisation of the drift velocity (1.14).

Figure 5.8: Extraction of the drift time and fit of the mobility and saturation drift velocity

Temperature in K	μ_0 in cm^2/Vs	$\Delta\mu_0$ in cm^2/Vs	v_s in $10^7\,cm/s$	Δv_s in $10^7\,cm/s$
80	17850	5023	1.27	0.828
103	13330	3076	1.275	0.854
151	8682	1323	1.23	0.738
200	6173	866	1.14	0.753
250	3707	495	1.15	1.000
296	2104	150	0.971	0.628

Table 5.2: Extracted drift parameters for $\beta = 0.75$

Such a fit is shown in Figure 5.8(a). The time of the inflection point is parameter t_0 and τ_2 should serve as a hint for the error.
The extracted drift times are plotted over the bias voltage in Figure 5.8(b). These values can be fitted using (4.6) and the full parametrisation of the drift velocity (1.14).
In such a way a large temperature range from $80\,K$ up to room-temperature was covered. The results are presented in Table 5.2. The low field mobility μ_0 might differ slightly from values found in literature. Especially at room-temperature, the mobility is found to be $\mu_0(T = 293\,K) \approx 1600$. This problem is related to the strong correlation of the parameters in the formula for the drift velocity. For another β the values are changed, but all combinations result in the same drift velocity as it was measured. Therefore, the parameters can be used only together with the formula they were extracted by. This was done in the calculation presented in Section 5.6.1.

5.5 Calculation of the Hall Factor

The Hall factor is important applying formula (5.2) to calculate the Lorentz shift. It takes into account that the drift is not parallel to the applied electric field. The Hall scattering factor was calculated after

$$r_H = \left\langle \frac{\tau^2}{1+(e/m^*\tau B)^2} \right\rangle \Big/ \left\langle \frac{\tau}{1+(e/m^*\tau B)^2} \right\rangle^2 \tag{5.6}$$

using the formulas for the different scattering times in (1.18) - (1.20) with the values summarised in Table 5.3.

Acoustic phonons	Ionised Impurities	Inter-valley
$\rho = 2329\,kg/m^3$	$\alpha = 0.5\,eV^{-1}$	
$\mathcal{E}_1 = 9\,eV$	$\varepsilon_r = 11.7$	$T_{iv} = 700\,K$
$u_l = 9037\,m/s$	$n = 10^{10}\,m^{-3}$	$D = 16 \cdot 10^{10}\,eV/m$
$m_D^* = 0.3216 \cdot m_e$	$N_m = 10^{10}\,m^{-3}$	
	$N_M = 6.5 \cdot 10^{17}\,m^{-3}$	

Table 5.3: Values used for the calculation of the Hall factor

The formulas are repeated here:

Acoustic phonon scattering

$$\tau_L = \frac{\hbar\rho u_l^2}{2\pi k_B T N(E)\mathcal{E}_1^2} \overset{(1.3)}{=} \frac{\pi\hbar^4\rho u_l^2}{(2m_D^*)^{\frac{3}{2}}\mathcal{E}_1^2}\frac{E^{-\frac{1}{2}}}{k_B T} = \tau_0 \frac{1}{k_B T\sqrt{E}} \tag{1.18}$$

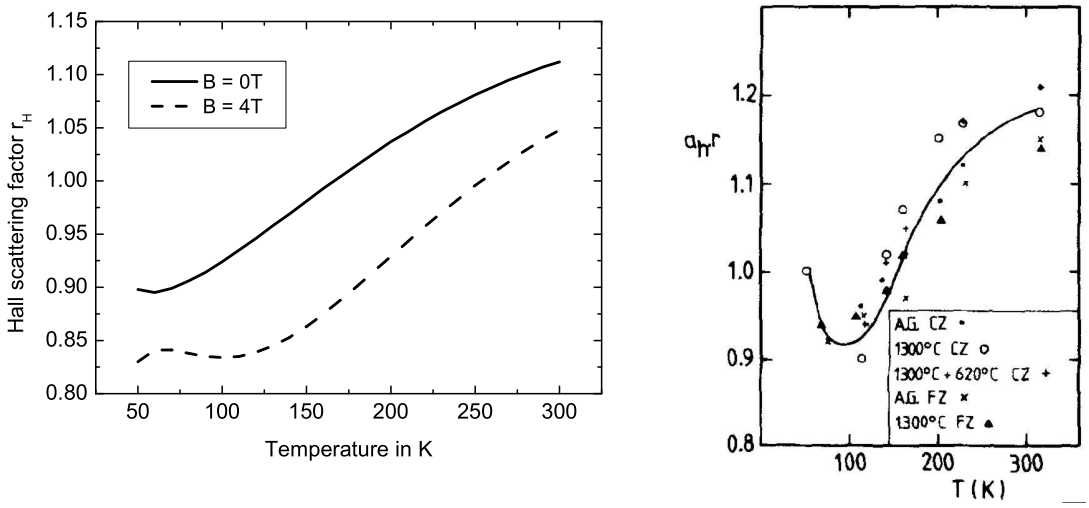

(a) Calculated Hall factor

(b) Data from [RGB81]

Figure 5.9: Calculated Hall factor including the anisotropy factor $a = 0.87$. The scattering times (1.18) - (1.20) are used with the values in Table 5.3 to calculate the Hall scattering factor according to (5.4). This calculation is very similar to the measurements from [RGB81] for czochralsci (CZ) and float zone (FZ) material and different heat treatments.

Scattering by Ionised impurities

$$\tau_i = \frac{\sqrt{2m_D^*}\varepsilon^2}{\pi q_{el}^4 N_I} \frac{E^{\frac{3}{2}}}{F(b)} \tag{1.19}$$

Inter-valley scattering

$$\tau_{iv} = \frac{1}{\alpha_{\pm}(n_{iv} + \frac{1}{2} \pm \frac{1}{2})} \tag{1.20}$$

The results for $B = 0\,T$ and $B = 4\,T$ are plotted in Figure 5.9(a) including the anisotropy factor $a = 0.87$. These values are comparable with the measurements in Figure 5.9(b) from [RGB81]. Considering the high magnetic induction decreases the Hall factor by about 5%.
In general, the Hall factor is $r_H \approx 1 \pm 0.1$ and only affects the Lorentz shift in a 10% range.

5.6 Modelling of the Lorentz shift

In this section two approaches to model the measured temperature dependance of the Lorentz shift are reported.

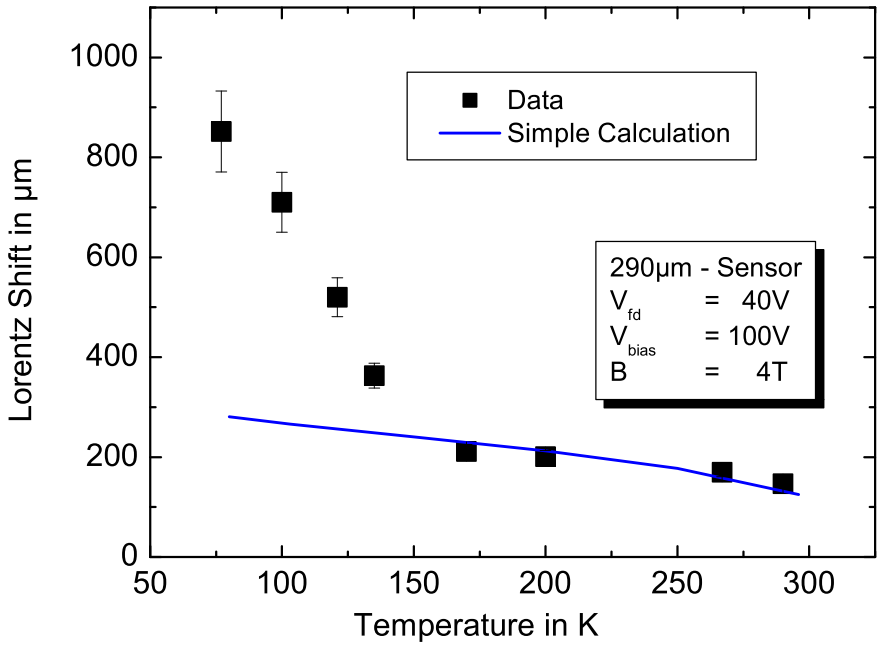

Figure 5.10: Measured Lorentz shift with the simple model described in the text

5.6.1 Simple Calculation of the Lorentz Shift

In this model the simple formula (5.2) was used to calculate the shift for small steps through the sensor:

$$\Delta_L = \sum_n r_H \cdot \mu(T,E) \cdot B \cdot D/n \qquad \text{with} \quad \mu(T,E) = \frac{\mu_0}{\left(1 + \left(\frac{\mu_0 E}{v_s}\right)^{\beta}\right)^{1/\beta}} \tag{5.7}$$

where D is the thickness of the sensor and n is the number of steps. The electric field was parameterised as

$$E(x) = \frac{2V_{fd}}{D}\left(1 - \frac{x}{D}\right) + \frac{V_{bias} - V_{fd}}{D} \tag{5.8}$$

The low field mobility μ_0, the saturation velocity v_s and β are taken from Table 5.2.
Using the calculated Hall factor one can derive the temperature dependance of the Lorentz shift shown in Figure 5.10. The model is in good agreement with the data at high temperatures but breaks down at low temperatures. It can not model the large Lorentz shift at cryogenic temperatures. Therefore a more microscopic method had to be applied.

5.6.2 Considering Random Scattering and Anisotropy

Implementation

This model considers the anisotropic energy surface of silicon (see Figure 1.4(b) on page 8 and a random scattering of the electrons using again the formulas (1.18) - (1.20).

Valley	m_x	m_y	m_z
[100]	$m_\parallel$	$m_\perp$	$m_\perp$
[010]	$m_\perp$	$m_\parallel$	$m_\perp$
[001]	$m_\perp$	$m_\perp$	$m_\parallel$

Table 5.4: Effective masses for the different valleys with electric field along the y-direction ([010])

The Lorentz force of an electric field in y-direction and a magnetic induction with components in x- and z-direction is applied to one electron, which results in a change of the wave-vector:

$$dk_x = -q_{el} \cdot v_y \cdot B_z/\hbar \cdot dt \tag{5.9}$$

$$dk_y = q_{el}(E_y + v_x \cdot B_z - v_z \cdot B_x)/\hbar \cdot dt \tag{5.10}$$

$$dk_z = q_{el} \cdot v_y \cdot B_x/\hbar \cdot dt \tag{5.11}$$

Remember that the constant energy surfaces of the six equivalent minima of the conduction band are ellipsoids, i.e. the effective mass depends on the drift direction. The drift velocity can be calculated via:

$$v_i = \hbar \cdot k_i/m_i \qquad \text{with} \quad i = x, y, z \tag{5.12}$$

The different effective masses for the different valleys are listed in Table 5.4. The acceleration of the particle is done until the next scattering event occurs, which stops it. During each time step ($\Delta t = 1\, fs$) the scattering time is calculated adding the different scattering processes:

$$\frac{1}{\tau(E,T)} = \frac{1}{\tau_L(E,T)} + \frac{1}{\tau_i(E,T)} + \frac{1}{\tau_{iv}(E,T)} \tag{5.13}$$

where T is the temperature and the energy is calculated as

$$E = \frac{\hbar^2}{2}\left(\frac{k_x^2}{m_x} + \frac{k_y^2}{m_y} + \frac{k_z^2}{m_z}\right) + \frac{3}{2}k_B T \tag{5.14}$$

According to [Mog87] (see Appendix F on page 135) the time of free flight t_f is determined by

$$\int_0^{t_f} \tau(t)^{-1} \exp\left[-\int_0^t \tau(t')^{-1}\, dt'\right] dt = r \tag{5.15}$$

where r is a flat random number between 0 and 1. This results in an exponential decaying probability distribution as shown in Figure 5.11. There is a probability of about 12% to get a time of free flight twice as large as the calculated scattering time. This is important for the explanation of the large Lorentz shift at low temperatures.
When a scattering event occurs another flat random number r' decides if it was an inter-valley scattering:

$$\frac{1}{\tau} \cdot r' > \frac{1}{\tau_L(E,T)} + \frac{1}{\tau_i(E,T)} \tag{5.16}$$

If so, the electron is scattered in the next valley, which is turned by 90°. The new set of effective masses is applied and the drift continues.
The sensor, which is investigated by the simulation and in the measurement, is $290\,\mu m$ thick with a full depletion voltage of $40\,V$. For the simulation the simple diode-type electric field from (5.8) was used and the bias voltage was set to $100\,V$.
The described procedure was tested without magnetic field to compare with available data.

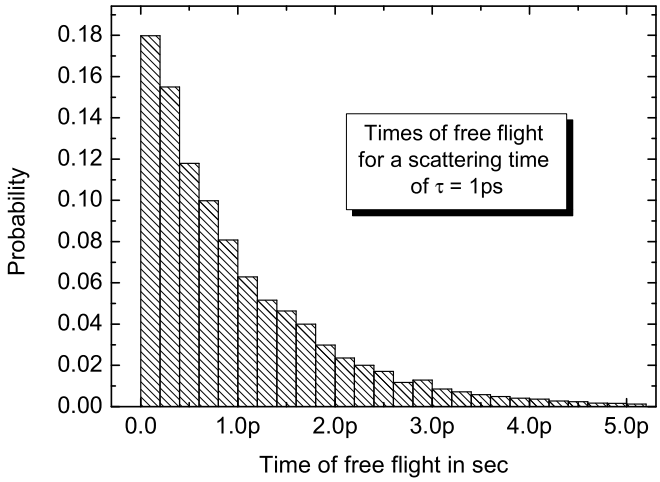

Figure 5.11: Probability distribution for the time of free flight as calculated by formula (5.15) for a scattering time of $\tau = 1 \cdot 10^{-12}\ s$. There is a finite probability to have a time of free flight larger than τ, which is important for the explanation of the large Lorentz shift at low temperatures.

Drift without magnetic field

The mean scattering time of the three processes was considered to calculate the low field mobility. The results are plotted in Figure 5.12(a) together with data extracted from [CJN$^+$75]. The calculation is in good agreement with the data at high temperatures. At low temperatures the

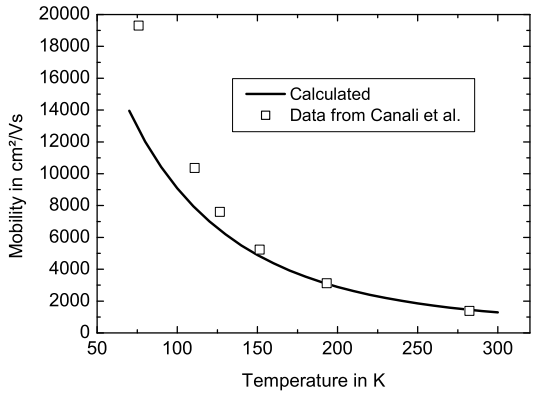

(a) Calculated low field mobility

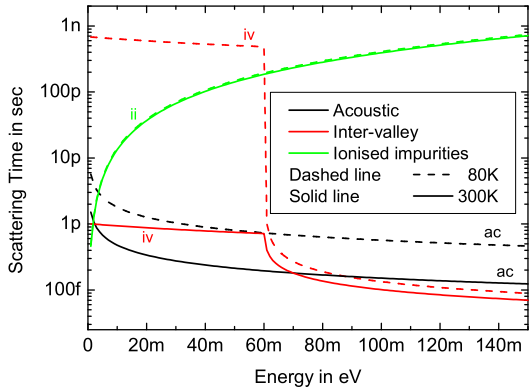

(b) Calculated scattering times

Figure 5.12: The low field mobility was calculated averaging the scattering times (1.18) - (1.20) like in the calculation of the Hall scattering factor. The data is compared with measurements from [CJN$^+$75]. There is a good agreement down to about 150 K. At low temperatures the mobility was calculated to be lower than the data. This is an advantage for the verification of the new method, since a high mobility would automatically result in a larger Lorentz shift. The used scattering times are presented on the right for 100 K and 300 K. The step in the inter-valley scattering reflects the opening of the phonon emission channel when the electron energy exceeds the chosen phonon energy of 700 $K \simeq 60\ meV$.

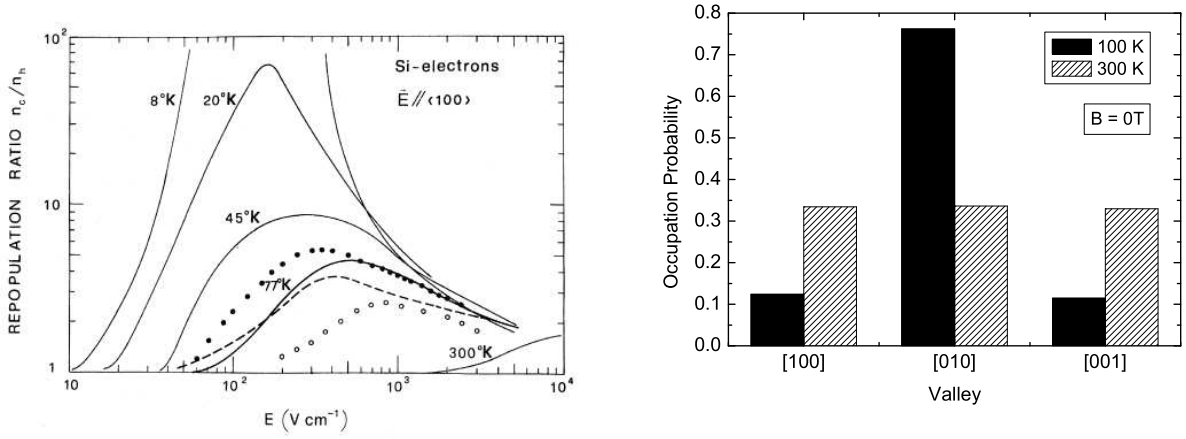

(a) Repopulation ratio from [CJN+75]

(b) Simulated occupation probability

Figure 5.13: The repopulation of the electrons from the hot to the cold valleys is more pronounced at low temperatures. This could be reproduced with the proposed simulation.

calculation results in a smaller mobility.
The drift through the sensor took 7.9 ns at 300 K and 4.1 ns at 100 K.
If only a spherical constant energy surface is considered with $m_{eff} = m_c$ the drift takes 7.8 ns at 300 K and 2.6 ns at 100 K, which reflects a higher drift velocity at low temperatures. At first glance, this should also result in a larger Lorentz shift. But as we will see in the next section, this is not the case.
To check if the inter-valley scattering works properly, the occupation probability of the three valleys was investigated.
In [CJN+75] the repopulation ratio between hot and cold valleys was measured and calculated (see Figure 5.13(a)). The hot valley has its short axis of the constant energy surface along the direction of the electric field, i.e. a small effective mass applies to the drift. Thus the energy of the electron for a given wave-vector is higher than in the cold valleys (large effective mass along drift direction) and inter-valley scattering is more likely.
The result of the simulation is shown in Figure 5.13(b). The occupation probability is an average over the whole drift. It is obvious that there is a repopulation at low temperatures of $n_c/n_h = 3.2$, which is not present at room-temperature. This reduces the average drift velocity.
Even though the simulation does not exactly fit measured data, it qualitatively follows the expectations.

Lorentz shift in magnetic field

Switching on the magnetic field the electrons start drifting in cycloids. Without any scattering they would fly perpendicular to the electric and the magnetic field and never reach the other side of the sensor. Electrons in different valleys show a different shape of the cycloid due to the different effective masses. The scattering processes interrupt the flight and a new cycloid begins. For a constant time of free flight this would result in different drift directions for different valleys. This is still true using the random algorithm described above as can be seen in Figure 5.14(a)). There is a clear change in the drift direction of the electron after the scattering from the [010]-

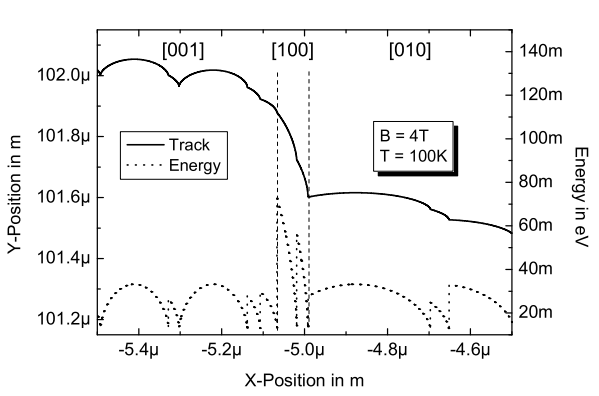

(a) Part of the track of an electron at 100 K and 4 T

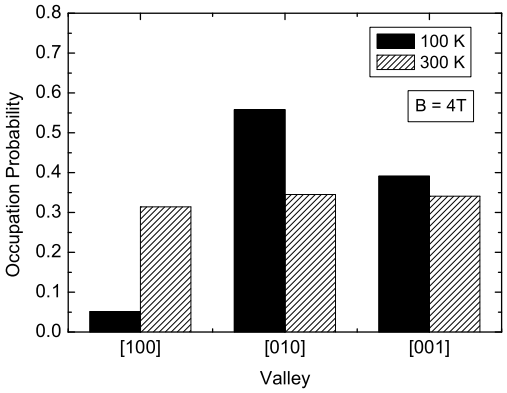

(b) Occupation probability with applied magnetic field of 4 T

Figure 5.14: In the [100]*-valley the drift velocity in X-direction is reduced by the large effective mass ($m_x = m_\perp = 0.9m_e$) and the particle continues accelerating in Y-direction. This rapidly increases energy and the probability of inter-valley scattering, which is assigned to a change of the valley. This results in a repopulation of the valleys.*

valley to the [100]-valley. There the drift velocity in X-direction is reduced by the large effective mass ($m_x = m_\perp = 0.9m_e$) and the particle continues accelerating in Y-direction. In the other valleys v_x becomes large enough so that the associated Lorentz force in negative Y-direction exceeds the electric field force and reduces the velocity in Y-direction. Thus the Lorentz shift in X-direction is increased in these valleys.
In the [010]-valley the energy rises rapidly and so does the probability for inter-valley scattering, which leads to a change of the valley. This reduces the occupation probability of the [010]-valley as calculated in Figure 5.14(b).
Another crucial point is the implementation of random scattering. The time of free flight can therefore exceed the mean scattering time. At low temperatures this leads to a finite probability to complete full cycloids, which results in a motion perpendicular to the electric field and no effective drift in field direction. One of these events happened during the drift in the [001]-valley in Figure 5.14(a). This can not be compensated by very short times of free flight, since also the drift velocity in field direction is small.
Using the mobility and expression (5.7) to calculate the Lorentz shift one considers average scattering times, which indeed satisfy the condition $\omega_c\langle\tau\rangle \ll 1$ even for low temperature. But the condition should be fulfilled for individual scattering events ($\omega_c\tau \ll 1$), which is not the case at low temperatures. The more microscopic model described in this section accounts for the possibility of complete cycloids and therefore is in better agreement with the measured data. The calculated Lorentz shift is plotted in Figure 5.15. There are two simulations for different orientations of the magnetic field with respect to the crystal orientation in the wafer plane, which is not known. For an applied magnetic field in [101]-direction the [100]- and [001]-valleys become equivalent, which results in a more equal distribution of the occupation probabilities of the three valleys, but only slightly reduces the Lorentz shift in comparison with a magnetic field in [001]-direction.

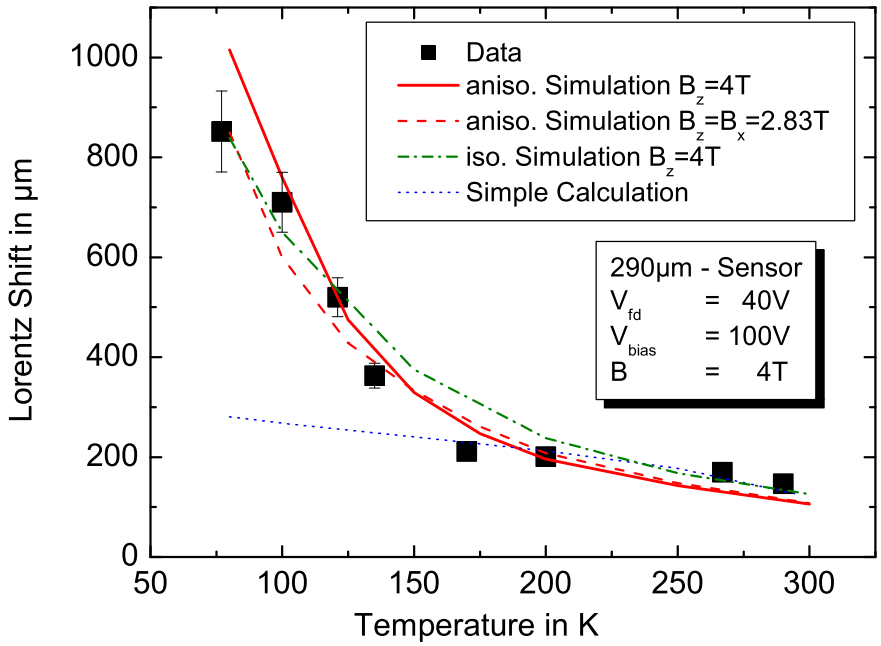

Figure 5.15: All 'simulations' consider the random scattering of the electron and already the isotropic simulation, which assumes a constant effective mass, describes the data quite well. The anisotropic simulations, in addition, consider the different effective masses and the rotated orientation of the constant energy surfaces of the different valleys.

Considering only a spherical constant energy surface ($m_{eff} = 0.26 m_e$ for all valleys) results in a similar Lorentz shift, which supports the statement that random scattering and a finite probability of long free flights is the main effect causing the high Lorentz shift at low temperatures. But the saturation of the drift velocity without magnetic field is not well described neglecting anisotropy, as was shown in Section 5.6.2.

5.7 Conclusion

The measurements of the Lorentz shift for electrons show a steep increase at low temperatures. This has to be taken into account in tracking systems using silicon sensors at low temperatures and high magnetic fields. The simple relation for the Lorentz angle $\tan\Theta_L = \mu_H B$ is derived under the condition $\omega_c \tau \ll 1$, which is not always fulfilled for the drift at temperature below about 150 K. Thus another approach was chosen, which considers the microscopic flight and random scattering events of an electrons. Considering inter-valley scattering results in the repopulation of the different valleys and thus accounts for the saturation of the drift velocity in high fields.
The implementation is based on classical assumptions without considering statistics in the valleys and using simple parameterisations for the scattering times. A more sophisticated approach would improve the results.
For holes the Lorentz shift can still be calculated with the standard formula, since the mobility

and the mean time of free flight is smaller than for electrons.

Chapter 6

Summary

The production of the CMS silicon strip tracker requires a detailed quality assurance. There are 24328 silicon sensors with a total active area of 206 m^2. They have to be operated for ten years in an experiment where access possibilities are limited. During that time the sensors are exposed to a harsh radiation environment, which requires tests on the radiation hardness of the delivered sensors.
The main part of this thesis covers the Irradiation Qualification of CMS silicon strip sensors with protons. The infrastructure for the irradiation tests was developed at the compact cyclotron at the Forschungszentrum Karlsruhe.
The 320μm (500μm) thick sensors are expected to receive equivalent fluences of $1.6{\cdot}10^{14} n_{1MeV}/cm^2$ ($0.35 \cdot 10^{14}\, n_{1MeV}/cm^2$). For the irradiation tests these fluences are multiplied with 1.5 for safety, since the simulation of the radiation environment contains some uncertainties.
The measured full depletion voltages on mini-sensors were used to adjust the parameters of the 'Hamburg'-model. Several scenarios of the annealing during 10 years of operation could be calculated with the resulting parametrisation. Two weeks of annealing at 20°C each year results in maximum full depletion voltages for the thin sensors of about 400 V after an exposure to $1.6 \cdot 10^{14}\, n_{1MeV}/cm^2$.
The leakage current of large sensors was measured to reach about 1.7 mA. This causes a power dissipation of 850 mW at 500 V and $-10°C$.
A big difference was observed in the inter-strip capacitance of thin and thick mini-sensors. The thin sensors show an immediate saturation of the capacitance with increasing bias voltage after irradiation, whereas a continuous decrease was measured for the thick material. In addition, a correlation of the initial flat-band voltage, which is an indication for the oxide quality, and the increase of the inter-strip capacitance after irradiation was observed. The measurements led to an acceptance limit for the flat-band voltage of $< 10\, V$. Despite these observations, all sensors passed the limit of 1.3 pF/cm at 400 V.
There were hardly any changes of the coupling capacitance. The bias resistance of the thin/thick sensors increased by about 20%/10% due to the change of the n-doping concentration of the polysilicon, which was still consistent with the upper limit of 2.0 $M\Omega$.
Even biasing and bonding did not promote development of pinholes!
Some of these test-structures were further investigated according to the depletion behaviour. The CV-curves of mini-sensors and diodes were compared. Before irradiation the full depletion voltage of the mini-sensor is higher than the corresponding diode due to the different electric field configuration. After type inversion of the n-doped silicon bulk the depletion starts at the

unstructured back electrode and full depletion, as extracted from the CV-curve, is close to that of the diode.
The type inversion was visualised by means of the Transient Current Technique, which also revealed the different field configurations of diode and mini-sensor.
A minimum ionising particle was simulated using an infra-red laser. This enables a measurement of the charge collection of the sensors. After irradiation the charge collection is reduced due to trapping effects, but increases with applied bias voltage. Thus one has to operate the irradiated sensors at voltages as high as possible.
The charge collection efficiency will drop rapidly when silicon sensors are exposed to very high fluences. This problem can be cured operating the sensors at cryogenic temperatures (Lazarus effect at $\sim 130\,K$). Now tracking systems use high magnetic fields ($\sim 4\,T$) for good momentum resolution. At such conditions, low temperature and high magnetic field, measurements have shown a huge Lorentz shift of electrons up to 850 mum for a 290 μm-sensor with a full depletion voltage of $40\,V$ and biased at $100\,V$. This could not be calculated using the usual formula $\tan\Theta_L = \mu_H B$. But it was possible to explain the huge Lorentz shift with a simulation considering random scattering processes (acoustic phonons, ionised impurities and inter-valley scattering) and the anisotropic effective mass of an electron drifting through the sensor exposed to the electric and magnetic fields. The random distribution of the time of free flight allows the electron to complete full cycloids, which results only in a motion perpendicular to the electric field and therefore increases the Lorentz shift. The repopulation of the different valleys in the conduction band due to inter-valley scattering reduces the average drift velocity in electric field direction. In addition the drift perpendicular to the electric field is enhanced, which again increases the Lorentz shift. So both features together explain the measured behaviour.
This large Lorentz shift has to be taken into account in the track reconstruction and can be calculated by this approach.

Appendix A

Symbols and Constants

A.1 Physical Constants

Symbol	Value	Unit	Meaning
ε_0	$8.854 \cdot 10^{-14}$	F/cm	Permittivity in vacuum
$\hbar$	$4.1357 \cdot 10^{-15}/2\pi$	eVs	Reduced Planck constant
k_B	$8.6174 \cdot 10^{-5}$	eV/K	Boltzmann constant
m_0	$9.11 \cdot 10^{-31}$	kg	Electron rest mass
q_{el}	$1.6022 \cdot 10^{-19}$	C	Elementary electronic charge

A.2 Properties of Silicon

Symbol	Value	Unit	Meaning
ε_s	11.7	1	Relative permittivity in silicon
ε_{ox}	3.9	1	Relative permittivity in silicon oxide
ρ	2.33	g/cm^3	Density
$\mathcal{E}_1$	9	eV	Deformation potential
m_D^*	$0.32\, m_0$	kg	Density-of-states effective mass
m_c	$0.26\, m_0$	kg	Conduction effective mass
$m_\perp$	$0.19\, m_0$	kg	Effective electron mass perpendicular to symmetry axis
$m_\parallel$	$0.92\, m_0$	kg	Effective electron mass along the symmetry axis
u_l	9037	m/s	Velocity of sound

A.3 List of Frequently Used Symbols

Symbol	Meaning
α	Current related damage rate
β	Transition coefficient for electric field dependence
$\vec{B}$	Magnetic induction
C_c	Coupling capacitance
C_{int}	Inter-strip capacitance
D	Thickness of diode or sensor
$D_{n,p}$	Diffusion coefficient
E	Energy
E_F	Fermi energy
E_C, E_V	Energy level of conduction and valence band edge
E_g	Band gap energy
E_i	Intrinsic Fermi level
$\vec{E}$	Electric field
F	Irradiation fluence
$\mathcal{F}(E)$	Fermi function
I_{leak}	Leakage current
$\vec{k}$	Wave vector
μ_0	Low field mobiliy
$N(E)$	Density of states
N_C, N_V	Density of states at conduction and valence band edge
n, p	Density of free electrons and holes
N_D, N_A	Donor and acceptor concentrations
N_{eff}	Effective doping concentration
n_i	Intrinsic carrier concentration
r_H	Hall Factor
R_{int}	Inter-strip resistance
R_{bias}	Bias resistance
T	Temperature
τ	Scattering time
v_{dr}	Drift velocity
v_s	Saturation velocity
V_{bias}	Applied bias voltage
V_{fd}	Full depletion voltage
V_{FB}	Flat-band voltage
W	Width of the space charge region

Appendix B

Sensor Geometries of the CMS Strip Tracker

B.1 Geometries of inner and outer barrel sensors

Type	Length in mm	Height in mm	Volume in cm^3	Pitch in μm	Strips	Multipl.
IB1	61.5	116.9	2.30	80	768	1536
IB2	61.5	116.9	2.30	120	512	1188
OB1	93.9	91.6	4.30	122	768	3360
OB2	93.9	91.6	4.30	183	512	7056

Inner barrel sensors are thin ($320\mu m$) and outer barrel sensors thick ($500\mu m$). All distances are active values.

B.2 Geometries of wedge shaped sensors

Type	L1 in mm	L2 in mm	Height in mm	Volume in cm^3	Pitch in μm	Thickn. in μm	Strips	Multi-plicity
W1 TEC	63.1	85.8	85.2	2.03	81-112	320	768	288
W1 TID	62.1	91.7	110.9	2.73	80.5-119	320	768	288
W2	86.6	110.1	88.2	2.78	113-143	320	768	864
W3	63.3	81.1	110.7	2.55	123-158	320	512	880
W4	58.1	71.3	115.2	2.39	113-139	320	512	1008
W5a	96.5	109.5	81.2	4.19	126-142	500	768	1440
W5b	110.0	120.1	63.2	3.64	143-156	500	768	1440
W6a	83.6	94.6	96.1	4.28	163-185	500	512	1008
W6b	94.5	104.7	84.9	4.23	185-205	500	512	1008
W7a	71.5	80.1	106.9	4.05	140-156	500	512	1440
W7b	80.4	88.0	94.9	4.00	156-172	500	512	1440

W1, W2 and W5 will be assembled in double sided modules, the other geometries in single-sided

modules. All distances are active values.

B.3 Encoding of the sensor number

The coding of the sensor number is explained on the following example:

30	**2**	**2**	**01**	**2**	**34**	**567**	**89**
Experiment	Subdetector	Supplier	Geometry	Year	Week	Batch	Sensor

The experiment number is 30 for CMS.
The Tracker has the subdetector number 2.
The supplier code is 1 for STM and 2 for HPK.
The geometries have the numbers:

1 = IB1	2 = IB2	2 = OB1	4 = OB2	5 = W1 TEC
6 = W2	7 = W3	8 = W4	9 = W5a	10 = W5b
11 = W6a	12 = W6b	13 = W7a	14 = W7b	15 = W1 TID

The year is the last digit of of the four-digit representation ($2003 \equiv 3$).
Both year and week represent the production date.

Appendix C

Example of the XML-file for the CMS Tracker Database

```
<?xml version="1.0" encoding="UTF-8"?>
<DBFile xmlns:xsi="http://www.w3.org/2001/XMLSchema-instance"
    xsi:noNamespaceSchemaLocation="calibration.xsd">
<unit><object id="30220722000104"/>
<composite>
<action_description input_id="235" name="IQCSEN"
    object_name="SEN" version="1"/>
<action>
<action_description input_id="233" name="IQCMini"
    object_name="SEN" version="1"/>
<input name="start_in_V" value="10"/>
<input name="stop_in_V" value="550"/>
<input name="delay_time_in_seconds" value="1"/>
<input name="Vstrip_before_in_V" value="400"/>
<input name="Vstrip_after_in_V" value="0"/>
<input name="V_Itot_in_V" value="450"/>
<input name="C_int_frequency_in_kHz" value="1000"/>
<input name="C_ac_frequency_in_Hz" value="100"/>
<result name="Test_center" value="KARLSRUHE-IEKP"/>
<result name="Irradiation_date" value="2002-09-11 13:30:00"/>
<result name="Duration_minutes" value="142.18"/>
<result name="Temp_start_after_irrad" value="20.24"/>
<result name="Humidity_start_after_irrad" value="4.89"/>
<result name="Temp_end_after_irrad" value="20.61"/>
<result name="Humidity_end_after_irrad" value="1.66"/>
<result name="Tool_id" value="70"/>
<result name="Tcomment" value="no_comment"/>
<result name="Operator" value="Cedric_Menge"/>
<result name="Tdate" value="2002-11-08 14:28:16"/>
<result name="Status" value="reference"/>
<result name="IQCMINI_val" value="0"/>
```

```
<result name="I_tot_V_Itot_before_irrad_nA" value="22.82"/>
<result name="I_tot_V_Itot_after_irrad_nA" value="66713.00"/>
<result name="I_tot_V_Itot_delta_nA" value="66690.18"/>
<result name="V_depl_before_irrad_V" value="175.81"/>
<result name="V_depl_after_irrad_V" value="285.14"/>
<result name="V_depl_delta_V" value="109.33"/>
<result name="V_break_before_irrad_V" value="552.00"/>
<result name="V_break_after_irrad_V" value="552.00"/>
<result name="C_TOT_before_irrad_pF" value="151.15"/>
<result name="C_TOT_after_irrad_pF" value="209.17"/>
<result name="C_TOT_delta_pF" value="58.02"/>
<result name="Rpoly_Vstrip_before_irrad_MOhm" value=" 1.65 1.66 ... 1.66 1.67"/>
<result name="Rpoly_Vstrip_after_irrad_MOhm" value=" 1.98 1.99 ... 1.98 1.99"/>
<result name="Rpoly_mean_delta_Vstrip_MOhm" value="0.32"/>
<result name="I_strip_Vstrip_before_irrad_nA" value=" 0.37 0.37 ... 0.35 0.34"/>
<result name="I_strip_Vstrip_after_irrad_nA"
    value=" 418.98 367.39 ... 280.28 277.16"/>
<result name="I_strip_mean_delta_Vstrip_nA" value="309.14"/>
<result name="C_ac_Vstrip_before_irrad_pF" value=" 68.32 68.28 ... 68.07 68.05"/>
<result name="C_ac_Vstrip_after_irrad_pF" value=" 67.39 67.52 ... 67.36 67.35"/>
<result name="C_ac_mean_delta_Vstrip_pF" value="0.78"/>
<result name="C_int_Vstrip_before_irrad_pF" value=" 0.77 0.81 ... 0.82 0.82"/>
<result name="C_int_Vstrip_after_irrad_pF" value=" 0.56 0.60 ... 0.61 0.60"/>
<result name="C_int_mean_delta_Vstrip_pF" value="0.21"/>
<result name="R_int_Vstrip_before_irrad_pF" value=" 80645.16"/>
<result name="R_int_Vstrip_after_irrad_pF"
    value=" 1156.07 778.21 ... 406.50 434.78"/>
<result name="T_for_alpha_degC" value="-9.67"/>
<result name="alpha_T_atto_Amp_per_cm" value="2.44"/>
<result name="alpha_20C_atto_Amp_per_cm" value="75.76"/>
<result name="p_k_factor" value="1.85"/>
<result name="p_fluence_e14_1MeV_Neq" value="2.32"/>
<result name="p_energy_MeV" value="26.00"/>
<result name="Voltage_V" value="10.00 20.00 ... 540.00 550.00"/>
<result name="I_tot_nA" value="16396.30 23123.00 ... 66704.00 66713.00"/>
<result name="C_tot_pF" value="743.72 637.98 ... 198.74 198.41"/>
<result name="Rpoly_MOhm" value="1.60 1.70 ... 1.91 1.89"/>
<result name="C_int_1MHz_pF" value="0.61 0.61 ... 0.62 0.62"/>
<result name="I_strip_nA" value="245.74 339.01 ... 929.17 934.38"/>
<result name="R_int_MOhm" value="70.06 122.25 ... 377.83 571.43"/>
</action>
</composite>
</unit>
</DBFile>
```

Appendix D

Finite-Element-Simulations with ISE T-CAD

In this work the software package ISE[(1)] T-CAD Release 6.1 was used for semiconductor device simulations. It is installed on a Sun-workstation (UltraSPARC I) running Solaris 7.
For device simulation the program *DESSIS* was used, which is a "multi-dimensional electrothermal mixed-mode device and circuit simulator for one, two and three-dimensional semiconductor devices". Two-dimensional devices can be created with a graphical user interface called *MDRAW*, which also generates the mesh. Output curves can be displayed and analysed using *INSPECT* and complete finite-element devices can be observed by *PICASSO*[(2)].

D.1 MDRAW

With the program MDRAW one can define the geometry of the device, the materials, the doping and refinements of the mesh. In Figure D.1(a) you can see the boundaries of a part (three strips) of a strip sensor with a thickness of 500 μm and a pitch of 120 μm. Contacts are defined at the implant positions and marked red. These contacts can be accessed in DESSIS.
In the doping section one can define the constant bulk doping and the implants, which are realised as analytical profiles. Additional refinements allow to influence the mesh, which is shown in Figure D.1(b). There you see a zoom out of the p-implant of one strip.
The output files of MDRAW are the grid file (`.grd`) containing the vertices of the grid points and the doping file (`.dat`), which stores the doping concentration at each grid point. The description of the geometry is saved in a boundary file (`.bnd`) and the description of doping and refinements is written to a command file (`.cmd`).

D.2 DESSIS

When the grid and the doping is defined the device simulation can start with DESSIS. In general, it discretises partial differential equations like

$$\nabla \vec{J} + R = 0 \tag{D.1}$$

(1) ISE Integrated Systems Engineering AG, Zurich, Switzerland
(2) Painting Interactively Colored And Shaded Simulation Objects

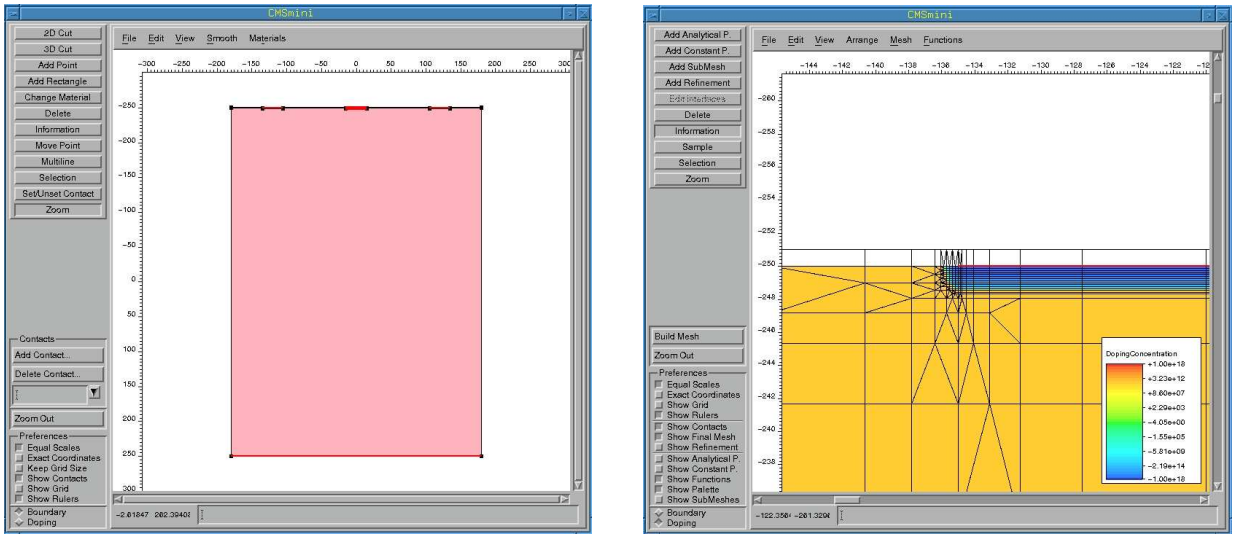

(a) Boundary section (b) Doping section

Figure D.1: Screenshots showing MDRAW in the boundary and doping mode

which can be the Poisson ($J \equiv \varepsilon E$ and $R \equiv -\rho$) or continuity equations ($J \equiv \mu n E$ and $R \equiv R + G + \dot{n}$).
One has to create a command file as input for DESSIS, which may contain the following parts:

D.2.1 Device section

```
Device minisens{
    File {
        Grid =    "CMSmini_ST_mdr.grd"
        Doping =  "CMSmini_ST_mdr.dat"
        Plot = "Traps"
        Current = "Traps"
        Parameters = "mydessis.par"
      }

    Electrode {
        { name="Contact_m"    voltage=0 }
        { name="Contact_l"    voltage=0 }
        { name="Contact_r"    voltage=0 }
        { name="Contact_b"    voltage=0 }
    }
}
```

In the example code above a device is named `minisens` and the previously generated grid and doping files are specified in the `File`-section. All parameters used in the simulation can be written in a parameter file, which can be modified according to the simulation conditions.
In the `Electrode`-section the used contacts, which were specified in MDRAW, are initialised with zero potential. They can also be set floating with a constant charge.

D.2.2 Physics section

```
Physics {
    Temperature = 293
    Recombination (SRH () )
    Mobility (HighFieldSaturation)
    Traps(
            (Acceptor Level EnergyMid=0.456 fromCondBand Conc=17.5e12
                eXsection=5.02e-15 hXsection=5.02e-15)
            (Donor Level EnergyMid=0.357 fromValBand Conc=55e12
                eXsection=2.05e-18 hXsection=2.45e-15)
    )
    OptBeam(    WaveInt = 1e20 WaveLength = 670e-7 SemAbsorption(Silicon)
                WaveTime = (0 50e-9)
                SemWind = ( (-1e-4,-1e-4)(1e-4 1e-4))
                SemSurf = -250e-4 )
}
```

In this section the physics models are activated. In this example the temperature is set to $293\,K$ and Shockley-Read-Hall recombination model is chosen:

$$R^{SRH} = \frac{np - n_{i,eff}^2}{\tau_p(n + n_1) + \tau_n(p + p_1)} \tag{D.2}$$

The minority lifetimes $\tau_{p,n}$ can be adjusted in the parameter file to generate the measured leakage current of the device.
The keyword `Mobility (HighFieldSaturation)` indicates the use of the Canali model, which accounts for the saturation of the drift velocity at high fields:

$$v_{dr} = \frac{\mu_0 E}{\left(1 + \left(\frac{\mu_0 E}{v_s}\right)^{\beta}\right)^{\frac{1}{\beta}}} \tag{D.3}$$

with a temperature dependent β.
Radiation induced traps can be introduced by defining the type (donor, acceptor, neutral electron or hole trap), the energy level, concentration and cross-sections. The formula for recombination through one trap is the same as for Shockley-Read-Hall recombination (D.2) defining $\tau_{p,n} = 1/\sigma_{p,n} v_{p,n}^{th} N_t$.
For transient calculations a laser beam can be defined with the keyword `OptBeam`. In this example a red laser ($670\,nm$) with an intensity of $1 \cdot 10^{20}\ (cm^2 s)^{-1}$ penetrates the device on an area of $2\,\mu m \times 2\,\mu m$ at the surface. The penetration depth is calculated for silicon. The effect of this $50\,ps$-pulse can be simulated specifying a transient calculation in the solve section.
There are many more physics models implemented. The interested reader is referred to the manual.

D.2.3 Plot section

```
Plot{   ElectricField   Potential   eDensity    hDensity
```

```
        eCurrent    hCurrent    eTrappedCharge  hTrappedCharge
        SpaceCharge
}
```

Many physical parameters can be extracted for every grid point of the device. Hence a `.dat`-file is produced including the parameters specified in the `Plot`-command. There are in total approximately 125 parameters to be plotted.

D.2.4 Math section

```
Math {
    Method = Blocked
    SubMethod = ParDiSo
    Iterations = 25
    Derivatives
    Extrapolate
    RelErrControl
}
```

The math section is used to specify defaults for the different solve commands. The `Blocked`-method has to be defined when using the multiple devices, i.e. two or more meshed devices as defined in the device section or one device and a circuit as defined in the system section.

D.2.5 System section

```
System {
    v v1 (1 gnd) {
       type = "dc"
        dc = 0
    }
    v v2 (2 gnd) {
       type = "dc"
        dc = 0
    }
    v v3 (3 gnd) {
       type = "dc"
        dc = 0
    }
    v vb (b gnd) {
       type = "dc"
        dc = 0
    }
    minisens mini(Contact_l=1 Contact_m=2 Contact_r=3 Contact_b=b)
    set (gnd = 0)
}
```

In the system section one can define a electronic circuit including the device. Here only voltage sources with initially zero potential are defined at each contact to prepare for the small signal analysis, which allows to calculate the conductance-capacitances matrix.

```
Solve   {
    poisson
    coupled {poisson electron hole}

    NewCurrentPrefix = "GlobalRamp"
    Quasistationary(InitialStep=0.01 MaxStep=0.02
                    Goal{parameter=vb.dc voltage=350}
                    Plot{Range=(0.0 1.0) Intervals=10})
                { accoupled (   StartFrequency = 1e3
                                EndFrequency   = 1e3
                                NumberOfPoints = 1
                                Node (b 1 2 3)
                                Exclude(vb v1 v2 v3))
                    {Poisson Electron Hole contact circuit}
        }

    NewCurrentPrefix = "TCT"
    Transient(  InitialTime = 0.0   FinalTime = 50.0e-9
                Plot { Range = (0 25.0e-9) Intervals=6 } )
            { Coupled{ Poisson Electron Hole } }
}
```

The solve sections defines the flow of the simulation. Here, the poisson equation is solved for the device first. Then the coupled set of poisson and continuity equations is treated. In a next step initiated by the keyword `Quasistationary` the bias voltage is applied to the back contact and ramped up to $350\,V$. At each step point the conductivity-capacitance matrix is calculated at $1\,kHz$ and on each contact (keyword `accoupled`). The data sets specified in the plot section are stored every $35\,V$.
When the target voltage is reached a transient calculation is performed. This simulates the time evolution after the laser pulse defined in the physics section.
During the whole simulation currents as well as voltages and charges are stored for each contact and each calculation step. These data files (`.plt`) can be visualised by INSPECT.

D.3 INSPECT and PICASSO

These two programs are used to analyse the data. INSPECT is used for 1-d data files like the current files and PICASSO visualises the multi-dimensional data defined in the plot section. Screenshots are shown in Figure D.2 and D.3.

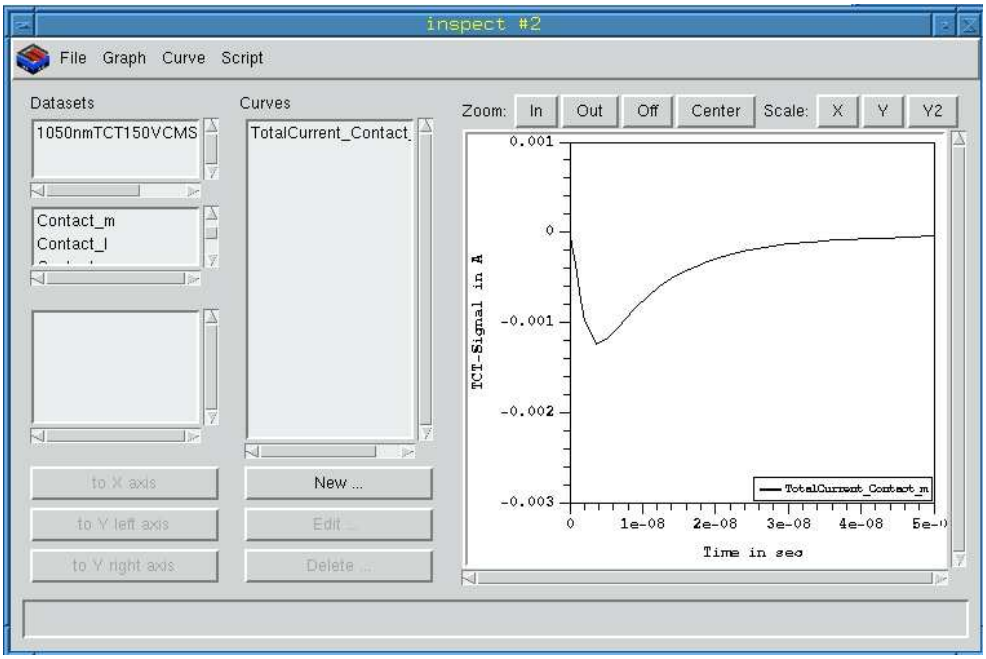

Figure D.2: Screenshot of the analysing tool INSPECT

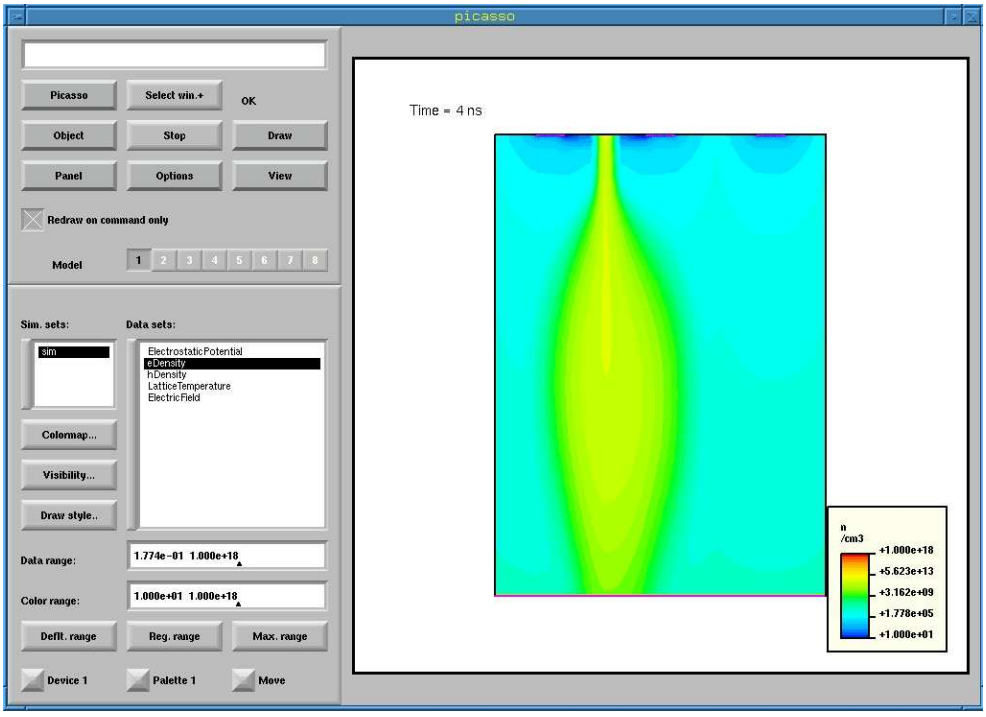

Figure D.3: Screenshot of PICASSO

Appendix E

Kinetic Equation Approach to the Hall Angle

The following derivation of the Lorentz angle follows [Pop91]:
The transport of the charge carriers is described by the Boltzmann kinetic equation:

$$\frac{\partial \mathcal{F}}{\partial t} = -\nabla_r \mathcal{F} \cdot \vec{v} - \nabla_k \mathcal{F} \frac{\vec{F}}{\hbar} - \nabla_k \mathcal{F} \cdot \frac{\vec{F}_c}{\hbar} \equiv \left(\frac{\partial \mathcal{F}}{\partial t}\right)_{ext.force} + \left(\frac{\partial \mathcal{F}}{\partial t}\right)_{collisions} \tag{E.1}$$

where $\mathcal{F} = \mathcal{F}(\vec{k}, \vec{r}, t)$ is the distribution function, $\vec{F}$ is the force caused by external fields and $\vec{F}_c$ represents the effect of scattering. In the relaxation time approximation the restoration rate back to equilibrium is proportional to the displacement from equilibrium and thus in steady state it becomes:

$$\frac{\vec{F}}{\hbar} \cdot \nabla_k \mathcal{F}(\vec{k}) = -\frac{\mathcal{F}(\vec{k}, t) - \mathcal{F}_0(\vec{k})}{\tau(\vec{k})} \tag{E.2}$$

The external fields cause a small disturbance $\mathcal{F}_1(\vec{k})$

$$\mathcal{F}(\vec{k}) = \mathcal{F}_0(\vec{k}) + \mathcal{F}_1(\vec{k}) \tag{E.3}$$

which is put into (E.2):

$$\mathcal{F}_1(\vec{k}) = -\frac{\tau(\vec{k})}{\hbar} \vec{F} \cdot \nabla_k [\mathcal{F}_0(\vec{k}) + \mathcal{F}_1(\vec{k})] \equiv -\frac{1}{\hbar} \frac{\partial \mathcal{F}_0}{\partial E} \vec{X} \frac{\partial E}{\partial \vec{k}} = -\frac{\partial \mathcal{F}_0}{\partial E} \vec{X} \cdot \vec{v} \tag{E.4}$$

where $\vec{v} = \hbar \vec{k}/m(\vec{k})$. The unknown trial function $\vec{X}$ must tend to $\vec{X} \simeq \tau(\vec{k}) e \vec{E}$ for vanishing magnetic field. Substituting (E.4) and the derivatives of $\mathcal{F}_0(\vec{k})$ and $\mathcal{F}_1(\vec{k})$ into (E.3) and considering only small electric fields one gets the vector equation

$$\vec{X} \simeq e\tau(\vec{k})\vec{E} + \frac{e\tau(\vec{k})}{m(\vec{k})} [\vec{X} \times \vec{B}] \tag{E.5}$$

with the solution

$$\vec{X} = \frac{e\tau(\vec{k})\vec{E} + (e^2\tau(\vec{k})^2/m(\vec{k}))[\vec{E} \times \vec{B}] + (e^3\tau(\vec{k})^3/m(\vec{k}^2))\vec{B}(\vec{E} \cdot \vec{B})}{1 + (e^2\tau(\vec{k})^2/m(\vec{k})^2)B^2} \tag{E.6}$$

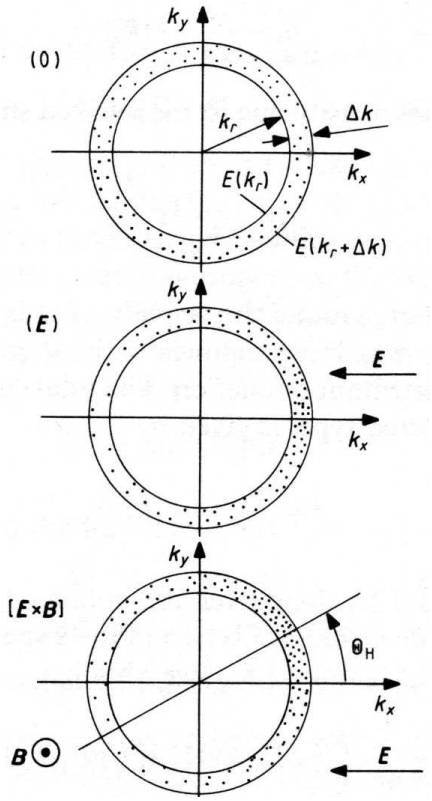

Figure E.1: Non-equilibrium distribution function after [Pop91]

With the assumption that $\vec{E} \cdot \vec{B} = 0$ one finally gets for the non-equilibrium distribution function [Pop91]:

$$\mathcal{F}(\vec{k}) \simeq \mathcal{F}_0(\vec{k}) - \frac{\partial \mathcal{F}_0}{\partial E} \mu(\vec{k}) \hbar \vec{k} \cdot \frac{\vec{E} + \mu(\vec{k})[\vec{E} \times \vec{B}]}{1 + \mu(\vec{k})^2 B^2} \tag{E.7}$$

with $\mu(\vec{k}) = q\tau(\vec{k})/m(\vec{k})$. The current density defined by

$$\vec{J} = \frac{e}{4\pi^3} \int_{dV_k} \vec{v} \mathcal{F}(\vec{k})\, dV_k \tag{E.8}$$

can be written as

$$\vec{J} = e^2 \mathcal{K}_1 \vec{E} + \frac{e^3}{m^*} \mathcal{K}_2 [\vec{E} \times \vec{B}] + \frac{e^4}{m^{*2}} \mathcal{K}_3 \vec{B} (\vec{E} \cdot \vec{B}) \tag{E.9}$$

with the kinetic coefficients

$$\mathcal{K}_s = -\frac{1}{4\pi^3} \int_{V_k} \left(\vec{v} \frac{\hbar \vec{k}}{m(\vec{k})} \right) \frac{\tau(\vec{k})^s}{1 + \mu(\vec{k})^2 B^2} \frac{\partial \mathcal{F}_0}{\partial E}\, dV_k \tag{E.10}$$

Considering (E.9) for $\vec{B} \perp \vec{E}$ reduces to

$$\vec{J} = \sigma_B \vec{E} + \sigma_B \mu_H [\vec{E} \times \vec{B}] \tag{E.11}$$

with $\sigma_B = e^2 \mathcal{K}_1$ and $\mu_H = e/m^* \mathcal{K}_2/\mathcal{K}_1$. The Hall angle is then given as:

$$\tan \Theta_H = \mu_H B \tag{E.12}$$

For small magnetic inductions the Hall mobility becomes $\mu_H = e/m^* \langle \tau^2 \rangle / \langle \tau \rangle$ and the Hall scattering factor $r_H = \langle \tau^2 \rangle / \langle \tau \rangle^2$.

The assumptions made here are:

- Applicability of the relaxation time approximation (E.2)
- Steady-state conditions
- Small disturbance of the distribution function (E.4)
- Spherical constant energy surfaces
- Low frequencies of the biasing current and the magnetic field
- Neutrality condition is fulfilled throughout the device; no space charge
- No generation and recombination of carriers
- No considerable gradients in carrier densities

Appendix F

Time of Free Flight

The derivation of formula (5.15), which gives the time of free flight, is presented in this chapter after [Mog87].
The duration of the free flight of particles is stochastically distributed. The probability that a scattering event happens in the k's time interval Δt_k is

$$P_k \Delta t_k = \Gamma(t_k)\Delta t_k \tag{F.1}$$

where t_k lies in that time interval. $\Gamma(t_k) = 1/\tau(t_k)$ is the scattering rate and just the inverse of the scattering time.
The chance that the event does not happen in a previous interval j is one minus the probability that it does happen:

$$P_j \Delta t_j = 1 - \Gamma(t_j)\Delta t_j \qquad \text{for} \quad j = 1, 2, 3, \ldots, k-1 \tag{F.2}$$

The probability P that the event happens just in the interval k is the product of (F.1) and the $k-1$ expressions in the form of (F.2), since an event in one interval is stochastically independent of what happens in any other:

$$P\Delta t_k = \prod_{j=1}^{k-1} P_j \Delta t_j P_k \Delta t_k = \prod_{j=1}^{k-1} (1 - \Gamma(t_j)\Delta t_j)\Gamma(t_k)\Delta t_k \tag{F.3}$$

To evaluate this expression take the natural logarithm:

$$\ln(P\Delta t_k) = \sum_{j=1}^{k-1} \ln[1 - \Gamma(t_j)\Delta t_j] + \ln[\Gamma(t_k)\Delta t_k] \overset{\Delta t_j \text{ small}}{\approx} -\sum_{j=1}^{k-1} \Gamma(t_j)\Delta t_j + \ln[\Gamma(t_k)\Delta t_k] \tag{F.4}$$

And for intervals of infinitesimal length the expression

$$P(t)\ dt = \Gamma(t) \exp\left[-\int_0^t \Gamma(t')\ dt' \right] dt \tag{F.5}$$

represents the probability density that the next event occurs at time t after the previous one. $P(t)$ is a monotonously growing function and satisfies:

$$\int_0^\infty P(t)\ dt = 1 \tag{F.6}$$

For any function $f(t)$, which satisfies these conditions, a random number r' can be generated with the stochastic density $f(t)$ by a flat random number r of uniform distribution:

$$\int_{t_s}^{r'} f(t)\ dt = r \tag{F.7}$$

This can now be applied to (F.5) and one can calculate the time of free flight t_f using a flat random number r:

$$\int_0^{t_f} \Gamma(t) \exp\left[- \int_0^t \Gamma(t')\ dt' \right] dt = r \tag{F.8}$$

Acknowledgement

This work covers a broad spectrum of topics and methods, which could not be realised without the support and help of my referents and colleagues. Here I would like to thank all of them.
I want to thank Prof. Wim de Boer for the opportunity to perform this work, for the scientific freedom he gave me and for his trust in my capabilities.
Prof. Thomas Müller gave me the pleasure to take the co-reference and for his support of my work I am very grateful.
Dr. Frank Hartmann always took the time for discussions. He is the guard of our probe lab and supported the IQC with his broad knowledge about sensor testing. Thank you Frank!
For the help in measuring the sensors and performing the irradiations I have to thank many people, as they are in alphabetic order: Hannes Bol, Alexander Furgeri, Eugene Grigoriev, Frank Hartmann, Cedric Menge and Thomas Punz.
Here I also want to thank the cyclotron crew at the Forschungszentrum, which did their best to deliver the protons and integrate our setup.
I would like to thank our 'module group' for the good collaboration and discussions: Guido Dirkes, Manuel Fahrer, Stefan Heier, Thomas Weiler.
Also many thanks go to Dr. Peter Blüm for the coordination of the CMS activities and to Dr. Hans-Jürgen Simonis for solving many computer and network problems.
For his help in constructing new mechanics and avoiding trouble with the workshop I want to thank Tobias Barvich.
The Lorentz angle measurements were performed together with Hannes Bol, Eugene Grigoriev, Florian Hauler, Stephan Heising and Levin Jungermann. They have also contributed to many fruitful discussions. Therefore I want to thank them.
Warm thanks also go to the administration in person Mrs. Haas and Mrs. Fellner-Thedens.
Last but not least I am grateful for the support from my girlfriend Nicole and my family.

List of Figures

List of Tables

Bibliography

[B+00a] K. Borer et al. Charge collection efficiency of irradiated silicon detector operated at cryogenic temperatures. *Nucl. Instrum. Meth.*, A(440):5 – 16, 2000. RD39 Collaboration.

[B+00b] S. Braibant et al. Investigation of design parameters and choise of substrate resistivity and crystal orientation for the CMS silicon mircostrip detector. CMS Note 2000/011, CERN, CH-1211 Geneva 23, Switzerland, 2000.

[Bla68] Frank J. Blatt. *Physics of Electronic Conduction in Solids.* McGraw-Hill, Hamburg, New York, London, Paris, Tokio, 1968.

[BMFM03] L. Borrello, A. Messineo, E. Focardi, and A. Macchiolo. Sensor Design for the CMS Silicon Strip Tracker. CMS Note 2003/020, CERN, CH-1211 Geneva 23, Switzerland, 2003.

[Bol00] Johannes Bol. Untersuchung von Streifen- und Pixeldetektoren bei starken Magnetfeldern und tiefen Temperaturen. Diplomarbeit, Universität Karlsruhe, 2000.

[C+00] C.Y. Chien et al. New design of CMS silicon pixel detectors for radiation hardness. *Nucl. Instrum. Meth.*, A(455):564 – 575, 2000.

[CJN+75] C. Canali, C. Jacoboni, F. Nava, G. Ottaviani, and A. Alberigi-Quaranta. Electron drift velocity in silicon. *Physical Review B*, 12(4):2265 – 2284, 1975.

[CMMO75] C. Canali, G. Majni, R. Minder, and G. Ottaviani. Electron and hole drift velocity measurements in silicon and their empirical relation to electric field and temperature. *IEEE Trans. on Electron Devices*, ED-22:1045–1047, 1975.

[CMS] Drawing from CMSIM. Web link. http://cmsinfo.cern.ch/Welcome.html/CMSdocuments/DetectorDrawings/DetectorDrawings.html.

[Col00] The CMS Collaboration. Addendum to the CMS tracker TDR. CERN/LHCC 2000/016, CERN, CH-1211 Geneva 23, Switzerland, 2000.

[Col02] RD39 Collaboration. Radiation hard cryogenic silicon detectors. *Nucl. Instrum. Meth.*, A(477):299 – 303, 2002.

[dB+01a] W. de Boer et al. Lorentz angle measurements in irradiated silicon detectors between 77 K and 300 K. *Nucl. Instrum. Meth.*, A461:200 – 203, 2001.

[dB+01b] W. de Boer et al. Lorentz angle measurements in silicon detectors. LC-DET-2001-028, DESY, 2001.

[Die02] A. Dierlamm. CMS Silicon Tracker - Milestone 200. In *Proceedings of the 7th International Conference on Advanced Technology & Particle Physics*, pages 219 – 223. World Scientific, 2002.

[Die03] A. Dierlamm. Irradiation Qualification of CMS Silicon Tracker Components with Protons. *Nucl. Instrum. Meth.*, A, 2003. to be published.

[Dir03] Guido Dirkes. *Development and Implementation of Quality Control Strategies for CMS Silicon Strip Tracker Modules.* PhD thesis, Inst. für Exp. Kernphysik, Univ. Karlsruhe, 2003.

[ES92] R. Enderlein and A. Schenk. *Grundlagen der Halbleiterphysik.* Akademie Verlag, 1992.

[ESVL96] V. Eremin, N. Strokan, E. Verbitskaya, and Z. Li. Development of transient current and charge techniques for the measurement of effective net concentration of ionized charge (n_{eff}) in the space charge region of p-n junction detectors. *Nucl. Instrum. Meth.*, A(372):388 – 398, 1996.

[FGH98] L. Feld, W.D. Glessing, and R. Hammerström. Thermal properties of the silicon microstrip endcap detector. CMS Note 1998/018, CERN, CH-1211 Geneva 23, Switzerland, 1998.

[Fis03] P. Fischer. Design considerations for pixel readout chips. *Nucl. Instrum. Meth.*, A(501):175 – 182, 2003.

[FKL+98] E. Fretwurst, M. Kuhnke, G. Lindström, M. Moll, and Z. Li. Damage results from Co60 gamma irradiation in Si-diodes fabricated from several different materials. In *4^{th} ROSE Workshop on Radiation Hardening of Silicon Detectors.* CERN/LEB 98-11, Dec 1998.

[Fri01] Markus Friedl. *The CMS Silicon Strip Tracker and its Electronic Readout.* PhD thesis, Vienna University of Technology, Vienna, May 2001.

[H+97] H. Hofer et al. CMS - The Electromagnetic Calorimeter. CERN/LHCC 1997/033, CERN, CH-1211 Geneva 23, Switzerland, Dec 1997.

[H+02] F. Hauler et al. Lorentz angle measurements in silicon detectors. *Nucl. Instrum. Meth.*, A478:330 – 332, 2002.

[Har01] Frank Hartmann. The CMS all-silicon tracker – strategies to ensure a high quality and radiation hard silicon detector. *Nucl. Instrum. Meth.*, A(478):285 – 287, 2001.

[Hau00] Floarian Hauler. Lorentzwinkelmessungen an bestrahlten Silizium-Streifendetektoren im Temperaturbereich T=77-300K. Diplomarbeit, Universität Karlsruhe, 2000.

[Hei00] Stephan Heising. *Halbleiterdetektoren für Hochenergie-Experimente bei tiefen Temperaturen und starken Magnetfeldern.* PhD thesis, Universität Karlsruhe, 2000.

[Hei03] S. Heier. Module qualification. Private communication, 2003.

[Huh01] M. Huhtinen. Simulation of non-ionising energy loss and defect formation in silicon. ROSE/TN/ 02, CERN, CH-1211 Geneva 23, Switzerland, 2001.

[J+99] L.L. Jones et al. The APV25 deep submicron readout chip for CMS detectors. In *5th Workshop on Electronics for the LHC Experiments (LEB99)*, Snowmass, Colorado, 1999.

[K+01] D. Kotlinski et al. The CMS pixel detector. *Nucl. Instrum. Meth.*, A(465):46 – 50, 2001.

[K+03] M Krammer et al. The Silicon Sensors for the Compact Muon Solenoid Tracker - Design and Qualification Procedure. CMS Note 2003/015, CERN, CH-1211 Geneva 23, Switzerland, 2003. submitted to NIM A.

[Kra01] Gregor Kramberger. *Signal development in irradiated silicon detectors*. PhD thesis, University of Ljubljana, 2001.

[KS01] Danek Kotlinski and Andrey Starodumov. High level tracker triggers for CMS. *Nucl. Instrum. Meth.*, A501:222 – 228, 2001.

[Len01] M. Lenzi. Performance of the all-silicon CMS tracker. *Nucl. Instrum. Meth.*, A(473):31 – 38, 2001.

[LHCa] LHC-drawing-half. Web link. http://livefromcern.web.cern.ch/livefromcern /antimatter/history/historypictures/LHC-drawing-half.jpg.

[LHCb] LHCtunnel2001. Web link. http://acwebimages.cern.ch/ImagesJPG/ LHCtunnel2001.jpg.

[LN62] J. Lindhard and V. Nielsen. Nuclear collisions and ionisation fluctuations in charged particle detectors. *Phys. Lett.*, 2(5):209 – 211, 1962.

[Lut96] G. Lutz. Effects of deep level defects in semiconductor detectors. *Nucl. Instrum. Meth.*, A(377):234 – 243, 1996.

[Lut99] Gerhard Lutz. *Semiconductor Radiation Detectors*. Springer, Berlin, Heidelberg, New York, London, Paris, Tokyo, 1999.

[MFF+97] M. Moll, H. Feick, E. Fretwurst, G. Lindström, and C. Schütz. Comparison of defects produced by fast neutrons and ^{6}0co-gammas in high-resistivity silicon detectors using deep-level transient spectroscopy. *Nucl. Instrum. Meth.*, A(388):335 – 339, 1997.

[MHG96] B.C. MacEvoy, G. Hall, and K. Gill. Defect evolution in irradiated silicon detector material. *Nucl. Instrum. Meth.*, A(374):12 – 26, 1996.

[Mog87] C. Moglestue. *Monte Carlo simulations in Semiconductors*. Chapman and Hall, London, Weinheim, New York, Tokyo, 1987.

[Mol99] Michael Moll. *Radiation Damage in Silicon Particle Detectors*. PhD thesis, DESY, Dec 1999.

[Mol00] M. Moll. Summary of the 3rd ROSE Status Report. In *5^{th} ROSE Workshop on Radiation Hardening of Silicon Detectors*, CERN, Geneva, Switzerland, 2000. CERN/LEB 2000-005.

[Moy55] J.E. Moyal. Theory of ionization fluctuations. *Phil. Mag.*, 46:263, 1955.

[Mül98] Th. Müller. The CMS tracker and its performance. *Nucl. Instrum. Meth.*, A(408):119 – 127, 1998.

[Outa] CMS Outreach. Heavy ions in CMS. Web link. http://cmsinfo.cern.ch/Welcome.html/CMSdetectorInfo/HeavyIons/page1.html.

[Outb] CMS Outreach. Supersymmetry physics in CMS. Web link. http://cmsinfo.cern.ch/Welcome.html/CMSdetectorInfo/NewPhysics/page1.html.

[Pop91] RS Popović. *Hall effect devices*. Adam Hilger, 1991.

[Pro98] The Tracker Project. Tracker technical design report. CERN/LHCC 1998/006, CERN, CH-1211 Geneva 23, Switzerland, 1998.

[RGB81] H.J. Rijks, L.J. Giling, and J. Bloem. Influence of charge carrier scattering on the exact form of the Hall curve. *J. Appl. Phys.*, 52:472 – 475, 1981.

[SL89] G.K. Schenter and R.L. Liboff. Analytical distribution for charge carriers in a semiconductor dominated by equivalent intervalley scattering. *Physical Review B*, 40(8):5624 – 5631, 1989.

[Str70] H.W. Streitwolf. Intervalley scattering selection rules for Si and Ge. *Physica Status Solidi*, 37:K47, 1970.

[Sze81] S.M. Sze. *Physics of Semiconductor Devices*. John Wiley and Sons, NewYork, Chichester, Brisbane, Toronto, 1981.

[vLFL$^+$80] V.A.J. van Lint, T.M. Flanagan, R.E. Leadon, J.A. Naber, and V.C. Rogers. *Mechanisms of radiation effects in electronic materials*, volume 1. John Wiley and Sons, NewYork, Chichester, Brisbane, Toronto, 1980.

[W$^+$01] J. Wüstenfeld et al. Surface effects before and after ionisation-induced surface defects. In *6th ROSE Workshop on Radiation Hardening of Silicon Detectors*, 2001.

[W$^+$03] Th. Weiler et al. Infrared LED Array for Silicon Strip Detector Qualification. CMS Note 2003/023, CERN, CH-1211 Geneva 23, Switzerland, 2003.

[Wei03] Th. Weiler. Module qualification. Private communication, 2003.

Index